ESKİŞEHİR TECHNICAL UNIVERSITY
JOURNAL OF SCIENCE AND TECHNOLOGY

A – Applied Sciences and Engineering

Eskişehir Technical University Journal of Science and Technology A - Applied Sciences and Engineering (Other variant title: **Estuscience-Se**) is a peer-reviewed and refereed international journal published by Eskişehir Technical University. Since 2000, it has been regularly published and distributed biannually and it has been published quarterly and only electronically since 2016.

The journal accepts only manuscripts written in English.
The journal issues are published electronically in **March, June**, **September**, and **December**.

Eskişehir Technical University Journal of Science and Technology A - Applied Sciences and Engineering is an international peer-reviewed and refereed journal published by Eskişehir Technical University.

The journal is dedicated to the dissemination of knowledge in applied sciences and engineering disciplines.

The journal aims to publish high quality, original international scientific research articles with specific contributions to the literature in the field of engineering and applied sciences. The journal publishes research papers in the fields of applied science and technology such as Physics, Biology, Mathematics, Statistics, Chemistry and Chemical Engineering, Environmental Sciences and Engineering, Civil Engineering, Earth and Atmospheric Sciences, Electrical and Electronical Engineering, Computer Science and Informatics, Materials Sciences and Engineering, Mechanical Engineering, Mining Engineering, Industrial Engineering, Aeronautics and Astronautics, Pharmaceutical Sciences.

The journal publishes original research articles and special issue articles. All articles are peer-reviewed and the articles that have been evaluated are ensured to meet with researchers as soon as possible.

"Anadolu Üniversitesi Bilim ve Teknoloji Dergisi A - Uygulamalı Bilimler ve Mühendislik (Anadolu University Journal of Science and Technology A - Applied Sciences and Engineering)" published within Anadolu University started to be published within Eskişehir Technical University which was established due to statute law 7141, in 2018. Hence, the name of the journal is changed to " Eskişehir Technical University Journal of Science and Technology A - Applied Sciences and Engineering (Eskişehir Teknik Üniversitesi Bilim ve Teknoloji Dergisi A - Uygulamalı Bilimler ve Mühendislik)".

The Journal's Other Variant Title: **Estusicence-Se;** aproved by ISSN National Centre for Türkiye on April 30, 2024.

Indexed by **ULAKBIM TR Dizin,**

ABOUT

Eskişehir Technical University Journal of Science and Technology A - Applied Sciences and Engineering (Estuscience-Se) is a peer-reviewed and refereed international journal published by Eskişehir Technical University. Since 2000, it has been regularly published and distributed biannually and it has been published quarterly and only electronically since 2016.

The journal accepts only manuscripts written in English.

The journal issues are published electronically in **MARCH, JUNE, SEPTEMBER**, and **DECEMBER.**

AIM AND SCOPE

Eskişehir Technical University Journal of Science and Technology A - Applied Sciences and Engineering is an international peer-reviewed and refereed journal published by Eskişehir Technical University.

The journal is dedicated to the dissemination of knowledge in applied sciences and engineering disciplines.

The journal aims to publish high quality, original international scientific research articles with specific contributions to the literature in the field of engineering and applied sciences. The journal publishes research papers in the fields of applied science and technology such as Physics, Biology, Mathematics, Statistics, Chemistry and Chemical Engineering, Environmental Sciences and Engineering, Civil Engineering, Earth and Atmospheric Sciences, Electrical and Electronical Engineering, Computer Science and Informatics, Materials Sciences and Engineering, Mechanical Engineering, Mining Engineering, Industrial Engineering, Aeronautics and Astronautics, Pharmaceutical Sciences.

The journal publishes original research articles and special issue articles. All articles are peer-reviewed and the articles that have been evaluated are ensured to meet with researchers as soon as possible.

PEER REVIEW PROCESS

Manuscripts are first reviewed by the editorial board in terms of its its journal's style rules scientific content, ethics and methodological approach. If found appropriate, the manuscript is then send to at least two renown referees by editor. The decision in line with the referees may be an acceptance, a rejection or an invitation to revise and resubmit. Confidential review reports from the referees will be kept in archive. All submission process manage through the online submission systems.

OPEN ACCESS POLICY

This journal provides immediate open access to its content on the principle that making research freely available to the public supports a greater global exchange of knowledge. Copyright notice and type of licence : **CC BY-NC-ND.**

PRICE POLICY

Eskişehir Technical University Journal of Science and Technology A - Journal of Applied Sciences and Engineering is an English, peer-reviewed, scientific, free of charge open-access-based journal. The author is not required to pay any publication fees or article processing charges (APCs) for peer-review administration and management, typesetting, and open-access. Articles also receive Digital Object Identifiers (DOIs) from the CrossRef organization to ensure they are always available.

ETHICAL RULES
You can reach the Ethical Rules in our journal in full detail from the link below:

https://dergipark.org.tr/en/pub/estubtda/policy

Ethical Principles and Publication Policy

Policy & Ethics
Assessment and Publication

As a peer-reviewed journal, it is our goal to advance scientific knowledge and understanding. We have outlined a set of ethical principles that must be followed by all authors, reviewers, and editors.

All manuscripts submitted to our journals are pre-evaluated in terms of their relevance to the scope of the journal, language, compliance with writing instructions, suitability for science, and originality, by taking into account the current legal requirements regarding copyright infringement and plagiarism. Manuscripts that are evaluated as insufficient or non-compliant with the instructions for authors may be rejected without peer review.

Editors and referees who are expert researchers in their fields assess scientific manuscripts submitted to our journals. A blind peer review policy is applied to the evaluation process. The Editor-in-Chief, if he/she sees necessary, may assign an Editor for the manuscript or may conduct the scientific assessment of the manuscript himself/herself. Editors may also assign referees for the scientific assessment of the manuscript and make their decisions based on reports by the referees. Articles are accepted for publication on the understanding that they have not been published and are not going to be considered for publication elsewhere. Authors should certify that neither the manuscript nor its main contents have already been published or submitted for publication in another journal.

The Journal; Implements the Publication Policy and Ethics guidelines to meet high-quality ethical standards for authors, editors and reviewers:

Duties of Editors-in-Chief and co-Editors

The crucial role of the journal Editor-in-Chief and co-Editors is to monitor and ensure the fairness, timeliness, thoroughness, and civility of the peer-review editorial process. The main responsibilities of Editors-in-Chief are as follows:

• Selecting manuscripts suitable for publication while rejecting unsuitable manuscripts,
• Ensuring a supply of high-quality manuscripts to the journal by identifying important,
• Increasing the journal's impact factor and maintaining the publishing schedule,
• Providing strategic input for the journal's development,

Duties of Editors

The main responsibilities of editors are as follows:

• An editor must evaluate the manuscript objectively for publication, judging each on its quality without considering the nationality, ethnicity, political beliefs, race, religion, gender, seniority, or institutional affiliation of the author(s). Editors should decline any assignment when there is a potential for conflict of interest.
• Editors must ensure the document(s) sent to the reviewers does not contain information of the author(s) and vice versa.
• Editors' decisions should be provided to the author(s) accompanied by the reviewers' comments and recommendations unless they contain offensive or libelous remarks.
• Editors should respect requests (if well reasoned and practicable) from author(s) that an individual should not review the submission.
• Editors and all staff members should guarantee the confidentiality of the submitted manuscript.
• Editors should have no conflict of interest with respect to articles they reject/accept. They must not have a conflict of interest with the author(s), funder(s), or reviewer(s) of the manuscript.
• Editors should strive to meet the needs of readers and authors and to constantly improve the journal.

Duties of Reviewers/Referees

The main responsibilities of reviewers/referees are as follows:

• Reviewers should keep all information regarding papers confidential and treat them as privileged information.
• Reviews should be conducted objectively, with no personal criticism of the author.
• Reviewers assist in the editorial decision process and as such should express their views clearly with supporting arguments.
• Reviewers should complete their reviews within a specified timeframe (maximum thirty-five (35) days). In the event that a reviewer feels it is not possible for him/her to complete the review of the manuscript within a stipulated time, then this information must be communicated to the editor so that the manuscript could be sent to another reviewer.
• Unpublished materials disclosed in a submitted manuscript must not be used in a reviewer's personal research without the written permission of the author. Information contained in an unpublished manuscript will remain confidential and must not be used by the reviewer for personal gain.
• Reviewers should not review manuscripts in which they have conflicts of interest resulting from competitive, collaborative, or other relationships or connections with any of the authors, companies, or institutions connected to the papers.

• Reviewers should identify similar work in published manuscripts that has not been cited by the author. Reviewers should also notify the Editors of significant similarities and/or overlaps between the manuscript and any other published or unpublished material.

__Duties of Authors__
The main responsibilities of authors are as follows:

• The author(s) should affirm that the material has not been previously published and that they have not transferred elsewhere any rights to the article.
• The author(s) should ensure the originality of the work and that they have properly cited others' work in accordance with the reference format.
• The author(s) should not engage in plagiarism or in self-plagiarism.
• On clinical and experimental humans and animals, which require an ethical committee decision for research in all branches of science;
All kinds of research carried out with qualitative or quantitative approaches that require data collection from the participants by using survey, interview, focus group work, observation, experiment, interview techniques,
Use of humans and animals (including material/data) for experimental or other scientific purposes,
• Clinical studies on humans,
• Studies on animals,
• Retrospective studies in accordance with the law on the protection of personal data, (Ethics committee approval should have been obtained for each individual application, and this approval should be stated and documented in the article.)
Information about the permission (board name, date, and number) should be included in the "Method" section of the article and also on the first/last page.
During manuscript upload, the "Ethics Committee Approval" file should be uploaded to the system in addition to the manuscript file.
In addition, in case reports, it is necessary to include information on the signing of the informed consent/ informed consent form in the manuscript.
• The author(s) should suggest no personal information that might make the identity of the patient recognizable in any form of description, photograph, or pedigree. When photographs of the patient were essential and indispensable as scientific information, the author(s) have received consent in written form and have clearly stated as much.
• The author(s) should provide the editor with the data and details of the work if there are suspicions of data falsification or fabrication. Fraudulent data shall not be tolerated. Any manuscript with suspected fabricated or falsified data will not be accepted. A retraction will be made for any publication which is found to have included fabricated or falsified data.
• The author(s) should clarify everything that may cause a conflict of interests such as work, research expenses, consultant expenses, and intellectual property.
• The author(s) must follow the submission guidelines of the journal.
• The author(s) discover(s) a significant error and/or inaccuracy in the submitted manuscript at any time, then the error and/or inaccuracy must be reported to the editor.
• The author(s) should disclose in their manuscript any financial or other substantive conflicts of interest that might be construed to influence the results or interpretation of their manuscript. All sources of financial support should be disclosed under the heading of "Acknowledgment" or "Contribution".
• The corresponding author(s) must ensure that all appropriate co-authors are not included in the manuscript, that author names are not added or removed and that the authors' address information is not changed after the review begins and that all co-authors see and approve the

final version of the manuscript at every stage of the manuscript. All significant contributors should be listed as co-authors. Other individuals who have participated in significant aspects of the research work should be considered contributors and listed under "Author Contribution".

Cancellations/Returns

Articles/manuscripts may be returned to the authors in order to increase the authenticity and/or reliability and to prevent ethical breaches, and even if articles have been accepted and/or published, they can be withdrawn from publication if necessary. The Editor-in-Chief of the journal has the right to return or withdraw an article/manuscript in the following situations:

• When the manuscript is not within the scope of the journal,
• When the scientific quality and/or content of the manuscript do not meet the standards of the journal and a referee review is not necessary,
• When there is proof of ruling out the findings obtained by the research, (When the article/manuscript is undergoing an assessment or publication process by another journal, congress, conference, etc.,)
• When the article/manuscript was not prepared in compliance with scientific publication ethics,
• When any other plagiarism is detected in the article/manuscript,
• When the authors do not perform the requested corrections within the requested time (maximum twenty-one (21) days),
• When the author does not submit the requested documents/materials/data etc. within the requested time,
• When the requested documents/materials/data etc. submitted by the author are missing for the second time,
• When the study includes outdated data,
• When the authors make changes that are not approved by the editor after the manuscript was submitted,
• When an author is added/removed, the order of the authors is changed, the corresponding author is altered, or the addresses of the authors are changed in the article that is in the evaluation process,
• When a statement is not submitted indicating that approval of the ethics committee permission was obtained for the following (including retrospective studies):
• When human rights or animal rights are violated,

ETHICAL ISSUES

Plagiarism

The use of someone else's ideas or words without a proper citation is considered plagiarism and will not be tolerated. Even if a citation is given, if quotation marks are not placed around words taken directly from other authors' work, the author is still guilty of plagiarism. Reuse of the author's own previously published words, with or without a citation, is regarded as self-plagiarism.

All manuscripts received are submitted to iThenticate®, which compares the content of the manuscript with a database of web pages and academic publications. Manuscripts are judged to be plagiarized or self-plagiarized, based on the iThenticate® report or any other source of information, will be rejected. Corrective actions are proposed when plagiarism and/or self-plagiarism is detected after publication. Editors should analyze the article and decide whether a corrected article or retraction needs to be published.

Open-access theses are considered as published works and they are included in the similarity checks.

iThenticate® report should have a maximum of 11% from a single source, and a maximum of 25% in total.

Conflicts of Interest

Eskişehir Technical University Journal of Science and Technology A - Applied Sciences and Engineering should be informed of any significant conflict of interest of editors, authors, or reviewers to determine whether any action would be appropriate (e.g. an author's statement of conflict of interest for a published work, or disqualifying a referee).

Financial

The authors and reviewers of the article should inform the journal about the financial information that will bring financial gain or loss to any organization from the publication of the article.

*Research funds; funds, consulting fees for a staff member; If you have an interest, such as patent interests, you may have a conflict of interest that needs to be declared.

Other areas of interest

The editor or reviewer may disclose a conflict of interest that, if known, would be embarrassing (for example, an academic affiliation or rivalry,a close relationship or dislike, or a person who may be affected by the publication of the article).

Conflict of interest statement

Please note that a conflict of interest statement is required for all submitted manuscripts. If there is no conflict of interest, please state "There are no conflicts of interest to declare" in your manuscript under the heading "Conflicts of Interest" as the last section before your Acknowledgments.

AUTHOR GUIDELINES

All manuscripts must be submitted electronically.

You will be guided stepwise through the creation and uploading of the various files. There are no page charges. Papers are accepted for publication on the understanding that they have not been published and are not going to be considered for publication elsewhere. Authors should certify that neither the manuscript nor its main contents have already been published or submitted for publication in another journal. We ask a signed copyright to start the evaluation process. After a manuscript has been submitted, it is not possible for authors to be added or removed or for the order of authors to be changed. If authors do so, their submission will be cancelled.

Manuscripts may be rejected without peer review by the editor-in-chief if they do not comply with the instructions to authors or if they are beyond the scope of the journal. After a manuscript has been accepted for publication, i.e. after referee-recommended revisions are complete, the author will not be permitted to make any changes that constitute departures from the manuscript that was accepted by the editor. Before publication, the galley proofs are always sent to the authors for corrections. Mistakes or omissions that occur due to some negligence on our part during final printing will be rectified in an errata section in a later issue.

This does not include those errors left uncorrected by the author in the galley proof. The use of someone else's ideas or words in their original form or slightly changed without a proper citation is considered plagiarism and will not be tolerated. Even if a citation is given, if quotation marks are not placed around words taken directly from another author's work, the author is still guilty of plagiarism. All manuscripts received are submitted to iThenticateR, a plagiarism checking system, which compares the content of the manuscript with a vast database of web pages and academic publications. In the received iThenticateR report; The similarity rate is expected to be below 25%. Articles higher than this rate will be rejected.

Uploading Articles to the Journal
Authors should prepare and upload 2 separate files while uploading articles to the journal. First, the Author names and institution information should be uploaded so that they can be seen, and then (using the additional file options) a separate file should be uploaded with the Author names and institution information completely closed. When uploading their files with closed author names, they will select the "Show to Referee" option, so that the file whose names are closed can be opened to the referees.

Prepatation of Manuscript

Style and Format
Manuscripts should be **single column** by giving one-spaced with 2.5-cm margins on all sides of the page, in Times New Roman font (font size 11). Every page of the manuscript, including the title page, references, tables, etc., should be numbered. All copies of the manuscript should also have line numbers starting with 1 on each consecutive page.

Manuscripts must be upload as word document (*.doc, *.docx vb.). **Please avoid uploading** *texts in *.pdf format.*

Symbols, Units and Abbreviations
Standard abbreviations and units should be used; SI units are recommended. Abbreviations should be defined at first appearance, and their use in the title and abstract should be avoided. Generic names of chemicals should be used. Genus and species names should be typed in italic or, if this is not available, underlined.

Please refer to equations with capitalisation and unabbreviated (e.g., as given in Equation (1)).

Manuscript Content
Articles should be divided into logically ordered and numbered sections. Principal sections should be numbered consecutively with Arabic numerals (1. Introduction, 2. Formulation of problem, etc.) and subsections should be numbered 1.1., 1.2., etc. Do not number the Acknowledgements or References sections. The text of articles should be, if possible, divided into the following sections: Introduction, Materials and Methods (or Experimental), Results, Discussion, and Conclusion.

Title and contact information
The first page should contain the full title in sentence case (e.g., Hybrid feature selection for text classification), the full names (last names fully capitalised) and affiliations (in English) of all authors (Department, Faculty, University, City, Country, E-mail), and the contact e-mail address for the clearly identified corresponding author. The first page should contain the full title, abstract and keywords (both English and Turkish).

Abstract
The abstract should provide clear information about the research and the results obtained, and should not exceed 300 words. The abstract should not contain citations and must be written in Times New Roman font with font size 9.

Keywords
Please provide 3 to 5 keywords which can be used for indexing purposes.

Introduction

The motivation or purpose of your research should appear in the "Introduction", where you state the questions you sought to answer, and then provide some of the historical basis for those questions.

Methods

Provide sufficient information to allow someone to repeat your work. A clear description of your experimental design, sampling procedures, and statistical procedures is especially important in papers describing field studies, simulations, or experiments. If you list a product (e.g., animal food, analytical device), supply the name and location of the manufacturer. Give the model number for equipment used.

Results

Results should be stated concisely and without interpretation.

Discussion

Focus on the rigorously supported aspects of your study. Carefully differentiate the results of your study from data obtained from other sources. Interpret your results, relate them to the results of previous research, and discuss the implications of your results or interpretations.

Conclusion

This should state clearly the main conclusions of the research and give a clear explanation of their importance and relevance. Summary illustrations may be included.

Acknowledgments

Acknowledgments of people, grants, funds, etc. should be placed in a separate section before the reference list. The names of funding organizations should be written in full.

Conflict of Interest Statement

The authors are obliged to present the conflict of interest statement at the end of the article after the acknowledgments section.

CRediT Author Statement

Write the authors' contributions in detail using the specified CRediT notifications. Authors may have contributed in more than one role. The corresponding author is responsible for ensuring that descriptions are accurate and accepted by all authors.

CRediT Notifications	Explanation
Conceptualization	Ideas; formulation or evolution of overarching research goals and aims
Methodology	Development or design of methodology; creation of models
Software	Programming, software development; designing computer programs; implementation of the computer code and supporting algorithms; testing of existing code components

Validation	Verification, whether as a part of the activity or separate, of the overall replication/ reproducibility of results/experiments and other research outputs
Formal analysis	Application of statistical, mathematical, computational, or other formal techniques to analyse or synthesize study data
Investigation	Conducting a research and investigation process, specifically performing the experiments, or data/evidence collection
Resources	Provision of study materials, reagents, materials, patients, laboratory samples, animals, instrumentation, computing resources, or other analysis tools
Data Curation	Management activities to annotate (produce metadata), scrub data and maintain research data (including software code, where it is necessary for interpreting the data itself) for initial use and later reuse
Writing – Original Draft	Preparation, creation and/or presentation of the published work, specifically writing the initial draft (including substantive translation)
Writing – Review & Editing	Preparation, creation and/or presentation of the published work by those from the original research group, specifically critical review, commentary, or revision – including pre-or post-publication stages
Visualization	Preparation, creation and/or presentation of the published work, specifically visualization/ data presentation
Supervision	Oversight and leadership responsibility for the research activity planning and execution, including mentorship external to the core team
Project administration	Management and coordination responsibility for the research activity planning and execution
Funding acquisition	Acquisition of the financial support for the project leading to this publication

References

Writting Style; **AMA; References Writting format** should be used in the reference writing of our journal. If necessary, at this point, the reference writings of the articles published in our article can be examined.

Citations in the text should be identified by numbers in square brackets. The list of references at the end of the paper should be given in order of their first appearance in the text. All authors should be included in reference lists unless there are 10 or more, in which case only the first 10 should be given, followed by 'et al.'. Do not use individual sets of square brackets for citation numbers that appear together, e.g., [2,3,5–9], not [2], [3], [5]–[9]. Do not include personal communications, unpublished data, websites, or other unpublished materials as references,

although such material may be inserted (in parentheses) in the text. In the case of publications in languages other than English, the published English title should be provided if one exists, with an annotation such as "(article in Turkish with an abstract in English)". If the publication was not published with an English title, cite the original title only; do not provide a self-translation. References should be formatted as follows (please note the punctuation and capitalisation):

Journal articles
Journal titles should be abbreviated according to ISI Web of Science abbreviations.
Guyon I, Elisseeff A. An introduction to variable and feature selection. J Mach Learn Res 2003; 3: 1157-1182.

Izadpanahi S, Ozcınar C, Anbarjafari G, Demirel H. Resolution enhancement of video sequences by using discrete wavelet transform and illumination compensation. Turk J Elec Eng & Comp Sci 2012; 20: 1268-1276.

Books
Haupt RL, Haupt SE. Practical Genetic Algorithms. 2nd ed. New York, NY, USA: Wiley, 2004.
Kennedy J, Eberhart R. Swarm Intelligence. San Diego, CA, USA: Academic Press, 2001.

Chapters in books
Poore JH, Lin L, Eschbach R, Bauer T. Automated statistical testing for embedded systems. In: Zander J, Schieferdecker I, Mosterman PJ, editors. Model-Based Testing for Embedded Systems. Boca Raton, FL, USA: CRC Press, 2012. pp. 111-146.

Conference proceedings
Li RTH, Chung SH. Digital boundary controller for single-phase grid-connected CSI. In: IEEE 2008 Power Electronics Specialists Conference; 15–19 June 2008; Rhodes, Greece. New York, NY, USA: IEEE. pp. 4562-4568.

Theses
Boynukalın Z. Emotion analysis of Turkish texts by using machine learning methods. MSc, Middle East Technical University, Ankara, Turkey, 2012.

Tables and Figures
All illustrations (photographs, drawings, graphs, etc.), not including tables, must be labelled "Figure." Figures must be submitted in the manuscript.

All tables and figures must have a caption and/or legend and be numbered (e.g., Table 1, Figure 2), unless there is only one table or figure, in which case it should be labelled "Table" or "Figure" with no numbering. Captions must be written in sentence case (e.g., Macroscopic appearance of the samples.). The font used in the figures should be Times New Roman. If symbols such as ×, μ, η, or ν are used, they should be added using the Symbols menu of Word.

All tables and figures must be numbered consecutively as they are referred to in the text. Please refer to tables and figures with capitalisation and unabbreviated (e.g., "As shown in Figure 2…", and not "Fig. 2" or "figure 2").

The resolution of images should not be less than 118 pixels/cm when width is set to 16 cm. Images must be scanned at 1200 dpi resolution and submitted in jpeg or tiff format. Graphs and diagrams must be drawn with a line weight between 0.5 and 1 point. Graphs and diagrams with

a line weight of less than 0.5 point or more than 1 point are not accepted. Scanned or photocopied graphs and diagrams are not accepted.

Figures that are charts, diagrams, or drawings must be submitted in a modifiable format, i.e. our graphics personnel should be able to modify them. Therefore, if the program with which the figure is drawn has a "save as" option, it must be saved as *.ai or *.pdf. If the "save as" option does not include these extensions, the figure must be copied and pasted into a blank Microsoft Word document as an editable object. It must not be pasted as an image file (tiff, jpeg, or eps) unless it is a photograph.

Tables and figures, including caption, title, column heads, and footnotes, must not exceed 16 × 20 cm and should be no smaller than 8 cm in width. For all tables, please use Word's "Create Table" feature, with no tabbed text or tables created with spaces and drawn lines. Please do not duplicate information that is already presented in the figures.

Article Corrections and Uploading to the System
Authors should upload the desired edits for their articles without destroying or changing the Template file of the article, by selecting and specifying the relevant edits as Colored, and also submit the Clean version of the article in 2 separate files (using the Additional file option if necessary). * In case of submitting a corrected article, a separate File in Reply to the Referees must be prepared and the "Reply to the Referees" option in the Add additional file option should be checked and uploaded. If a separate file is not prepared in response to the referees, the Author will definitely be asked to upload the relevant file again and the evaluation will be in the pending phase.

CONTENTS

RESEARCH ARTICLE

INVESTIGATION OF THE USE OF KÜTAHYA REGION KAOLIN IN WALL TILES

Senem ALGAN [1] [*], Fatih ÖZTÜRK [2], Büşra YAY [2], Zehra Emel OYTAÇ [2], Eda TAŞÇI [1]

[1] Kütahya Dumlupınar University, Department of Metallurgical and Materials Engineering, 43100, Kütahya, Türkiye
senemalgan4306@gmail.com - 0009-0008-6136-1631
[2] NG Kütahya Seramik A.Ş, Ar-Ge Merkezi, 43001, Kütahya, Türkiye
fatihozturk4388@gmail.com - 0009-0006-3625-5402
[3] NG Kütahya Seramik A.Ş, Ar-Ge Merkezi, 43001, Kütahya, Türkiye
busrayay@ng.com.tr - 0000-0003-4320-0881
[4] NG Kütahya Seramik A.Ş, Ar-Ge Merkezi, 43001, Kütahya, Türkiye
emeloytac@ngkutahyaseramik.com.tr - 0000-0002-6486-2094
[5] Kütahya Dumlupınar University, Department of Metallurgical and Materials Engineering, 43100, Kütahya, Türkiye
eda.tasci@dpu.edu.tr - 0000-0003-3346-8833

Abstract

The main raw materials in the ceramic wall tiles are clay, kaolin, calcite, and feldspar. The technical properties of the tiles (water absorption, total shrinkage, dry firing strength, fracture strength) and the desired physical properties (L, a, b, surface smoothness) vary depending on the raw material content in the recipe. Rheological parameters are crucial in the formulation development stages to avoid production problems and to ensure the final desired product parameters. Density, viscosity, and sieve analysis have therefore been included in the developed formulations.

The use of raw materials from the region close to the production facility facilitates easy access to these materials. Thanks to this advantage, the use of domestic raw materials is becoming more widespread. In addition to the use of alternative raw materials, it contributes to the reduction of greenhouse gas emissions.

The aim of this study, is to formulate a recipe for wall tiles using kaolins from the Kütahya region instead of clay from the Afyon region. Recipes containing 2%, 4%, 6%, and 8% of Kütahya region kaolin, with a corresponding reduction in clay from the Afyon region, were developed and sintered at 1130-1150°C with a 29-minute firing cycle.

By analyzing the technical properties of the developed formulations, it was found that a maximum of 2% of Kütahya region kaolin could be used in the wall tile formulation. It was found that exceeding this percentage was not feasible due to the associated increase in water absorption, expansion of product size, and decrease in dry strength.

1. INTRODUCTION

For the ceramic industry, which is rapidly developing in our country and has an important position in the world market, raw material accesibility, location of raw material resources, raw material reserves of our country and usage characteristics of reserves of our country and usage characteristics of reserve areas are important issues. In the globalizing world and increasing competitive environment,

companies that produce at low costs without compromising quality and keeping customer satisfaction high tend to constantly grow in the sector. It requires the research and development of quality raw materials resources, which are depleted day by day, the discovery of new raw material areas and the more efficient use of existing raw materilas resources. Additionally, the increasing need for raw materials suitable for producing this material [1, 2].

In the basic components of ceramic wall tiles establishing an optimum clay composition is important for companies in terms of standardising properties such as plasticity, raw strength and firing colour. In addition to quartz, iron oxide and titania are present as impurities in the clay mixture, which is generally formed by combining kaolinitic based clays. The geological formation, structure, mineralogical and other physico-chemical properties of various clays used in recipes have been widely investigated and discussed in the literature [3, 4].

In parallel with the increase of population in the world and in our country, clays are constantly on the agenda as one of the most important raw materials in every period of the ceramic sector [5,6]. Based on these reasons, the properties, applications and production characteristics of kaolinite group clays were examined in this study, and the possibilities of using kaolins in Kütahya region in wall tiles were studied

In the ceramic industry, kaolins containing 75-80% kaolinite minerals are generally preferred. Ceramic kaolins are required to have properties such as firing colour, viscosity, friction resistance, low Fe_2O_3 and TiO_2 ratios and 83-91% brightness, high water dispersibility, plasticity, low firing shrinkage, white firing colour. In addition, physical and chemical properties such as purity, whiteness, grain size distribution, thermal behaviour and high Al_2O_3 content [refractoriness] are important factors affecting that influence the location and amount of kaolin used in ceramics [7].

Clay is a very fine-grained sediment with a grain size of less than 0,02 mm. The elements that make up clay are minerals with a high Al content. Kaolinites, which are the most important of these minerals, are hydrosilicates with Al_2O_3, $2SiO_2$, $2H_2O$ composition, SiO_2 is 46,54% Al_2O_3 39,50% H_2O 13,96%, Kaolinite group clay minerals are white in colour when pure and have a matt appearance, its hardness is 1, specific gravity is 2,1 gr/cm^3, It loses water at 330-450 °C. The main constituent is aluminum silicate. In case of its decrease, a small amount of iron sulphur or potassium is mixed into the composition [8].

One of the most important determinants of quality is silica. Intensive removal of silica from the structure, produces high quality kaolin ore. The kaolin that remains as free silica grains gains the quality of leachable kaolin as it is easier to separate. One of the most important criteria is that the iron in the original rock should not be present in kaolin. However, during the chemical process of kaolinization, some of the iron remains without being removed. Kaolinisation occurs as a result of the decomposition of the feldspars mentioned in the formation of kaolin. The more the feldspar decomposes, the more K_2O is removed from the environment, the more this is removed, the higher the Al_2O_3 ratio which determines kaolinisation [9,10].

Clay-kaolin, quartz and pegmatites are the main raw materials of the wall tile structure. Kaolin is the most important raw material for porcelain and wall tiles. For this reason, the raw material properties of kaolin have a significant impact on its field of application. The technological value of kaolin is closely linked to the oxides that affect the firing colour and the feldspar and quartz that can be removed by washing [11].

The limits of kaolin use in the ceramic industry are determined according to TSE (10545 standards. According to these standards, kaolin is expected to be fired white up to 1300 °C, maximum solid concentration limited to 67-71%, deformation of 5 mm, total shrinkage 0,07%, maximum water absorption 0,2% and dry strength 25 kg/cm^2 Al_2O_3 15-32%, SiO_2 48% [max ,] Fe_2O_3 1% [max ,] is expected.

Clay and kaolin group raw materials provide strength in aqueous mixtures as plastic raw materials, being plastic, they increase the raw strength required during moulding. DTA analysis, chemical and mineralogical analysis are carried out to determine the reactions that will take place in the clay such as moisture content and grain size distribution, iron and titanium content [directly affecting the firing colour], control of carbonates, sulphate and carbon impurities and organic matter content, slurry density, viscosity and pH, plasticity and dry strength, firing shrinkage at firing temperatures, determination of thermal expansion coefficient [12, 13].

Within the framework of this study, research was conducted to develop new recipe compositions that exploit the effectiveness of kaolins from Kütahya region kaolin in wall tile composition recipes. The chemical, physical, and mineralogical properties, dry strength, particle size, viscosity, firing color, rheological properties, moulding parameters, drying behavior, and firing behavior of the kaolins from Kütahya region were investigated in order to fully understand the characteristics of the region.

2. MATERIALS AND METHOD

In the wall tile composition, A-1, A-2, A-3 clays, Kütahya region kaolin, F coded feldspar, K coded calcite raw materials were obtained from NG Kütahya Seramik, the chemical, physical, and firing properties of all raw materials used were prepared according to standard test procedures, and all results are shown in Tables 1-2.

Table 1. Body recipe compositions of standard tile [D-1] and new tile [D-2 , D-3, D- 4, and D-5] [% wt,]

Raw materials	D-1	D-2	D-3	D-4	D-5
A-1	13	11	9	7	5
A-2+A-3	56,5	56,5	56,5	56,5	56,5
F	18	18	18	18	18
K	12,5	12,5	12,5	12,5	12,5
Kütahya region kaolin	/	2	4	6	8

The chemical analysis results of the clays used in the study are shown in Table 2. Figures 1 and 2 show the TG-DTA analyses of these clays, while Figure 3 shows the XRD analyses. The raw materials were weighed according to the recipe proportions, taking into account the moisture values, and ground in ball mills with the addition of water and electrolyte to a density of approximately 1680 g/lt and 63 μm sieve balance of 6-6.5%.

Density [g/lt], viscosity [pour sec], and sieve balance [+63 μm] values of the prepared slurries were measured. The sludge obtained was dried in a laboratory oven at 150 ℃ and crushed in a mortar and pestle. After sieving through a 650 μm sieve, it was humidified to 5.5-6% moisture content and kept for one day to ensure homogeneity.

Samples were prepared by forming granules with dimensions of 110x55mm under a pressure of 320kg/cm^2 using a laboratory-type press. These samples were then dried in a laboratory oven at 150 ℃ for 2 hours to dry. The prepared samples was carried out in NG Kütahya Seramik Tile Factory at 1120-1140 ℃ for 29 minutes, following the firing conditions for wall tiles.

The sintering behaviour of the concretes after firing can be explained by water absorption [%] and firing shrinkage [%]. In addition, the firing strength of the samples, fired in an industrial roller kiln, was measured using a triaxial compression gauge [Gabbrielli SRL, Italy]. Colour measurements (L, a*, and b*) of the baked specimens were also conducted using a Minolta 3600d device. XRD analyses

[Rigaku brand model Miniflex, Japan] were carried out to determine the crystalline phases formed in both the unfired samples.

Measurements were performed with a step size of 0.02° to cover the 2θ angle range of 5°-70°. The results of the phase analysis for all samples examined are available in the JADE analysis programme, including qualitative phase values and PDF cards.

3. RESULTS AND DISCUSSION

For the recipe compositions are shown in Table 1, clay was formulated as a recipe composition with increasing proportions of kaolin from the Kütahya region, while keeping the proportions of feldspar, calcite and A-2+A-3 clay constant compared to the standard D-1 recipe composition, prepared with the standard blending recipe. Accordingly, the increasing proportions of the D-1 formula are coded as D-2, D-3, D-4 and D-5.

In the study, Kütahya region kaolin and A-1 clay obtained from NG Kütahya Seramik were used to prepare a standard wall tile recipe. The X-Ray Fluorescence [XRF] analyses of the clays used in the study are provided in Table 2.

Table 2: Chemical compositions [% wt] determined by X-Ray Fluorescence [XRF] in the standard body recipe.

Element	A-1	Kütahya region kaolin
L.O.I	2,39	5,10
Na_2O	0,43	0,08
MgO	0,17	0,19
Al_2O_3	14,80	13,95
SiO_2	75,14	78,66
SO_3	0,12	0,25
K_2O	5,51	0,05
CaO	0,26	0,18
TiO_2	0,07	0,73
Fe_2O_3	1,16	0,50

Clays initiate viscous flow with melting in their structure at lower temperatures due to impurities such as Na_2O, K_2O, CaO and MgO in their content.

The wall tile recipe in Table 1 is designed to maintain a fixed ratio of A-2 and A-3 clays with a total clay content of 56.5%, determined by correlating X-ray fluorescence [XRF], X-ray diffraction [XRD], DTA, SEM analyses of A-1 clay, and Kütahya region kaolin with the physical and mechanical properties in all recipes. The usage rate and effect of Kütahya region kaolin in the recipe are observed.

According to the results of the chemical analyses shown in Table 1, the total alkali content of the Kütahya Region kaolin is about 0.5%, and the sum of Fe_2O_3 and TiO_2 is 1.28%. In contrast, the total alkali content of A-1 clay is about 6.37%, and the sum of Fe_2O_3 and TiO_2 is 1.23%. There are significant differences between kaolin from Kütahya region and A-1 clay, including a difference of about 53.13% in fire loss rates. Kütahya region kaolin has a much higher fire loss value, a difference also evident in the TG-DTA analysis shown in Figure 1.

Kütahya Region Kaolin
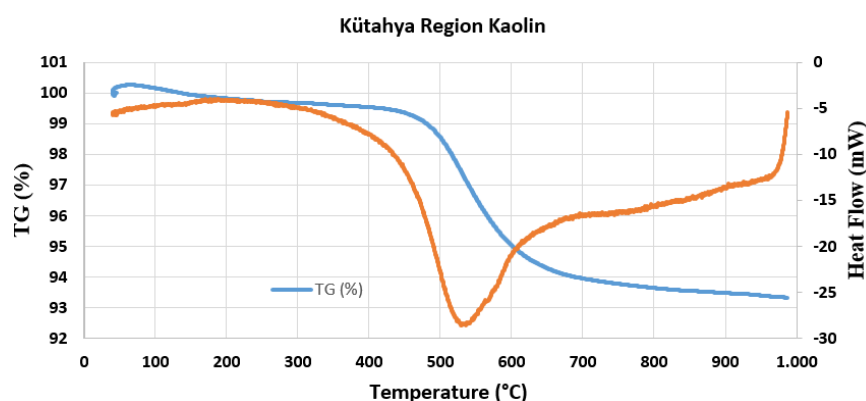
Figure 1. Kütahya Region kaolin TG-DTA Curve

Kütahya Region Kaolin
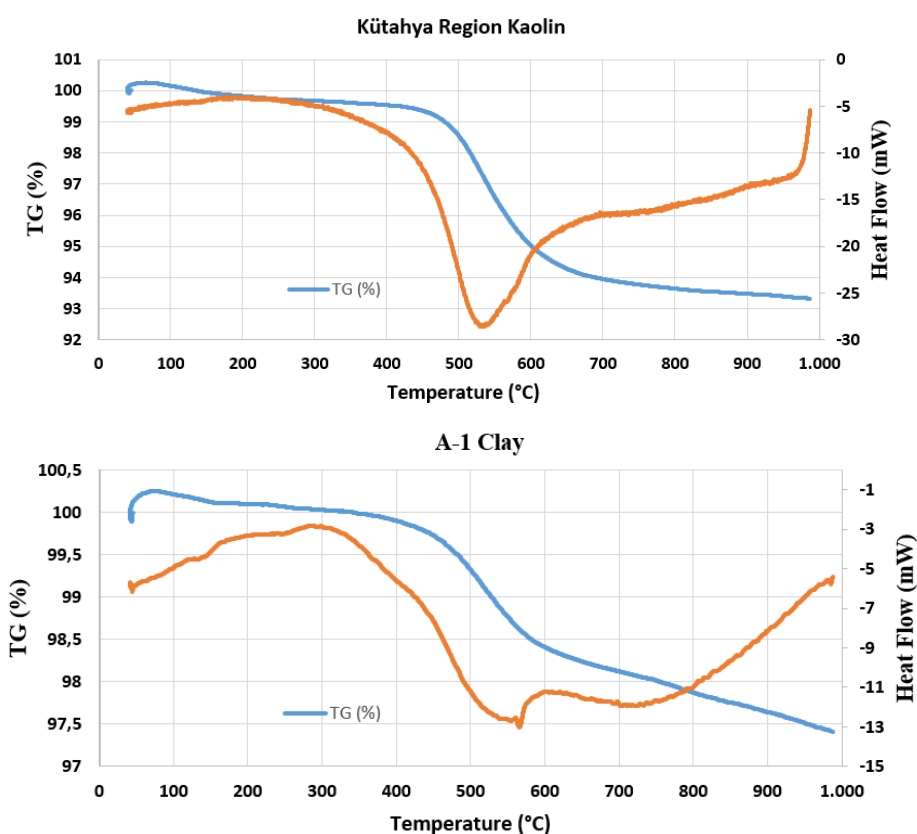
A-1 Clay

Figure 2. TG-DTA Curve of Standard A-1 clay

When the TG analysis of kaolin from the Kütahya region is analysed, a total mass loss of 6,93%, physical water loss of 0,39% between about 62-181℃, removal of 0,17% organic matter between 181,68-265,05℃, and formation of meta-kaolin between 434,91-698,8℃ are observed.

Figure 2 shows a total mass loss of 2.838% in A-1 clay. The kaolin from Kütahya region contains 1.98% melter addition, and A-1 clay contains 7.6% melter addition. This proportional difference is shown in the DTA analysis in Figure 2 as a temperature-dependent DTA analysis. The endothermic peak observed at 572 ºC is attributed to quartz transformation, and a gradual weight loss is observed in

the sample. The total weight loss was determined to be 1.32%. It is suggested that this weight loss is due to the loss of crystal water from the micaceous compounds in the sample.

When the DTA analyses of the kaolin and A-1 clay from the Kütahya region used in the study were examined in detail, the structural changes clays with temperature were compared. Changes occur in the clay mineral structure depending on the Al_2O_3: SiO_2 ratio, the grain size of the clays, and the presence of alkali oxides in the layered structure.

Figure 2 shows 1 sharp peak at A-1 and a small peak at 1 point. While the small endothermic peak around 200 ºC indicates the removal of water adsorbed on the surface, the second sharp endothermic broad peak at 470,13 ºC indicates the dehydration of kaolinite, The fact that the temperature and intensity of the dehydration peak in this sample are lower compared to the kaolin of Kütahya region indicates that the amount of kaolinite in this sample is lower and the amount of smelter is higher, While Al_2O_3 / SiO_2: 0,19 in A-1 clay, Al_2O_3 / SiO_2 : 0,17 in Kütahya region kaolin, the similarity of this value caused no significant peak at 700 and 900 ℃ in both clays.

The results of the physical property tests applied to all recipes are summarised in Table 2. All prepared recipes were dried prior to fast firing, and the strength values after drying are shown in Table 2. When the measurement results are analysed, there is a change in the dry strength value in the form of both increase and decrease, which is due to the decrease in the proportion of core raw material and the increase in the proportion of glassy phase with the incorporation of Kütahya region kaolin into the recipe.

After 29 min, roll sintering at a temperature of about 1130-1150 ℃, an increase and decrease in strength value is observed with the increase of Kütahya region kaolin in D-1 standard recipe and D-4 recipe in the recipe composition with the addition of Kütahya region kaolin, a loss in strength value about 5% is observed between D-1 recipe and the D-4 recipe, water absorption values increase with the increase of Kütahya region kaolin compared to D-1 recipe and the lowest strength and highest water absorption values are observed in D-2.

The ratio of Al_2O_3 /SiO_2 in Kütahya region kaolin is [0,17] and the ratio of Al_2O_3 / SiO_2 in A-1 clay structure is [0,19]. The kaolin from the Kütahya region has a total ratio of NaO_2, MgO, K_2
O, and CaO that is about 92% lower than that of A-1 clay. This discrepancy leads to a reduction in strength and an increase in water absorption."

A fixed amount of electrolyte was used in the prepared recipes. In addition, grinding times varied between 11 and 12.5 minutes. Changes in grinding times were made to achieve standard density and sieve balance in the recipes. The proportion of coreless raw materials in the kaolin from Kütahya region was reflected in the grinding time. The sieve balance values show a decreasing trend between D-1 and D-2 as the grinding time is adjusted, ranging from 1700 to 1704 gr/cm³. In addition, the flow times increase by 17.85% with the increase in the incorporation of kaolin from Kütahya region

Table 3 summarises the physical analysis results obtained after firing at 1130-1150 ℃ of the prepared recipes.

Table 3. Standard **D-1** Physical properties of recipes **coded D-2, D-3, D-4, D-5** with the addition of Kütahya Region kaolin.

Parametre	D- 1	D-2	D-3	D-4	D- 5
Size (mm)	110,33	110,27	110,25	110,18	110,19
Total Shrinkage (%)	0,33	0,38	0,4	0,46	0,46
Water Absorption (%)	18,26	17,79	18,34	18,88	19,14
Dry Strength (N/mm^2)	14,13	17,4	15,51	15,54	14,95
Baking Strength (N/mm^2)	182,3	204,6	208,1	214	192,3
Firing Breaking Strength (N)	876	611	660	846	820
L	75,9	74,61	75,64	75,19	75,64
a	7,83	7,88	7,92	8,53	7,84
b	19,06	19,5	19,87	20,52	19,87

An increase in the total shrinkage amount, an increase in the water absorption amount, an increase and decrease in the dry strength value, an increase and decrease in the dry strength value, and an increase and decrease in the firing strength value were observed with the increase of Kütahya region kaolin in the formulation. In addition, a decrease in the L* value, an increase and decrease in the a* value and an increase and decrease in the b* values are observed after firing compared to the D-1 standard formulation.
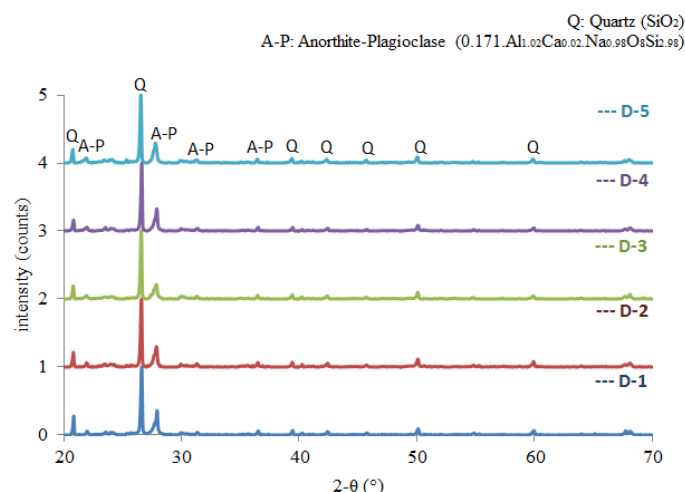
Figure 3. XRD analysis results taken after firing of recipes coded D-1, D-2, D-3, D-4 and D-5
[Q: Quartz, AP: Anorthite-Plagioclase]

When the X-ray diffraction [XRD] analysis of the D-1, D-2, D-3, D-4, and D-5 coded formulations is examined after firing, it is observed that similar phases are formed within the mineralogical structures of the formulations. The intensity of the quartz and plagioclase phases in the structure is very low, and the peak sharpness is significantly reduced in the D-1 formula where the A-1 clay content is minimal. The X-ray diffraction [XRD] analysis results indicate that the intensity of anorthite plagioclase phase does not change significantly with the addition of kaolin from the Kütahya region and the decrease in A-1 clay. (PDF card no for anorthite-plagioclase: 98-009-0142; 0.171. Al1.02 Ca0.02. Na0.98 O8 Si2.98) .

It can be observed that the higher sieve balance and grinding time in recipe D-4 results in a larger quartz grain size and a lower quartz anorthite-plagioclase value compared to the recipe D-1. While a sharp and intense peak was observed in the quartz phase in the D-4 formulation, the peak intensity decreased slightly in the D-5 formulation and the sharp peak changed to a slightly broadened peak. Figures 4-7 show the SEM and EDX analyses of the standard body and the standard body with

technical specifications. The microstructure of both bodies is similar, containing irregularly shaped quartz grains, anorthite-plagioclase phase, and pores found in a typical wall tile body.

According to the results of the EDX analysis carried out on the indicated points, the crystals formed in the region contain aluminium, silica, and calcium, in agreement with existing literature. In the backscattered electron images, heavy elements appear whiter than other elements. In the microstructural images, the dark grey tones represent quartz grains, while the black tones indicate porosity.

Figures 4-7 show the SEM images and EDX analysis results of formulations D-1, D-2, D-3, D-4, and D-5 at x10,000 magnification. These samples were sintered at the standard firing temperature. Observation of the SEM images shows vitrification in the structures, with grains coalescing to form a sinter. This phenomenon is indicative of high temperature sintering, which creates an environment where clay grains react with other minerals to form a vitreous phase.

While the firing strength decreases with the addition of A-1, the water absorption rate increases according to the physical properties table. SEM and EDX analysis show that the glassy phase ratio is the highest in the D-4 recipe, which exhibits the highest strength.

Element	Weight %	Atomic %
Na_2O	0,00	0,00
MgO	1,34	2,57
Al_2O_3	57,54	43,67
SiO_2	26,19	33,72
K_2O	1,01	0,83
CaO	13,92	19,21
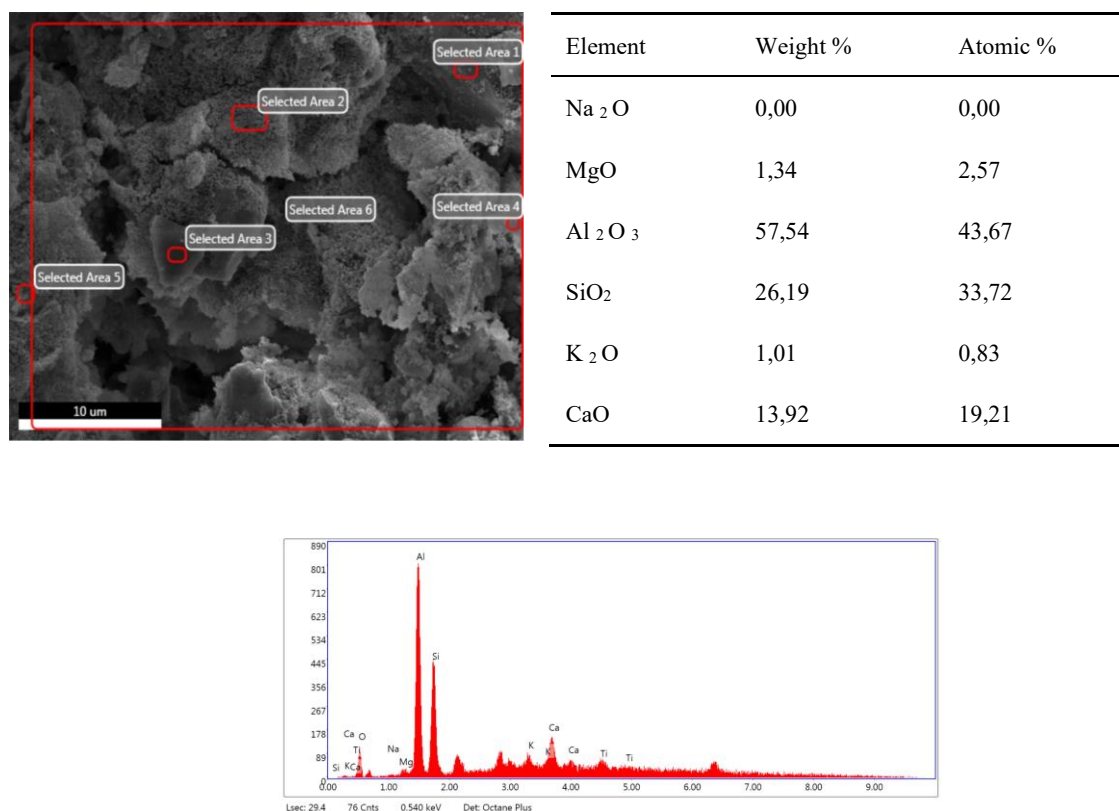
Figure 4b. SEM-EDX analysis result of the D-1 coded sample (Selected area 2 for EDX) sintered in the wall tile regime [x10000 magnification]

Element	Weight %	Atomic %
Na$_2$O	0,00	0,00
MgO	0,26	0,43
Al$_2$O$_3$	35,78	23,75
SiO$_2$	9,94	11,19
K$_2$O	1,16	0,83
CaO	52,87	63,80
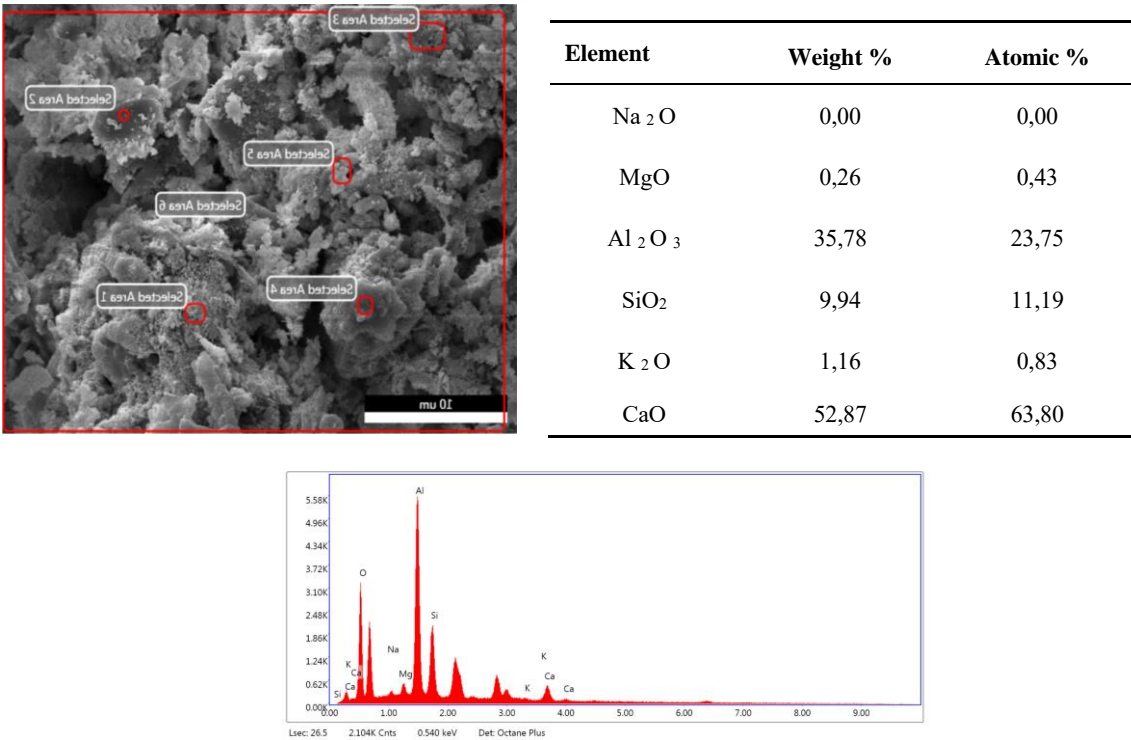
Figure 5. SEM-EDX analysis result of the D-2 coded sample (Selected area 4 for EDX) sintered in the wall tile regime [x10000 magnification]

Element	Weight %	Atomic %
Na$_2$O	0,00	0,00
MgO	0,26	0,43
Al$_2$O$_3$	35,78	23,75
SiO$_2$	9,94	11,19
K$_2$O	1,16	0,83
CaO	52,87	63,80
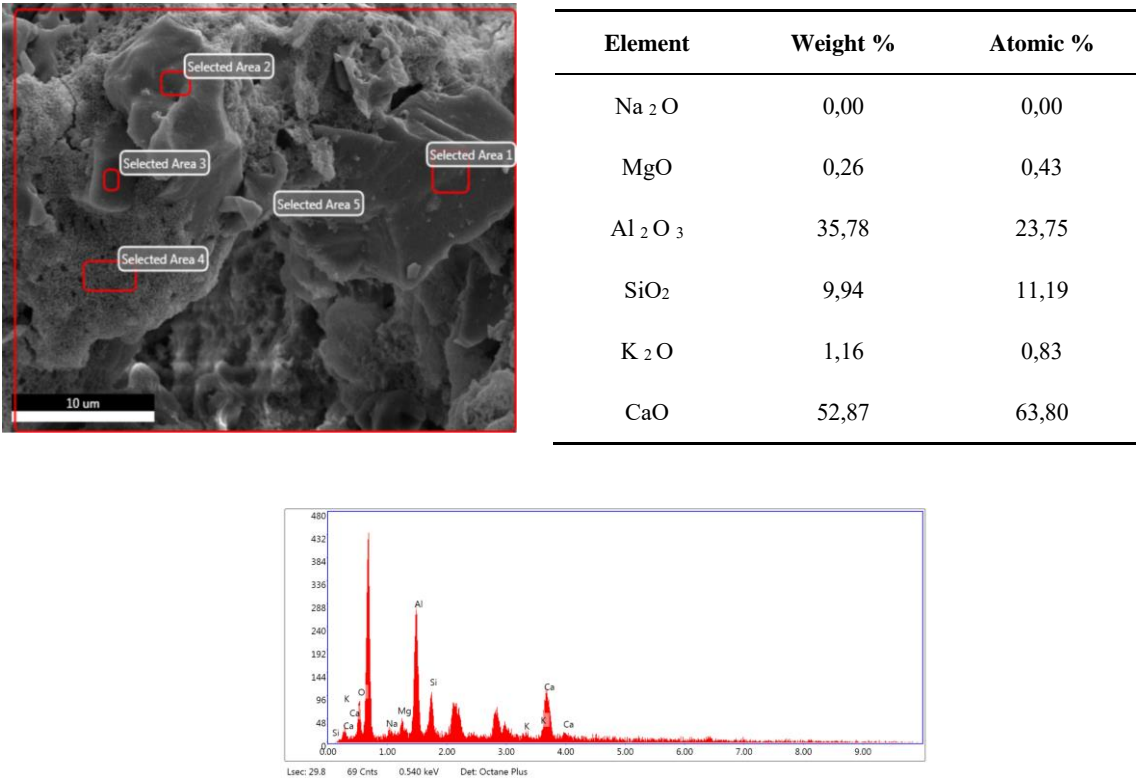
Figure 6. SEM-EDX analysis result of the D-3 coded sample (Selected area 4 for EDX) sintered in the wall tile regime [x10000 magnification]

Element	Weight %	Atomic %
Na$_2$O	2,67	4,54
Al$_2$O$_3$	27,03	18,17
SiO$_2$	48,59	55,45
K$_2$O	9,52	6,93
CaO	12,20	14,91
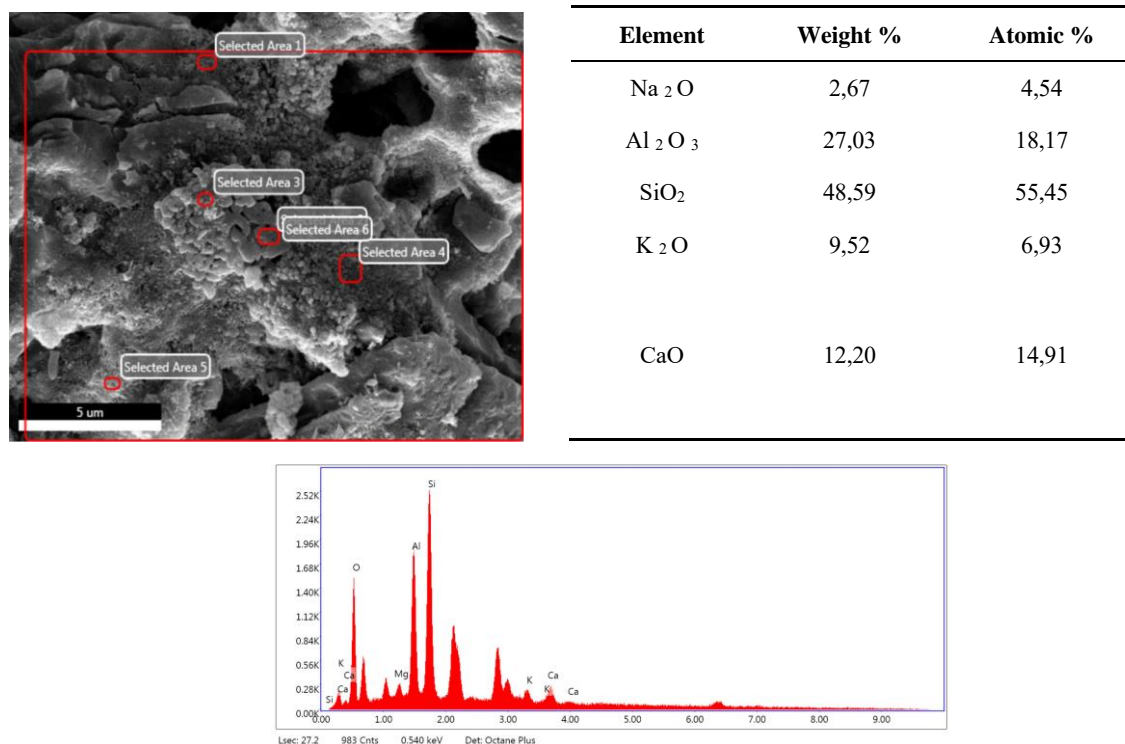
Figure 7. SEM-EDX analysis result of the D-4 coded sample (Selected area 6 for EDX) sintered in the wall tile regime [x10000 magnification]

4. CONCLUSIONS

The study investigated, the properties of Kütahya region kaolin and A-1 coded clay raw materials. The results show that the inclusion of Kütahya region coded kaolin in the recipe composition, increased the structure, grinding time and the sieve balance. In addition, the raw strength value decreased. However, its low deformation value suggests that its use will darken the final product (L* whiteness and a* redness values are high). Investigations into its use rate in the formulation are ongoing.

The use of this kaolin in excess of the established standard formulation ratio has a significant effect on the deformation and colour values of the structure. However, the dry strength value remains very close to the dry strength value of the standard formulation.

In all recipes, the amount of electrolyte was kept constant for a constant litre weight due to the reduction in particle size. The raw strength and raw density values increased, indicating that the packing density of the moulded sample increased. Water absorption and firing shrinkage increased. Microstructure images showed that the number of pores decreased slightly, and their size decreased with the increase of raw material A-1 kaolin. These results were supported by SEM and XRD analyses.

CONFLICT OF INTEREST

The authors stated that there are no conflicts of interest regarding the publication of this article.

CRediT AUTHOR STATEMENT

Senem Algan: Formal analysis, Investigation, Conceptualization. **Fatih Öztürk:** Formal analysis, Investigation, Conceptualization. **Büşra Yay:** Formal analysis, Investigation, Conceptualization. **Zehra Emel Oytaç:** Formal analysis, Writing - original draft, Visualization, Conceptualization, Supervision. **Eda Taşçı:** Formal analysis, Writing - original draft, Visualization, Conceptualization, Supervision.

REFERENCES

[1] Yıldız A, Bagci M, Dumlupinar I, Basaran C. Afyonkarahisar Province's Ceramic Sector Raw Material Potential, Afyon Kocatepe University Journal of Science and Engineering Sciences, 2013; 3, 553-554.

[2] Kuşcu M and Yıldız A. Geology, Mineralogy and Firing Properties of Kaolinitic Clay From Akharım Afyonkarahisar, 15th National Clay Symposium Proceedings Book, Niğde, 2012, 389.

[3] Çiftlik S. Removal of Metals From Kaolin Ore By Leaching Method, Süleyman Demirel University, Institute of Science and Technology, Isparta, 2010.

[4] Carbajal L, Rubio-Marcos F, Bengochea MA, Fernandez JF. Properties Related Phase Evolution In Porcelain Ceramics, Journal of the European Ceramic Society, 2007; 27, 13-15.

[5] Genç C. Characterisation of Zeolitic Tuffites in Biga Region and Investigation of the Possibilities of Use in Wall Tiles, Afyon Kocatepe University Journal of Science and Engineering Sciences, 2019; 19, 310-320.

[6] Lee WE, Iqbal IY. Influence of Mixing on Mullite formation in Porcelain, Journal of European Ceramic Society, 2001; 21, 2583 – 2586.

[7] Ispalarlı M. Evaluation of Domestic Clays as an Alternative to Imported Clays in Ceramic Floor Tile Production on Recipe Basis, Kütahya Dumlupınar University, Institute of Postgraduate Education Department of Material Sciences and Engineering Master's Thesis, Kütahya, 2021.

[8] Kılıç C, Çam A. Denizli Tekkeköy Thermal Mud and the Use of Regional Clay in Ceramic Structure , SDÜ Art-E Faculty of Fine Arts Art Journal, 2023;16-31, 474-492.

[9] Kara A, Ozer F, Kayacı K, Ozer P. Development of A Multipurpose Tile Body: Phase and Microstructural Development, Journal of European Ceramic Society, 2006; 26, 3769-3782.

[10] Çelik H, Ertürk Ö and Day N, Characterisation of Afyon Region Clay and Investigation of Its Use ın Ceramic Floor Tiles, Proceedings of the 21st International Mining Congress and Exhibition of Antalya, 2009;571-578.

[11] Tarhan M, Tarhan B. Investigation of the Use of Afyon Clay in Porcelain Tile Components, International Journal of Engineering Research and Development, 2019; 11-1, 275-281.

[12] Lee WE, Souza GP, McConville CJ, Tarvornpanich T and Iqbal Y. Mullite Formation ın Clays and Clay-Derived Vitreous Ceramics, Journal of European Ceramic Society, 2008;28, 465-467.

[13]   Ozer MF, Use of Common Composition in Floor and Wall Tiles, Anadolu University, Institute of Science and Technology, Department of Ceramic Engineering, Master's Thesis, Eskişehir, 2014.

RESEARCH ARTICLE

MODELLING STOCK PRICES OF A BANK WITH EXTREME VALUE DISTRIBUTIONS

Ceren ÜNAL [1],* Gamze ÖZEL KADILAR [2]

[1] Department of Statistics, Faculty of Science, Hacettepe University, 06800, Ankara, Türkiye
cerenunal@hacettepe.edu.tr - 🆔 *0000-0002-9357-1771*

[2] Department of Statistics, Faculty of Science, Hacettepe University, 06800, Ankara, Türkiye
gamzeozl@hacettepe.edu.tr - 🆔 *0000-0003-3886-3074*

Abstract

The study investigates the application of Extreme Value Theory in modelling stock prices, aiming to capture the tail behaviour and extreme movements that conventional distributions often fail to represent accurately. The use of Extreme Value Theory has gained considerable attention in the field of finance due to its ability to model rare events, such as financial crises or market crashes. By incorporating Extreme Value Theory, researchers aim to improve risk management, portfolio optimization, and pricing of financial derivatives. In this study, the Log-normal, Weibull, Gamma, and Normal distributions were used to model the stock price closing data, with a specific focus on extreme value distributions. Both graphical explorations and goodness-of-fit criteria were considered together to evaluate the suitability of these distributions. When assessing the data, it was observed that the Weibull distribution provided the best fit for the given stock price closing data.

1. INTRODUCTION

One of the most crucial challenges in mathematical finance revolves around determining the distribution of speculative prices. This problem holds significant theoretical and practical implications, yet it remains unsolved. The initial solution proposed by Bachelier [1] was the random walk process, where price movements were modelled as independent rises and falls [2]. According to this model, returns were assumed to follow a Normal (Gaussian) distribution. Stock price modelling with statistical distributions involves fitting historical stock price data to a specific distribution to capture the underlying patterns and behaviour of the stock.

The Normal distribution is widely employed in finance for measuring security prices. However, in reality, the distribution of financial assets is typically non-normal [3, 4]. Empirical studies consistently demonstrate that actual stock price returns exhibit skewness, kurtosis, and heavy tails [5]. The presence of heavy tails in price distributions holds significant importance in financial risk analysis. Consequently, it is crucial to obtain a reliable distribution [6]. Thus, alternative distributions are explored as substitutes for the Normal distribution.

Mandelbrot [7] was among the first to propose an explanation for the presence of long tails in financial data, leading to the development of a leptokurtic distribution. However, this initial attempt resulted in probability density function moments that were not finite. Subsequently, the Log-normal distribution

---

*Corresponding Author: cerenunal@hacettepe.edu.tr

gained widespread usage for describing the distributions of financial assets, including share prices. The Log-normal distribution provided more reliable outcomes than the Normal distribution since asset prices could not be negative. This viewpoint influenced the development of the Black-Scholes model, a widely used framework for pricing options in finance, which is based on the assumption of a Log-normal distribution for determining option prices. Building upon the Log-normal distribution, extreme value distributions (EVDs) emerged as a tool for analysing the tail behaviour of distributions and estimating tail probabilities, enabling the modelling of asymptotic behaviour. EVDs primarily address probabilistic and statistical inquiries related to exceptionally small or large values within a set of random variables. Extreme events, which occur with low probabilities, hold significant importance in financial risk management. In order to quantify the level of risk involved, it becomes necessary to estimate probabilities in the tail region of the distribution for the given process.

Extreme Value Theory (EVT) is a statistical approach used for modelling extreme events, such as extreme stock price movements, which are of great interest in financial risk management. EVT is based on the analysis of the tail behaviour of probability distributions and focuses on estimating the probabilities of rare events that fall beyond the threshold of Normal distributions. In EVT, three types of extreme value distributions are commonly used: the Gumbel distribution, the Fréchet distribution, and the Weibull distribution. These distributions are known as the Generalized Extreme Value (GEV) distributions. The Weibull distribution is one of the alternative distributions used in financial analysis and risk management. It is particularly useful for modelling extreme events and tail values. This distribution is defined by the Weibull function and has shape and scale parameters. In financial markets, the Weibull distribution is commonly employed for extreme value analysis and risk management [8]. Extreme value analysis involves studying unexpected and rare events, and the Weibull distribution provides a suitable framework for capturing such events. The distribution allows for a flexible modelling approach that can account for the heavy-tailed nature of financial data. The Weibull distribution has applications in various areas of finance, including risk modelling, asset pricing, and insurance. It can be used to estimate tail probabilities, quantify the likelihood of extreme events, and assess the associated risks. By understanding the behaviour of extreme values, financial practitioners can make more informed decisions regarding risk management strategies, portfolio optimization, and pricing of financial derivatives [9].

The Log- normal distribution became widely adopted in finance due to its ability to provide more accurate results compared to the Normal distribution when describing the distributions of financial assets, including share prices. The Log-normal distribution is particularly advantageous as it ensures that asset prices cannot take negative values, which is a fundamental characteristic in financial markets [10]. The application of the Log-normal distribution extended to the development of the Black-Scholes model, a widely used framework for pricing options in finance. The model relies on the assumption of a Log-normal distribution for the underlying asset price to determine option prices. This assumption has proven to be effective in capturing the behaviour of financial markets and has played a significant role in options pricing and risk management [11].

The Gamma distribution is a widely used probability distribution in finance due to its ability to model positive random variables with skewed and positively skewed distributions. The Gamma distribution provides a versatile framework for modelling various financial variables and risk measures in finance. Its ability to capture skewness and positive skewness makes it a valuable tool for understanding the distributions of asset returns, estimating risks, and pricing financial derivatives [12].

In this study, we compare the statistical distributions to model stock price data. The paper is organised as follows: In Section 2, statistical distributions used for stock modelling is defined. Section 3 describes data set and its' statistical properties. Section 4 presents the results. Conclusion is given in Section 5.

2. METHODOLOGY

Extreme value distributions, such as the Log-normal, Gamma, and Weibull distributions, are commonly used in various fields to model extreme events or rare occurrences. In this section, we define normal distribution and extreme value distributions used in the study briefly.

The normal distribution is often used as a starting point for modelling stock prices. It assumes that stock returns follow a bell-shaped curve, with most returns clustering around the mean and tails becoming less likely as they move away from the mean. However, stock returns often exhibit characteristics such as skewness and excess kurtosis, which are not captured by the normal distribution [13]. If a random variable X has a normal distribution with mean μ and variance σ^2 ($\sigma^2 > 0$), then probability density function (pdf) of the form is given by

$$f(x) = \frac{1}{\sigma\sqrt{2\pi}} e^{-\frac{1}{2}\left(\frac{x-\mu}{\sigma}\right)^2}. \tag{1}$$

The log-normal distribution is widely used to model variables that are the result of the exponential growth of underlying processes. It is characterized by its skewed and right-tailed shape. In finance, the log-normal distribution is often applied to model stock prices, as it accounts for the positive-only nature of prices and the tendency for large price movements. The log-normal distribution is commonly used for modeling stock price data due to its ability to handle variables that are inherently positive and have skewed distributions. It assumes that the logarithm of the variable follows a normal distribution. The pdf of the log-normal distribution is given by

$$f(x) = \frac{1}{x\sigma\sqrt{2\pi}} e^{-\frac{1}{2}\left(\frac{(lnx-\mu)^2}{\sigma^2}\right)}. \tag{2}$$

The gamma distribution is a generalization of the exponential distribution which is a versatile distribution commonly used to model positive continuous variables. It has two shape parameters that allow for various shapes, including right-skewness and left-skewness. In finance, the gamma distribution is often used to model waiting times, insurance claims, and the distribution of returns. The pdf of the gamma distribution with a shape parameter (θ) and scale parameter (λ) is given by

$$f(x) = \frac{\lambda^\theta}{\Gamma(\theta)} x^{\theta-1} exp(-\lambda x), \tag{3}$$

where $x > 0, \theta > 0, \lambda > 0$ and $\Gamma(\theta)$ is the gamma function.

The Weibull distribution was introduced by the Swedish physicist Weibull [14] and is a flexible distribution that can model a wide range of shapes, including both right-skewed and left-skewed distributions [15]. It is often used to model time-to-failure data or the distribution of extreme events. In finance, the Weibull distribution is sometimes employed to model the tail behaviour of asset returns or the distribution of extreme returns. The Weibull distribution is a statistical distribution commonly used in reliability analysis to model the time to failure of a system or an event. However, it is not commonly used for directly modelling stock price data. The pdf of the Weibull distribution is given by

$$f(x) = \lambda\theta x^{\theta-1} exp(-\lambda x^\theta), \quad x > 0. \tag{4}$$

The Weibull distribution is characterized by its shape parameter (θ) and scale parameter (λ). It has a flexible shape that can be either positively skewed $(\theta > 1)$ or negatively skewed $(\theta < 1)$, and it allows for modelling different hazard rates (the probability of an event occurring over time).

3. DATA SET

HDFC Bank is one of the largest and most prominent private sector banks in India. As a publicly traded company, HDFC Bank's stock price data refers to the historical prices at which its shares have traded on the stock market over a specific period. This data includes the opening price, closing price, high price, low price, and trading volume of HDFC Bank's stock on different trading days.

The stock price of HDFC Bank is influenced by various factors, including the overall performance of the banking sector, the bank's financial results, macroeconomic conditions, interest rates, market sentiment, and news or events that may affect the banking industry or the company specifically. By analysing HDFC Bank's stock price data, investors, traders, and analysts can gain insights into the past performance, volatility, trends, and potential future movements of the stock. This data can be used for various purposes, including technical analysis, fundamental analysis, risk assessment, and investment decision-making [16]. In this study, previous close price is used to analyse stock price data and previous close price refers to the prior day's value of a stock, bond, commodity, futures or any other security. Descriptive statistics is presented in Table 1.

Table 1. Descriptive statistics for previous close price of stock price.

Min. Value	Q_1	Median	Mean	Q_3	Max. Value	Variance	St. Deviation
157.4	479.9	934.8	1007.1	1421.0	2565.8	404187.9	635.757

In the analysis, the Agostino test for skewness and the Anscombe test for kurtosis were performed using R software with "moments" package. The skewness value was calculated as 0.5637, with a p-value that is very close to zero. This indicates that the data is positively skewed, as the p-value is less than the significance level of 0.05. The kurtosis value obtained was three, which suggests a Normal distribution. If the kurtosis value is greater than three, it indicates a leptokurtic distribution with thicker tails and sharper peaks. On the other hand, if the kurtosis value is less than 3, it indicates a platykurtic distribution with thinner tails and flatter peaks. In this case, since the kurtosis value is less than three, the data exhibits a platykurtic distribution. According to the Anscombe test, the kurtosis value is determined to be 2.2974. This further confirms that the data follows a platykurtic distribution with thin tails. Additionally, the p-value obtained from the Anscombe test is less than 0.05, suggesting that the data is not normally distributed at a significance level of 0.05.

To visually assess the data for outliers and its adherence to a normal distribution, a box plot in Figure 1 was constructed. From the box plot, it can be observed that there are no outliers present in the dataset. However, the data does not exhibit a Normal distribution, as evidenced by the non-symmetrical shape of the box plot. Overall, the analysis indicates that the data is positively skewed, has a platykurtic distribution with thin tails, and does not follow a Normal distribution.
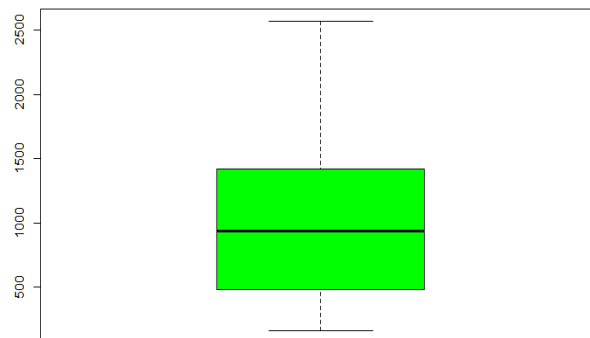
Figure 1. Box-plot for previous close price data.

Figure 2 displays a histogram plot of the dataset, providing a visual representation of the distribution of the data. Histograms divide the data into bins or intervals and display the frequency or count of data points falling into each bin. In this case, the histogram reveals important insights about the distribution of the dataset. From the histogram in Figure 2, it is evident that the data exhibits right skewness. This means that the data is skewed towards the higher values, with a longer tail on the right side of the distribution. The majority of the data points are concentrated towards the lower values, while there are fewer data points towards the higher values. Observing a right-skewed distribution in a financial stock chart provides insights into certain trends and characteristics of price movements. Right-skewness indicates that stock prices tend to exhibit an upward trend, with lower values being more common and higher values being relatively rare.

In this case, a right-skewed stock chart suggests that the stock prices have a tendency to increase over time, with occasional spikes or surges in value. This could be indicative of positive market sentiment and investor optimism surrounding the stock. Traders and investors may interpret this pattern as an opportunity for potential gains, as the stock shows a tendency to experience upward movements.
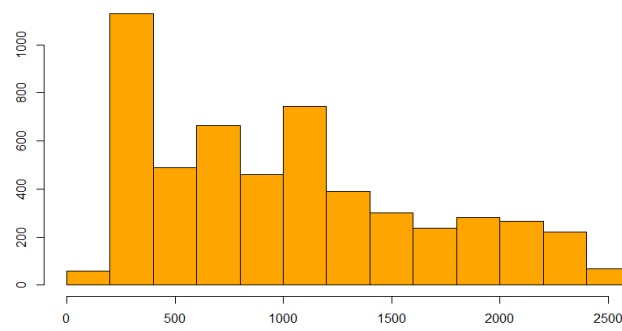
Figure 2. Histogram for the close price data.

Before selecting a distribution for the price data, a preliminary analysis was performed using the Cullen and Frey plot. The Cullen and Frey plot is a graphical tool that helps assess the skewness and kurtosis of a dataset. It is used to gain insights into the underlying distribution and determine potential candidate distributions. In the plot, the skewness of the data is represented on the x-axis, while the kurtosis is represented on the y-axis. The observed values are indicated by blue dots on the plot. The position of each dot on the plot provides information about the shape of the data [17]. Based on the Cullen and Frey plot in Figure 3, it can be inferred that the Weibull, Gamma, Log-normal, and beta distributions are potential candidates for fitting the data. This inference is made by examining the location of the blue dot in relation to the expected ranges for skewness and kurtosis associated with these distributions.
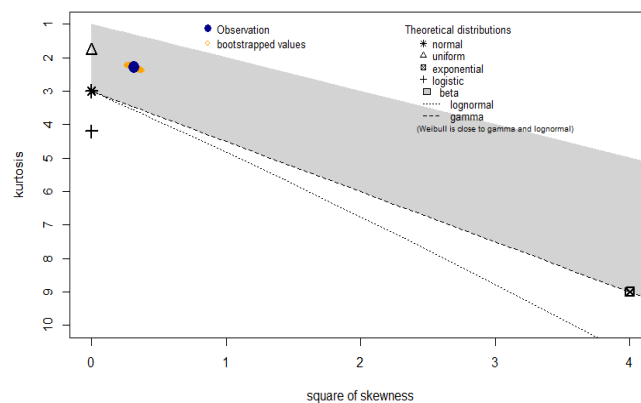
Figure 3. Cullen and Frey graph of competitive distributions for the close price data.

4. RESULTS

In this section, we assessed the suitability of alternative distributions for fitting the HDFC Bank closing price data through graphical evaluation. We employed the "fitdistrplus" package in R to examine the fit of various distributions, namely Normal, Log-normal, Weibull, and Gamma distributions. We generated histogram plots to visualize the distribution of the data. Additionally, we utilized quantile-quantile (Q-Q) plots to compare the observed quantiles of the data against the quantiles of the selected distributions. Moreover, we plotted the empirical cumulative distribution function (CDF) and the theoretical CDF of each distribution to evaluate the overall fit. Lastly, we examined probability-probability (P-P) plots to compare the observed probabilities against the theoretical probabilities derived from the fitted distributions. These graphical representations can be found in Figures 4-7.
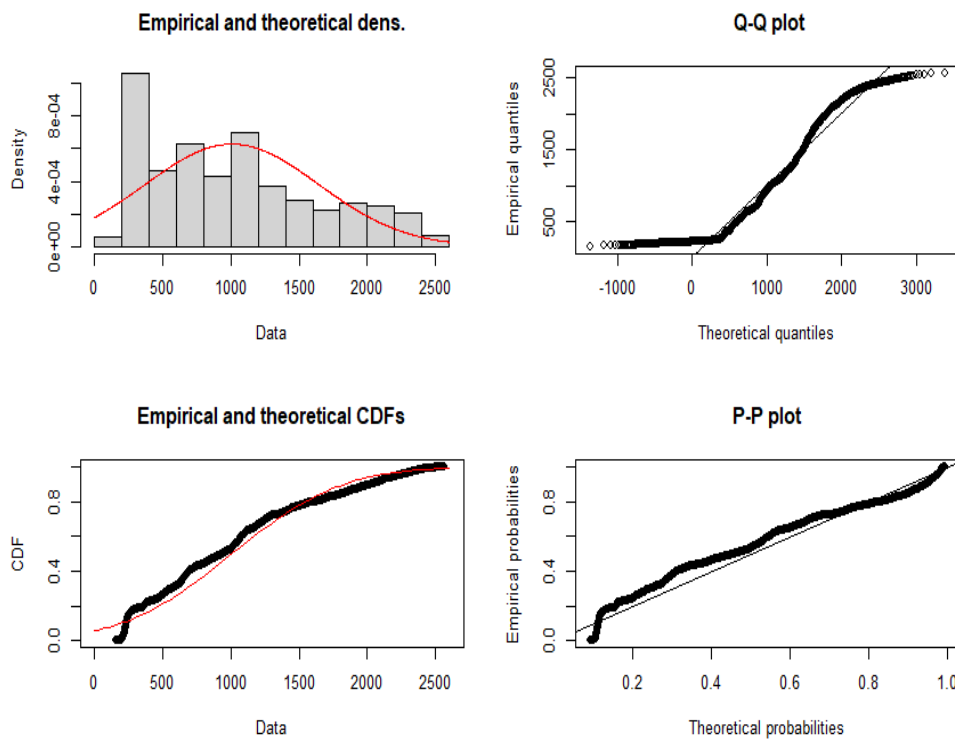
Figure 4. Graphs of goodness of fit of the Normal distribution for the close price data
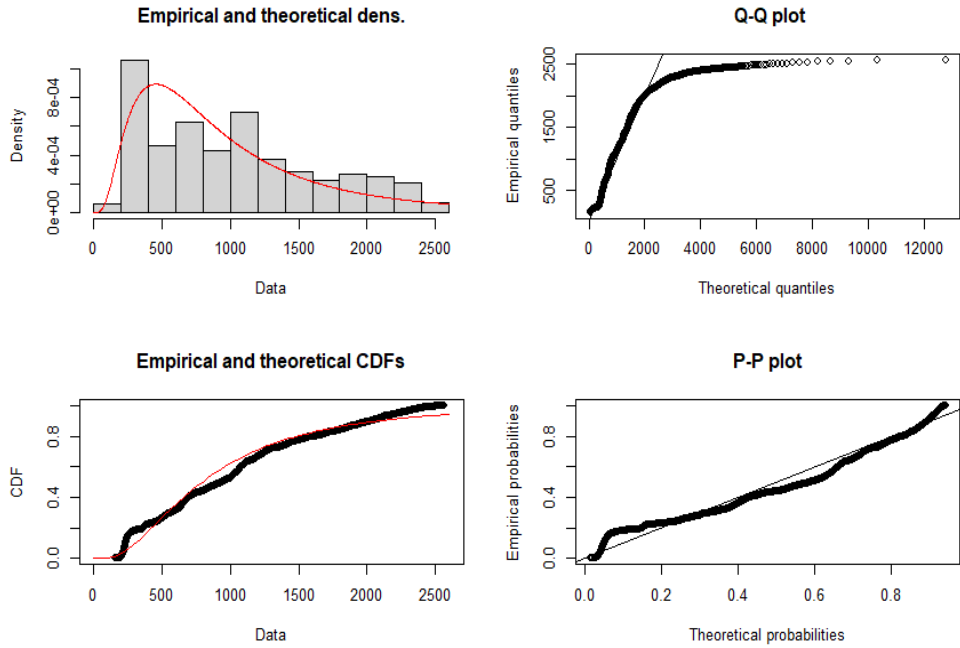
Figure 5. Graphs of goodness of fit of the Log-normal distribution for the close price data
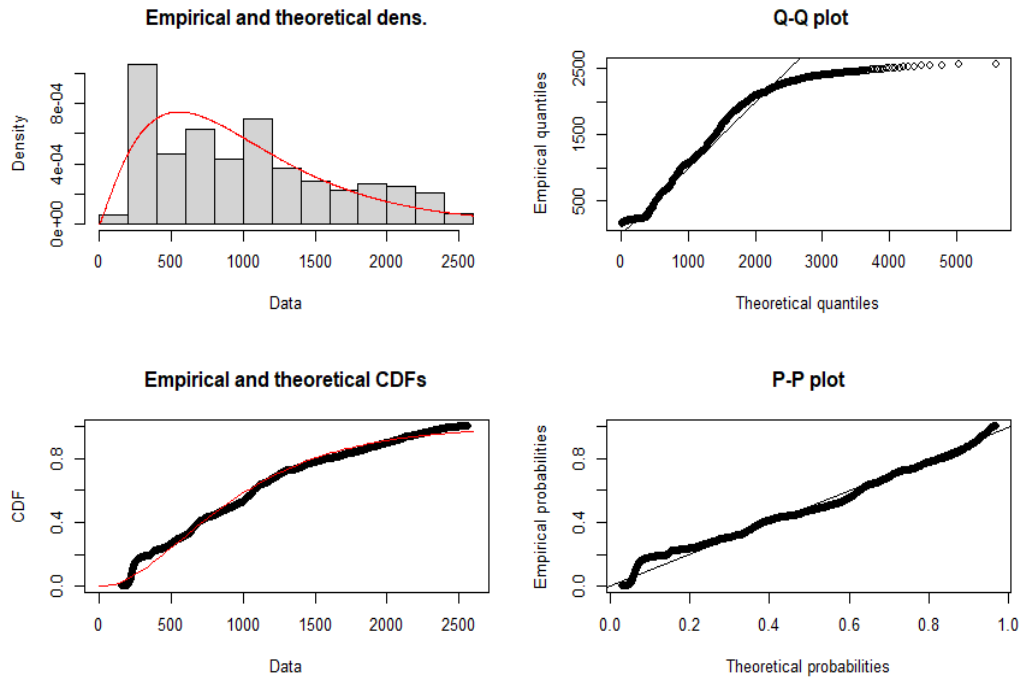
Figure 6. Graphs of goodness of fit of the Gamma distribution for the close price data
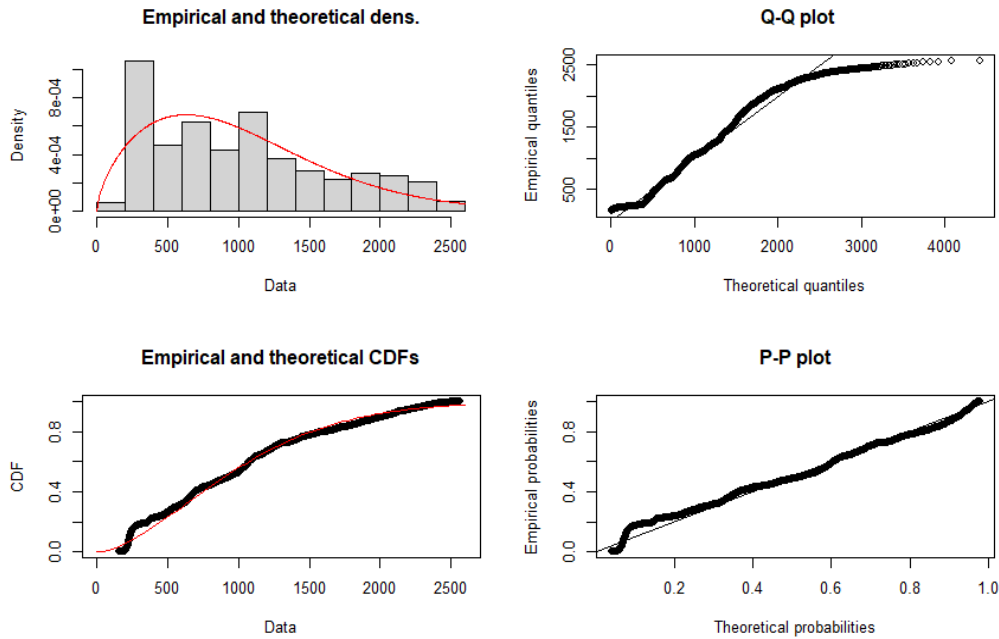
Figure 7. Graphs of goodness of fit of the Weibull distribution for the close price data

Upon examining the graphs presented in Figures 4 to 7, it can be observed that the Normal distribution does not fit the stock closing price data. Additionally, a careful examination of the P-P plot suggests that the Gamma and Weibull distributions in Figures 6 – 7 exhibit better fit to the stock closing data compared to the other distributions. Figure 4 shows the histogram of the data, where the shape of the distribution is not symmetrical and does not resemble a Normal distribution. This supports the finding that the Normal distribution is not suitable for modelling the stock closing prices. Figure 5 displays the Q-Q plot, which compares the quantiles of the observed data against the quantiles of the theoretical distribution. The deviations from the straight line indicate that the log Normal distribution is not a good fit for the data.

We also give the all distributions used in the study together in Figure 8 to compare them at the same time. Based on the graphical analysis in Figure 8, it is also evident that the Weibull and Gamma distributions provide better fits to the stock closing price data compared to the Normal distribution. These distributions can be considered as potential models for further analysis and modelling of the stock price behaviour.
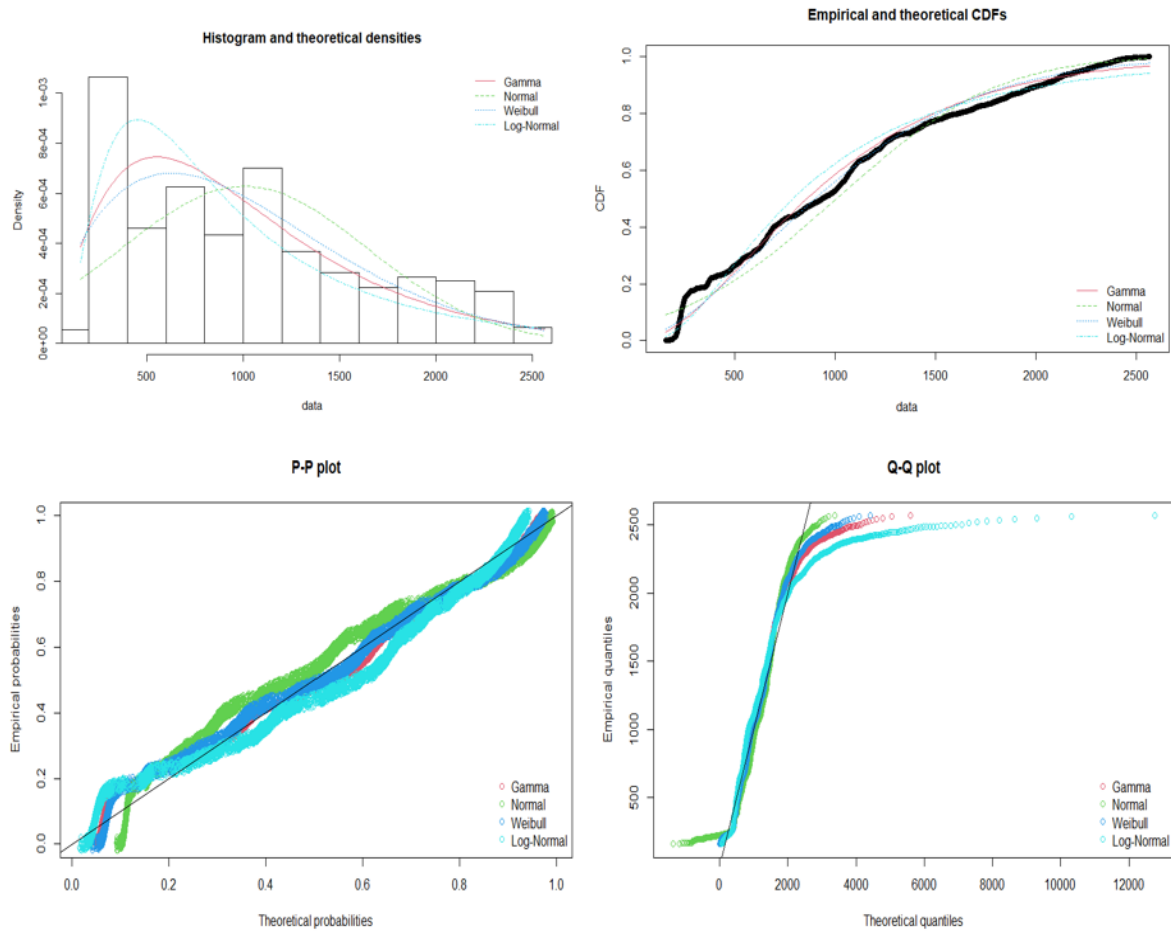
Figure 8. Plots of all competitive distributions for the close price data

To determine which alternative distribution is statistically better, Table 2 provides the AIC, BIC, and log-likelihood (log L) values. Additionally, the table includes the parameter values obtained using the maximum likelihood estimation method for the Normal, Log-normal, Exponential, Gamma, and Weibull distributions. Upon examining Table 2, it can be observed that the Weibull distribution has the smallest AIC and BIC values. This suggests that the Weibull distribution provides a better fit to the data compared to the other distributions. The log-likelihood value also supports this finding, as it is maximized for the Weibull distribution. These statistical criteria indicate that the Weibull distribution is the most suitable distribution for modelling the stock price data in terms of goodness-of-fit and model complexity. Therefore, the Weibull distribution can be considered as the preferred distribution for further analysis and modelling of the stock price behaviour.

Table 2. Parameter estimations with standard errors in parenthesis and the results of model selection criteria.

Model	a	b	logL	AIC	BIC
Normal	1007.0939 (8.7272)	635.6978 6.1708	-41777.65	83559.3	83572.45
Log-normal	6.67319 (0.0102)	0.7448 (0.0072)	-41374.18	82752.36	82765.51
Gamma	2.22138 (0.00243)	0.00220 (0.00001)	-41212.17	82428.34	82441.50
Weibull	1.631792 (0.01785)	1128.1181 (10.011)	-41189.58	82383.16	82396.32

The AIC and BIC values in Table 2 were close to each other, so non-parametric tests such as the Kolmogorov-Smirnov (KS), Cramer-von Mises (CVM), and Anderson-Darling (AD) tests were also employed to make a decision regarding the stock price data. The results of these tests are presented in Table 3. According to the results of these tests, it was determined that the Weibull distribution is the best fit for modelling the stock price data.

When applying the Weibull distribution to stock price data, the shape parameter (k=1.631792) can be useful in capturing the tail behaviour of the data. A higher value of the shape parameter indicates a heavier tail, indicating a higher likelihood of extreme price movements. On the other hand, a lower value of the shape parameter indicates a lighter tail, implying a lower likelihood of extreme events. The scale parameter (λ=1128.1181) influences the overall level or magnitude of the data. It determines the average or typical value around which the stock prices fluctuate. Adjusting the scale parameter can help align the distribution with the specific dataset being analysed.

Table 3. Results of KS, CVM and AD test for the close price data.

Model	KS	CVM	AD
Normal	0.0959	13.2550	98.272
Log-normal	0.0965	13.3609	99.417
Gamma	0.0826	6.1121	56.027
Weibull	0.0762	4.7887	47.812

These additional non-parametric tests provide further evidence supporting the selection of the Weibull distribution. The tests evaluate the goodness-of-fit between the empirical distribution of the stock price data and the theoretical Weibull distribution. Based on the results, it can be concluded that the Weibull distribution provides the most accurate representation of the stock price behaviour. Therefore, combining the findings from the AIC, BIC, and non-parametric tests, it can be confidently stated that the Weibull distribution is the optimal choice for modelling the stock price data in terms of both parametric and non-parametric approaches.

According to the KS test results for HDFC closing price data for the period 2023 to April 2024 (KS Statistic: 0.07198, p-value: 0.06628), because the p-value is greater than 0.05, we can conclude that the HDFC closing prices from 2023 to April 2024 fit the Weibull distribution. This suggests that the data is consistent with the Weibull distribution. Overall, the histogram and the Weibull fit curve in Figure 9 visually support the statistical conclusion that the closing prices of HDFC from 2023 to April 2024 follow a Weibull distribution.
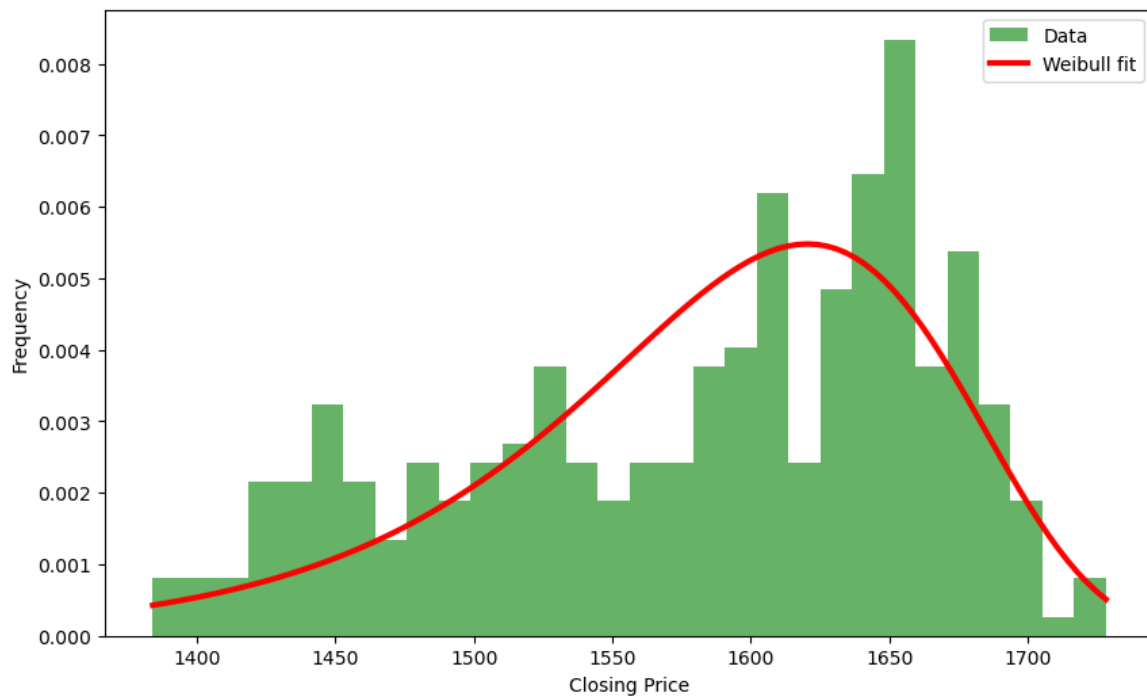
Figure 9. Weibull distribution fit to HDFC closing prices

5. CONCLUSION

Extreme value distributions play a crucial role in modelling stock price data, particularly when analysing tail behaviour and estimating tail probabilities. Extreme value distributions are designed to capture the behaviour of rare and extreme events, which occur with low probabilities but can have significant impacts on financial markets. These events include market crashes, large price fluctuations, and other extreme market conditions. In summary, extreme value distributions are valuable tools for understanding and quantifying the tail behaviour of stock price data. Their application in risk management, portfolio optimization, VaR estimation, tail risk hedging, and insurance highlights their importance in the financial industry.

The Weibull distribution is a probability distribution frequently used in modelling stock price data. It is a versatile distribution that can capture a wide range of shapes, including both heavy-tailed and light-tailed distributions. One advantage of the Weibull distribution is its flexibility in fitting a wide range of data shapes. By estimating the parameters of the Weibull distribution from historical stock price data, it is possible to model the future behaviour of stock prices, estimate tail probabilities, and assess the risk associated with extreme events. However, it is important to note that the choice of distribution should be based on the characteristics of the specific dataset and the research objectives. Other distributions, such as the Log-normal, Gamma, or generalized extreme value distributions, may also be appropriate depending on the characteristics of the stock price data being analysed.

Overall, the Weibull distribution can be a valuable tool for modelling stock price data and analysing tail behaviour, providing insights into the likelihood of extreme price movements and assisting in risk management and decision-making processes in the financial industry.

CONFLICT OF INTEREST

The authors stated that there are no conflicts of interest regarding the publication of this article.

CRediT AUTHOR STATEMENT

Ceren Ünal: Formal analysis, Visualization, Writing – Original Draft,
Gamze Özel Kadılar: Supervision, Formal analysis, Writing – Review & Editing

REFERENCES

[1]   Bachelier L. Théorie de la spéculation. in annales scientifiques de l'école normale supérieure 1900; 17: 21-86, http://dx.doi.org/10.24033/asens.476.

[2]   Țițan AG. The efficient market hypothesis: review of specialized literature and empirical research. Procedia Economics and Finance 2015; 32: 442-449.

[3]   Masoliver J, Montero M, Porrà JM. A dynamical model describing stock market price distributions. Physica A: Statistical Mechanics and its Applications 2000; 233(3-4): 559-567.

[4]   Cont R. Empirical properties of asset returns: stylized facts and statistical issues. Quantitative Finance 2001; 1(2): 223–236.

[5]   Mirsadeghpour Zoghi SM, Sanei M, Tohidi G, Banihashemi S, Modarresi N. The effect of underlying distribution of asset returns on efficiency in dea models. Journal of Intelligent & Fuzzy Systems 2021; 40(5): 10273-10283.

[6]   Ahmad Z, Mahmoudi E, Dey S. A new family of heavy tailed distributions with an application to the heavy tailed insurance loss data. Communications in Statistics-Simulation and Computation 2022; 51(8): 4372-4395.

[7]   Mandelbrot BB. The Variation of Certain Speculative Prices. Springer, New York, 1997.

[8]   Yousof HM, Tashkandy Y, Emam W, Ali MM, Ibrahim M. A new reciprocal Weibull extension for modelling extreme values with risk analysis under insurance data. Mathematics 2023; 11(4): 966.

[9]   Gebizlioglu OL, Şenoğlu B, Kantar YM. Comparison of certain value-at-risk estimation methods for the two-parameter Weibull loss distribution. Journal of Computational and Applied Mathematics 2011; 235(11): 3304-3314.

[10]   Kowan T, Mahalapkorkiat C, Samakrat T, Sumritnorrapong P. Probability distributions for modelling of covid-19 cases and deaths in Thailand. Computer Science 2022; 17(4): 1499-1506.

[11]   Campbell JY, Lo AW, MacKinlay AC. The Econometrics of Financial Markets. Princeton University Press, Princeton, NJ, 1997.

[12]   Bhaumik DK, Kapur K, Gibbons RD. Testing parameters of a gamma distribution for small samples. Technometrics 2009; 51(3): 326-334.

[13]   Tong YL. The Multivariate Normal Distribution. Springer Science & Business Media, 2012.

[14]   Weibull W. A statistical distribution function of wide applicability. Journal of Applied Mechanics 1951; 18: 293-297.

[15] Almalki SJ, Nadarajah S. Modifications of the Weibull distribution: a review. Reliability Engineering and System Safety 2014; 124, 32-55.

[16] Yahoo Finance (2023, Jun 10). [Online] Available: https://finance.yahoo.com

[17] Cullen AC, Frey HC, Frey CH. Probabilistic techniques in exposure assessment: a handbook for dealing with variability and uncertainty in models and inputs. Springer Science & Business, 1999.

RESEARCH ARTICLE

ASSESSING THE DYNAMIC RESPONSE OF SAND INCORPARATING EXPANDED GLASS GRANULES THROUGH RESONANT COLUMN TEST

Seyfettin Umut UMU [1,*]

[1] Transportation Vocational School, Eskisehir Technical University, Eskişehir, Türkiye
suumu@eskisehir.edu.trr - 0000-0002-5901-2626

Abstract

In contemporary geotechnical stabilization applications, there is a simultaneous drive to make applications as light and durable as possible while also preferring the utilization of waste products in soil improvement endeavors due to their dual merits of fostering environmental sustainability and conferring economic benefits. In this study, the use of expanded glass granules as a waste material was implemented to harmonize with this perspective, wherein reference sand and expanded glass granules were systematically mixed in varying proportions by mass and volume. Subsequently, the dynamic behavior of the mixture samples was rigorously assessed through a resonant column test between 0.001 - 0.1% shear strain amplitude and under various cell pressures. The variations in modulus reduction and initial shear modulus of the expanded glass granules added specimens were subjected to analysis, the shear modulus values of the samples mass-prepared (1, 2%) were obtained at least 12% and 21% higher than the reference sand, respectively. Similarly, the shear modulus values of the mixture sample prepared at 2.5% by volume were 20% higher than the reference sand at different effective pressures. The specimens prepared at 5% by volume demonstrate shear modulus values that were akin to those of the reference sand. The shear modulus values of the mixture samples prepared by volume (7.5, 10 and 15%) were found to be relatively lower than those of the reference sand. In the experimental study, it was discovered that the high angle of internal friction of the expanded glass granules exerts an influence on the variation in modulus reduction. According to the results of the experimental study, expanded glass granules show positive results in shallow geotechnical soil stabilization applications.

1. INTRODUCTION

The world is grappling with an escalating volume of waste material, surpassing the capacity of our storage infrastructure. Based on projections, the global waste generation is expected to double by 2050 and triple by 2100 compared to 2016 levels. A substantial portion of this waste, approximately 30%, originates from construction activities, playing a pivotal role in contributing over 33% of the world's carbon emissions[1-3]. In addition, recycling one kilogram of glass effectively replaces for 1.2 kilograms of newly extracted raw materials, leading to a reduction in both CO_2 emissions and the requirement for pristine natural resources. This makes a significant contribution to preventing the depletion of our natural resources[4]. In an effort to handle these issues, a potential remedy lies in repurposing these waste materials across diverse engineering applications.

In the field of geotechnical engineering, while lime, bitumen, and cement etc. have been widely used as conventional soil stabilizers for a considerable period of time, recent advances in research have revealed the potential effectiveness of several chemical and chemical-free substances as alternatives or

---

*Corresponding Author: suumu@eskisehir.edu.tr

supplements to lime or cement, including fly ash, geotextile, waste stone powder, polymers, geofoam, polyurethane, waste tire scraps and waste glass etc. [5-13]. The results of related studies conducted to improve the dynamic parameters of soils have shown that the strength of soils can be increased with various waste additives.

From this perspective, the primary focus in this study is to investigate the shallow improvement of soils, especially sands, with expanded glass granules obtained from waste glass by using resonant column test. The manufacturing stage of expanded glass granules (GG) initiates with the comminution of waste glass fragments, reducing them to smaller pieces while simultaneously eliminating extraneous elements like aluminum and steel. Following this, the recycled glass material is subjected to a precise fine grinding process, which is a crucial factor in determining the final quality of the foam glass. To attain the desired characteristics, the resultant product undergoes a surface treatment involving the application of a composite consisting of glass flower, binder, and a foaming agent, followed by an expansion process. These expanded glass granules (GG) serve as innovative constituents in the fabrication of superior-grade building materials and essential industrial resources. Converting recycled glass materials into diverse-sized white granules is achieved through a manufacturing process that entails blending finely ground glass with expanding agents. These mixtures are subsequently subjected to exceedingly high temperatures, resulting in granules ranging from 0.045 mm to sizes surpassing 16 mm. These granules have varying bulk densities, commencing at 140 kg/m^3 and extending upwards of 500 kg/m^3. The distinctive porous composition of expanded glass granules excels in enhancing thermal and acoustic properties by adeptly ensnaring air in its voids[4, 14, 15].

Expanded glass granules possess a diverse array of uses owing to their production in various sizes. They are used in a wide range of industries, including agriculture, automotive, oil and gas, machinery, biofiltration, and construction engineering. While their widespread use in construction for thermal insulation, they also serve as a constituent in the formulation of the subsequent items: dry blends like plaster, mortar, shotcrete, aerated autoclaved concrete, construction bricks and barriers, drainage systems, stone aggregate, acoustic insulation, and fire-resistant materials[16-19]. In the geotechnical engineering applications, including railway and road embankments and artificially engineered slopes, the utilization of recycled materials, particularly glass, has experienced a surge in popularity due to its commendable durability and eco-friendly attributes[20-24]. The Fine Recycled Glass (FRG), Medium Recycled Glass (MRG) samples were found to exhibit behavior similar to the geotechnical engineering behavior of well-graded natural sand and gravel mixtures, and the evaluations proved that they comply with the requirements published by EPA Victoria for the use of aggregates as poor materials[20]. The results of numerical simulations show that lightweight materials derived from glass tend to slightly reduce rail vibration in the critical speed range[21]. Another study confirmed that permeable concrete road subgrade made of expanded glass granules has similar mechanical properties to natural fine aggregate subgrade and can act as a frost protection layer for road subgrade[23]. Recent scientific research has demonstrated that recycled glass and their byproducts, bearing similarities in origin to natural sand, can serve as viable substitutes in construction endeavors encompassing both superstructures and infrastructure[13, 25-29]. Furthermore, empirical evidence from diverse investigations has underscored the discernible influence of glass fragment characteristics, including size and form rounded or angular), on their efficacy within geotechnical implementations[30]. Despite the obvious advantages of expanded glass granules, their underutilization in soil stabilization and lack of dynamic studies persist. Recognizing this gap, the research aims to provide insight into this subject.

Consequently, in the study, the modulus reduction variation and the initial shear modulus of sand prepared by mixing with expanded glass granules at different ratios (1, 2, 2.5, 5, 7.5, 10, 15%) were investigated through a resonant column test between 0.001 – 0.1% shear strain amplitude and under different effective pressures (25, 50, 75, 100 kPa). In order to fully understand the interaction of between the glass granules and reference sand, the tests were carried out dry and independent of the dynamic effect of water. The scientific investigation furnishes persuasive substantiation affirming the

advantageous impact exerted by GG on both the modulus reduction variation and initial shear modulus. The evidence clearly underscores that the high angle of internal friction, as well as the volumetric characteristics inherent to expanded glass granules, bestow substantial advantages upon the engineering properties of sand.

2. TEST METHOD, MATERIAL and PREPARATION

Seismic hazard assessment examines the impact of earthquakes on structures, particularly during sudden ground movements. The response of structures to seismic vibrations depends on the dynamic properties of the soil like shear resistance. Grasping these attributes is crucial for foreseeing potential harm and crafting resilient constructions. The initial shear modulus, known as G_{max} or G_0 ($\approx$ at 0.001 %), is a foundational factor that imparts crucial insights into the resilience and stiffness of the ground under cyclic dynamic loading. This characteristic, often denoted as the initial, maximum or low-level shear strength, is established over laboratory or in-situ studies employing various techniques for instance dynamic triaxial, the bender element and resonant column (RC) test methods. Among these tests, RC test stands out as a dependable means of gauging shear strength across a strain spectrum of 0.001 to 0.1 %, turning it an indispensable laboratory instrument for assessing dynamic response of soil. The RC test involves subjecting a hollow type or solid type soil column to vibration in one of its inherent modes. As part of this research, solid specimens were meticulously prepared. Subsequently, the computation of the wave propagation velocity is undertaken, utilizing the resonant frequency as a foundational parameter. The RC device in operation employs an electric motor to induce harmonic torsional vibrations to the specimen. This excitation imposes a consistent amplitude torsional harmonic load across a spectrum of frequencies, with concurrent measurement of the response curve. The initial-mode resonant frequency measurement is employed to deduce the shear wave velocity. The shear wave velocity and soil density are used to calculate the initial shear modulus. Gradually escalating the amplitude of the torsional harmonic load during each test session yields the shear modulus across diverse strain ranges[31, 32].

As previously noted, following the production phase, the expanded glass granules (GG) undergo sorting based on various grain size distributions. Prior to determining the expanded glass granule size employed for the investigation, a numbers of RC tests were carried out using a range of grain diameters, spanning from 0.25 to 8 mm. Based on the findings of these tests, the GG diameter of 2 – 4 mm, which exhibited the highest initial shear modulus, was singled out from the six distinct grain diameters. The physical and chemical properties of the expanded glass granules provided by the manufacturer are given in Table 1 and Table 2 respectively. The fundamental fractional data meet the criteria of LST EN 13055–1:2004/AC:2016[33, 34]. Because of its granular composition, GG effectively preserve temperature by ensnaring air within. Owing to its distinctive hollow framework, it takes in no more than 15% of its overall weight, even when entirely immersed in water. It's crucial that water absorption doesn't escalate over time, and the material retains its original thermal isolation properties and stability. Resistance to both organic and inorganic chemicals is a characteristic of expanded glass granules, preventing any decomposition or deterioration. The sealed voids within the expanded glass granules pores guarantee this material remains unaltered for numerous years (https://stikloporas.com/expanded-glass).

The reference sand (RS), laboratory properties are given in Table 3, is a non-uniform natural sand that complies with UNE EN 196-1 standards with a silica content of 98% and a generally round grain diameter[35].

Table 1. The physical properties of GG provided by manufacturer

GG	G_s	D (mm)	Moisture absorption % by mass	φ	$\rho_{d(max)}$ (gr/cm^3)	CS MPa
	0.34	2 – 4	15	45^0	0.275	1.4

Gs: Relative density; D: Used diameter; φ: Angle of internal friction; CS: Compressive strength

Table 2. The chemical properties of GG provided by manufacturer

GG	pH	SiO_2	Al_2O_3	$Ka_2O + Na_2O$	$CaO + MgO$	Fe_2O_3	Heat Resistant / Melt ^0C
	9–11	71–73	1.5–2.0	13–14	8–10.5	<0.3	750 / 1000

Table 3. The laboratory properties of reference sand (RS).

Reference Sand (RS)	D_{50} (mm)	D_{10} (mm)	C_u	C_c	φ	G_s	e_{min}	e_{max}
	0.63	0.13	6	1.28	33^0	2.637	0.415	0.674

D_{50}: Mean diameter; D_{10}: Effective particle size; C_u & C_c:Uniformity and curvature coefficient; φ: Internal friction angel; G_s: Relative density; e_{max} & e_{min}: Max. and min. void ratio

Following the previous clarification, this study involved the preparation of test samples at varying volumetric mixing ratios (2.5, 5, 7.5, 7.5, 10%) and mass proportions (1, 2%). The RS and GG underwent mechanical mixing within a pan, adhering to designated proportions, for a designated duration to guarantee even distribution (Figure 1a). It is well known that the presence of water significantly outweighs other factors in its impact on the response of soils, particularly granular ones, under cyclic dynamic loads. Consequently, to explore the dynamic interaction between GG and RS, the composite specimens were prepared in a completely dry state. In both volume and mass combinations, the volume and mass of RS and GG were steadfastly maintained and then subjected to RC testing (Figure 1b). The reference specimens (Reference sand and expanded glass granules) and mixture specimens, as per the specifications outlined in Table 4 and Table 5, were placed within the RC testing apparatus.

Table 4. The RC test properties of reference specimens (RS&GG) and mixed specimens by mass.

		Reference Samples		Mixed Samples by Total Mass	
		GG100	RS100	RS99/GG1	RS98/GG2
M_T (gr)	GG	70.19	0	4.35	8.70
	RS	0	435	430.65	426.30
	Total	70.19	435	435	435
M_W	gr			0	
D	mm			50	
H	mm			130	
V_T	cm^3			255.25	
σ'_0	kPa			25; 50; 75; 100	
ρ_d	gr/cm^3	0.275	1.704	1.704	1.704

M_T & M_W: Total and water mass; H & D: Height and diameter;
V_T: Volume; σ'_0:Effective pressure; ρ_d: Dry density

Table 5. The RC test properties of mixed specimens by volume.

		Mixed Samples by Total Volume				
		RS97.5/GG2.5	RS95/GG5	RS92.5/GG7.5	RS90/GG10	RS85/GG15
M_T (gr)	GG	1.75	3.51	5.26	7.02	10.53
	RS	424.36	413.48	402.60	391.72	369.96
	Total	426.12	416.99	407.87	398.74	380.49
M_W	gr			0		
D	mm			50		
H	mm			130		
V_T	cm^3			255.25		
σ'_0	kPa			25; 50; 75; 100		
ρ_d	gr/cm^3	1.669	1.634	1.598	1.562	1.491

M_T & M_W: Total and water mass; H & D: Height and diameter;
V_T: Volume; σ'_0:Effective pressure; ρ_d: Dry density

Geotechnical engineering practices, including building slope reinforcement, providing constructing road and railway embankments or backfill support for retaining walls, primarily focus on shallow soil improvement and rehabilitation processes. Therefore, for this research, all the samples were subjected to effective cell pressures of 25, 50, 75, and 100 kPa.

(a)   (b)
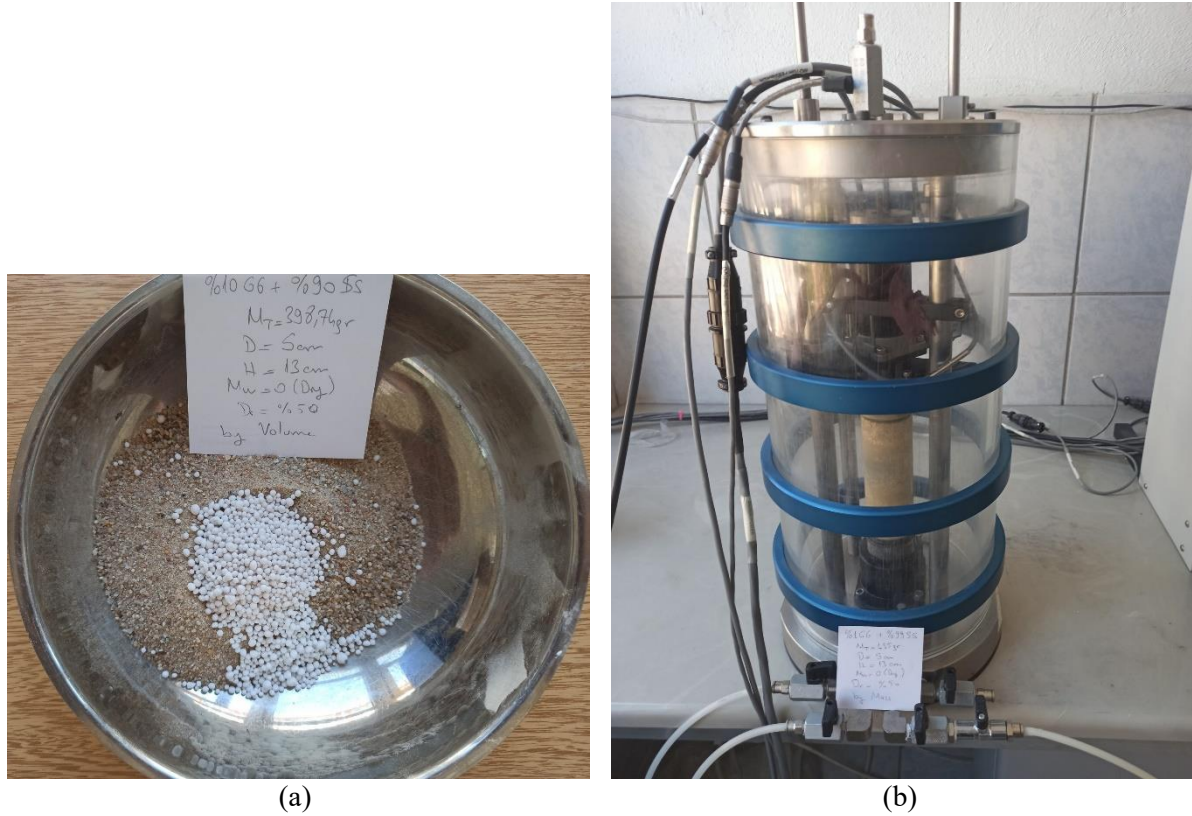
Figure 1. An example of mixture samples (GG10RS90) and RC test apparatus located at ESOGU Lab.

3. EXPERIMENTAL RESULTS

3.1. Results of Reference Samples (RS100&GG100)

In order to compare the experimental results, RS100 and GG100 specimens were first subjected to RC testing under the specified effective cell pressures. The shear modulus and modulus reduction graphs of both RS100 and GG100 along wide range of shear strain amplitudes are given in Figure 2. Upon analyzing the results depicted in the relevant graphs, considerably higher shear modulus values for RS100 were observed compared to GG100 between $\gamma = 0.001 - 0.03\%$ (Figure 2a, 2b). Significantly higher shear modulus values for RS100, as compared to GG100, were recorded as the effective cell pressure applied (75 – 100 kPa) to the specimens was increased (Figure 2a). The graphs show that, as the shear strain amplitude increases, the relative difference in shear modulus values for RS100 compared to G100 decreases, and even at high shear strain amplitude levels (as approaches to 0.1%), the data of GG100 remains higher (Figure 2a, 2b). Considering that the primary purpose of the study was to investigate the effects of GG on soil improvement due to their high angle of internal friction, the resilience of the shear modulus values of GG100 to decrease becomes evident as the deformation level increase. The modulus reduction graphs of both RS100 and GG100are also given in Figure 2 to support the corresponding case (Figure 2c, 2d).
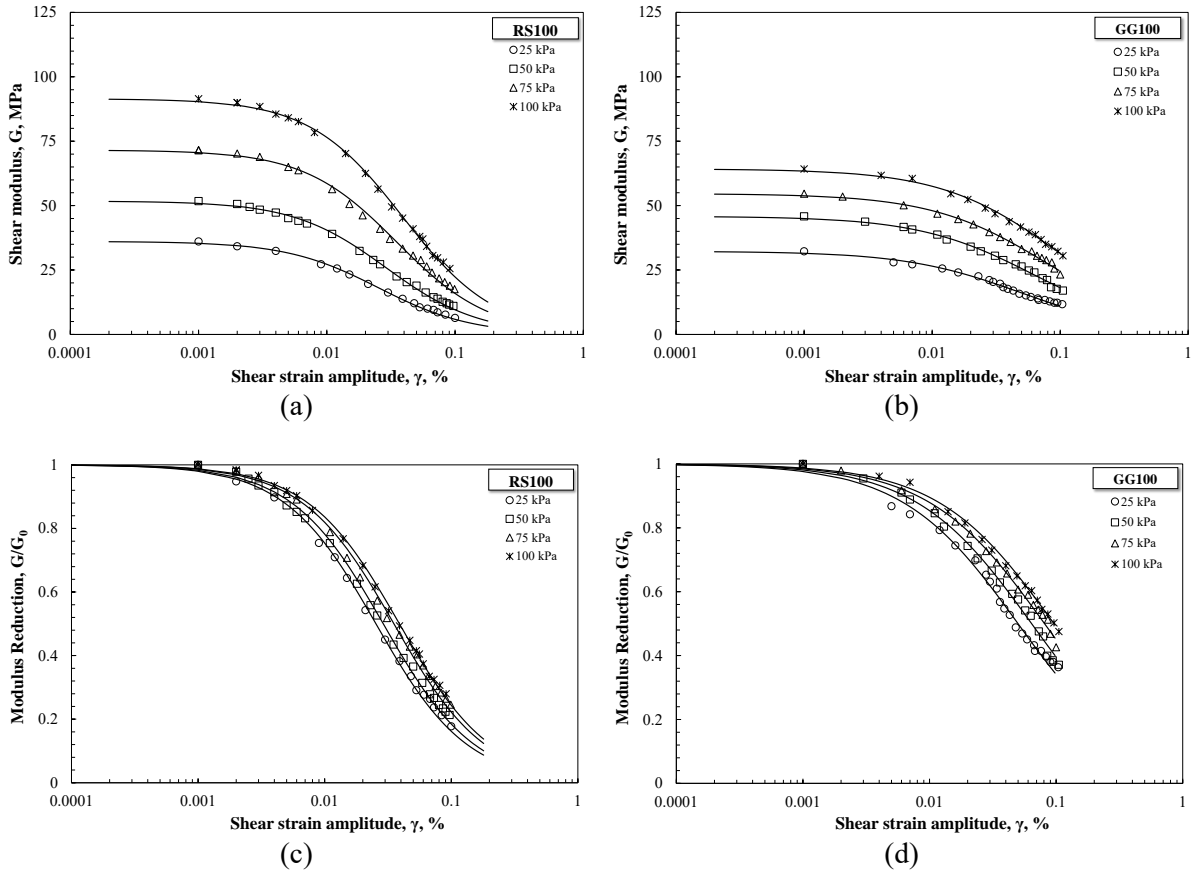
Figure 2. Shear modulus of RS100 (a) and GG100 (b); modulus reduction of RS100(c) and GG100(d).

3.2. Mathematical Model of Reference Sample (RS100&GG100)

The hyperbolic model is employed to forecast soil behavior in boundary value problems and provides the mathematical framework for describing nonlinear soil behavior. The reference shear strain amplitude (γ_r) within the hyperbolic model is defined as the strain that aligns with halve of the shear modulus. In the hyperbolic model, two tangent lines shape and limit the stress-strain curve of the analyzed samples. Small strains are characterized by G_0 in the tangent, which illustrates the elastic modulus, while the upper limit of the stress τ_f, representing the soil resistance, is denoted by the horizontal asymptote at large strains. The following differential expression of the stress-strain curve enclosed by tangents is presented where n is arbitrarily chosen [13, 36].

$$\frac{d\tau}{d\gamma} = G_0 \left(1 - \frac{\tau}{\tau_f}\right)^n \tag{1}$$

This statement expresses that the tangent to the stress-strain curve gets a value of G_0 at $\tau = 0$ and undergoes a decreasing trend as stress levels increase, eventually reaching zero at $\tau = \tau_f$. Excluding the situation when n = 1, by integrating Eq. 1, the condition can be fulfilled, $\gamma = 0$ when $\tau = 0$ where (γ_r) is defined as the reference strain[36].

$$\gamma = \frac{\gamma_r}{n-1} \left[\frac{1}{\left[1 - (\tau/\tau_f)\right]^{n-1}} - 1 \right] \tag{2}$$
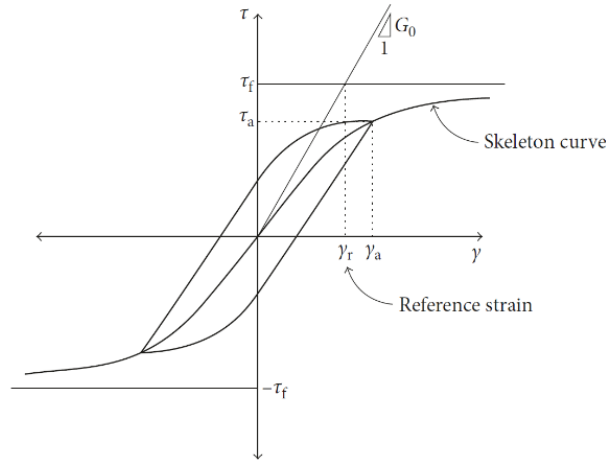
Figure 3. Reference strain definition in hyperbolic model[36]

Defined as follows, it represents the strain value in an elastic material when it reaches its failure stress;

$$\gamma_r = \frac{\tau_f}{G_0} \tag{3}$$

The reference strain represents the strain a soil would reach at the point of failure stress if it exhibited purely elastic behavior, as shown in Figure 3. The stress-strain curve can be derived as follows from Eq. 2. by assigned n = 2;

$$\tau = \frac{G_0 \gamma}{1 + \dfrac{\gamma}{\gamma_r}} \tag{4}$$

The modulus reduction is calculated using the following formula;

$$\frac{G}{G_0} = \frac{1}{1 + \dfrac{\gamma_a}{\gamma_r}} \tag{5}$$

where γ_a is the cyclic shear strain amplitude and $G = \tau_a / \gamma_a$. It has been found that when the shear strain reaches the reference strain, the secant shear modulus is reduced to half of its initial value[36]. The hyperbolic model exhibited in Eq. 5 is associated with the curvature coefficient (n), which influences the curvature of the modulus reduction trend lines, according to Darendeli[37]. The following correlation (Eq. 6) was employed to generate the trend lines concerning modulus reduction and initial shear modulus for both RS100 and GG100 in Figure 2, within the scope of the analyses. The curves obtained from the given equation were used to compare the test result graphs of the mixture samples with the test results of the RS100. The curvature coefficient (n) and reference strain values (γ_r) of the RS100 and GG100 are given in Table 6 according to the effective cell pressure variation.

$$\frac{G}{G_0} = \frac{1}{1 + \left(\dfrac{\gamma_a}{\gamma_r}\right)^n} \tag{6}$$

Table 6. The reference strain and coefficient of curvature values of RS100&GG100 to obtain the mathematical model

σ_0' (kPa)	RS100		GG100	
	n	γ_r **%**	**n**	γ_r **%**
25		0.0254		0.050
50	1.2	0.0290	0.95	0.064
75		0.0352		0.081
100		0.0389		0.096

σ_0': Effective cell pressure; γ_r: Reference strain; n: Coefficient of curvature

3.3. RC Results of Samples with GG

3.3.1. Results of mass-mixture samples

As mentioned before, the mixed specimens were prepared as a percentage of the total mass (1 and 2%). In Figure 4, the shear modulus and modulus reduction graphs of the mass-mixture specimens prepared at 1% and 2% (RS99/GG1 and RS98/GG2) ratios are given in comparison with RS100 values. The straight lines shown in the graphs are obtained from the RS100 test results and are derived from Eq. 6. When the shear modulus & shear deformation amplitude graph of the RS99/GG1, which has the same dry unit density as that of RS100 and is calculated to be 1.704 gr/cm³, was examined, the shear modulus values of the RS99/GG1 specimen were significantly higher than those of RS100 at all effective cell pressures (Figure 4a).
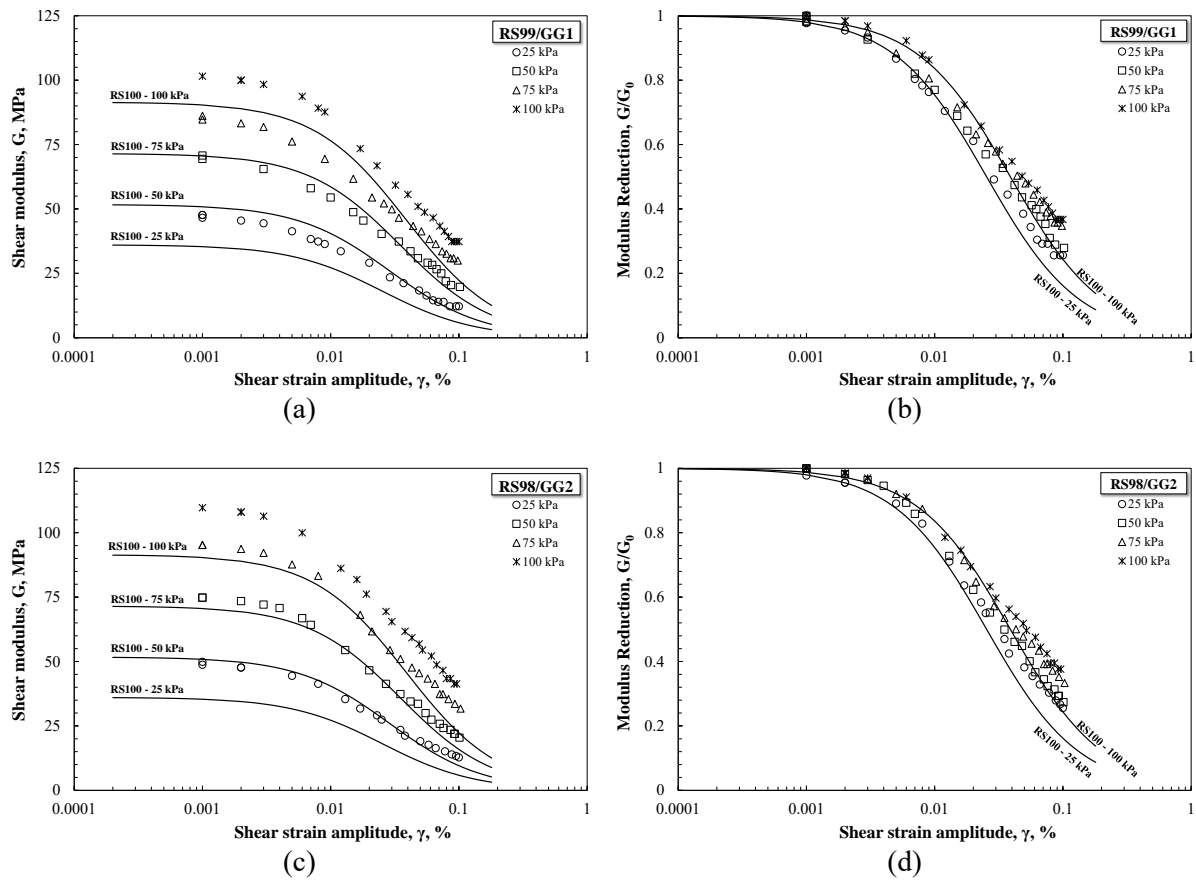
Figure 4. Shear modulus of RS99/GG1(a) and RS98/GG2 (c), modulus reduction of RS99/GG1(b) and RS98/GG2 (d)

When the modulus reduction graph of RS99/GG1 was analyzed, between $\gamma = 0.03 - 0.1\%$, higher modulus reduction values than RS100 were observed (Figure 4b). Similarly, the shear modulus values of the RS98/GG2 specimen were significantly higher than the RS100 under all effective cell pressures, when the comparison between the shear modulus values of the RS98/GG2 specimen and RS100 was conducted (Figure 4c). In Figure 4d, the shear modulus of RS98/GG2 specimen also resists to decrease as the shear deformation amplitude increases between $\gamma = 0.03 - 0.1\%$. RS99/GG1 and RS98/GG2 specimens, both specimens have a dry density of 1.704 gr/cm^3, when compared among themselves, the shear modulus values of RS98/GG2 specimen were significantly higher (Figure 4a, 4c). Both samples have significantly higher shear modulus than RS100. The main reason for this result is that the GG fills the voids in the solid specimen, resulting in compact specimens in comparison with the reference sample. Furthermore, when the modulus reduction graph of GG100 was examined, the effect of the high angle of internal friction of GG100 on the modulus reduction was emphasized (Figure 2d). It can be asserted that the modulus reduction values of the mass-mixed specimens are similarly influenced by the high angle of internal friction of GG between $\gamma = 0.03 - 0.1\%$ (Figure 4b, 4d).

3.3.2. Results of volume-mixture samples

As mentioned in the study, the mixed samples were prepared as a percentage of the total volume (2.5, 5, 7.5, 10 and 15%). Figure 5 shows the shear modulus and modulus reduction graphs of RS97.5/GG2.5 and RS95/GG5. The dry densities of both samples were 1.669 gr/cm^3 and 1.634 gr/cm^3 respectively, which are lower than RS100.
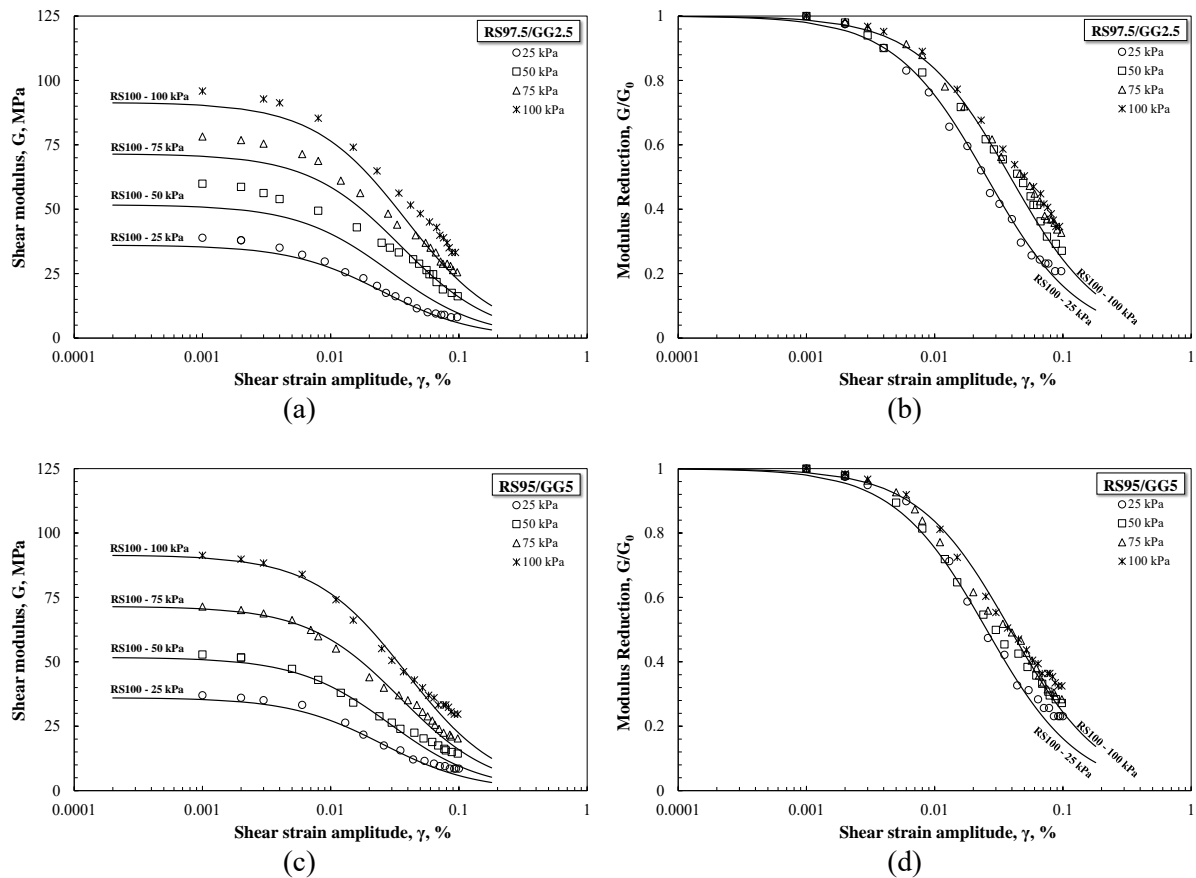
Figure 5. Shear modulus of RS97.5/GG2.5(a) and RS95/GG5 (c), modulus reduction of RS97.5/GG2.5(b) and RS95/GG5 (d)

The graph shows that the shear modulus values of RS97.5/GG2.5 are significantly higher compared to RS100 at all effective cell pressures (Figure 5a). RS97.5/GG2.5 followed a similar trend with RS100 between $\gamma = 0.01 – 0.05\%$ and below 25 kPa pressure (Figure 5a). It can be seen that the void filling effect of GG is also effective on RS97.5/GG2.5. Except for the 25 kPa values, the modulus reduction values of RS97.5/GG2.5 were higher than those of RS100 at all remaining cell pressure values between $\gamma = 0.03 – 0.1\%$ (Figure 5b).

At all effective cell pressures and between $\gamma = 0.001 – 0.08\%$, RS95/GG5, whose dry density was calculated to be 4% lower than the RS100, obtained similar shear modulus values to the RS100 (Figure 5c). The shear modulus value of the RS95/GG5 specimen was slightly higher than RS100 between $\gamma = 0.08 – 0.1\%$ (Figure 5c). The modulus reduction values of RS95/GG5 were higher than the RS100 at all remaining cell pressure values between $\gamma = 0.03 – 0.1\%$ except 25 kPa.

Figure 6 shows the shear modulus and modulus reduction graphs of RS92.5/GG7.5, RS90/GG10 and RS85/GG15 specimens with mixed ratios of 7.5, 10 and 15% by volume, respectively. The unit density values of these samples were 7, 8.5 and 12% lower than RS100. When the shear modulus graphs of all three specimens are examined, it is evident that the shear modulus values of the respective samples are lower than RS100 along $\gamma = 0.001 – 0.035\%$ under all effective cell pressures (Figures 6a, 6c and 6e). On the other hand, it can also be seen from the graphs that the shear modulus values of all three specimens are higher than RS100 due to the increasing shear strain amplitudes after $\gamma = 0.035\%$ under all effective pressures (Figure 6a, 6c and 6e).

When the modulus reduction graphs of RS92.5/GG7.5, RS90/GG10 and RS85/GG15 are examined, it is clear that the modulus reduction values of all samples follow a similar trend with the variation of RS100 modulus reduction along $\gamma = 0.001 – 0.035\%$ under all effective cell pressures (Figures 6b, 6d and 6f). Nevertheless, it is also seen from the graphs that the modulus reduction values of RS92.5/GG7.5, RS90/GG10 and RS85/GG15 are higher than the modulus reduction values of RS100 with increasing shear strain amplitudes after $\gamma = 0.035\%$ under all effective pressures (Figures 6b, 6d and 6f).

To explain the behavior of RS92.5/GG7.5, RS90/GG10 and RS85/GG15 shown in Figure 6, it should first be noted that these specimens contain a high volume of expanded glass granules, which causes the specimens to contain many voids. The voids in the RS92.5/GG7.5, RS90/GG10 and RS85/GG15 cause the shear modulus values to be low compared to RS100 $\gamma = 0.001 – 0.035\%$ at all effective cell pressures. The most important feature of granular soils is that they can be compacted by vibration. Increasing the shear strain amplitude during the RC experiment is possible by increasing the applied torque, which also increases the vibration on the specimen. With increasing shear strain amplitude, RS92.5/GG7.5, RS90/GG10 and RS85/GG15 become relatively dense and the high angle of internal friction of GG reduces the decrease of the shear modulus, which also explains the behavior of RS92.5/GG7.5, RS90/GG10 and RS85/GG15 after shear strain amplitude $\gamma = 0.035\%$.

4. CONCLUSION

The main objective of this experimental investigation involves the study of the dynamic behavior exhibited by a composite material composed of reference sand (RS) mixed with expanded glass granules (GG) by using a (RC) resonant column test device. The mixture specimens prepared both by mass (1, 2%) and volume (2.5, 5, 7.5, 10 and 15%), test details given in Table 4 and 5, were tested in the shear deformation range of $\gamma = 0.001 - 0.1\%$ under effective cell pressures of 25, 50, 75 and 100 kPa. As previously explained, the fact that GG is a chemically inert material, allows us to attribute the results of this research to the physical interactions between RS and GG. It is also known that water has an effect on the behavior of granular soils under dynamic loading, so all mixture samples were prepared dry to avoid the effects of water.
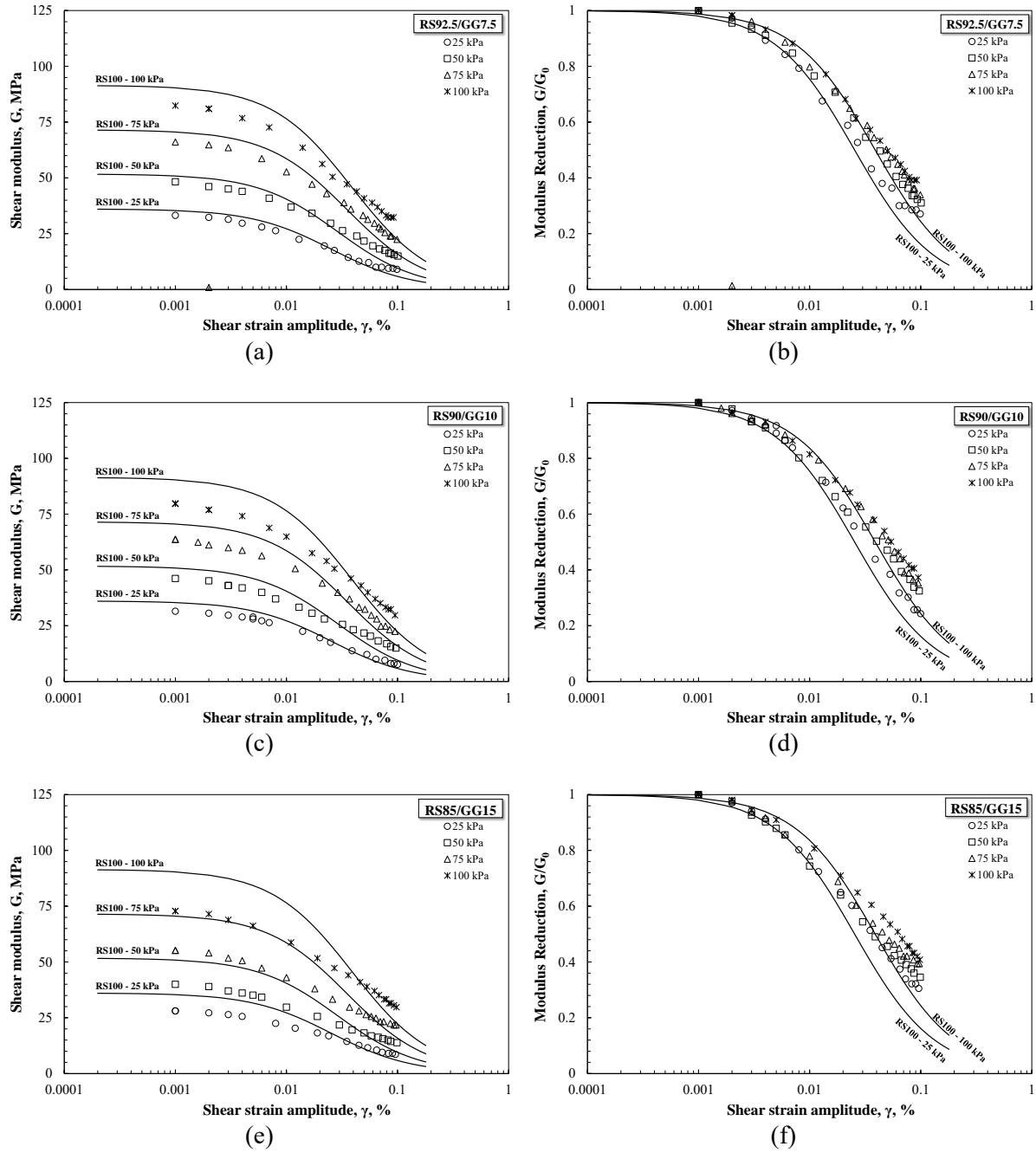
Figure 6. Shear modulus of RS92.5/GG7.5(a), RS90/GG10 (c) and RS85/GG15 (e), modulus reduction of RS92.5/GG7.5(b), RS90/GG10 (d) and RS85/GG15 (f)

When the behavior of the RS99/GG1 and RS98/GG2 prepared with the same grain density as RS100 was examined, it was found that the expanded glass granules filled the voids in these samples quite well. Both specimens have very high shear modulus values compared to RS100, although they have the same density as RS100 at all effective cell pressures through all shear strain amplitudes. Upon examination of the modulus reduction variations of both samples, it was once more observed from the experiments that the modulus reduction values exceeded RS100 after $\gamma = 0.03\%$. It is clear that the effect of GG on the mass-prepared samples is twofold. First of all, the GG were well dispersed in the mass-prepared specimens and provided compression, which resulted in higher shear modulus values than RS100 along

all shear strain amplitudes. The second positive aspect is the effect of the high angle of internal friction of GG on the modulus reduction values with increasing shear strain amplitudes. The expanded glass granule has been a crucial aspect in ensuring that the modulus reduction values of the mass-prepared specimens remained higher than RS100 with increasing deformation after $\gamma = 0.03\%$ at all effective pressures.

RS97.5/GG2.5 and RS95/GG5, which are prepared by volume, are 2% and 4% lighter than RS100, respectively. RS97.5/GG2.5 has relatively higher shear modulus values than RS100, on the other hand, RS95/GG5 has similar values with RS100. Similar to the results of the mass-prepared samples, RS97.5/GG2.5 and RS95/GG5 can be used as a substitute for RS100 depending on the test results. The similar results of the effects of expanded glass granules on samples prepared by mass can also be observed in the results of these two samples.

RS92.5/GG7.5, RS90/GG10 and RS85/GG15 samples, prepared by volume, have densities that are 7%, 8.5% and 12% lower than that of RS100, respectively. The test results indicate that RS92.5/GG7.5, RS90/GG10 and RS85/GG15 exhibit lower shear modulus values when compared to RS100 along $\gamma = 0.001 - 0.035\%$ at all effective cell pressures. On the contrary, the shear modulus values of all three specimens exceed RS100 as the shear strain amplitudes increase after $\gamma = 0.035\%$ under all effective pressures. A similar assessment applies to the modulus reduction variation of these specimens.

As expected under the corresponding test conditions, the favorable impact on both especially modulus reduction values and the shear modulus values of mixed samples is considered to be influenced by the high angle of internal friction exhibited by the GG (effective along $\gamma = 0.03 - 0.1\%$) and the physical volume occupied by the GG (effective along $\gamma = 0.001 - 0.03\%$). It was observed that the results obtained from this study were in agreement with the results obtained by mixing expanded glass granules with clays[13]. When the ratios recommended in the study are increased, the amount of the main soil material decreases. In this case, the behavior of expanded glass granules is dominant. The feasibility of using expanded glass granules as a soil stabilization agent in shallow geotechnical applications is elucidated by the present study. It is underscored by experimental evidence that, depending on the specified boundary conditions, expanded glass granules can be used as a viable modality. To comprehensively understand its potential contributions, subsequent investigations into the attributes of the material and its application in different soil types and boundary frameworks are considered imperative.

ACKNOWLEDGEMENTS

CONFLICT OF INTEREST

The author(s) stated that there are no conflicts of interest regarding the publication of this article.

CRediT AUTHOR STATEMENT

Seyfettin Umut Umu: Conceptualization, Methodology, Formal Analysis, Investigation, Resources, Writing - Original Draft, Writing - Review&Editing, Visualization

REFERENCES

[1]   Ferdous W, Manalo A, Siddique R, Mendis P, Yan Z, Wong H, Lokuge W, Aravinthan T, Schubel P. Recycling of landfill wastes (tyres, plastics and glass) in construction - A review on global waste generation, performance, application and future opportunities. Resources Conservation and Recycling. 2021;173.

[2]   Akinade O, Oyedele L. Integrating construction supply chains within a circular economy: An ANFIS-based waste analytics system (A-WAS). Journal of Cleaner Production. 2019;229:863-73.

[3]   Baek C, Park S, Suzuki M, Lee S. Life cycle carbon dioxide assessment tool for buildings in the schematic design phase. Energy and Buildings. 2013;61:275-87.

[4]   Sommariva L, Weinberger K, Pierucci S, Klemes J. Energy and Natural Resources Saving In The Production of Expanded Glass Granules. Icheap12: 12th International Conference on Chemical & Process Engineering. 2015;43:2437-42.

[5]   Shi J, Xiao Y, Hu J, Wu H, Liu H, Haegeman W. Small-strain shear modulus of calcareous sand under anisotropic consolidation. Canadian Geotechnical Journal. 2022;59:878-88.

[6]   Ashango AA, Patra NR. Behavior of Expansive Soil Treated with Steel Slag, Rice Husk Ash, and Lime. Journal of Materials in Civil Engineering. 2016;28:06016008.

[7]   Sarajpoor S, Ghalandarzadeh A, Kavand A. Dynamic behavior of sand-bitumen mixtures using large-size dynamic hollow cylinder tests. Soil Dynamics and Earthquake Engineering. 2021;147:106801.

[8]   Lang L, Li F, Chen B. Small-strain dynamic properties of silty clay stabilized by cement and fly ash. Construction and Building Materials. 2020;237:117646.

[9]   Saride S, Dutta TT. Effect of Fly-Ash Stabilization on Stiffness Modulus Degradation of Expansive Clays. Journal of Materials in Civil Engineering. 2016;28:04016166.

[10]   El-kady MS, Azam A, Yosri AM, Nabil M. Modelling of railway embankment stabilized with geotextile, geo-foam, and waste aggregates. Case Studies in Construction Materials. 2023;18:e01800.

[11]   Umu SU, Okur D, Yilmaz G, Firat S. A Study on The Stiffness and Damping Characteristics of Sand/Rubber Mixtures Under Dynamic Loading Conditions. Journal of Polytechnic-Politeknik Dergisi. 2014;17:13-21.

[12]   Okur DV, Umu SU. Dynamic properties of clean sand modified with granulated rubber. Advances in Civil Engineering. 2018;2018.

[13]   Umu SU. Assessment of sustainable expanded glass granules for enhancing shallow soil stabilization and dynamic behaviour of clay through resonant column tests. Engineering Science and Technology, an International Journal. 2023;42:101415.

[14]   da Silva RC, Puglieri FN, de Genaro Chiroli DM, Bartmeyer GA, Kubaski ET, Tebcherani SM. Recycling of glass waste into foam glass boards: A comparison of cradle-to-gate life cycles of boards with different foaming agents. Science of The Total Environment. 2021;771:145276.

[15] Rodrigues C, König J, Freire F. Prospective life cycle assessment of a novel building system with improved foam glass incorporating high recycled content. Sustainable Production and Consumption. 2023;36:161-70.

[16] Adewoyin O, Adesina A, Das S. Performance Evaluation of Thermal-Efficient Lightweight Mortars Made with Expanded Glass as Aggregates. Journal of Materials in Civil Engineering. 2022;34.

[17] Lecheb S, Chellil A, Chahour K, Safi B. Foamed glass granulated-based self-compacting mortars: open-porosity effect on rheological and mechanical properties. Cement Wapno Beton. 2021;26:242-52.

[18] Augonis A, Ivanauskas E, Bocullo V, Kantautas A, Vaiciukyniene D. The Influence of Expanded Glass and Expanded Clay on Lightweight Aggregate Shotcrete Properties. Materials. 2022;15.

[19] Guo P, Meng W, Du J, Stevenson L, Han B, Bao Y. Lightweight ultra-high-performance concrete (UHPC) with expanded glass aggregate: Development, characterization, and life-cycle assessment. Construction and Building Materials. 2023;371:130441.

[20] Disfani M, Arulrajah A, Bo M, Hankour R. Recycled crushed glass in road work applications. Waste Management. 2011;31:2341-51.

[21] Lenart S, Kaynia A. Dynamic properties of lightweight foamed glass and their effect on railway vibration. Transportation Geotechnics. 2019;21.

[22] Kazmi D, Serati M, Williams D, Qasim S, Cheng Y. The potential use of crushed waste glass as a sustainable alternative to natural and manufactured sand in geotechnical applications. Journal of Cleaner Production. 2021;284.

[23] Kurpińska M, Grzyl B, Pszczola M, Kristowski A. The Application of Granulated Expanded Glass Aggregate with Cement Grout as an Alternative Solution for Sub-Grade and Frost-Protection Sub-Base Layer in Road Construction. Materials. 2019;12:3528.

[24] Saberian M, Li J, Boroujeni M, Law D, Li C-Q. Application of demolition wastes mixed with crushed glass and crumb rubber in pavement base/subbase. Resources, Conservation and Recycling. 2020;156:104722.

[25] Baldovino JdJA, Izzo RLdS, Silva ÉRd, Rose JL. Sustainable Use of Recycled-Glass Powder in Soil Stabilization. Journal of Materials in Civil Engineering. 2020;32:04020080.

[26] Baradaran MS, Qazanfari R, Baradaran S. Study of soil reinforcement in the east of Mashhad using glass granule. Materials Research Express. 2023;10:055202.

[27] Benny JR, Jolly J, Sebastian JM, Thomas M. Effect of glass powder on engineering properties of clayey soil. International Journal of Engineering Research & Technology. 2017;6:228-31.

[28] Otsubo M, Towhata I, Hayashida T, Liu B, Goto S. Shaking table tests on liquefaction mitigation of embedded lifelines by backfilling with recycled materials. Soils and Foundations. 2016;56:365-78.

[29] Sandiani M, Tanzadeh J. Laboratory assessing of the liquefaction potential and strength properties of Sand soil treated with mixture of nanoclay and glass fiber under dynamic and static loading. Journal of Materials Research and Technology. 2020;9:12661-84.

[30] Xiao Y, Long L, Evans TM, Zhou H, Liu H, Stuedlein AW. Effect of Particle Shape on Stress-Dilatancy Responses of Medium-Dense Sands. Journal of Geotechnical and Geoenvironmental Engineering. 2019;145:04018105.

[31] Drnevich VP. Recent Developments in Resonant Column Testing. ASCE annual meeting Proceedings, Richart Commemorative Lectures, . Detroit, MI.1985.

[32] ASTM. Standard test methods for modulus and damping of soils by the resonant-column method. American Society for Testing & Materials2000. p. 582-601.

[33] EN13055-1. 13055-1. Lightweight Aggregates—Part 1: Lightweight Aggregates for Concrete, Mortar and Grout. British Standard: London, UK2004.

[34] EN13055. EN 13055:2016, Lightweight aggregates. 2016.

[35] UNE.EN.196-1:2018. Methods of testing cement - Part 1: Determination of strength. 2018. p. 36.

[36] Ishihara K. Soil Behaviour in Earthquake Geotechnics: Clarendon Press; 1996.

[37] Darendeli MB. Development of a new family of normalized modulus reduction and material damping curves: The University of Texas at Austin; 2001.

RESEARCH ARTICLE

THE MECHANICAL CHARACTERIZATION OF CARBON BASED NANOPARTICLE REINFORCED EPOXY COMPOSITES: A COMPARATIVE STUDY

Fatih TURAN [1],*

[1] Department of Mechanical Engineering, Faculty of Engineering, Eskisehir Technical University, Eskisehir, Turkey
fatihturan@eskisehir.edu.tr - 🆔 *0000-0002-7197-3892*

Abstract

This comparative study experimentally investigates the effect of both the type and content of carbon based nanoparticles on the mechanical properties of epoxy composites. For this purpose, carbon nanotubes (CNTs), expanded graphite (EG), and carbon black (CB) were used as reinforcing nanoparticles at various concentrations within the epoxy polymer. The nanoparticles were dispersed by ultrasonication method. CNTs incorporated up to 0.4% by weight (wt.) while EG and CB nanoparticles were employed at 4%, 8%, 10%, and 12% concentrations by weight. Tensile tests of the nanocomposites were conducted according to ASTM D680 to determine the mechanical properties of nanocomposites including ultimate tensile strength and modulus. The results revealed that all types of nanoparticles have a strong reinforcing effect on the mechanical properties depending on their concentrations. When carbon nanotubes (CNTs) were used, the highest improvement in strength, by 84.7% at 0.1% wt., and in modulus, by 32.1% at 0.2% wt. content, was observed. EG nanoparticles exhibited improvement in both strength and modulus at all contents. The highest improvement in strength, by 109.6% at 4% wt., and in modulus, by 95.6% at 10% wt. concentration, was observed. In the case of carbon black (CB), improvement in strength was observed only at 4% wt. concentration, by 44.9%. On the other hand, enhancement in modulus was seen at all CB contents, with the greatest improvement at 10% wt., reaching 58.2%.

1. INTRODUCTION

Due to their high modulus, strength, electrical insulating properties, and chemical stability, epoxy resins have found extensive application in structural engineering as adhesive or matrix materials in the aerospace, marine, and automotive industries [1–3]. The widespread adoption of epoxy materials in engineering applications is hindered by their inherent brittleness, a drawback resulting from their highly cross-linked microstructure [4, 5]. Therefore, enhancing the mechanical properties of epoxy is crucial to obtain functional composite materials.

One of the effective ways is to improve the mechanical properties of epoxy composites is to introduce a secondary phase of carbon-based nano fillers such as carbon nanotube (CNT) [6], silicon carbide (SiC) [7] carbon black (CB) [8], expanded graphite (EG) and graphene nanoplatelet (GNP) [9] within epoxy matrix. Beside the improvement in the mechanical properties, the addition of nanoparticles into the polymer materials enhance the thermal [10] and electrical properties [11] of the epoxy phase as well. CNTs have gained widespread popularity due to their remarkable mechanical [12], electrical [13], and thermal properties [14]. CNTs are nano-sized cylindrical structures made of carbon. CNTs have gained widespread popularity due to their remarkable mechanical [12], electrical [13], and thermal properties [14]. CNTs are nano-sized cylindrical structures made of carbon. They can exist as either single-walled

---

carbon nanotubes (SWCNTs), comprising a single graphene layer rolled into a cylindrical shape; double-walled carbon nanotubes (DWCNTs), composed of exactly two single-walled carbon nanotubes, one nested in another; or multi-walled carbon nanotubes (MWCNTs), consisting of multiple concentric cylindrical layers of graphene. They are extensively employed in CNT/polymer composites for both functional and structural applications [15, 16]. EG is a versatile carbon-based nanomaterial characterized by its low density, high aspect ratio, porous structure, excellent thermal and electrical conductivity, ease of preparation, and cost-effectiveness [17]. Consequently, numerous studies have explored the incorporation of EG as a functional filler in polymer composites for diverse applications, including conductive polymer components, high-temperature resistant parts, sealing gaskets, and flame-retardant composites [18–22]. CB produced by the incomplete combustion of carbonaceous or petroleum products stands out as one of the primary reinforcing fillers within the polymer industry due to its readily available source, lightweight nature, high electrical conductivity, and low cost [23, 24]. Possessing superior characteristics such as the ability to absorb UV energy and high electrical and thermal conductivity make CB an excellent candidate to form functional thermoset composites. CB essentially consists of elemental carbon in the form of extremely fine particles with a partially amorphous molecular structure. The typical size of CB particles ranges from 5 to 100 nm, however they have tendency to form cluster resulting in bigger size aggregates up to 500 nm.

The reinforcing effect of the carbon-based nanoparticles on the mechanical properties depends on some parameters such as morphological structure, particle size, distribution level, and volume fraction of nanoparticles in the epoxy structure [14]. CBs, CNTs, and EGs can be classified as 0D, 1D, and 2D based on their morphological structure, respectively. This diversity on the morphological structure might lead to the different surface areas in these nanoparticles. The surface area of nanotubes can act as desirable interface for efficient stress transfer from the epoxy matrix to the nanoparticles [25]. In other words, the higher the interfacial area between the nanoparticles and the matrix phase, the greater load transfer capability. Table 1 lists some of the published works related to the mechanical performance of CNT, CB, and EG filled epoxy composites at various nanoparticle concentrations.

Table1. Some published works related to mechanical performance of CNT, CB, and EG filled epoxy composites.

Nanoparticle	Nanoparticle content (wt.%)	Mechanical property	Improvement (%)	Reference
DWCNT	1	Tensile modulus	6.4	[26]
SWCNT	0.3	Tensile strength Tensile modulus	8.2 5.5	[27]
MWCNT	0.3	Tensile strength Tensile modulus	- 8.5	[27]
SWCNT	1	Tensile strength	30	[28]
MWCNT	2	Tensile strength Tensile modulus	24 -	[29]
MWCNT	3	Tensile strength Tensile modulus	- 16	[30]
MWCNT	0.5	Flexural strength Flexural modulus	29.5 32.3	[31]
CB	5	Flexural modulus	23	[32]
CB	2	Tensile strength Flexural strength Impact strength	32 88 10	[13]
CB	0.3 1	Flexural strength	8 12	[33]
CB	5	Flexural strength	22	[34]
CB	1	Tensile strength Tensile modulus	4 1	[35]
EG	1	Tensile modulus	4	[18]
EG	9	Tensile strength	30	[36]
EG	2.5 5	Tensile strength	21 12	[37]
EG	2.5 5	Tensile modulus	10 25	[37]
EG	1	Impact strength	21	[38]

It is evident from the literature that, in general, CNTs have a reinforcing effect on the mechanical properties of epoxy resin at lower contents, up to 1% wt. Conversely, when using expanded graphite (EG) and carbon black (CB) as fillers, the enhancement in mechanical performance occurs at higher contents, beyond 1% wt. Additionally, while the electrical percolation of CNTs ranges between 0.1% and 0.5% [39], it falls within the range of 1% wt. and 10% wt. in CB/epoxy composites [40] and 1% wt. and 5% wt. in EG/epoxy composites [36] . This difference can be attributed to the high aspect ratio and intrinsically high electrical conductivity of CNTs, resulting in significant improvements in both the mechanical and electrical properties of polymer composites at low contents. Conversely, the comparatively lower surface area of CB and EG nanoparticles requires higher contents for efficient functionality in polymer composites. Therefore, understanding the effect of various nanoparticles, such as MWCNTs, CBs, and EGs, with different morphological structures on the mechanical properties of epoxy nanocomposites at various nanoparticle contents is crucial. However, the effect of nanoparticle contents on the mechanical properties of these epoxy nanocomposites has not been comparatively studied to the best of the author's knowledge. Hence, this study aimed to conduct comparative experimental work to investigate the effect of nanoparticle concentration on the tensile strength and elasticity modulus of MWCNT, CB, and EG reinforced epoxy composites. For this purpose, epoxy composites filled with 0.1% wt., 0.2% wt., 0.3% wt., and 0.4% wt. MWCNTs, 4% wt., 8% wt., 10% wt., and 12% wt. CBs, and 4% wt., 8% wt., 10% wt., and 12% wt. EGs were manufactured. The ultrasonication method was employed for nanoparticle distribution within the epoxy. There are two main methods for the distribution characterization of nanoparticles: these are direct microscopic observation [41] and indirect estimation methods [42]. For a good nanoparticle distribution characterization, it is necessary to use direct observation and indirect estimation methods together. In the direct microscopic method, observations are made using methods such as optical microscope (OM), scanning electron microscope (SEM), atomic force microscope (AFM), and transmission electron microscope (TEM). On the other hand, the electrical resistance measurement technique is one of the indirect estimation methods of nanoparticle distribution quality within polymer materials [43]. In this study, the dispersion quality of nanoparticles within epoxy resin was measured based on the electrical resistance measurement. Subsequently, tensile tests were performed to evaluate the mechanical properties of these nanocomposites.

2. MATERIALS AND METHODS

The epoxy-based matrix material used in this study was sourced from Duratek™, Turkey. This matrix consisted of two components: DTE 1000 resin and DTS 1105 hardener. The weight ratio for mixing DTE 1000 resin to DTS 1105 hardener was 100:35. Multi-wall carbon nanotube (MWCNT), expanded graphite (EG), and carbon black (CB), were employed as carbon nanofillers in the epoxy composites. MWCNT nanoparticles were supplied from Nanografi Co., Ltd., Turkey. EG (TIMREX® C-THERM™301) and CB (ENSACO) were kindly provided by TIMCAL (Switzerland). Table 2 presents selected physical properties of the fillers.

Table 2. The physical properties of the nano fillers.

Property	CNT	CB	EG
Density (g/cm^3)	0.25	0.182	0.19
Surface area (m^2/g)	250-300	66.2	27
Particle size	diameter: 8-10 nm length: 1.5 μm		

2.1. Dispersion Process

Nanoparticle dispersion within a polymer matrix has been accomplished using several methods, including ultrasonication, calendaring, and high shear mixing [13]. Among these techniques, ultrasonication is a commonly utilized and effective method for dispersing carbon based nanoparticles

in polymers [44]. Since epoxy has a high viscosity, its viscosity is required to be reduced using a solvent such as acetone for efficient dispersion of nanoparticles. In this study, no solvent was employed in the dispersion process of nanoparticles through ultrasonication to eliminate the residual solvent effect on the mechanical performance of nanocomposites for the purpose of obtaining reliable test data. Therefore, strong ultrasonication process was performed at 150 W for 20 min to disperse the nanoparticles in small amount of epoxy of 50 g as seen in Figure 1.

- CNT+epoxy
- 150 W
- 20 min.
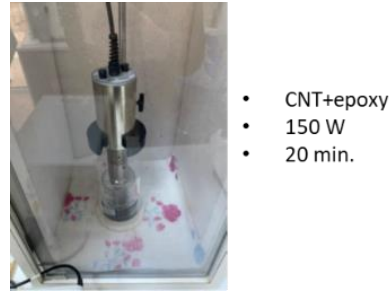
Figure 1. Ultrasonication process

2.2. Optical Microscopy

The dispersion of nanoparticles within epoxy was characterized by optical images taken in transmission mode using a microscope (Nikon Eclipse) equipped with a camera having a 20X objective lens. Samples for optical imaging were prepared by pressing a small droplet of the composite mixture between two glass slides.

2.3. Electrical Resistance Measurement

Since the dispersion quality of nanoparticles within a polymer is strongly dependent on both sonication power and time, we selected the optimum ultrasonication power and dispersion time based on the indirect measurement of dispersion quality. This was achieved by measuring the electrical resistance of 0.2 %wt. MWCNT-filled epoxy mixtures that were dispersed at various ultrasonication powers and times. The electrical percolation threshold of MWCNT was preliminary found as 0.1 %wt. based on electrical conductivity measurements [6]. Therefore, 0.2 %wt. MWCNT was employed in the optimization process of ultrasonication. It is important to note that the ultrasonication parameters may vary for carbon black (CB) and expanded graphite (EG) nanoparticles due to their inherently different electrical conductivity and morphological dimensions. However, since multi-walled carbon nanotubes (MWCNTs) exhibit electrical conductivity at lower contents compared to CB and EG nanoparticles, an optimization study of ultrasonication parameters based on electrical resistance measurement was conducted using MWCNTs at a content of 0.2% by weight within epoxy. Rectangular specimens of about 70 mm in length, 10 mm in width, and 3 mm in thickness were molded for electrical resistance measurement as seen in Fig. 2. Whiskered carbon fibers were used at both ends of the specimens to obtain good contact with the filler network in the specimen. Electrical resistance measurement was achieved using a LCR meter. Two batches with three specimens were prepared for consistency. The measured resistance values are the functions of the geometrical aspects of the specimens such as length and the cross sectional area. Therefore, the measured resistance values were normalized to determine the specific electrical resistivity of the specimens using using equation 1. In this equation, ρ, R, A, and L represent sthe specific resistivity, measured resistance, cross – sectional area, and length, respectively.

$$\rho = \frac{RA}{L} \tag{1}$$
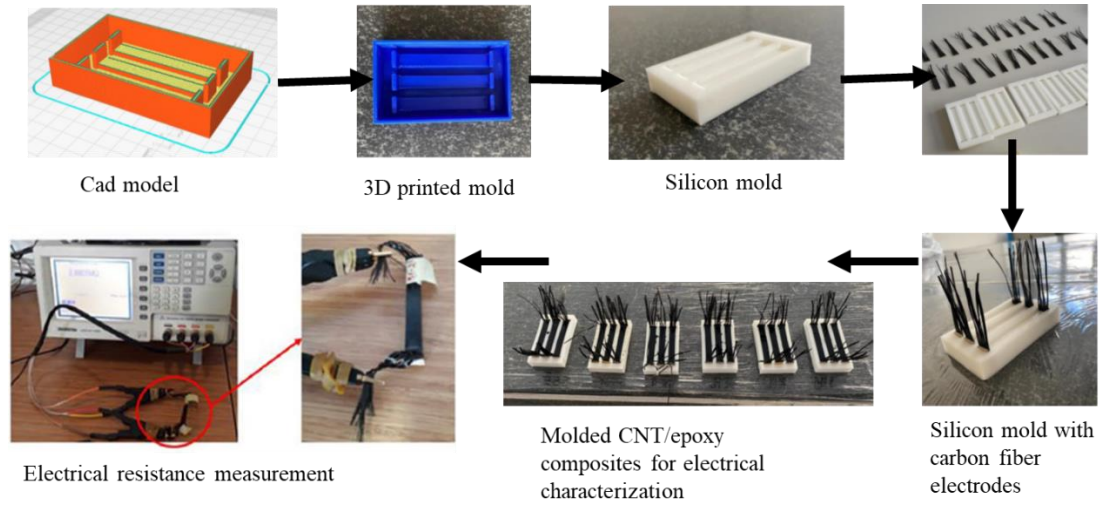
Figure 2. Manufacturing steps of specimens for electrical resistance measurement.

2.4. Tensile Tests

The tensile tests were carried out to investigate the effect of the nanoparticle content on the mechanical properties of nanoparticle reinforced epoxy composites. The rectangular tensile test specimens with the dimensions of 127 × 12.7 × 3.2 mm were molded according to ASTM D680 as shown in Fig 3. Tensile tests were conducted using universal tensile testing machine at a displacement rate of 2 mm/min up to the specimen failure. The tensile tests were repeated three times for consistency. Displacements (ΔL) and loads (F) were automatically recorded using a computer system and consequently the stress (σ) and strain (ε) values were calculated using equation 2 and equation 3, respectively.

$$\sigma = \frac{F}{A} \tag{2}$$
$$\varepsilon = \frac{\Delta L}{L_0} \tag{3}$$
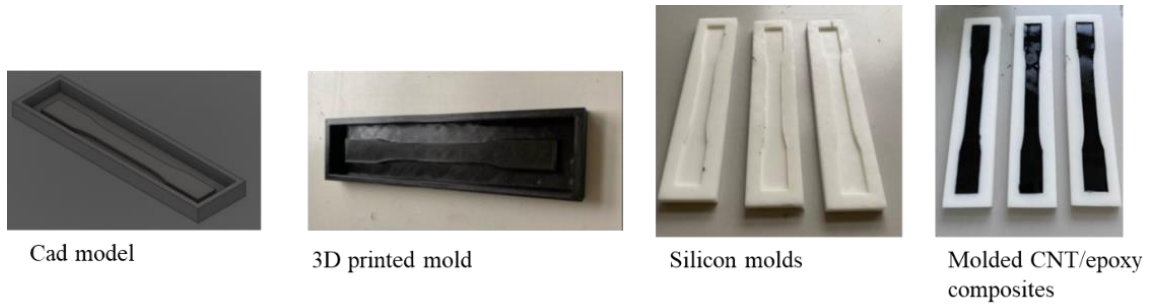
Figure 3. Manufacturing of tensile test specimens.

Table 3 lists the nanoparticle contents by weight for different nanoparticles used within the epoxy. Because CNTs possess a larger surface area compared to EG and CB nanoparticles, they exhibit stronger intermolecular interactions through van der Waals forces. This strong interaction increases the possibility of agglomerate formation within the CNTs and consequently results in a more challenging dispersion process due to the increase in viscosity. Therefore, CNTs were not utilized at concentrations higher than 0.4% by weight within the epoxy. Since EG and CB nanoparticles exhibit very low reinforcing effect at contents up to 0.5 %wt., the investigation aimed to explore the effect of nanoparticle content on mechanical properties at higher concentrations, particularly above the percolation threshold for these nanoparticles.

Table 3. The nanoparticle contents by weight for different nanoparticles used within the epoxy.

Nanofiller	Content (% wt.)
MWCNT	0.1-0.2-0.3-0.4
CB	4-8-10-12
EG	4-8-10-12

3. RESULTS and DISCUSSION

3.1. Optical Microscopy

Figure 4 shows the optical microscopy images of EG and CB filled epoxy blends at the concentrations of 4% wt. and 10% by weight. It is seen from the optical images at 4% concentration that EG-filled epoxy sample exhibits transparency, owing to its tendency to spread easily between glass plates compared to the CB-filled sample. This result indicates the fact that EG nanoparticles having lower surface area are less likely to increase the viscosity of epoxy compared to CB nanoparticles at the same concentration. The resulting high viscosity leads to challenges during ultrasonication process, causing nanoparticle agglomeration within epoxy mixture. Moreover, the formation of agglomerates is more likely to occur as the nanoparticle content increases. The optical images give some useful insight in macro scale about the effect of nanoparticle morphology on the dispersion quality. However, it should be noted that the dispersion quality of nanoparticle filled polymer resins needs to be examined in micro scale using SEM for better understanding of size and distribution of both nanoparticles and agglomerations within resin.
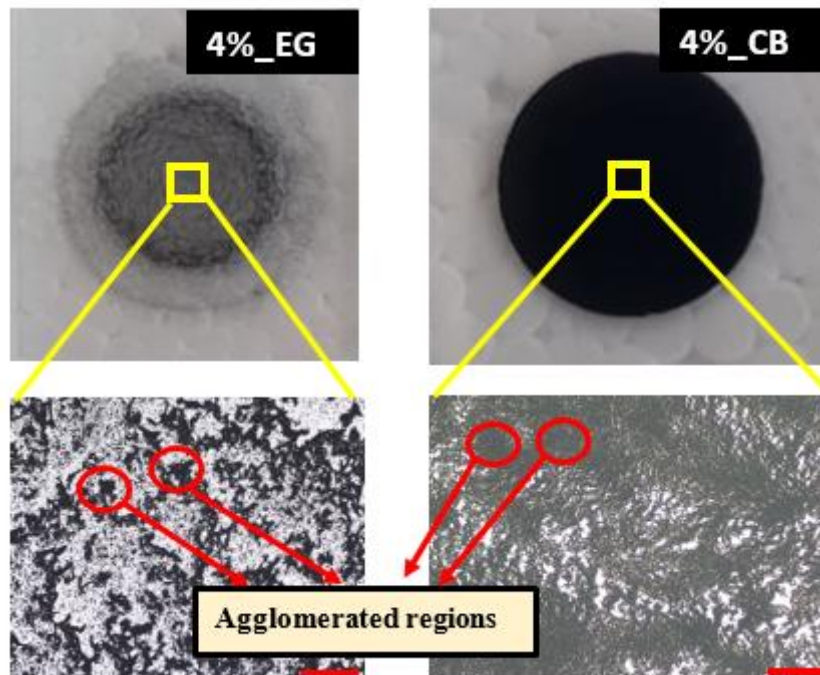
Figure 4. The optical images of CB and EG filled epoxy mixtures at 4% and 10% concentrations by weight. Scale: 32 µm.

3.2. Electrical Measurement

The purpose of the electrical resistance measurement was to determine the optimum dispersion parameters of ultrasonication method. Figure 5 compares the specific electrical resistance values of 0.2

% wt. MWCNT-filled epoxy composites dispersed at varying power for 20 min as a column bar. The average values of electrical resistance change were determined from two batches of epoxy composites filled with 0.2% wt. MWCNTs, utilizing a total of six specimens.
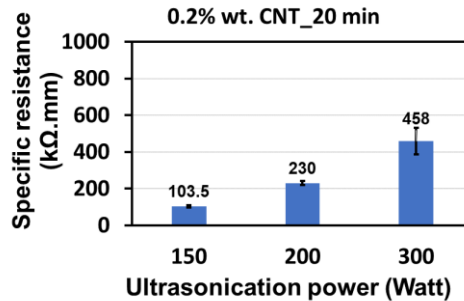
Figure 5. The specific electrical resistance values of 0.2 %wt. MWCNT-filled epoxy composites dispersed at varying power for 20 min.

The results show that the lowest and highest resistance is seen at 150 W and 300 W, respectively. Since it is known that the better dispersion of MWCNTs in epoxy results in lower electrical resistivity (or higher conductivity) the ultrasonic dispersion at a greater power than 150 W is not efficient in terms of dispersion quality. Therefore, the effect of the dispersion time was investigated on the dispersion quality in terms of electrical resistivity at 150 W. Figure 6 compares the specific electrical resistance values of 0.2 %wt. CNT-filled epoxy composites dispersed at 150 W power for varying dispersion time as a list and column bar. The results indicate that the lowest resistance is seen at 20 min of dispersion time. Based on these findings, the optimum dispersion parameters of nanoparticles in epoxy matrix was decided as 150 W for power and 20 min for dispersion time. It would be expected that the higher ultrasonication power and the dispersion time, the greater the electrical conductivity and consequently better dispersion quality. However, the electrical properties do not only depend on the dispersion level but also the aspect ratio of the filler material. Therefore, these results in this study might be due to reduction in the aspect ratio of CNTs as a result of aggressive dispersion process of ultrasonication at higher ultrasonication power and longer dispersion time as discussed in the literature [45].
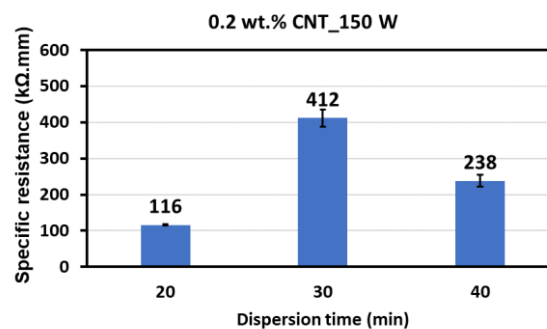
Figure 6. The specific electrical resistance values of 0.2 %wt. CNT-filled epoxy composites dispersed at 150 W for varying dispersion time.

3.3. Tensile Tests

The column graphs comparing the average mechanical properties for different CNT contents are seen in Figure 7. The results indicate that the incorporation of CNTs into the epoxy results in enhancement in the mechanical properties of the epoxy material. The improvement in the mechanical strength was

achieved as 84.7%, 62.9%, 25.1%, and 4.2% for 0.1%, 0.2%, 0.3%, and 0.4% CNT content by weight, respectively. In addition, the improvement in the elasticity modulus was realized as 32.1%, 9%, and 11.4% for 0.1%, 0.2%, and 0.3% CNT content by weight, respectively. On the other hand, the slight reduction in the elasticity modulus was observed in the case of using % 0.4 CNT content. The results indicate that the reinforcing effect on the mechanical properties of the epoxy decreases with increasing CNT content. CNTs are one dimensional nanoparticles with a very high aspect ratio (length/diameter) leading strong van der Waals forces between individual nanotubes. Therefore, CNTs tend to agglomerate due to this strong van der Waals forces [46]. This tendency needs to be overcome by dispersion techniques such as ultrasonication to obtain mechanically strong and electrically and thermally conductive functional materials for practical applications. However, this task is challenging, particularly at higher CNT contents due to the significant increase in the viscosity resulting in poor dispersion quality of CNTs within the epoxy. Hence, the larger agglomerates at the higher CNT contents lead to reduction in the load bearing capacity acting as defects within the structure.
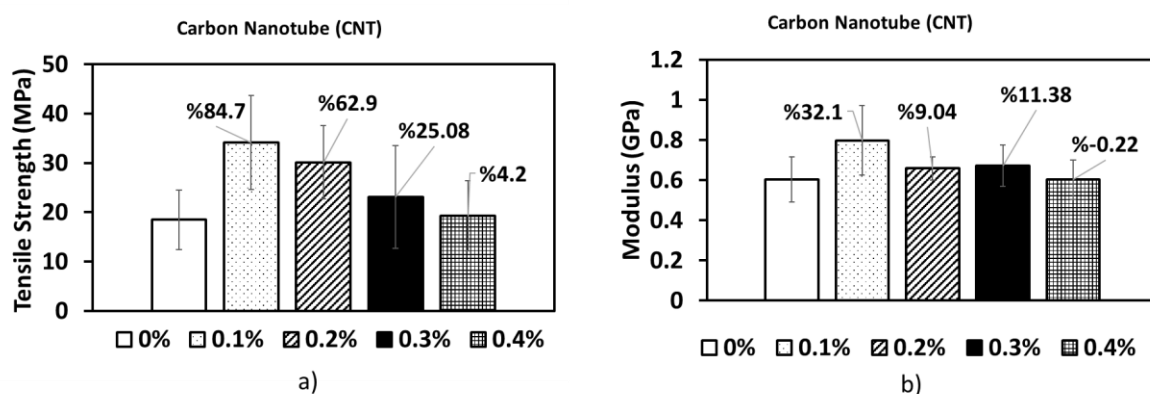
Figure 7. a) The average a) tensile strength and b) elastic modulus for different CNT contents.

Figures 8 and 9 compare the effect of nanoparticle type on the tensile strength and elasticity modulus for EG and CB nanoparticles at various concentrations. Since the CNTs were not employed at concentrations higher than 0.4 wt.%, only the EG and CB nanoparticles are included in these graphs. It is seen that the reinforcing effect of the EG on both the strength and modulus is significantly greater than that of CB at all concentrations. This might be attributed to the fact that the 2D nature of EG nanoparticles, providing a higher aspect ratio, results in a greater reinforcing effect compared to CB nanoparticles, which have a lower aspect ratio due to their spherical dimension. The results indicate that the incorporation of EGs into the epoxy results in enhancement in the mechanical strength as 109.6%, 87.4%, 73.3%, and 58.2% for 4%, 8%, 10%, and 12% EG content by weight, respectively. In addition, the improvement in the elasticity modulus was realized as 3.3%, 59.3%, 95.7%, and 65.1% for 4%, 8%, 10%, and 12% EG content by weight, respectively. The reinforcement effect of EG is seen at higher EG contents as opposed to CNTs. This is due to the fact that EG has lower aspect ratio and surface area compared to CNTs leading to better dispersion of EG nanoparticles without significant increase in the viscosity at higher concentrations. The strong reinforcing effect of EG is the clear indication of efficient mixing of the EG particles resulting in good filler/matrix adhesion [47]. Thanks to having very high modulus of the rigid graphite layers, significant enhancement in the modulus occurs as a result of EG modification in the epoxy [48]. Similar to the CNT modified composites, the reinforcing effect seems to reduce at the higher EG content due to the fact that viscosity at the higher EG content prevents the better dispersion of individual EG particles within the epoxy.

The results show that the improvement in the strength is observed at %4 CB content by %45 indicating that the CB is a promising reinforcing nanoparticle. However, the higher CB content incorporation into the epoxy leads to reduction in the epoxy strength. This reduction in the strength at the higher CB content might be attributed to viscosity increase at higher CB contents [49] which also are the case for the CNT

and EG nanoparticles. CBs have a high tendency to form large aggregates due to the strong Van der Waals force at higher concentrations. Large agglomerates cause bad interfacial interaction between epoxy phase and decrease the mechanical properties. Moreover, the high viscosity at high CB contents prevents the easy movement of CB particles and causes the non-uniform distribution of CB particles within epoxy. On the other hand, the improvement in the modulus was observed at all CB contents. This improvement in the elasticity modulus was realized as 55.3%, 13.6%, 58.2%, and 36.9% for 4%, 8%, 10%, and 12% CB content by weight, respectively. It should be noted that there is no correlation between the CB content and the enhancement level in the modulus.
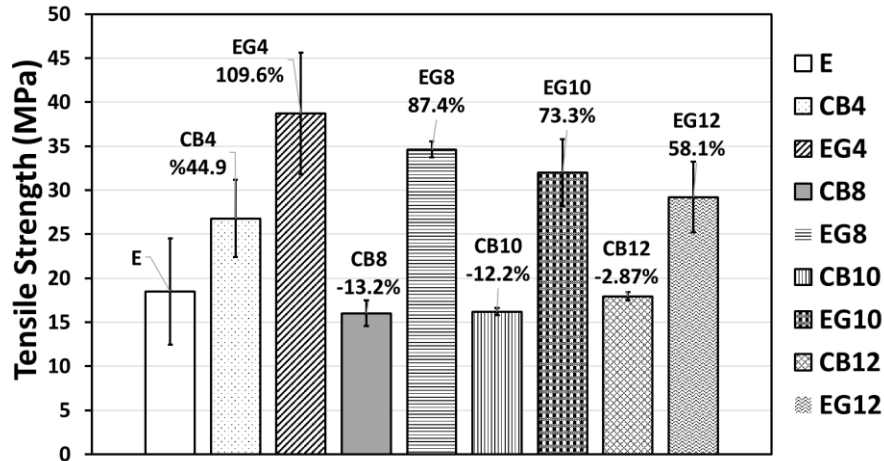
Figure 8. The average tensile strength of nanoparticle filled epoxy composites.
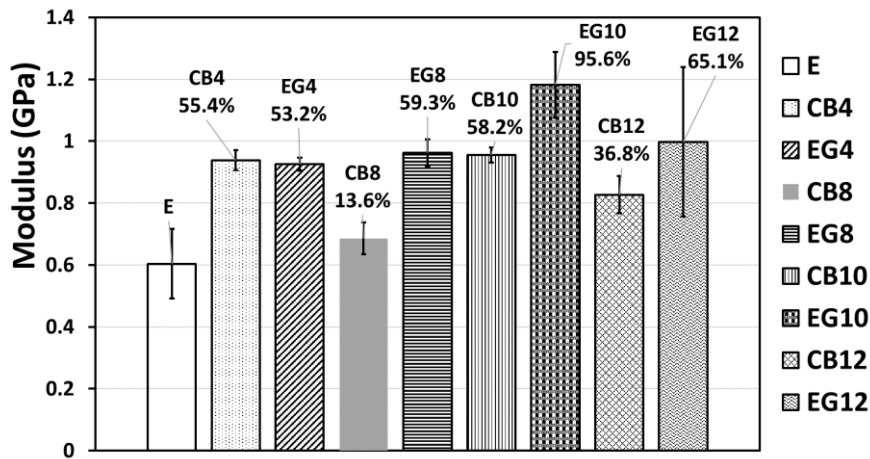
Figure 9. The average tensile modulus of nanoparticle filled epoxy composites.

4. CONCLUSION

In this study, a comparative experimental study was conducted to investigate the effect of the nanoparticle type and content on the mechanical properties of the epoxy composites. The main conclusions of this study were summarized as follows:

In general, all type of nanoparticles exhibit improvement on the mechanical properties of the epoxy composites at different concentrations.

CNTs were used up to 0.4% by weight due to the challenges in achieving proper dispersion at higher concentrations. The improvements in the strength were observed as 84.7%, 62.9%, 25%, and 4.2% for 0.1 %wt., 0.2 %wt., 0.3 %wt., and 0.4 %wt. CNT concentrations, respectively. The enhancement in the modulus was achieved as 32.1%, 9%, and 11.4% for 0.1 %wt., 0.2 %wt., and 0.3 %wt. CNT concentrations whereas an impairment in the modulus was realized at 0.4% wt. CNT concentration.

The improvements in both the strength and modulus were observed at all EG concentrations. This improvement in the strength was achieved as 109.6%, 87.4%, 73.3%, and 58.2% for 4 %wt., 8 %wt., 10 %wt., and 12 %wt., EG concentrations, respectively. Similarly, the modulus showed enhancements of as 53.2%, 59.3%, 95.6%, and 65.1% for the same concentrations.

Unlike the EG, the reinforcing effect of CB nanoparticles on the strength was seen only at 4 CB %wt . concentration by 44.9%. The reduction in the strength was observed by 13.2%, 12.2%, and 2.9% for 8 %wt., 10 %wt., and 12 %wt. CB concentrations, respectively. On the other hand, the improvement in the modulus at all CB concentrations was achieved as 55.4%, 13.6%, 58.2%, and 36.9%, for 4 %wt., 8 %wt., 10 %wt., and 12 %wt., CB concentrations respectively.

The highest improvement in the strength was realized as 84.7%, 109.6%, and 44.9% for 0.1 %wt. CNT, 4 % wt. EG, and 4% wt. CB nanoparticles, respectively. The improvement in modulus occurred as 32.1%, 95.6%, and 58.2% for 0.1%wt. CNT, 10% wt. EG, and 10% wt. CB contents, respectively. On the other hand, the least reinforcing effect on the strength was found as 4.2% and 58.2% at 0.4% wt. and 12% wt. contents for CNT and EG nanoparticles, respectively. No enhancement was observed in the strength for CB nanoparticle beyond 4% wt. content. The tendency of exhibiting a weaker reinforcing effect at higher nanoparticle concentrations can be attributed to the higher viscosity at these concentrations, which hinders efficient nanoparticle dispersion, promotes agglomeration, and ultimately leads to a reduction in mechanical properties.

The reduction of reinforcing effect on modulus was not found proportional with increasing nanoparticle content which is case in the strength. This might be due to the fact that very high stiffness of nanoparticles increases the resistance against deformation.

ACKNOWLEDGEMENTS

CONFLICT OF INTEREST

The author stated that there are no conflicts of interest regarding the publication of this article.

CRediT AUTHOR STATEMENT

Fatih Turan: Formal analysis, Writing - original draft, Visualization, Conceptualization, Investigation, Writing – Original Draft, Funding acquisition, Methodology.

REFERENCES

[1]   Karnati SR, Agbo P, Zhang L. Applications of silica nanoparticles in glass/carbon fiber-reinforced epoxy nanocomposite. Composites Communications 2020; 17: 32–41.

[2]   Gao J, Patterson BA, Kashcooli Y, et al. Synergistic fracture toughness enhancement of epoxy-amine matrices via combination of network topology modification and silica nanoparticle reinforcement. Compos B Eng 2022; 238: 109857.

[3]   Ren J, Li Q, Yan L, et al. Enhanced thermal conductivity of epoxy composites by introducing graphene@boron nitride nanosheets hybrid nanoparticles. Mater Des 2020; 191: 108663.

[4]   Lin L, Wang Y, Lin Z, et al. A simplified reinforcement and fracture mechanism analysis model of epoxy nanocomposites based on finite element simulation. Polymer (Guildf) 2022; 250: 124879.

[5]   Liu H-Y, Wang G-T, Mai Y-W, et al. On fracture toughness of nano-particle modified epoxy. Compos B Eng 2011; 42: 2170–2175.

[6]   Turan F, Guclu M, Gurkan K, et al. The effect of carbon nanotubes loading and processing parameters on the electrical, mechanical, and viscoelastic properties of epoxy-based composites. Journal of the Brazilian Society of Mechanical Sciences and Engineering 2022; 44: 93.

[7]   Metin F, Avci A, Eskizeybek V. Compression and interlaminar shear properties of nanoparticle doped hybrid nanofiber interleaved glass/epoxy composites. Eskişehir Technical University Journal of Science and Technology A - Applied Sciences and Engineering. Epub ahead of print 7 November 2021. DOI: 10.18038/estubtda.976016.

[8]   Bannov AG, Brester AE, Shestakov AA, et al. Technological characteristics of epoxy/carbon black composites. Mater Today Proc 2020; 31: 496–498.

[9]   ÖZTÜRKMEN MB, ÖZKUTLU DEMİREL M, ÖZ Y. INVESTIGATION OF MECHANICAL AND PHYSICAL PROPERTIES OF GRAPHENE WITH EPOXY MATRIX. Eskişehir Technical University Journal of Science and Technology A - Applied Sciences and Engineering 2021; 22: 112–119.

[10]   Wijerathne D, Gong Y, Afroj S, et al. Mechanical and thermal properties of graphene nanoplatelets-reinforced recycled polycarbonate composites. International Journal of Lightweight Materials and Manufacture 2023; 6: 117–128.

[11]   Xia T, Zeng D, Li Z, et al. Electrically conductive GNP/epoxy composites for out-of-autoclave thermoset curing through Joule heating. Compos Sci Technol 2018; 164: 304–312.

[12]   Treacy MMJ, Ebbesen TW, Gibson JM. Exceptionally high Young's modulus observed for individual carbon nanotubes. Nature 1996; 381: 678–680.

[13]   Ma PC, Siddiqui NA, Marom G, et al. Dispersion and functionalization of carbon nanotubes for polymer-based nanocomposites: A review. Compos Part A Appl Sci Manuf 2010; 41: 1345–1367.

[14]   Chakraborty AK, Plyhm T, Barbezat M, et al. Carbon nanotube (CNT)–epoxy nanocomposites: a systematic investigation of CNT dispersion. Journal of Nanoparticle Research 2011; 13: 6493–6506.

[15]   Thakur RK, Singh KK. Influence of fillers on polymeric composite during conventional machining processes: a review. Journal of the Brazilian Society of Mechanical Sciences and Engineering; 43. Epub ahead of print 1 February 2021. DOI: 10.1007/s40430-021-02813-z.

[16]   Nurazzi NM, Sabaruddin FA, Harussani MM, et al. Mechanical performance and applications of cnts reinforced polymer composites—a review. Nanomaterials; 11. Epub ahead of print 1 September 2021. DOI: 10.3390/nano11092186.

[17]   Goudarzi R, Motlagh GH. The effect of graphite intercalated compound particle size and exfoliation temperature on porosity and macromolecular diffusion in expanded graphite. Heliyon 2019; 5: e02595.

[18]   Yasmin A, Luo J-J, Daniel IM. Processing of expanded graphite reinforced polymer nanocomposites. Compos Sci Technol 2006; 66: 1182–1189.

[19]   Wang L, Zhang L, Tian M. Effect of expanded graphite (EG) dispersion on the mechanical and tribological properties of nitrile rubber / EG composites. Wear 2012; 276–277: 85–93.

[20]   Murariu M, Laure A, Bonnaud L, et al. The production and properties of polylactide composites fi lled with expanded graphite. Polym Degrad Stab 2010; 95: 889–900.

[21]   Jia W, Tchoudakov R, Narkis M. Performance of Expanded Graphite and Expanded Milled-Graphite Fillers in Thermosetting Resins. Polym Compos 2005; 26: 526–533.

[22]   Wei B, Yang S. Polymer composites with expanded graphite network with superior thermal conductivity and electromagnetic interference shielding performance. Chemical Engineering Journal 2021; 404: 126437.

[23]   Mamunya YeP, Davydenko VV, Pissis P, et al. Electrical and thermal conductivity of polymers filled with metal powders. Eur Polym J 2002; 38: 1887–1897.

[24]   Li Y, Wang S, Zhang Y, et al. Carbon black-filled immiscible polypropylene/epoxy blends. J Appl Polym Sci 2006; 99: 461–471.

[25]   Rafiee R, Pourazizi R. Influence of CNT functionalization on the interphase region between CNT and polymer. Comput Mater Sci 2015; 96: 573–578.

[26]   Gojny FH, Wichmann MHG, Köpke U, et al. Carbon nanotube-reinforced epoxy-composites: enhanced stiffness and fracture toughness at low nanotube content. Compos Sci Technol 2004; 64: 2363–2371.

[27]   Gojny F, Wichmann M, Fiedler B, et al. Influence of different carbon nanotubes on the mechanical properties of epoxy matrix composites – A comparative study. Compos Sci Technol 2005; 65: 2300–2313.

[28]   Zhu J, Peng H, Rodriguez-Macias F, et al. Reinforcing Epoxy Polymer Composites Through Covalent Integration of Functionalized Nanotubes. Adv Funct Mater 2004; 14: 643–648.

[29]   Guo P, Chen X, Gao X, et al. Fabrication and mechanical properties of well-dispersed multiwalled carbon nanotubes/epoxy composites. Compos Sci Technol 2007; 67: 3331–3337.

[30]   Breton Y, Désarmot G, Salvetat JP, et al. Mechanical properties of multiwall carbon nanotubes/epoxy composites: influence of network morphology. Carbon N Y 2004; 42: 1027–1030.

[31] Nadler M, Werner J, Mahrholz T, et al. Effect of CNT surface functionalisation on the mechanical properties of multi-walled carbon nanotube/epoxy-composites. Compos Part A Appl Sci Manuf 2009; 40: 932–937.

[32] Bera T, Acharya SK, Mishra P. Synthesis, mechanical and thermal properties of carbon black/epoxy composites. International Journal of Engineering, Science and Technology 2018; 10: 12–20.

[33] Öner GA. Flexural strength and thermal properties of carbon black nanoparticle reinforced epoxy composites obtained from waste tires. Open Chem 2022; 20: 863–872.

[34] Abdul Khalil HPS, Jawaid M, Firoozian P, et al. Tensile, Electrical Conductivity, and Morphological Properties of Carbon Black–Filled Epoxy Composites. International Journal of Polymer Analysis and Characterization 2013; 18: 329–338.

[35] Krieg AS, King JA, Jaszczak DC, et al. Tensile and conductivity properties of epoxy composites containing carbon black and graphene nanoplatelets. J Compos Mater 2018; 52: 3909–3918.

[36] Gantayat S, Prusty G, Rout DR, et al. Expanded graphite as a filler for epoxy matrix composites to improve their thermal, mechanical and electrical properties. Xinxing Tan Cailiao/New Carbon Materials 2015; 30: 432–437.

[37] Yasmin A, Daniel IM. Mechanical and thermal properties of graphite platelet/epoxy composites. Polymer (Guildf) 2004; 45: 8211–8219.

[38] Kang W-S, Rhee KY, Park S-J. Thermal, impact and toughness behaviors of expanded graphite/graphite oxide-filled epoxy composites. Compos B Eng 2016; 94: 238–244.

[39] Sumfleth J, Buschhorn ST, Schulte K. Comparison of rheological and electrical percolation phenomena in carbon black and carbon nanotube filled epoxy polymers. J Mater Sci 2011; 46: 659–669.

[40] Ali Raza M, Westwood A, Stirling C, et al. Effect of nanosized carbon black on the morphology, transport, and mechanical properties of rubbery epoxy and silicone composites. J Appl Polym Sci 2012; 126: 641–652.

[41] Chakraborty AK, Plyhm T, Barbezat M, et al. Carbon nanotube (CNT)–epoxy nanocomposites: a systematic investigation of CNT dispersion. Journal of Nanoparticle Research 2011; 13: 6493–6506.

[42] Song YS, Youn JR. Influence of dispersion states of carbon nanotubes on physical properties of epoxy nanocomposites. Carbon N Y 2005; 43: 1378–1385.

[43] Mitchell CA, Bahr JL, Arepalli S, et al. Dispersion of Functionalized Carbon Nanotubes in Polystyrene. Macromolecules 2002; 35: 8825–8830.

[44] Martone A, Formicola C, Giordano M, et al. Reinforcement efficiency of multi-walled carbon nanotube / epoxy nano composites. Compos Sci Technol 2010; 70: 1154–1160.

[45] Lu KL, Lago RM, Chen YK, et al. Mechanical damage of carbon nanotubes by ultrasound. Carbon N Y 1996; 34: 814–816.

[46]   Gao C, Guo M, Liu Y, et al. Surface modification methods and mechanisms in carbon nanotubes dispersion. Carbon N Y 2023; 212: 118133.

[47]   Chen G-H, Wu D-J, Weng W-G, et al. Dispersion of graphite nanosheets in a polymer matrix and the conducting property of the nanocomposites. Polym Eng Sci 2001; 41: 2148–2154.

[48]   Chen G, Wu D, Weng W, et al. Preparation of polystyrene–graphite conducting nanocomposites via intercalation polymerization. Polym Int 2001; 50: 980–985.

[49]   Abdel-Aal N, El-Tantawy F, Al-Hajry A, et al. Epoxy resin/plasticized carbon black composites. Part I. Electrical and thermal properties and their applications. Polym Compos 2008; 29: 511–517.

DETECTION OF CERVICAL CANCER FROM UTERINE CERVIX IMAGES USING TRANSFER LEARNING ARCHITECTURES

Hanife GÖKER [1], *

[1] Health Services Vocational College, Gazi University, 06830, Ankara, Türkiye
gokerhanife@gazi.edu.tr - 0000-0003-0396-7885

Abstract

Cervical cancer is a common and serious cancer affecting more than half a million women worldwide. For cervical cancer disease management, prognosis prediction, or optimizing medical intervention, early detection of the disease is critical. It is one of the types of cancer that can be successfully treated, as long as it is diagnosed early and managed effectively. In this study, an image processing-based solution was proposed for the diagnosis of cervical cancer from uterine cervix images using transfer learning architectures to reduce the workload and assist the experts. The proposed transfer learning model was tested using a publicly available dataset, which includes 917 uterine cervix images. Uterine cervix images were enhanced and brightness level using the histogram equalization method and denoised using the Gaussian filter. Then, the performances of AlexNet, DenseNet201, MobilenetV2, Resnet50, Xception, and VGG19 transfer learning architectures were compared. The transfer learning model performance was evaluated using the 10-fold cross-validation method. VGG19 transfer learning algorithm had the highest performance. VGG19 transfer learning algorithm achieved 98.26% accuracy, 0.9671 f1-measure, 0.9896 specificity, 0.9631 sensitivity, 0.9711 precision, 0.9552 Matthews correlation coefficient (MCC), and 0.955 kappa statistic. The combination of histogram equalization, Gaussian filter, and the VGG19 transfer learning approach can be used for accurate and efficient detection of cervical cancer from uterine cervix images. In this study, more accuracy was achieved compared to the known related studies in the literature.

1. INTRODUCTION

Cervical cancer is a serious and common disease and affects the cervix, an important element of a woman's reproductive system. The disease is the fourth most typical cause of disease mortality among women worldwide. Every year, 604 000 women are thought to be diagnosed with cervical cancer, and about 342 000 of them pass away from the disease [1]. Developing countries have much higher mortality and morbidity rates compared to developed countries [2]. The health burden associated with this inequitable rate is expected to intensify, given that cervical cancer death rates are predicted to increase by about 22% between 2015 and 2030 [3]. Moreover, these cancer cells can spread to other organs including the liver, rectum, lungs, and bladder [4]. Preventable if caught early, cervical cancer is becoming an increasingly common disease of inequality and lack of access to healthcare due to shortcomings in accountable social and health systems [5].

In clinical practice, detection of tumor biomarkers, pap-smear tests, colposcopy, and medical imaging techniques are among the examinations for the diagnosis of cervical cancer [6]. Cervical cancer has a

high cure rate if found at an early stage [7]. However, since cervical cancer is asymptomatic in its early stages, it is often undetectable and can only be identified by routine checkups or pelvic exams [8]. Therefore, regular scanning is imperative to reduce mortality rates. By detecting color changes in the cervix, the healthcare professional can identify the presence of potential malignant or pre-cancerous lesions [9]. Pre-cancer scanning has played a crucial role in reducing the mortality rate and incidence of cervical cancer in the last fifty years. Unfortunately, because of the increased workload, vision scanning results in misdiagnosis and ineffective diagnostic methods [10]. In addition, significant regional and global disparities in cervical cancer outcomes have prompted international gynecological cancer societies to pursue evidence-based methods aimed at improving the quality of care for patients [11]. Cervical cancer is frequently detected using three-dimensional (3D) medical imaging techniques including computed tomography (CT), nuclear magnetic resonance imaging (MRI), and positron emission tomography (PET). 3D images may include invaluable information on medical results [12]. The pap-smear test detects changes in cervical cells and shows whether the cells are prone to cancer. It requires a small scraping of cervical tissue and analysis in a lab. Sample cell images are collected in a container with additional liquid and these cell images are manually analyzed by a qualified pathologist. This procedure is time-consuming and tedious given the total number of specialist pathologists [13]. However, specialist pathologists with the ability to diagnose images often require long-term training, and the diagnosis of images is a subjective, uncertain process, and its accuracy is greatly influenced by the experience and condition of the experts [6]. In addition, it takes a lot of time to analyse hundreds of images for 3D medical imaging analysis, and the intensive image scanning job has greatly hampered clinicians [14]. For the diagnosis of cervical cancer in practice; computer-aided diagnosis systems that can automatically analyze medical images are needed due to reasons such as the need for routine checks, pelvic examinations, and expert pathologists [9], the high workload of specialists [10], and the diagnostic procedure being time-consuming, boring, and subjective [13]. Transfer learning-based models have a great capacity to automatically process complex and very large image data and the models are strong candidates to overcome these limits. Transfer learning models store the information obtained in solving any problem and use that information when faced with another problem. Features and weights obtained from previously trained models are used for new tasks with transfer. Thus, by using previous knowledge with transfer, models with higher success and faster learning are obtained with less training data.

In recent years, machine learning and deep learning methods have gained popularity for the detection of cervical cancer. Ahishakiye et al. (2020) performed a classification model for the detection of cervical cancer using the ensemble learning approach. The model achieved 87.21% accuracy [15]. Chandran et al. (2021) proposed an ensemble deep learning-based classification model to detect cervical cancers from colposcopy images. They adopted VGG19 and colposcopy ensemble network (CYENET) algorithms. VGG19 algorithm achieved 73.30% accuracy and CYENET algorithm achieved 92.30% accuracy [10]. Saini et al. (2020) presented a deep-learning-based method for detection of cervix cancer from colposcopy images. They compared transfer learning models, including LeNet, VGG16, DenseNet, AlexNet, ResNet50, GoogleNet, and ColpoNet, for classifying cervical cancer. The ColpoNet algorithm classified cervical cancer with 81.353% accuracy [16]. Similarly, Priyanka and Raju (2021) developed deep learning models to automatically classify cervical cancer. They performed image preprocessing such as resizing the images, converting the images into grayscale images, and expanding the dimensions of the images. Then, their proposed study classified cervical cancer and predicted it with an accuracy of 74.04% using ResNet50 algorithm [17]. Mehmood et al. (2021) proposed a hybrid approach that combines Random Forest (RF) and shallow neural networks for cervical cancer detection. The hybrid approach used the Pearson correlation between the input variables and the output variable to preprocess the data and achieved an accuracy of 93.6% [18]. Alsmariy et al (2020) used the ensemble voting classifier by combining Decision Tree (DT), Logistic Regression (LR), and RF machine learning algorithms to find a model that can diagnose cervical cancer with high accuracy and sensitivity. They used a cervical cancer dataset from the University of California at Irvine (UCI). The highest accuracy (97.44%) was achieved using SMOTE, voting, and Principal Component Analysis (PCA) [19]. Kalbhor et al (2023) used the publicly available Herlev pap-smear dataset. In the study,

features were extracted using pre-trained convolution neural networks such as Alexnet, Googlenet, Resnet18, and Resnet50. The cervix images were classified with machine learning algorithms, namely simple logistic, RBFNetwork, BayesNet, Naive Bayes (NB), RF, random tree, and decision table. The highest accuracy of 96.01% was achieved using GoogleNet [20]. Early detection of cervical cancer is critical in the treatment of the disease, prognosis prediction, and optimizing the treatment. If it is identified early and treated appropriately, cervical cancer is among the most successfully treatable forms of cancer. However, there are deficiencies in its correct diagnosis. Although there is increasing interest in deep learning-based models for automated analysis of image data, further studies are required to make deep learning-based models reliable and practical for clinical use. Studies investigating early diagnosis of cervical cancer from medical images are limited. There is a need for new studies to be conducted, to compare the results, and to improve accuracy.

In the study, we proposed an image processing-based solution to detect cervical cancer from uterine cervix images using transfer learning architectures to assist the experts and reduce the workload of the experts. The significant contributions of this study are summarized below.

a)   An image processing-based solution model was proposed for the detection of cervical cancer from uterine cervix images.
b)   The best classification performance model was chosen after comparing the transfer learning architectures, namely AlexNet, DenseNet201, MobilenetV2, Resnet50, Xception, and VGG19.
c)   In this study, more accuracy was achieved compared to the known related studies in the literature.
d)   Early diagnosis of cervix cancer from uterine cervix images offers opportunities for early intervention and effective management of the process.

2.   MATERIAL AND METHODS

2.1. Proposed Model

The proposed model contains the following implementation phases: i) Firstly, the image preprocessing was performed on the uterine cervix images. In the image preprocessing phase, the images were resized, the images were sharpened using histogram equalization, and the noise on the images was removed using the Gaussian filter, ii) Then, the classification successes of the transfer learning architectures were compared. iii) The 10-fold cross-validation was adopted to assess the proposed model performance, due to the low estimation bias and error of this method. iv) Finally, the model evaluation metrics of the transfer learning architectures were calculated, and the transfer learning architecture with the highest performance was adopted. The implementation phases of the proposed model are given in Figure 1.
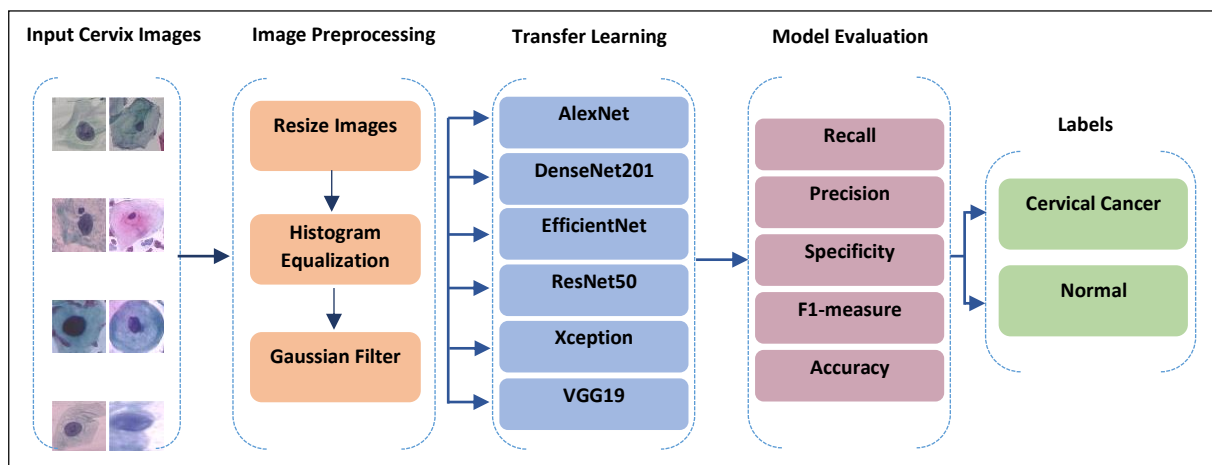
Figure 1. The implementation phases of the proposed transfer learning model

2.2. Dataset

The study was conducted on the publicly available Herlev pap-smear dataset [21]. The image dataset was gathered by the Technical University of Denmark and Herlev University Hospital. It consisted of 917 uterine cervix images. 242 images were normal cells and 675 images were cervix cancer cells. The pap-smear image has a resolution of 0.201 f.J.m per pixel. As part of the smear inspection, sample uterine cervix tissues were used to create the dataset [21]. The dataset has 7 cell types. The distribution of the image dataset is given in Table 1:

Table 1. The distribution of the dataset

Number	Cell Type	Counts	Category
1	Superficial epithelial	74	Normal cells (242 images)
2	Intermediate epithelial	70	
3	Columnar epithelial	98	
4	Mild squamous non-keratinizing dysplasia	182	Cervix cancer cells (675 images)
5	Moderate squamous non-keratinizing dysplasia	146	
6	Severe squamous non-keratinizing dysplasia 1	197	
7	Squamous cell carcinoma in sti intermediate	150	

In this study, the dataset was divided into 2 categories (normal and cervical cancer) and focused on the detection of cervical cancer from the uterine cervix images. Samples of cervix cancer images and normal cervix images are given in Figure 2 and Figure 3:
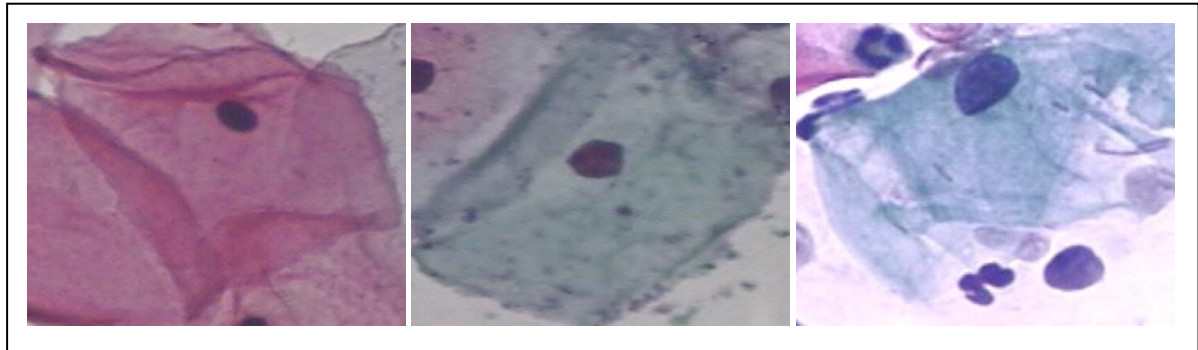
Figure 2. Samples of normal cervix image
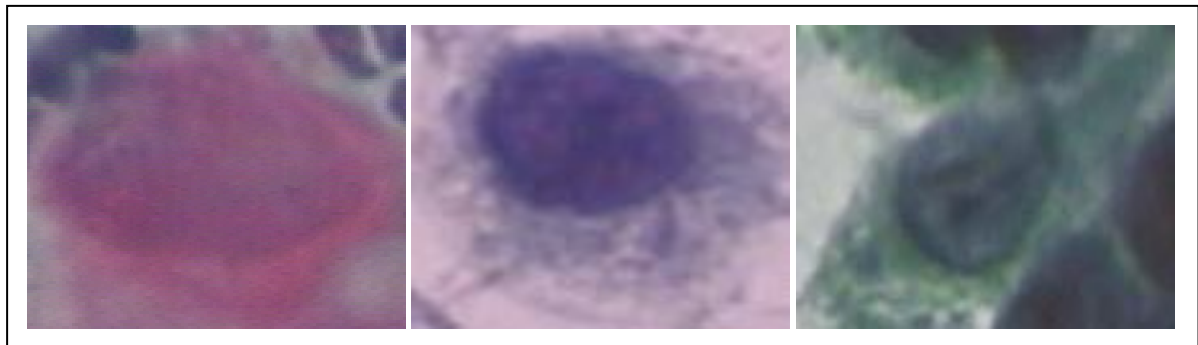
Figure 3. Samples of cervix cancer image

2.3. Image Preprocessing

In the image preprocessing stage, the images were converted to .jpeg format and resized according to the default input sizes used by the transfer learning architectures. Uterine cervix images resized to 227x227x3 for AlexNet, 224x224x3 for DenseNet201, 224x224x3 for MobilenetV2, 224x224x3 for RestNet50, 224x224x3 for Xception, and 224x224x3 for VGG19. Then, at this stage, histogram equalization was used for image enhancement, and a Gaussian filter was used to reduce noise on the images. After applying histogram equalization, the samples of cervix images are given in Figure 4:
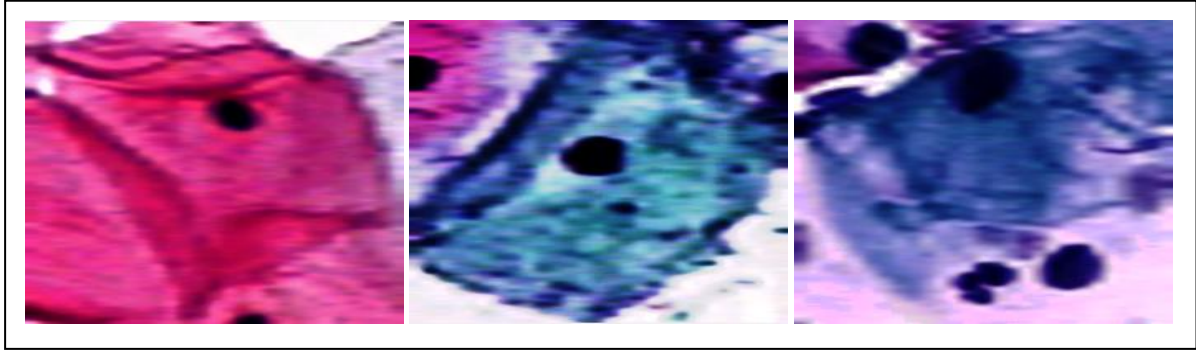
Figure 4. Samples of cervix images after applying histogram equalization

Image enhancement might be considered as one of the critical steps for image analysis. The image enhancement aims to improve an image's quality to make it better suited for a certain application. Histogram equalization is a popular and straightforward image enhancement method. It aims to have the output image histogram in a uniform distribution. By ensuring that there are approximately the same number of pixels for each brightness level, the brightness level of the image is adjusted, thereby sharpening the image [22]. It deals with the overall appearance of an image and shows the relationship between the quantity of pixels and each intensity value. It provides the likelihood of occurrence of a pixel with a certain density. In the histogram equalization method, during the whole dynamic density range, the pixels are evenly dispersed. The general formula of the histogram equalization is given below [23]:

$$p_r(r_k) \quad = \quad \frac{n_k}{n} \quad k= 0, 1 , 2 , \ldots , \text{L-1} \tag{1}$$

p(r_k) shows the ratio of the k.th tone value represented in the image, n_k shows the number of k.th tone in the image, and n shows the total number of pixels. In histogram equalization, firstly the s_k cumulative probability is calculated as in equation 2. Then, by performing an inverse transformation as in equation 3, what color tone will replace is calculated.

$$s_k \qquad = \quad T(r_k) = \quad \sum_{j=0}^{k} p_r(r_j) = \quad \sum_{j=0}^{k} \frac{n_j}{n} \qquad k= 0, 1, 2, \ldots , \text{L-1} \tag{2}$$

$$r_k \qquad = \quad T^{-1}(s_k), \qquad\qquad 0 \ll s_k \ll 1$$
$$T^{-1}(s_k) \quad = \quad (L - 1) * T(r_k), \qquad\qquad k= 0, 1, 2, \ldots , \text{L-1} \tag{3}$$

The samples of cervix images after applying the gaussian filter are given in Figure 5:
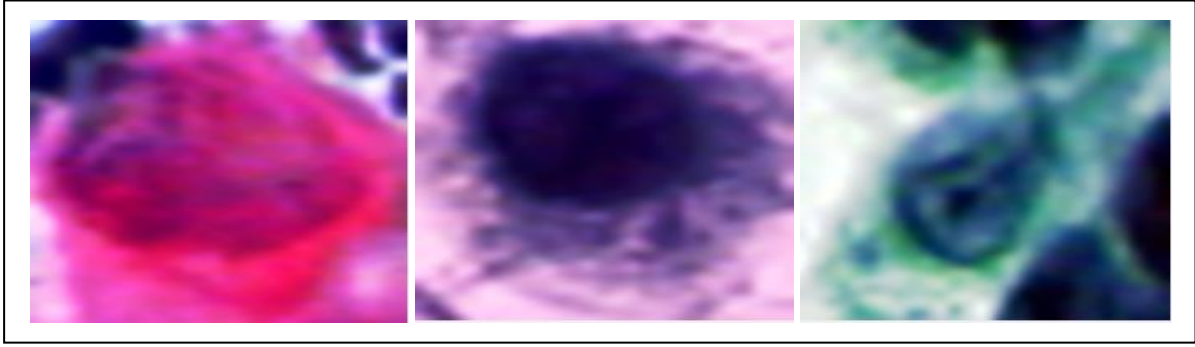
Figure 5. Samples of cervix images after applying the gaussian filter

The reason for using the Gaussian filter in this study is to protect the spatial-spatial frequency components on the images, that is, it protects the changes on the images at very frequent intervals. Gauss subtracts the weighted average of each pixel region. The weighting increases as you get closer to the center pixel value. This filter provides a finer trim, unlike other filters, and preserves edges better than other filters of a similar size. Most other image filters behave like a low-pass filter, which adopts the all-or-nothing rule and exhibits oscillations as a frequency response. The Gaussian filter, on the other hand, does not oscillate. The general formula of the Gaussian filter is given below [24]:

$$G(r) = \frac{1}{(2\pi\sigma^2)^{N/2}} e^{-r^2/(2\sigma^2)} \tag{4}$$

2.4. 10-Fold Cross-Validation

The k-fold cross-validation is used to assess whether the model performance is random and has an overfitting problem. The dataset is split into k separate subgroups. The k value is usually chosen as 5 or 10. In this study, the k value was adopted as 10. One of the groups serves as the test set, and the other groups serve as the training set. The model is trained and tested with the other group by iteratively repeating each group. The overall performance and error rate of the model are calculated as the average of the 10 results obtained. This minimizes deviations and mistakes from dispersion and fragmentation and reduces prediction bias by allowing each part to be utilized alternately for both training and testing. However, training and testing the model for each k requires overhead and time. The 10-fold cross-validation was used in this study because it overcomes overfitting, minimizes prediction bias and error, and enables the model to be trained using several training-test groups. The performances of AlexNet, DenseNet201, MobilenetV2, ResNet50, Xception, and VGG19 transfer learning architectures were compared.

2.5. Transfer Learning

Transfer learning architectures are a type of machine learning where a model created for another task is used to solve different or similar problems. It is frequently simpler and faster to use a pre-trained network with transfer learning than training a network from scratch. The most important ones are network speed, accuracy, and size. The tradeoff between these characteristics should be taken into account when choosing a network. These architectures can be used for different purposes such as classification or feature extraction. In this study, AlexNet, DenseNet201, MobilenetV2, Resnet50, Xception, and VGG19 transfer learning architectures were used for classification tasks. Different experiments were performed on the selection of hyper-parameters for transfer learning architectures whose performances were compared in the study, and optimum hyper-parameters were discovered. In the experiments, "sgdm", "adam", and "rmsprop" were performed for the "optimizer" hyper-parameter in transfer learning architectures and the "sgdm" value, which achieved the best performance, was selected. The

"MiniBatchSize" hyper-parameter was tried as "16" and "32" values and the "16" value, which achieved the best performance, was selected. Also, "30" and "60" were performed for the "MaxEpochs" hyper-parameter, and the "30" value, which achieved the best performance, was selected. The transfer learning architectures and optimizer parameters used are given in Table 2.

Table 2. Transfer learning architectures and optimizer parameters

Hyper-Parameters	AlexNet	DenseNet201	MobilenetV2	ResNet50	Xception	VGG19
Input size	227x227x3	224x224x3	224x224x3	224x224x3	224x224x3	224x224x3
Optimizer	sgdm	sgdm	sgdm	sgdm	sgdm	sgdm
MiniBatchSize	16	16	16	16	16	16
MaxEpochs	30	30	30	30	30	30
InitialLearnRate	1e-4	1e-4	1e-4	1e-4	1e-4	1e-4
ValidationFrequency	3	3	3	3	3	3
Momentum	0.9	0.9	0.9	0.9	0.9	0.9
LearnRateDropPeriod	10	10	10	10	10	10
L2Regularization	0.005	0.005	0.005	0.005	0.005	0.005
WeightLearnRateFactor	20	20	20	20	20	20
BiasLearnRateFactor	20	20	20	20	20	20

2.5.1. AlexNet

AlexNet is a fundamental, effective, and simple transfer learning architecture. It mainly consists of five convolutional layers; the first layer to the fourth layer, followed by the pooling layer, and the fifth layer, followed by three fully connected layers. The image input size is 227 x 227 x 3 in AlexNet transfer learning architecture. The structure of the AlexNet is given in Figure 6 [25].
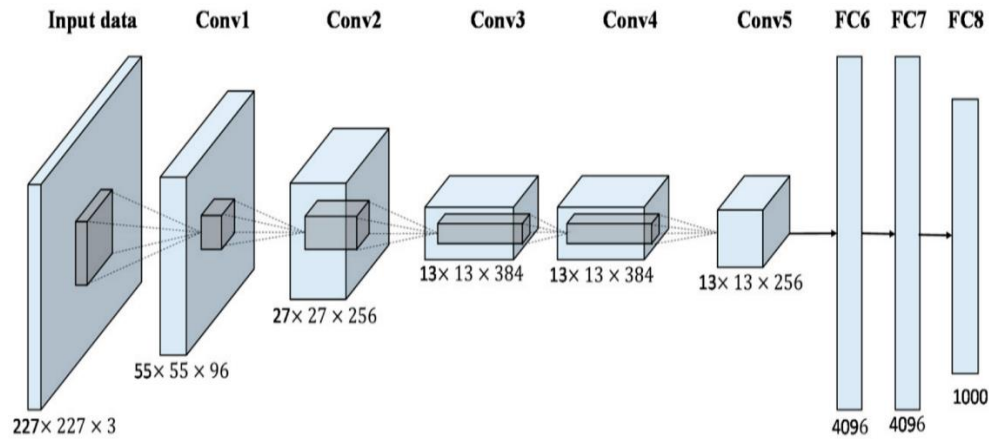
Figure 6. The AlexNet architecture.

2.5.2. DenseNet201

The DenseNet201 architecture achieves the highest possible amount of information flow density between network layers. Because the feature maps produced by the input from the previous layers are transmitted to the next layer by each layer. The biggest advantage of this architecture is that it guarantees the reuse of the features acquired by making sure that the features created in each layer pass on to the following layers. In this architecture, all layers are related to one another. Its name is a dense connected convolutional network as a result. A DenseNet architecture with L layers has L(L+1)/2 direct connections. For each layer, the feature maps of all previous layers are used as input. The image input

size is 224 x 224 x 3 in DenseNet201 transfer learning architecture. The structure of the DenseNet is given in Figure 7 [26].
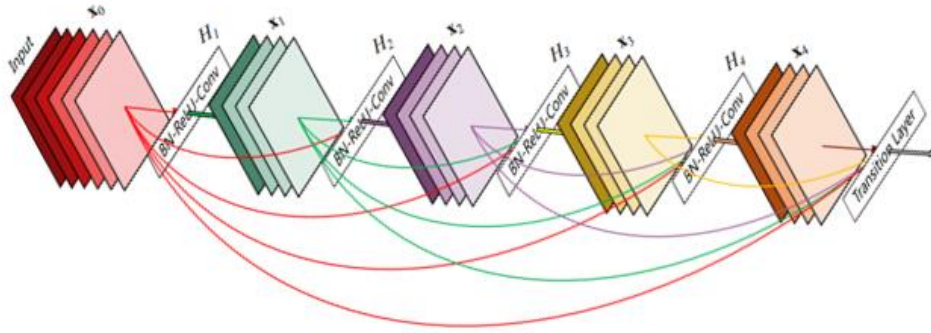
Figure 7. The DenseNet architecture (5-layer dense block)

2.5.3. MobilenetV2

MobileNet is a simple deep convolutional neural network model that is much smaller in size and faster in performance than many other popular models. In depth separable convolutions, a single filter is applied to each input channel. A batchnorm and rectified linear unit (ReLU) nonlinear activation layer comes after all layers, except the fully connected layer that feeds the softmax layer to classify the output. MobileNet has 28 layers except for depth and point convolutions [27]. The image input size is 224 x 224 x 3 in the MobilenetV2 transfer learning architecture. The structure of the MobilenetV2 is given in Figure 8 [28].
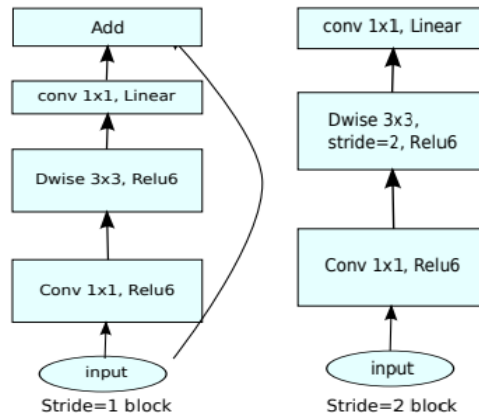
Figure 8. The MobilenetV2 architecture

2.5.4. ResNet50

In the ResNet50 architecture, allowing the transition to the lower layers by ignoring the changes in some layers has increased the success rates. There is information about a 50-layer network structure and the connections between layers in the Resnet50 architecture. ResNet architecture uses convolution layers (1x1), (3x3), (1x1) instead of using 2 (3x3) convolutions. The structure of the ResNet50 is given in Figure 9 [29]. The image input size is 224 x 224 x 3 in ResNet50 transfer learning architecture.
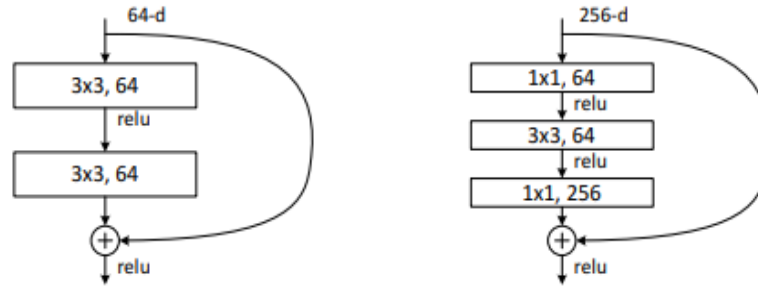
Figure 9. The ResNet architecture

2.5.5. Xception

The Xception architecture has been a developing network by building on top of the InceptionV3 network. In this architecture, the convolutional part is different from other architectures. A classic network moves a filter over multidimensional matrices such as height, width, and depth in the convolutional part. In this convolutional part, Xception network provides two different approaches in addition to the developments in InceptionV3. These are pointwise convolution and depthwise convolution. In the depthwise convolution part, it reaches the result by processing only one channel, not every channel. It is also called "Extreme Inception". The addition it adds to InceptionV3 is that 1x1 convolution uses convolution for each of its output channels. Figure 10 shows Inception architecture and Extreme Inception architecture [30]. The image input size is 299 x 299 x 3 in Xception transfer learning architecture.
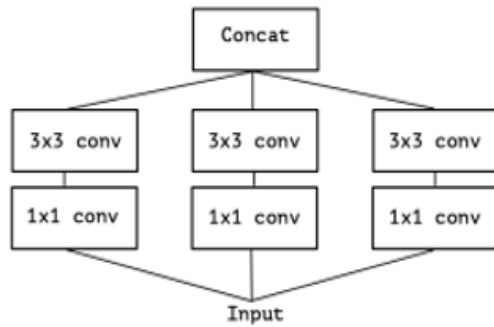
Figure 10.a. Simplified Inception module   **Figure 10.b.** Extreme Inception module
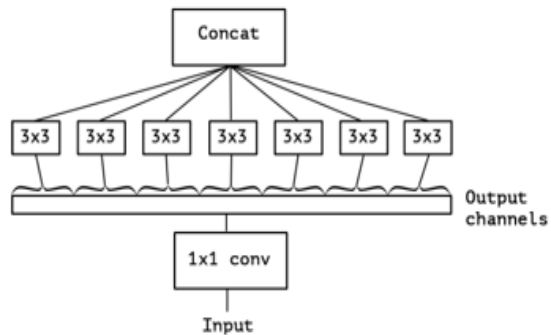
The Xception architecture includes depthwise separable convolutions. As an alternative to classical convolutions, which are assumed to be much more efficient in terms of computation time, depthwise separable convolutions are offered. It is not only concerned with spatial dimensions, but also with the dimension of depth and the number of channels. Depthwise separable convolutions split a core (filter) into two different cores that do two separate convolutions. While one of these kernels is deeply convoluted, the other is point convolution.

2.5.6. VGG19

VGG is a classical convolutional neural network architecture with multiple layers and was developed to enhance the performance of the model by increasing the depth of convolutional neural networks. "16" and "19" represent the number of convolutional layers in the model. VGG19 architecture is a variant of the VGG model which in short consists of 19 layers. This means that VGG19 has three more convolutional layers than VGG16. The architecture includes 16 convolutions, 3 fully connected layers,

5 maxpools layers, and 1 softmax layer. The structure of the VGG19 is given in Figure 11 [31]. The image input size is 224 x 224 x 3 in VGG19 transfer learning architecture.
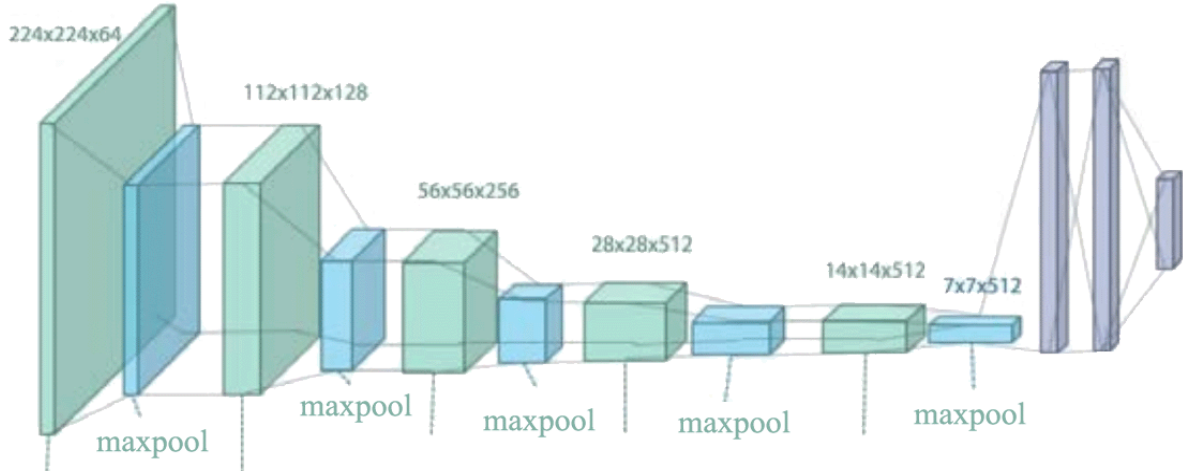
Figure 11. The VGG19 architecture

2.6. Performance evaluation metrics

Performance evaluation metrics, namely accuracy, f1-measure, specificity, sensitivity, precision, MCC, and kappa statistics are widely used to evaluate the performance of classification models [32]. These performance evaluation metrics are calculated using the confusion matrix, which is a table containing four different parameters of predicted and actual samples. These are false positive (FP), true positive (TP), false negative (FN), and true negative (TN). The mathematical formulas for these metrics are given below:

$$\text{Precision} = TP / (TP + FP) \tag{5}$$

$$\text{Sensitivity} = TP / (TP + FN) \tag{6}$$

$$\text{Specificity} = TN / (TN + FP) \tag{7}$$

$$\text{MCC} = (TN \times TP - FP \times FN)/\sqrt{(FN + TN) \times (FP + TP) \times (TN + FP) \times (TP + FN)} \tag{8}$$

$$\text{F1-measure} = (2 \times \text{Precision} \times \text{Sensitivity}) / (\text{Precision} + \text{Sensitivity}) \tag{9}$$

$$\text{Accuracy} = (TN + TP) / (TP + FN + FP + TN) \tag{10}$$

Kappa statistic is calculated by following the mathematical formula steps below [33]:

$$P_o = (TP + TN) / (TP + FP + FN + TN)$$

$$P_1 = [(FN + TP) / (FP + FN + TP + TN)] \times [(FP + TP) / (TP + FN + FP + TN)]$$

$$P_2 = [(TN + FP) / (TP + TN + FP + FN)] \times [(FN + TN) / (TP + FP + FN + TN)]$$

$$P_e = P_1 + P_2$$

$$\text{Kappa statistic} = (P_o - P_e) / (1 - P_e) \tag{11}$$

3. EXPERIMENTAL RESULTS AND DISCUSSION

In the study, a deep learning model for the diagnosis of cervical cancer was proposed using uterine cervix images. The dataset contains 917 images, of which 675 are cancer images and 242 are normal. The images were resized according to the input image size appropriate for each transfer learning architecture. The images were sharpened and brightness levels were adjusted using histogram equalization. Gaussian filters were used to reduce noise in images. The performances of AlexNet, DenseNet201, MobilenetV2, Resnet50, Xception, and VGG19 transfer learning architectures were compared. The model performance was evaluated using the 10-fold cross-validation. The total dataset was divided into 10 folds in this method. For each fold, 9 parts were used alternately for training and 1 part for testing. Thus, all images were evaluated as both training and test datasets. While evaluating the performance of the model, the average of 10 folds was calculated. 10-fold cross-validation is generally the preferred method because it allows training the proposed model with more than one training-test group, thus reducing the prediction bias. The performances of the transfer learning architectures were compared. The confusion matrix of the architectures, showing the number of images included in the correct label and the number of images included in the incorrect label, are given in Table 3.

Table 3. The confusion matrix of the transfer learning architectures

Transfer Learning Architectures	Labels	Confusion matrix parameters		Classified	
		Normal	Cervical Cancer	Correctly (TP+TN)	Incorrectly (FP+FN)
AlexNet	Normal	216	26	873	44
	Cervical Cancer	18	657		
DenseNet201	Normal	224	18	872	45
	Cervical Cancer	27	648		
MobilenetV2	Normal	219	23	870	47
	Cervical Cancer	24	651		
ResNet50	Normal	215	27	866	51
	Cervical Cancer	24	651		
Xception	Normal	206	36	855	62
	Cervical Cancer	26	649		
VGG19	Normal	235	7	901	16
	Cervical Cancer	9	666		

When Table 3 was examined, the VGG19 transfer learning architecture had the highest number of correctly classified images. VGG19 transfer learning architecture was followed by AlexNet, DenseNet201, MobilenetV2, ResNet50, and Xception, respectively. In the confusion matrix of VGG19 transfer learning architecture, the total number of incorrectly classified images (FN+FP) was 16 and the total number of correctly classified (TN+TP) images was 901. The model evaluation metrics, which are accuracy, f1-measure, specificity, sensitivity, precision, MCC, and kappa statistics are calculated using the parameters in the confusion matrix, which are FP, TP, FN, and TN. The success of the models is evaluated using these model evaluation metrics. The performance analysis results of the transfer learning are given in Table 4:

Table 4. The performance analysis results of the transfer learning architectures

Architectures	Model Evaluation Metrics						
	Sensitivity	Precision	Specificity	MCC	F1-measure	Kappa	Accuracy
AlexNet	0.9231	0.8926	0.9619	0.8754	0.9076	0.875	0.9520
DenseNet201	0.8924	0.9256	0.9730	0.8755	0.9087	0.875	0.9509
MobilenetV2	0.9012	0.9050	0.9659	0.8683	0.9031	0.868	0.9487
ResNet50	0.8996	0.8884	0.9602	0.8563	0.8940	0.856	0.9444
Xception	0.8879	0.8512	0.9474	0.8240	0.8692	0.824	0.9324
VGG19	0.9631	0.9711	0.9896	0.9552	0.9671	0.955	0.9826

When the performance analysis results of the architectures are examined in Table 4, the VGG19 transfer learning architecture has the highest success (accuracy = 98.26%). The performance analysis results of VGG19 architecture were calculated as 0.9671 f1-measure, 0.9896 specificity, 0.9631 sensitivity, 0.9711 precision, 0.9552 MCC, and 0.955 kappa statistic. Model performance criteria should be close to 1. If performance evaluation metrics are close to 1, it proves that the model does not have an accidental success. In addition, the kappa statistic between 0.81-1.00 shows an almost "perfect match". Kappa statistic values of all transfer learning architectures were above 0.81. While evaluating the success of the model, the f1-measure should be examined together with the accuracy. The accuracy is the correct predictions divided by the total number of datasets. The f1-measure is the harmonic mean of the sensitivity and precision. Accuracy may not produce reliable results if the intergroup distribution is not balanced in the data set, but the f1-measure produces accurate results even if the intergroup distribution is not even. For this reason, it is more appropriate to present the f1-measure together with the accuracy in the analysis of the models. The f1-measure values of transfer learning architectures were close to 1. In Figure 12, the accuracy and f1-measure of transfer learning architectures are given.
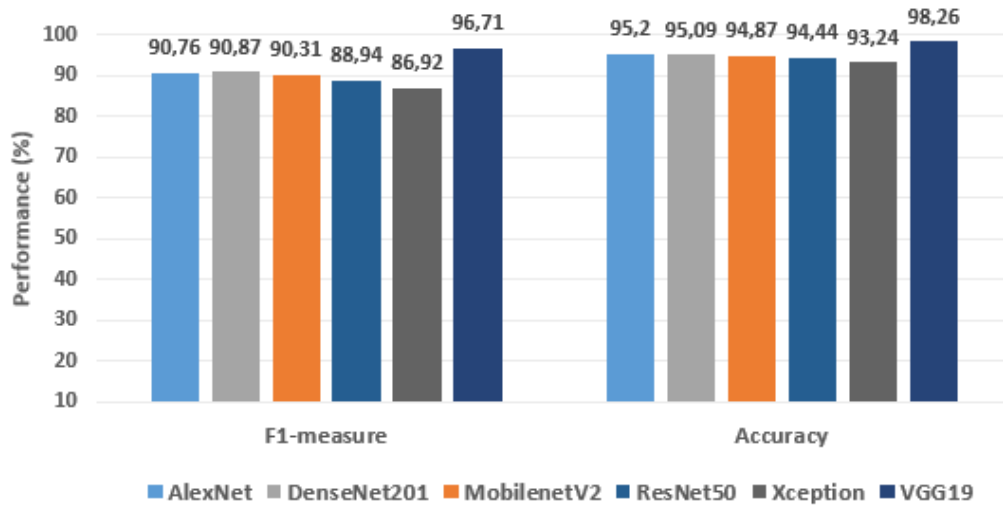
Figure 12. The accuracy and f1-measure of transfer learning architectures

The performance results of the VGG19 transfer learning architecture, which had the highest performance, were compared with the related studies that included cervical cancer detection from cervical images. The comparative analysis is given in Table 5.

Table 5. Comparative analysis of related studies using the same dataset about cervical cancer detection

Researchers	Data Preprocessing	Classifier	Accuracy
Arora et al. (2021) [4]	Geometrical features, Texture features, Feature selection with PCA	Polynomial SVM	95%
		Gaussian SVM	85%
		Quadratic SVM	85%
Priyanka & Raju (2021) [17]	Resize, convert to grayscale, expand the dimensions of the images	ResNet50	74.04%
Sun et al. (2017) [34]	11 nucleus features and 9 cytoplasm features. Feature selection with Relief	NB	92.04%
		C4.5	92.80%
		LR	93.13%
		RF	94.44%
Malli & Nandyal (2017) [35]	Colour quantization, fuzzy c, detected nucleus, nucleus marked area	kNN	88.04%
		ANN	54%
Nguyen et al (2019) [36]	Ensemble of Resnet152, Inception-Resnet-v2 and Inception-v3, feature concatenation	InceptionV3+ Resnet152+ Inception-Resnet-v2	93.04%
Lin et al (2019) [37]	Data augmentation, cell morphology and image patch extraction	GoogLeNet-5C	94.5%
			71.3%
			64.5%
Khamparia et al. (2020) [38]	Feature extraction with convolutional neural network encoder (ResNET50)	kNN	97.67%
		NB	96.08%
		LR	93.45%
		RF	97.89%
		SVM	97.44%
Ravindran et al. (2021) [39]	Reduce sounds with median sensor, Boost comparison with CLAHE	Ensemble	95.12%
Lavanya Devi & Thirumurugan (2022) [40]	Feature extraction with modified fuzzy c-means, Data augmentation with PCA	KNN	94.86%
Shinde et al. (2022) [41]	PCA and machine learning ensemble	SVM	79.89%
		RF	86.41%
		FCNN	87.50%
		Voting Ensemble	87.90%
The Proposed Method	Resize images, Histogram equalization, Gaussian Filter	ANN	97.95%
		AlexNet	95.20%
		DenseNet201	95.09%
		MobilenetV2	94.87%
		ResNet50	94.44%
		Xception	93.24%
		VGG19	98.26%

The performance analysis results of this study were discussed with the related studies according to data preprocessing, feature extraction and feature selection methods, classification algorithms, and accuracy. The histogram equalization method was used to enhance and sharpen the images, and the Gaussian filter to reduce noise in this study. When the methods used in related studies in the literature are examined in Table 5, geometrical features and texture features [4], nucleus features and cytoplasm features [34], image patch and cell morphology extraction [37], convolutional neural network encoder [38] and modified fuzzy c-means [40] were used for feature extraction. PCA [4] and Relief [34] methods were used for feature selection. Color quantization [35], resize images, and convert to grayscale [17] were used for data pre-processing. The median sensor was used to reduce sounds, and CLAHE was used to boost comparison [39]. In this study, Gaussian filter was adopted to reduce noise. Because this filter, unlike other filters, does not adopt the all-or-nothing rule, it does not oscillate, preserves the edges better, and provides a finer trim [24]. Histogram equalization is one of the popular, fastest, and most straightforward image processing methods to improve contrast in images [23]. Therefore, histogram equalization was adopted to boost contrast in images in the study. In this study, the performances of AlexNet, DenseNet201, MobileNetV2, ResNet50, Xception, and VGG19 transfer learning architectures were analyzed. When the studies on the detection of cervical cancer are examined in Table 5, machine learning algorithms, namely NB [34, 38], LR [34, 38], RF [34, 38, 41], SVM [4, 38, 41], kNN [35, 38,

40], transfer learning algorithms, namely ResNet [17, 36], Inception [36], and ensemble learning algorithm [39, 41] are used. The accuracy of the VGG19 transfer learning architecture (98.26%) was higher than the other studies in Table 5 [34, 36, 38-41]. The VGG transfer learning architecture is a famous and widely used CNN that demonstrated for the first time that accurate image processing is possible with a deep network and small convolutional filters. VGG19 performs well in image processing and generalizes well to related tasks because a) it is trained on millions of images, b) it uses very small receptive fields (3x3 with a stride of 1 step), and c) the decision function is more distinctive because it has 3 ReLU units instead of just one. VGG transfer learning architecture pioneered in making the network deeper and the filter compact (3x3). A stack of three convolutional layers with three-layer filters has the same receptive space as one convolutional layer with seven layers but only requires 45% fewer parameters to train. Additionally, the activation is sharper than the single-layer design since the stack has three activation functions. As the network gets deeper, the same architecture (layer groups followed by pooling) is repeated. Deeper levels generally have more filters than those nearer the input. While the deeper layers might need to recognize the full image, the first layers only need to distinguish shapes like lines and edges [42-43]. Deep layers contain the largest number of convolutional filters, as there are more complex object combinations. A greater number of filters allows the network to recognize a variety of complex shapes and objects, and as a result, more filters enhance the performance of the VGG transfer learning architecture.

4. CONCLUSION

In conclusion, we compared the performance of transfer learning architectures for the detection of cervical cancer from uterine cervix images in this study. Firstly, the images were resized to the appropriate input size for all architectures. Then, the histogram equalization method was used to enhance the images, and the Gaussian filter was applied to reduce the noise on the images. Finally, the performances of AlexNet, DenseNet201, MobilenetV2, Resnet50, Xception, and VGG19 transfer learning architectures were compared. The models were evaluated according to model evaluation metrics using the 10-fold cross-validation method. The strengths of the proposed model are to boost comparison in images using the histogram equalization method, denoised from images using the Gauss filter method, reduce prediction bias and error using the 10-fold cross-validation method, and provide a high and satisfactory performance by comparing transfer learning architectures. Performance analysis results showed that the VGG19 transfer learning algorithm obtained higher success than other transfer learning algorithms. The VGG19 algorithm had 98.26% accuracy, 0.9671 f1-measure, 0.9896 specificity, 0.9631 sensitivity, 0.9711 precision, 0.955 kappa statistic, and 0.9552 MCC. The fact that performance evaluation metrics are very close to 1 proves that the model did not have an accidental success. In addition to the high accuracy in the test results, a kappa statistical value between 0.8-1.0 indicates a "perfect match". The accuracy achieved with the VGG19 transfer learning algorithm was higher compared to known related studies.

There are several limitations to the study. Firstly, transfer deep learning algorithms require a large number of images. Obtaining images for biomedical image processing is a very difficult and time-consuming process. Therefore, a public database was used in this study and the results of the study are limited to this database. For future studies, it is recommended to combine and analyze different cervical cancer databases. Secondly, transfer learning algorithms need high-quality hardware. Therefore, it is very time-consuming to run many experiments repeatedly. For future studies, a CNN algorithm with fewer layers and a simpler structure can be designed instead of highly computational and multi-layer transfer learning architectures such as AlexNet, DenseNet201, MobilenetV2, Resnet50, Xception, or VGG19. The results of the designed CNN algorithm can be compared with the transfer learning algorithms. Despite these limitations, the proposed model has many strengths. A high-performance deep learning solution based on transfer learning is presented to support expert opinion for the detection of cervical cancer from uterine cervix images. The performance of the proposed model is high because the images have gone through the data preprocessing process, which includes using the histogram

equalization method to improve the images and implementing the Gaussian filter to reduce the noise in the images. Moreover, prediction bias and error were minimized and overfitting was overcome using 10-fold cross-validation in the study. Consequently, the practical contributions of the proposed model can be summarized as follows: (i) The proposed transfer learning-based model provides a solution to support expert decision and classify cervical cancer with high performance and low cost. (ii) This study constitutes a successful example of how transfer learning models can be used for the diagnosis of diseases. (iii) Besides, the study contributed practically to the development of diagnostic decision support systems. (iv) Using the proposed model in clinical studies minimizes subjectivity, reduces the workload of experts, and enables rapid decision-making. The transfer learning-based model can achieve a high classification performance for the detection of different diseases from images.

CONFLICT OF INTEREST

The author stated that there are no conflicts of interest.

CRediT AUTHOR STATEMENT

Hanife Göker: Conceptualization, Methodology, Software, Formal analysis, Validation, Visualization, Writing.

REFERENCES

[1]   Sung H, Ferlay J, Siegel RL, Laversanne M, Soerjomataram I, Jemal A, Bray F. Global cancer statistics 2020: GLOBOCAN estimates of incidence and mortality worldwide for 36 cancers in 185 countries. CA: A Cancer Journal for Clinicians 2021; 71: 3, 209-249.

[2]   Siegel RL, Miller KD, Jemal A. Cancer statistics 2019. CA: A Cancer Journal for Clinicians 2019; 69: 1, 7-34.

[3]   World Health Organization. Projections of mortality and causes of death 2015 and 2030. Online available: https://www.who.int/health-topics/cervical-cancer#tab=tab_1. [Accessed: 02-January-2023]

[4]   Arora A, Tripathi A, Bhan A. Classification of cervical cancer detection using machine learning algorithms. In 2021 6th International Conference on Inventive Computation Technologies (ICICT) 2021; pp. 827-835.

[5]   Freeman HP, Wingrove BK. Excess cervical cancer mortality: a marker for low access to health care in poor communities. National Cancer Institute, Center to Reduce Cancer Health Disparities Rockville, MD. 2005.

[6]   Li C, Xue D, Zhou X, Zhang J, Zhang H, Yao Y, Kong F, Zhang L, Sun, H. Transfer learning based classification of cervical cancer immunohistochemistry images. In Proceedings of the Third International Symposium on Image Computing and Digital Medicine 2019; pp. 102-106.

[7]   Sompawong N. Automated pap smear cervical cancer screening using deep learning. In 2019 41st Annual International Conference of the IEEE Engineering in Medicine and Biology Society (EMBC) 2019; pp. 7044-7048.

[8]   Cohen PA, Jhingran A, Oaknin A, Denny L. Cervical cancer. The Lancet 2019; 393: 10167, 169-182.

[9]   Tao L, Amanguli A, Li F, Wang YH, Y, Yang, L, Mohemaiti M, Zhao J, Zou XG, Saimaiti A, Abudu M, Maimaiti M, Chen SY, Abudukelimu R, Maimati A, Li SG, Zhang W, Aizimu AA, Yang AQ, Wang J, Pang LJ, Cao YG, Gu WY, Zhang WJ. Cervical screening by Pap test and visual inspection enabling same-day biopsy in low-resource, high-risk communities. Obstetrics & Gynecology 2018; 132: 6, 1421-1429.

[10] Chandran V, Sumithra MG, Karthick A, George T, Deivakani M, Elakkiya B, Subramaniam U, Manoharan S. Diagnosis of cervical cancer based on ensemble deep learning network using colposcopy images 2021; BioMed Research International. 5584004: 1-15.

[11] Cibula D, Pötter R, Planchamp F, Avall-Lundqvist E, Fischerova D, Haie-Meder C, Köhler C, Landoni F, Lax S, Lindegaard JC, Mahantshetty U, Mathevet P, McCluggage WG, McCormack M, Naik R, Nout R, Pignata S, Ponce J, Querleu D, Raspagliesi F, Rodolakis A, Tamussino K, Wimberger P, Raspollini MR. The european society of gynaecological oncology/european society for radiotherapy and oncology/european society of pathology guidelines for the management of patients with cervical cancer. Virchows Archiv 2018; 472: 919-936.

[12] Luo W.Predicting cervical cancer outcomes: statistics, images, and machine learning. Frontiers in Artificial Intelligence 2021; 4: 627369, 1-5.

[13] Nayar S, Panicker JV, Nair JJ. Deep learning based model for multi-class classification of cervical cells using pap smear images. In 2022 IEEE 7th International Conference for Convergence in Technology (I2CT) 2022; pp. 1-6.

[14] Ming Y, Dong X, Zhao J, Chen Z, Wang H, Wu N. Deep learning-based multimodal image analysis for cervical cancer detection. Methods 2022; 205: 46-52.

[15] Ahishakiye E, Wario R, Mwangi W, Taremwa D. Prediction of cervical cancer basing on risk factors using ensemble learning," In 2020 IST-Africa Conference (IST-Africa) 2020; pp. 1-12.

[16] Saini SK, Bansal V, Kaur R, Juneja M. ColpoNet for automated cervical cancer screening using colposcopy images. Machine Vision and Applications 2020; 31: 1-15.

[17] Priyanka BJ, Raju B. Machine learning approach for prediction of cervical cancer. Turkish Journal of Computer and Mathematics Education (TURCOMAT) 2021; 12: 8, 3050-3058.

[18] Mehmood M, Rizwan M, Gregus ml M, Abbas S. Machine learning assisted cervical cancer detection. Frontiers in Public Health 2021; 9: 788376, 1-14.

[19] Alsmariy R, Healy G, Abdelhafez H. Predicting cervical cancer using machine learning methods. International Journal of Advanced Computer Science and Applications 2020; 11(7).173-184

[20] Kalbhor M M., Shinde S V. Cervical cancer diagnosis using convolution neural network: feature learning and transfer learning approaches. Soft Computing 2023, 1-11.

[21] Jantzen J, Dounias G. Analysis of pap-smear image data. The database can be downloaded at https://mde-lab.aegean.gr/index.php/downloads/. In Proceedings of the Nature-Inspired Smart Information Systems 2nd Annual Symposium 2006; 10: 1-11.

[22] Mustafa WA, Kader MMMA. A review of histogram equalization techniques in image enhancement application. In Journal of Physics: Conference Series 2018; 1019: 1, pp. 1-7.

[23] Dhal KG, Das A, Ray S, Gálvez J, Das S. Histogram equalization variants as optimization problems: a review. Archives of Computational Methods in Engineering 2021; 28: 3, 1471-1496.

[24] Escorcia-Gutierrez J, Mansour RF, Beleño K, Jiménez-Cabas J, Pérez M, Madera N, Velasquez K. Automated deep learning empowered breast cancer diagnosis using biomedical mammogram images. Computers, Materials and Continua 2022; 71: 3, 4221-4235.

[25] Han X, Zhong Y, Cao L, Zhang L. Pre-trained alexnet architecture with pyramid pooling and supervision for high spatial resolution remote sensing image scene classification. Remote Sensing 2017; 9: 848, 1-22.

[26] Huang G, Liu Z, Van Der Maaten L, Weinberger KQ. Densely connected convolutional networks. In Proceedings of the IEEE Conference on Computer Vision and Pattern Recognition 2017; pp. 4700-4708.

[27] Howard AG, Zhu M, Chen B, Kalenichenko D, Wang W, Weyand T, Andreetto M, Adam H. Mobilenets: Efficient convolutional neural networks for mobile vision applications. arXiv 2017; 1704.04861.

[28] Sandler M, Howard A, Zhu M, Zhmoginov A, Chen LC. Mobilenetv2: Inverted residuals and linear bottlenecks. In Proceedings of the IEEE Conference on Computer Vision and Pattern Recognition 2018; pp. 4510-4520.

[29] He K, Zhang X, Ren S, Sun J. Deep residual learning for image recognition. In Proceedings of the IEEE Conference on Computer Vision and Pattern Recognition 2016; pp. 770- 778.

[30] Chollet F. Xception: Deep learning with depthwise separable convolutions. In Proceedings of the IEEE Conference on Computer Vision and Pattern Recognition 2017; pp. 1251-1258.

[31] Zheng Y, Yang C, Merkulov A. Breast cancer screening using convolutional neural network and follow-up digital mammography. In Computational Imaging III 2018; 10669: 1066905.

[32] Cantor AB. Sample-size calculations for Cohen's kappa. Psychological Methods 1996; 1: 2, 150-153.

[33] Çimen E. A transfer learning approach by using 2-d convolutional neural network features to detect unseen arrhythmia classes. Eskişehir Technical University Journal of Science and Technology A-Applied Sciences and Engineering 2021; 22.1: 1-9.

[34] Sun G, Li S, Cao Y, Lang F. Cervical cancer diagnosis based on random forest. International Journal of Performability Engineering 2017; 13: 4, 446-457.

[35] Malli PK, Nandyal S. Machine learning technique for detection of cervical cancer using k-NN and artificial neural network. International Journal of Emerging Trends & Technology in Computer Science (IJETTCS) 2017; 6: 4, 145-149.

[36] Nguyen LD, Gao R, Lin D, Lin Z. Biomedical image classification based on a feature concatenation and ensemble of deep CNNs. Journal of Ambient Intelligence and Humanized Computing 2019. 1-13.

[37] Lin H, Hu Y, Chen S, Yao J, Zhang L. Fine-grained classification of cervical cells using

morphological and appearance based convolutional neural networks. IEEE Access 2019. 7: 71541-71549.

[38] Khamparia A, Gupta D, de Albuquerque VHC, Sangaiah AK, Jhaveri RH. Internet of health things-driven deep learning system for detection and classification of cervical cells using transfer learning. The Journal of Supercomputing 2020; 76: 11, 8590-8608.

[39] Ravindran K, Rajkumar S, Muthuvel K. An investigation on cervical cancer with image processing and hybrid classification. International Journal of Performability Engineering 2021; 17: 11, 918-925.

[40] Lavanya Devi N, Thirumurugan P. Cervical cancer classification from pap smear images using modified fuzzy C means, PCA, and KNN. IETE Journal of Research 2022; 68: 3, 1591-1598.

[41] Shinde S, Kalbhor M, Wajire P. DeepCyto: A hybrid framework for cervical cancer classification by using deep feature fusion of cytology images. Math. Biosci. Eng 2022; 19: 6415-6434.

[42] Simonyan K, Zisserman A. Very deep convolutional networks for large-scale image recognition. arXiv 2014; 1409.1556.

[43] Tammina S. Transfer learning using VGG-16 with deep convolutional neural network for classifying images. International Journal of Scientific and Research Publications (IJSRP) 2019; 9: 10, 143-150.

ARTIFICIAL NEURAL NETWORK BASED FAULT DETECTION AND CLASSIFICATION METHOD FOR AIR CONDITIONERS

Cengizhan ABAY [1], [*], Hanife APAYDIN ÖZKAN [2]

[1] Eskisehir Technical University, Faculty of Engineering, Department of Electrical and Electronics Engineering 26555 Eskisehir, Turkey
cengizhanabay@gmail.com - *0000-0002-7484-2687*

[2] Eskisehir Technical University, Faculty of Engineering, Department of Electrical and Electronics Engineering 26555 Eskisehir, Turkey
hapaydin1@eskisehir.edu.tr - *0000-0003-2932-0166*

Abstract

Air Conditioners (AC)s are devices that balance the air exchange and humidity rate as well as provide heating/cooling functions in order to keep the temperature of the environment within the desired conditions and needs. In this study, a new fault detection and classification method for AC is proposed. The method is based on the fact that power consumptions of appliances imply significant information about the appliances' health. Hence, according to the proposed method, power profiles of considered AC are created during its operations. Artificial Neural Network (ANN) configuration of AC is specifically designed and trained by created power profiles. Trained ANN is used to detect and classify faults in the present power profile before major malfunctions occur. Taking action against detected faults helps prevent increased power consumption and serious security issues. Performance and efficiency of the Method designed for classification and detection of errors is between 95.1% - 97.01%.

1. INTRODUCTION

In recent years, devices have started to gain the ability to update status information by communicating with people owing to the development of the Internet of Things (IoT) technology. Hence, people gain opportunity to observe and control appliances from anywhere, anytime.

IoT concept improved many technologies that facilitate human life and provide significant improvements in appliance features. Companies offer their products to the markets with these features [1-2-3-4-5]. One of the emerging technologies in this context is early fault detection in appliances.

During utilization of appliances, aging effect or user errors may result in some malfunctions that decrease durability, increase power consumption, and also create serious safety problems, such as electric shock, fire, etc. [5,6]. Consequently, early detection of faults in appliances avoids these undesired situations. Therefore, studies on fault detection of appliances have increased considerably in recent years: At [7], the vibration data of an asynchronous motor of oven extractor hood is analyzed and fault estimation is made. Some of fault detection studies are generally based on monitoring the operation of appliances with multiple sensors: For example, in [8], a model is proposed to identify and predict faults in boilers of heating and ventilation systems. In the proposed approach, each boiler has sensors to observe

temperature, number of starts and heating requests and the duration of each cycle. Boiler faults are tried to be predicted by training sensor data with a machine learning method. In [9], fault detection by sound sensor data is studied for air conditioner, while the authors of [6] considered a washing machine. In that work, fault classification is performed by training the data obtained from accelerometer, force, gas, sound, and temperature sensors with an attribute learning model. A fault prediction system based on IoT is proposed for some mechanical equipment groups in [10]. Table 1 summarizes remarkable fault detection studies in the literature by means of their methods, considered appliances and sensor types.

Table 1. Synthesis of Remarkable Appliance Fault Detection Studies in the Literature

Study	Method Used	Application Area	Sensors
(Prist et al. 2020)	Machine learning	Commercial kitchen	Vibration
(Fernandes et al. 2020)	Machine learning	HVAC systems	Temperature
(Yang et al, 2019)	Principal component analysis	Air-conditioner	Sound
(Gupta et al. 2021)	Semantic information	Washing machine	Accelerometer, force, gas, sound, temperature
(Hosseini et al. 2020)	Time deviation	Refrigerator	Power meter

Although above mentioned studies have contributed to the literature significantly, they have some limitations, such as, the necessity of multiple sensors and mounting these sensors on the products properly.

An alternative study to these multi-sensor-based works is given in [11]. In that work, continuously monitored power consumption of a refrigerator -instead of multi-sensors data- is considered for detecting faults. However, the proposed method is based on durations of on-off cycles of refrigerator operation and is not applicable to all appliances.

In this study, a new fault prediction method for Air Conditioner (AC) is proposed. Outdoor temperature, indoor temperature and the user's setting for indoor temperature are important factors in the operation of an air conditioner. Both outdoor and indoor temperature values and user's setting determine the cooling or heating operation modes. Any fault in any component affects the power consumption of that component during its operation. The proposed method consists of measuring AC power consumption, which provides important information about the health of the component. The method uses ANN since it provides accurate, reliable, and fast solutions. In the proposed method, power consumption measurements are held for a number of ACs during their operations and the corresponding power profiles are created. Specifically designed ANN, namely AC-ANN, is trained by created power profiles and the temperature values (outdoor temperature, indoor temperature, and the user's setting for indoor temperature). AC-ANN is used to detect the anomalies in the power profiles of the AC for detecting faults and fault classes. Feedforward ANN configuration with a single hidden layer trained by Bayesian regularization-based backpropagation is used for AC-ANN. Input layer of AC-ANN has equal number of nodes consisting of features extracted from power profiles, while the output layer presents the fault-free situation and defined faulty situation(s). Hidden layer is designed experimentally due to the training performance of AC-ANN. The efficiency and performance of the method is validated by simulations, where the ability to detect the presence of considered situations is found to be in 95.1%–97.01%. Unlike other studies in the literature, the proposed method not only detects whether there is a fault or not in a home appliance (such as an air-conditioner), but also enables the cause of the fault to be found in detail.

1.1 Air Conditioner

Air Conditioners (AC)s are devices that balance the air exchange and humidity rate as well as provide heating/cooling functions in order to keep the temperature of the environment within the desired conditions and needs.

AC is composed of the indoor and outdoor units. Outdoor unit is composed of passive components such as condenser and expansion valve that provide heat conversion, and active components such as a compressor and outdoor unit fan. Indoor unit, on the other hand, consists of a passive component such as an evaporator, which provides heat conversion, and an active component, i.e., blower fan. During the operation of AC, active components are activated in certain sequences and consume electricity. Passive components do not consume electricity directly, but any anomaly in the passive components will affect the electricity consumption of the active components. Active components have different electricity consumption rates and operating times. For example, the compressor is the highest power consuming component, while the blower fan is the least power consuming component. AC operations are affected by the temperature of the indoor and outdoor environments. For example, if the outdoor environment is very hot, the indoor environment is cooled in a longer time, otherwise the indoor environment can be cooled in a shorter time. Therefore, the operating time of the components and the corresponding electricity consumption of AC vary according to indoor and outdoor temperatures. For example, power consumption graphs of an AC's cooling operation under similar conditions for different temperature settings ($T_1 set$ and $T_2 set$) such that $T_1 set < T_2 set$ are represented in Figure 1. During cooling operation, decreasing room temperature to a lower degree ($T_1 set < T_2 set$) should consume more electricity because the duration for activating compressor + outer fan + blower fan is longer.
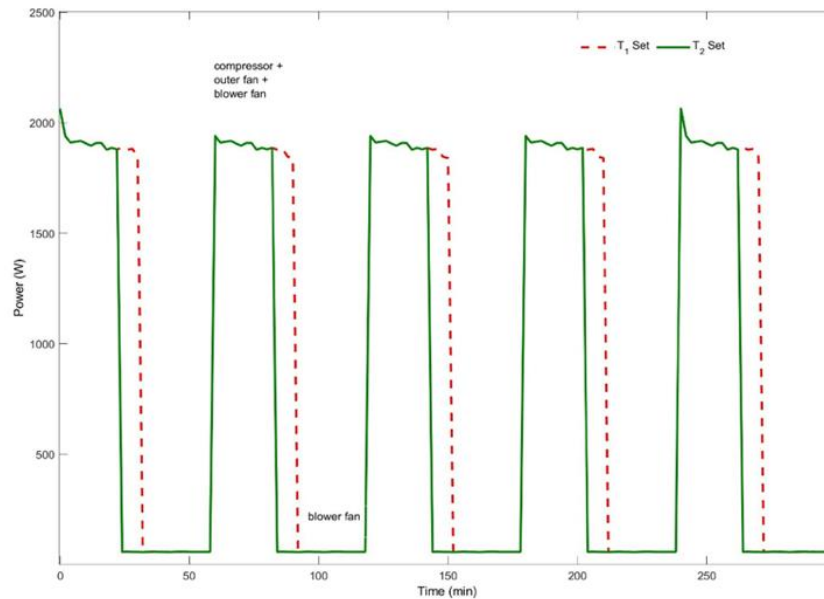
Figure 1. Power consumption of AC for different temperature set values

2. ARTIFICIAL NEURAL NETWORK

An Artificial Neuron Network (ANN) is developed with inspiration from biological nervous system.

An ANN model consists of layers such as, an input layer which receives outer data, an output layer which produces the definitive result, and a number of hidden layer(s) between them. Layers are made up of a number of interconnected nodes, namely neurons [12]. Each neuron has weighted inputs, a transfer function, and an output. The number of hidden layers and neurons in the layers depends on the

problem studied [13]. Each neuron of a layer connects only to the neurons of the previous and next layers.

The feedforward architecture, which is one of the most commonly used architectures among ANN architectures, is the type of architecture that does not have a direct connection from the output neurons to the input neurons and therefore does not keep track of the previous output data. In Figure 2, a typical feed-forward ANN consisting of the input layer with n input nodes, the hidden layer with m hidden nodes and the output layer with k output nodes.

Back Propagation Algorithm (BPA) is the most commonly used training algorithm through many different learning rules for feed-forward multilayered ANNs.

According to BPA, information from input neurons is transmitted by ANN to optimize weights between neurons. Optimization of the weights is made by propagating the error backwards during the training phase. The input and output values in the training data set are read by the ANN so that the weight values of the connections are adjusted to reduce the difference between the predicted values and target values. By ANN, the error in the predicted output value is minimized with many training cycles (epochs) until it reaches a certain level of accuracy.

In the BPA procedure, a random number with a value less than 1.0 is initially assigned to the weight of each connection. Then, inputs received by input layer propagate in forward direction through the hidden and output layers for producing their outputs. With each training data, error related to the output response is calculated and a backpropagation algorithm is used for updating weights and biases of the ANN. The details about the update procedure are summarized as follows:
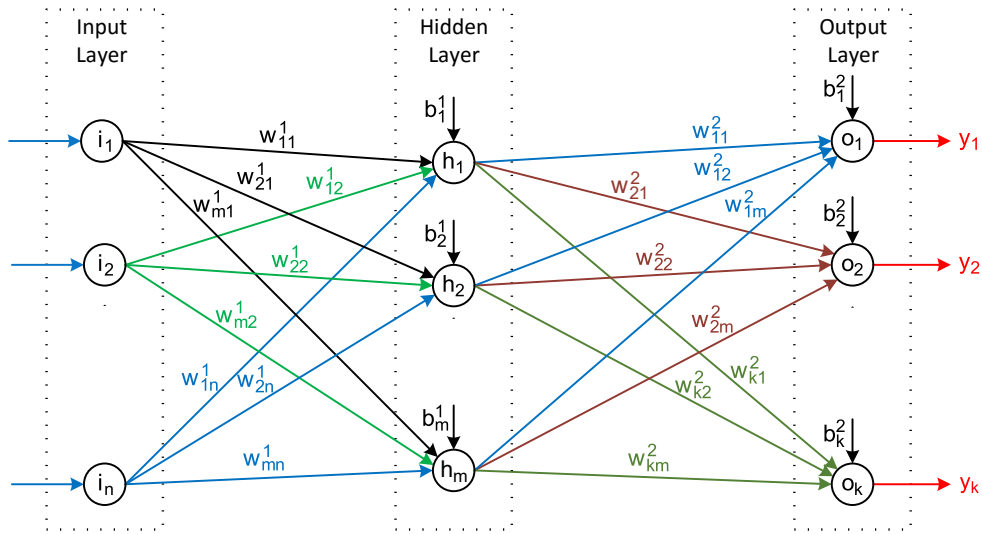
Figure 2. General View of ANN

Each neuron in hidden layer(s) and output layer forms its activation quantity as the sum of weighted average of inputs and corresponding bias which is added to shift the sum relative to origin. Thus, the activation quantity of ith neuron of mth layer is calculated as follows [14]:

$$z_i^m = \sum_{j=1}^{p_{m-1}} w_{ij}^m x_j^{m-1} + b_i^m \tag{1}$$

where, p_{m-1} stands for the number of neurons in $(m-1)$th layer; w_{ij}^m represents the weight of the connection which is between the jth neuron of the $(m-1)$th layer and the ith neuron of the mth layer;

x_j^{m-1} represents the input from jth neuron of the $(m-1)$th layer to the mth layer while b_i^m is the bias of the ith neuron in the mth layer.

Then, in order to obtain the neuron's own scalar output, the activation quantity of each neuron passes through a nonlinear activation function (i.e., step, sign, sigmoid, linear functions and etc.) which express the relationship between the input data and output data. For sigmoid activation function, the output of the ith neuron in the mth layer is calculated as follows [14,15]:

$$y_i^m = f(z_i^m) = \frac{1}{1+e^{-z_i^m}} \qquad (2)$$

Here, y_i^m represents the mth output neurons in the ith layer. Error related to the output response is calculated as the sum of the squared error [14,15].

$$\epsilon(t) = \frac{1}{2}\sum_{i=1}^{n_o}(yd_i(t) - y_i(t))^2 \qquad (3)$$

where n_o is the number of output layer neurons (for example, n_o is k for the output layer in Figure 2) yd_i is the desired output of the ith output neuron and y_i is the actual output of the ith output neurons. Obtained error is backpropagated to the preceding layers for minimizing the error via adjusting weights and biases of the ANN as follows [14,15]:

$$\Delta w_{ij}^m(t) = \eta_w \delta_i^m(t) x_j^{m-1}(t) \qquad (4)$$
$$\Delta b_i^m(t) = \eta_b \delta_i^m(t) \qquad (5)$$

where $\delta_i^m(t) = g'(z_i^m(t))(\sum_{j=1}^{n_m}\delta_j^{m+1}(t)w_{ij}^{m+1}(t-1))$ in the hidden layer and $\delta_i^m(t) = (yd_i(t) - y_i(t))$ in the output layer. Here, $g'(z_i) = \partial g(z_i)/z_i$ and $g(z_i)$ represents the activation of neuron i. The constants $\eta_w (0 < \eta_w < 1)$ and $\eta_b (0 < \eta_b < 1)$ express the learning rates for the weights and biases. After calculating the adjustment factors of the weights and biases, each weight and bias is updated [14,15].

$$w_{ij}^m(t) = w_{ij}^m(t-1) + \Delta w_{ij}^m(t) \qquad (6)$$
$$b_i^m(t) = b_i^m(t-1) + \Delta b_i^m(t) \qquad (7)$$

The process described above is repeated for each training data, updating the input forwards and the output error backwards until a predefined termination condition is met. In order to eliminate underfitting and overfitting problems and to improve the success of the standard BPA applications many regulation methods such as Levenberg-Marquardt, Quasi-Newton, Scaled Conjugate Gradient, Gradient Descent, Resilient Backpropagation, Bayesian Regularization [16] have been developed over the past few years.

In this work, the training data set consists of data to be collected during the durability test that the manufacturer performs at the end of the production process. Therefore, limited number of data is available. Hence, Bayesian Regularization which is more useful [16,17] than other regulation methods in solving problems with scarce of data, is used in this work. Also, adding a penalty term consisting of the squares of all mesh weights and adjusting the objective function accordingly makes the network more responsive [17].

$$\epsilon(t) = \alpha \sum_{i=1}^{n_o}(yd_i(t) - y_i(t))^2 + \beta \sum_{i,j}^{n_o, p_o}(w_{ij})^2 \qquad (8)$$

Here, α and β are regularization parameters and their taking the most appropriate value allows the model to be generalized. The complexity of the ANN model is governed by regularization parameters

α and β, which need to be estimated from the data [17]. Where, p_o is the number of nodes of jth layer connected to the weights w_{ij} based on ith layer.

ANNs are trained by training algorithms (which is BPA in this work) using training data set until predefined terminating error condition is met. Then the performance and accuracy of the trained ANN is estimated by testing data set.

3. FAULT DETECTION AND CLASSIFICATION METHOD FOR ACs

In this study, a fault prediction and classification method for AC by using the developed ANN, i.e., AC-ANN, is proposed.

The proposed method takes into account the fact that any fault occurring in the components of an air conditioner has an impact on the power consumption of this component during its operation. For example, in case of a fault in high power consuming components, the maximum power consumption in the power profile is affected when this faulty component starts operating. Additionally, failure of any component affects the average of the overall power profile. Hence, power profiles are decisive for detecting probable faults at any component. In devices such as air conditioners, components do not work continuously; thus, they work on and off for certain periods of time according to the operating program of the device. Frequency decomposition of power profiles is also decisive for detecting the faults that may occur in device components. Because activation of faulty components reveals unexpected amplitudes at some frequency points. In this work, the frequency decomposition of power profiles has been carried out with Fast-Fourier-Transform (FFT), which is an efficient method to compute the Discrete-Fourier-Transform.

In this work, power consumption values of ACs are monitored during their operations. During the operation of AC, connected smart plug to the appliance continuously sends measurement results of instantaneous power consumption to Main Controller (MC) which creates the corresponding power profile P^{AC}. Power profile is a chronologically ordered array of power consumption values, sampled every 1 min. In order to discard unnecessary information and reduce the size of the network, not directly the power profile but some features extracted from P^{AC} and FFT of P^{AC}, i.e., P_{FFT}^{AC}, are interpreted by appliance specific designed ANNs to predict the faults. Developed AC-ANN configuration for detection and classification of AC faults is given in Figure 3.
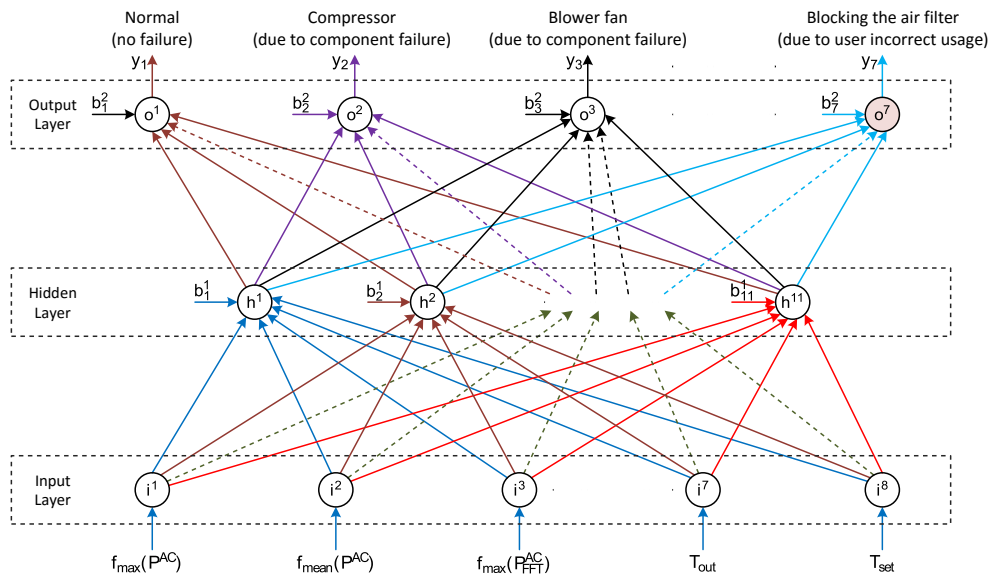
Figure 3. AC-ANN configuration

Input layer of AC-ANN has eight nodes which welcome the considered features of power profiles as inputs. The features are as follows: maximum amplitude in P^{AC}, i.e., $f_{max}(P^{AC})$, mean amplitude of in P^{AC}, i.e., $f_{mean}(P^{AC})$, maximum amplitude in P_{FFT}^{AC}, i.e., $f_{max}(P_{FFT}^{AC})$, sum of all amplitudes in P_{FFT}^{AC}, i.e., $f_{sum}(P_{FFT}^{AC})$, sum of the top n amplitudes in P^{AC}, i.e., $f_{sum_n}(P_{FFT}^{AC})$, indoor temperature (T_{in}), outdoor temperature (T_{out}) and user's set temperature for indoor (T_{set}).

Output layer of AC-ANN presents fault states of the appliance by 1 and 0 which represent the corresponding fault has occurred or not, respectively. AC-ANN has 7 output nodes, for 6 failure situations and the fault-free situation, such as y_1 represents the fault-free (Normal) situation, y_2 represents the compressor failure, y_3 represents the blower fan failure, y_4 represents the outer unit fan failure, y_5 represents the expansion valve failure, y_6 represents the open door/window failure and y_7 represents the blocking the air filter failure.

Training data set of ANNs consists of vectors of input data and the associated output data. Each input data is formed with 5 features extracted from the power profiles and FFT of power profiles, while the corresponding faulty situation or fault-free situation is the associated output data. Note that, in this work power profiles for training data sets are supposed to be created by appliance manufacturers during appliance durability tests. In this work, 6 independent faults are defined for an AC; such as component failures (compressor failure, blower fan failure, outer unit fan failure, expansion valve failure), user-related failures (open door/window failure and blocking the air filter failure). In order to obtain the corresponding power profiles, temporary failures were created by interfering with the mechanics of the components or by creating the misuse of the air-conditioner. For example, deflecting the shaft eccentricity of outer unit fan causes the outer fan failure, similarly deflecting the shaft eccentricity of blower fan causes the blower fan failure. Expansion valve failure is created by shifting the bulb position of the expansion valve. Opening the door or window of the room where the indoor unit is located for a long time provokes the open door/window failure. Blocking the air filter with an object is another user-related failure.

Figure 4 shows the Mean Square Error (MSE) vs. number of epochs graphs for various AC-ANN structures with different number of hidden layer neurons.
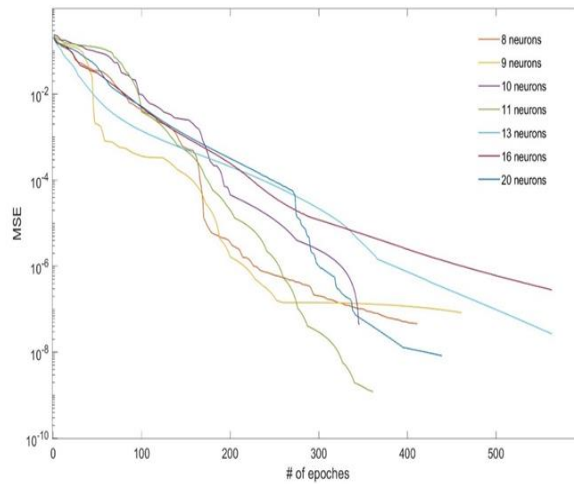
Figure 4. Training performance of AC-ANN

For analysis of the reliability and performance of AC-ANN, several experiments and simulations have been done by using Keysight VEE program and MATLAB Neural Network Toolbox.

In these experiments, an AC which performs both cooling and heating functions with a cooling capacity of 24000 BTU/h and a heating capacity of 25590 Btu/h is used. For the experiments, 180 power profiles are created and the corresponding input-output patterns are obtained for six faulty situations and the fault-free situation under different outdoor and indoor temperature conditions. Some examples of input-output patterns from the training data set are given in Table 2.

Table 2. Training Data Samples for AC-ANN

Input								Output						
$f_{max}(P^{AC})$	$f_{mean}(P^{AC})$	$f_{max}(P_{FFT}^{AC})$	$f_{sum}(P_{FFT}^{AC})$	$f_{sum_n}(P_{FFT}^{AC})$	T_{in}	T_{out}	T_{set}	y_1	y_2	y_3	y_4	y_5	y_6	y_7
(Watts)	(Watts)	(Watts)	(Watts)	(Watts)	(°C)	(°C)	(°C)							
2013.8	520.14	634.45	5781.6	3089.35	25	35	25	1	0	0	0	0	0	0
2013.8	520.14	634.45	5781.6	3088.57	25	35	25	1	0	0	0	0	0	0
--	--	--	--	--	--	--	--	--	--	--	--	--	--	--
2042.1	545.39	652.65	5799.4	3145.34	26	36	25	0	1	0	0	0	0	0
2043.0	545.89	653.89	5798.8	3151.87	25	35	25	0	1	0	0	0	0	0
--	--	--	--	--	--	--	--	--	--	--	--	--	--	--
2024.2	531.04	642.38	5788.9	3100.90	25	35	25	0	0	0	0	0	0	1
2024.8	530.88	642.96	5789.1	3102.85	24	35	25	0	0	0	0	0	0	1

After training by using 140 input-output patterns, the accuracy and performance of AC-ANN was tested with testing data set which consists of 40 input-output patterns. Due to the limited size of the dataset, Bayesian Regularization is chosen for training. Bayesian regularization does not require the validation data set to be separate from the training data set; it uses all the data [16]. The overall mean square error of this validation is 1.66E-09 and the computational time is 0.262 seconds. The confusion matrix in Table 3 represents the performance and efficiency of the trained AC-ANN. By using that confusion matrix, accuracy, precision, recall and F1-score values are obtained for each anomaly class. As a result, for considered anomaly classes AC-ANN provides accuracy in 95.1% - 97.01%, precision in 95.2% - 97.11%, recall in 96.2% - 97.01% and F1-score in 96.67% - 96.93%.

Table 3. Confusion matrix of AC-ANN testing

		Predicted						
		y_1	y_2	y_3	y_4	y_5	y_6	y_7
Actual	y_1	7						
	y_2		8					
	y_3			6				
	y_4				5			
	y_5		1			6		
	y_6						4	
	y_7		1					2

4. RESULTS

Early detection of faults in appliances avoids undesirable situations, such as increasing power consumption and safety problems. The works on early detection of appliances have increased in recent years due to the advancement of IoT technologies.

AC-ANN is designed as a feedforward ANN configuration with 1 hidden layer trained by BPA. Input layer of AC-ANN has input nodes assigned to decisive features obtained from power profiles and the

output layer presents the fault-free and defined faulty situations, while the hidden layer is designed experimentally by considering the training performance of the configuration.

In this work, in order to provide a valuable contribution to the fault detection and classification works, a new fault prediction method for AC is proposed. The method is based on measuring power consumptions of AC at different operating temperatures (outdoor, indoor and user's set) and uses extracted features of power profiles to train the AC-ANN. There are a few similar studies in the literature; however, this study strongly distinguishes itself from the others. This is because, in this study, not only the presence of a fault is detected, but also whether the fault originates from a specific component or is due to a usage error is determined. For example, [9], which is the most similar study in the literature, claims only to detect the presence of faults in AC.

The efficiency and performance of the proposed method is justified by simulations, where the ability to detect the presence of considered situations is found to be in 95.1%–97.01%. Due to this promising result, direction of feature work will be to extend this method to other electrical appliances.

ACKNOWLEDGEMENT

CONFLICT OF INTEREST

The authors stated that there are no conflicts of interest regarding the publication of this article.

CRediT AUTHOR STATEMENT

Cengizhan Abay: Writing – Review & Editing, Visualization. **Hanife Apaydın Özkan:** Methodology, Investigation, Formal analysis, Visualization, Supervision, Project administration, Funding acquisition, Writing – Original Draft.

REFERENCES

[1] https://www.apple.com/lae/ios/home/. Access date: 26.02.2019.

[2] https://developer.amazon.com/en-US/alexa. Access date: 20.02.2022.

[3] https://www.smartthings.com/. Access date: 26.05.2021.

[4] https://xiaomi-mi.com/mi-smart-home/. Access date: 26.02.2022.

[5] https://www.apple.com/lae/ios/health/. Access date: 26.04.2021.

[6] Gupta A, Gupta HP, Biswas B and Dutta T. An unseen fault classification approach for smart appliances using ongoing multivariate time series. IEEE Transactions on Industrial Informatics 2020; 17.6 3731-3738.

[7] Prist M, Monteriù A, Freddi A, Pallotta E, Ciabattoni L, Cicconi P, ... & Longhi S. Machine learning-as-a-service for consumer electronics fault diagnosis: A comparison between Matlab and Azure ML. In 2020 IEEE International Conference on Consumer Electronics (ICCE) (pp. 1-5), IEEE, 2020.

[8] Fernandes S, Antunes M, Santiago AR, Barraca JP, Gomes D and Aguiar RL. Forecasting appliances failures: A machine-learning approach to predictive maintenance. Information 2020; 11(4) 208.

[9] Yang H, Yang Z, Yang H and Xie Y. Fault detection for air conditioner using PCANet. In 2019 Chinese Control Conference (CCC), pp. 3363-3366, IEEE, 2019.

[10] Xu X, Chen T, and Minami M. Intelligent fault prediction system based on internet of things. Computers and Mathematics with Applications, 2012;64(5), 833-839,.

[11] Hosseini SS, Agbossou K, Kelouwani S, Cardenas A and Henao N. A practical approach to residential appliances on-line anomaly detection: A case study of standard and smart refrigerators. IEEE Access 8, 2020; 57905-57922.

[12] Okut H. Bayesian regularized neural networks for small n big p data. Artificial neural networks-models and applications, 2016; 28-48.

[13] Da Silva IN, Spatti DH, Flauzino RA, Liboni LHB and Franco S. Artificial Neural Networks. A Practical Course, Springer, 2017.

[14] Toplak H, Uzmay I and Yildirim S, An artificial neural network application to fault detection of a rotor bearing system. Industrial Lubrication and Tribology, 2006;58/1,32-44.

[15] Vyas NS and Satishkumar D. Artificial neural network design for fault identification in a rotor-bearing system. Mechanism and Machine Theory, 2001;36, 157-175.

[16] Beale MH, Hagen MT and Demuth HB, MATLAB Deep Learning Toolbox User's Guide, The Mathworks Inc, 2020.

[17] Gouravaraju S, Narayan J, Sauer RA and Gautam SS, A Bayesian regularization-backpropagation neural network model for peeling computations, The Journal of Adhesion 2021; 97/13, 1234-1254.

RESEARCH ARTICLE

TRANSIENT SIMULATION OF WIND ENERGY PRODUCTION FOR ELECTRIC MARKET STABILITY

Huseyin Gunhan OZCAN [1],*

[1] Department of Energy Systems Engineering, Faculty of Engineering and Natural Sciences, Bahcesehir University, Istanbul, Türkiye

ozcanhuseyingunhan@gmail.com - 🆔 *0000-0002-8639-6338*

Abstract

Today, energy sustainability, which is one of the most significant concerns in the energy industry, is of utmost importance. In this context, investments and interest in renewable energy sources are growing. As a nation with vast wind energy potential, Türkiye is at the forefront of expanding investments in this sector. This study highlights the significance of wind power plants in electricity market and the relevance of wind energy forecasts, as well as the significance of ensuring the imbalance in energy supply and enhancing electricity market stability. Parallel to this, the transient system simulation (TRNSYS) model was used to determine annual energy generation of a wind power plant in Izmir with a capacity of 18 MW, and the obtained results were compared with the real-time generation data from EPİAŞ transparency platform. The model had two approaches, one based on standard data from the second generation of a typical meteorological year (Plan (1)), and the other on actual field data collected in the plant (Plan (2)).

The numerical findings indicate that the annual energy generation values for Plan (1) and Plan (2) are 24,018.1 MWh and 61,699.1 MWh, respectively. Additionally, the real-time production yields a total of 60,176.2 MWh. In a meantime, Plan (1) generated a positive imbalance value of 45,726.7 MWh, whereas Plan (2) has 6,651.3 MWh over the course of one year. In contrast, the annual sum of negative imbalance values was determined to be 9,475.9 MWh for Plan (1) and 8,368.6 MWh for Plan (2). The analysis yielded annual figures of 2,379,110.4 TL and 351,318.3 TL for positive and negative imbalance penalties, respectively, for Plan (1). For Plan (2), the corresponding amounts were 310,875.9 TL and 337,186.4 TL. Consequently, the total penalty payments for Plan (1) amounted to 2,730,428.8 TL, while for Plan (2) it reached 648,062.3 TL.

1. INTRODUCTION

Due to its geographical location and climatic conditions, Türkiye possesses a substantial wind energy potential. According to the Electricity Affairs Survey Administration, there is 131,756.0 MW of onshore wind potential at 50.0 m altitude across the nation. Based on the wind energy potential atlas provided by Republic of Türkiye Ministry of Energy and Natural Resources, the average wind speed in Türkiye is 5.5 m/s in the northwest and 7.5 m/s in the southeast at a height of 50.0 meters. Wind speeds range from 7.0 to 8.5 m/s along the coasts and from 6.5 to 7.0 m/s in the interior areas between the western and northeastern parts of the country, with the greatest potential in the west [1]. This provides a good opportunity for the construction of wind farms and the production of energy. According to the Turkish Wind Energy Association, the country's wind power facilities have a combined installed capacity of 11.1 GWm as of 2021, allowing them to produce 30.9 TWh of electricity, or 9.8% of total electricity production [2].

Presently, all wind energy plants in Türkiye are located onshore, and studies of the nation's wind energy potential have focused on onshore installations. Gönül et al. [1] conducted a comprehensive analysis of the existing status of wind energy in Türkiye in 2019 relative to 2023 goals. At the conclusion of the study, a number of recommendations were made, such as providing improved credit options, forming partnerships with well-established companies, fixing the feed-in tariff for an extended period, and considering mini-YEKAs (renewable energy resource areas). Arslan et al. [3] examined wind energy potential over Türkiye using wind speed data from 1980 to 2013 based on 335 stations. According to the results by Weibull distribution, Çatalca has the greatest wind energy potential in Türkiye, not only because it has the highest average wind speed with a rate of 7.1 m/s but also because it has vast rural districts for the possible installation of wind farms. Kılıç [4] analyzed the wind energy potential in Türkiye's Burdur province using weather data collected from four distinct nearby stations. The 2009-2016 data was used to train an artificial neural network methodology, which was then used to predict 2030 data for use in a geographic information system. The applied stages revealed that the regions of Burdur, Çeltikci, Ağlasun, and Bucak have greater potential. Kaytez [5] assessed strategies for expanding Türkiye's wind power capacity using a hybrid fuzzy analytic network process analysis. Priority strategies with the highest scores include "development of domestic and efficient technologies" and "sustaining support mechanisms in investments and technical research" among others. Ma and Mei [6] used a hybrid attention-based deep learning approach to predict wind power, and actual data collected from the Yalova farm in Türkiye indicates that the developed model achieves substantially superior prediction accuracy. On the basis of measured wind data, Yaniktepe et al. [7], Akpınar [8], and Bilir et al. [9] statistically investigated the wind energy potential in Türkiye's Osmaniye province, northeastern coast, and Ankara province, respectively. The average wind energy potentials were determined to be 24.5 W/m^2 at 10.0 meters, 64.3 W/m^2 at 10.0 meters, and 40.5 W/m^2 at 20.0 meters.

Numerous investigations on determining wind energy production have been conducted worldwide as well. Examining the most recent ones, Qian and Ishihara [10] proposed a novel probabilistic power curve model for wind farms, and the derived results were compared with the measured one over complex terrain in the northern region of Japan using a variety of statistical indicators. With consideration of wake effects, the proposed model reduces the weighted mean absolute percentage error in mean value from 18.1% to 7.2% and that in standard deviation from 100.0% to 15.6%. Kim and Kim [11] examined the association between atmospheric stability and wind energy production. According to a case study of a 30 MW onshore wind farm in South Korea, the effects of the atmospheric regimes (unstable, neutral, and stable) result in a 5.0–7.0 percent variation in production. Hassanian et al. [12] evaluated the energy production of wind farm in Iceland using 5 years of empirical data and the Jensen-Katic model in deep learning training for wake loss. According to their findings, the optimal capacity factor is 26.1%, and the turbines produce an average of less than 30.0% of their rated power. Cuevas-Figueroa et al. [13] analyzed the precision of weather prediction models and the influence of neighboring wind farms on the energy output of a wind farm operating in complex terrain in Mexico. According to the Rapid Update Cycle and Pleim-Xu models, the measured energy production of the considered wind farm was between 2.0 and 5.3 percent. In a meantime, the ripples of nearby wind farms extend over 12 kilometers downwind, with 5 MW turbines having a larger wake footprint. These farm wakes resulted in a 1.3–1.7% annual energy loss. Moradian et al. [14] estimated the wind resource's potential by calculating the annual energy production based on future climate change scenarios and global circulation models in Ireland. At the conclusion of the investigation, wind speed was predicted to decrease by 7.0% (1981-2010) – 2.0% (2021-2050). Paraschiv et al. [15] assessed the wind energy potential in the south-east of Romania using the Weibull distribution function. At the conclusion of the study, the annual values of the shape and scale parameters were determined to be 1.1 and 5.6 m/s, respectively, indicating that the chosen location is adequate with a monthly average power density of 113.0 and 768.0 W/m^2 at a height of 80.0 meters. Daoudi et al. [16] also used the Weibull distribution function to determine the wind energy potential in Morocco using 24 years of wind data at 10.0 m height. Based on the results obtained, the shape and scale factors are 1.5-1.8 and 2.8-3.6 m/s, respectively, yielding a power density of 16.0-40.5 W/m^2.

In addition to the feasibility analyses provided below, wind energy studies conducted recently have placed a greater emphasis on the energy market both in Türkiye and throughout the globe. Ağbulut [17] proposed a variance sensitive exponential smoothing model to determine wind energy in short term ranges of 30 min, 1-hour, and 3-hour for intraday market in İzmir Province. On the basis of statistical assessment criteria (mean absolute deviation, the mean squared error, the mean absolute percentage error and the root mean square error), the suggested model provides competitive and satisfactory outcomes compared to the regularly used stochastic models (Trigg & Leach, Pantazopoulos & Pappis and optimized simple exponential smoothing) in the literature. Dinler [18] utilized a method of deep learning to reduce electricity market balancing costs. Regarding four tested wind power plants in Türkiye, the proposed methodology allowed for a reduction in balancing cost from 6.2 to 11.2%. Sirin and Yilmaz [19] analyzed Turkish balancing market with the impact of wind and run-of-river hydro energy technologies based on quantile regression. The researchers found that Türkiye's current market structure needed to be revised to account for the geographical and temporal peculiarities of the creation of these technologies. The real value of energy production may be reflected in the balancing market if settlement durations were shorter and there was more than one market zone. Quint and Dahlke [20] examined the impact of wind energy production on the electricity market using Midcontinent Independent System Operator, the second largest competitive wholesale electricity market in the United States. The results indicated that the wholesale price of electricity decreases by $0.01 to $0.03 per MWh for every 100 MWh of additional wind generation. Hu et al. [21] studied the impact of wind power on the intraday market price of electricity in Sweden. The results indicated that wind energy forecast errors have a substantial impact on prices in the country's central and southern regions, but not in the north, where wind energy capacity is low. Liu and Xu [22] evaluated integration of wind power in spot electricity markets in China and found that relaxing bidding regulations can allow wind power producers to develop more profitable bidding strategies and the rise in wind power capacity can decrease the market clearing price.

As evidenced by the aforementioned literature, the intermittent nature of wind energy production makes its prediction a difficult task. In the interim, the forecasted quantity of wind energy production influences intraday, day-ahead, and balancing prices on the energy market, which are of importance to producers, regulators, and policymakers. In this study, annual energy generation of a wind power plant in Izmir with a capacity of 18 MW was calculated with a series of TRNSYS simulations. During simulations, two methodologies were utilized: one based on standard data from the second generation of a typical meteorological year, and the other on actual field data collected at the plant. The obtained results were then compared to the real-time generation data from the EPİAŞ transparency platform. The economic equivalence of the simulated outcomes on the energy market has subsequently been determined using two distinct methodologies. The novelty of this study can be summarized as follows:

   i.   On the basis of two distinct climate data sets, the TRNSYS model, which is primarily employed in practical and energy systems, was evaluated.
   ii.   In one of the methods, direct measurements from the power plant were employed.
   iii. Using a case study, the TRNSYS model's outcomes based on two distinct climate data sets were incorporated into the energy market price.

The structure of this paper is as follows. In section 2, a detailed overview of the Turkish electricity market, a developed numerical model for wind electricity production, and a developed case study in the energy market are provided. In section 3, the energy projections' outcomes are presented, discussed, and contrasted to actual data. In the interim, the incorporation into market prices for energy is presented and discussed. The paper concludes with a discussion of the conclusions in section 4.

2. METERIALS AND METHODS

2.1. An Overview of the Turkish Electricity Market

In the last 30 years, Türkiye's electricity consumption has risen by an average of 6.0% per year, which is about 1.5 times the average growth rate for the rest of the world. As 2019 draws to a close, annual electricity consumption in Türkiye will reach 300.0 TWh. [23]. Despite the fact that the country's renewable potential capacity along a year is quite high (130.0 TWh for wind, 140.0 TWh for hydro, and 380.0 TWh for solar), coal is still the largest source, accounting for 37.0%, followed by hydro, natural gas, and wind, with respective shares of 30.0%, 20.0%, and 7.5%. Since Türkiye must rely on imports for the vast majority of its primary energy needs, its energy strategy centers on ensuring the country's continued access to reliable energy while decreasing its reliance on foreign suppliers. Concurrently, in 2001, Türkiye passed the Energy Market Law, and in 2005, it implemented the Renewable Energy Support Mechanism, both of which are designed to improve the effectiveness of the energy sector by allocating its resources more effectively. These regulations included the liberalization of the market for private investment, the privatization of formerly government-owned electrical producing and distribution firms, and the launch of day-ahead, intra-day and balancing (real-time) electricity markets [23, 24].

In 2011, the day-ahead market (DAM) system was implemented and the Turkish Electricity Market was given a new sense of dynamism and vision, as well as the ethos of a competitive market. In this market, producers declare how much they wish to sell at what price for the next day, with a minimum volume of 0.1 MW for individual hours and blocks, and suppliers declare how much they wish to purchase at what price. Energy Exchange Istanbul (EXIST) combines the proposals for producers and suppliers to determine market clearing price (MCP) for the next day's delivery hour. All EXIST-accepted bids must trade at the derived spot price, regardless of initial price offers or location, and transmission constraints are not taken into account when determining the MCP. There is no requirement for participation in the DAM. Players who do not participate in the DAM can sell the electricity they produce through bilateral agreements and purchase the electricity they consume through bilateral agreements as well. Daily (advance period) and hourly (settlement period) market transactions are conducted in DAM. Each day consists of hourly time periods that begin at 00:00 and conclude the following day at 00:00. To alleviate market imbalances caused by inaccurate forecasts or utility disruptions, the intra-day market (IDM) was introduced in 2016. In contrast to DAM, IDM matches orders based on the offered price. Bids per minute are sorted by hourly price (up-regulation is at the top, down-regulation is at the bottom), and the system marginal price (SMP) is calculated hourly based on the offer volume and price. In balancing market (BM), Turkish Electricity Transmission Company (TEIAS) is the system operator instead of EXIST.

2.2. A Developed Numerical Model for Wind Electricity Production

In this research, an Izmir wind farm with a capacity of 18 MW was chosen. The primary rationale for this selection is that Izmir is the leading city for the installation of wind farms, and that the employed turbine manufacturer and turbine type are the most frequently used, among others. The wind farm is situated at 38.3°N and 26.3°E and is comprised of six 3 MW turbines with the characteristics listed in Table 1.

Table 1. The main characteristics of wind turbine

Property	Value	Unit
Rated power	3	MW
Rated speed	12	m/s
Cut-in wind speed	3	m/s
Cut-out wind speed	25	m/s
Rotor diameter	116.8	m
Swept area	10,715	m^2
Number of blades	3	-
Hub height	120	m

As shown in Figure 1, a TRNSYS-Type 90 mathematical model for a wind energy conversion system was constructed in the simulation studio based on the properties listed in Table 1. The model computes the output power of a wind energy conversion system using a power versus wind speed characteristic. This model also simulates the effects of air density changes and wind speed increases with altitude. The model's wind speed is derived from an external file that can be serviced by TRNSYS-Type 15-6 (standard format weather data reading and processing) or TRNSYS-Type 99 (user defined weather data reading and processing) models. On the other hand, the TRNSYS-Type 65a online plotter with file model can collect and analyze the model's power output.
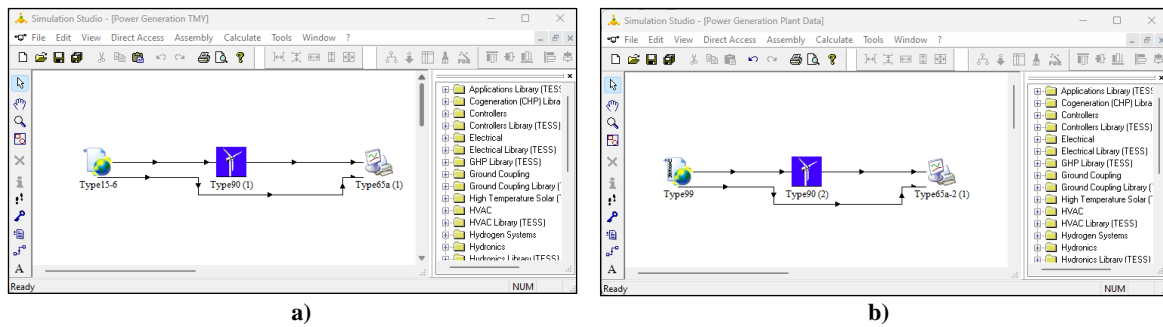
Figure 1. The developed TRNSYS models for wind energy conversion system based on **a)** standard data from the second generation of a typical meteorological year, **b)** actual field data collected at the plant.

The following describes the work performed to construct a numerical model for wind energy production using two distinct climate data sets (standard data from the second generation of a typical meteorological year and actual field data collected at the plant):

i. TRNSYS-Type 90 (1) and TRNSYS-Type 90 (2) parameters were defined as 5 m, 30 m, 120 m, 0.1, 3, and 31 for site elevation, data collected height, hub height, turbine power loss (from turbine output to transformer center), number of turbines, and logical unit of file containing power curve data, respectively.

ii. TRNSYS-Type 90 (1) and TRNSYS-Type 90 (2) external file was generated based on the employed wind turbine characteristics. Regarding this, the rotor center height, rotor diameter, sensor height for data pairs, power-law exponent, turbulence intensity, air density, rated power, rated speed, and number of pairs were specified as 120 meters, 116.8 meters, 120 meters, 0.3, 0.1, 1.225 kilograms per cubic meter, 3 megawatts, 12 meters per second, and 38, respectively.

iii. The external file "TR-Izmir-Cigli-Airp-172180.tm2" was selected as the TRNSYS-Type 15(6) external file.

iv. An external file for TRNSYS-Type 99 was created using actual field data collected at the plant and the power versus this data taking into account the wind turbine in use.

v. Using the wind velocity parameter, the outputs of TRNSYS-Type 15(6) and TRNSYS-Type 99 were connected to the inputs of TRNSYS-Type 90 (1) and TRNSYS-Type 90 (2), respectively.

vi. Using parameters for power output, turbine working hours, and power coefficient, the outputs of TRNSYS-Type 90 (1) and TRNSYS-Type 90 (2) were connected to the inputs of TRNSYS-Type 65a (1) and TRNSYS-Type 65a (2), respectively.

vii. Using wind velocity, the outputs of TRNSYS-Type 15(6) and TRNSYS-Type 99 were connected to the inputs of TRNSYS-Type 65a (1) and TRNSYS-Type 65a (2), respectively.

2.3. A Developed Case Study in Energy Market

The determination of imbalance penalties in the Turkish energy market relies on the values of market clearing price (MCP) and system marginal price (SMP). The observed disparity indicates a discrepancy between the actual energy production (E_{act}) and the intended quantities as per the plan (E_{plan}). When the level of production exceeds the predetermined plan, it is referred to as a positive imbalance. In such cases, a positive imbalance penalty (PIP) is imposed, which can be determined using the equation (1) given below.

$$PIP = \left(E_{act} - E_{plan}\right) \cdot [MCP - min(MCP, SMP) \cdot 0.97)] \qquad (1)$$

In the event that production falls short of the intended target, it is referred to as a negative imbalance. The consequence for this inconsistency is referred to as the negative imbalance penalty (NIP), which may be determined using equation (2) in the following manner.

$$NIP = \left(E_{act} - E_{plan}\right) \cdot [(max(MCP, SMP) \cdot 1.03) - MCP] \qquad (2)$$

The determination of the SMP in the aforementioned equations is contingent upon the indication of an energy deficit or surplus in the system's direction within the energy market. In the event of an energy deficit, the system considers all offers within the balancing power market, prioritizing those with the lowest load purchase bid prices. The price at which the net order volume is determined is referred to as the SMP. In the event that the system exhibits surplus energy, a comparable computation is initiated, commencing with the load shedding bid price that is the greatest.

The concept of MCP pertains to the established electricity price that arises from the equilibrium between supply and demand in day ahead power markets. The maintenance of equilibrium between production and consumption within the energy sector holds significant importance. Insufficient fulfillment of consumption demand results in the occurrence of shortages and disruptions in the provision of power. MCP is the price at which the most costly power plant in the system supplies energy, ensuring that the balance between generation and consumption is attained. The determination of this pricing in Türkiye is conducted by the utilization of the merit order approach. The objective of this approach is to efficiently incorporate manufacturing facilities that can effectively satisfy the consumption requirements inside the system. The merit order model is utilized to forecast the quantity of electrical energy for a given day, considering the hourly consumption demands, using a one-day advance estimation. Based on this assessment, the power plants responsible for meeting the hourly electricity demand are arranged and commissioned in ascending order of cost. The market clearing price is determined by the cost of the most recent power plant that satisfies the demand for electricity. Market players inform EPİAŞ with their demand projections for the subsequent day. The offers are assessed by EPİAŞ, and afterwards, the indeterminate MCP for the following day is announced. Subsequently, any objections, if present, are assessed and the ultimate decision about the MCP is made [25].

The values of the 1.03 and 0.97 coefficients utilized in the computation of the energy imbalance amount have been established in 01 May 2015. Furthermore, individuals who fail to disclose unfulfilled orders within a 4-hour timeframe, resulting in a modification of the SMP, are required to bear the financial burden associated with the resulting price discrepancy. The objective of this endeavor is to ensure the effective administration of the instruction reconciliation function and the SMF decision process.

3. RESULTS AND DISCUSSION

The present study involved the estimation of the yearly energy production of an 18 MW wind power facility located in Izmir through a sequence of TRNSYS simulations using one-hour data. In the course of the simulations, two distinct techniques were employed: one relied on standard wind data derived

from the second generation of a representative meteorological year, while the other drew upon real-world wind data obtained on-site at the facility. In a meantime, the real-time generation data was gathered from the EPİAŞ transparency platform. Figure 2 depicts the wind data in a monthly format, whereas Figure 3 shows the simulated results for annual energy generation together with real-time production at the facility from the EPİAŞ transparency platform. Table 2 displays the outcomes of the economic assessment carried out in this study, with respect to the quantities of energy produced.
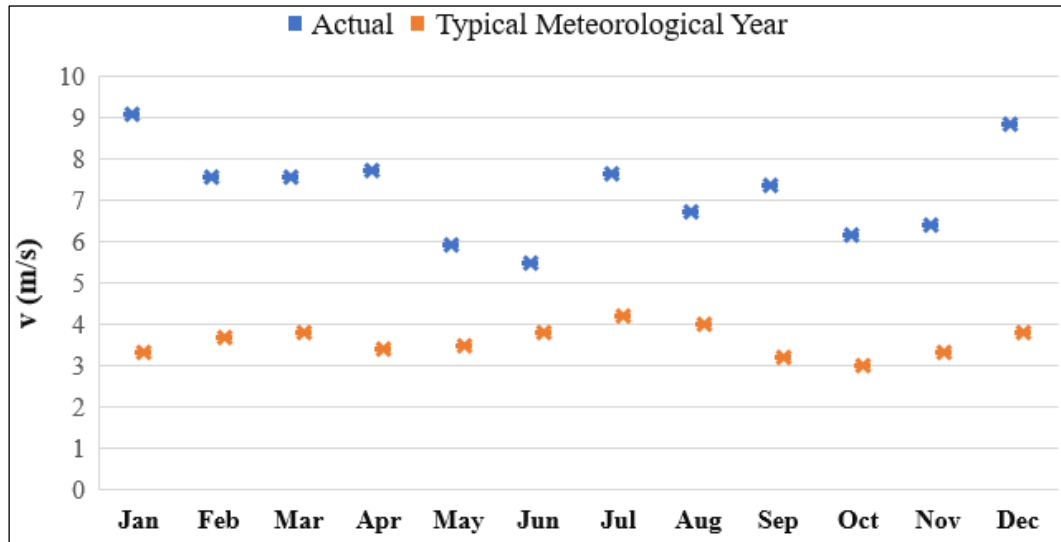
Figure 2. The wind velocity amounts on the side based on plant readings and TRNSYS simulations.

The figure 2 illustrates that the collected wind velocity readings throughout the year exceeded the average values often observed in meteorological records. The observed velocity readings from the plant range from 5.48 m/s (in June) to 9.08 m/s (in January), with an average of 7.20 m/s over the course of a year. However, typical meteorological velocities vary between 2.99 m/s (in October) and 4.20 m/s (in July), with an annual average of 3.58 m/s. The variability observed in the actual wind data is significantly more than that often observed in meteorological wind data.
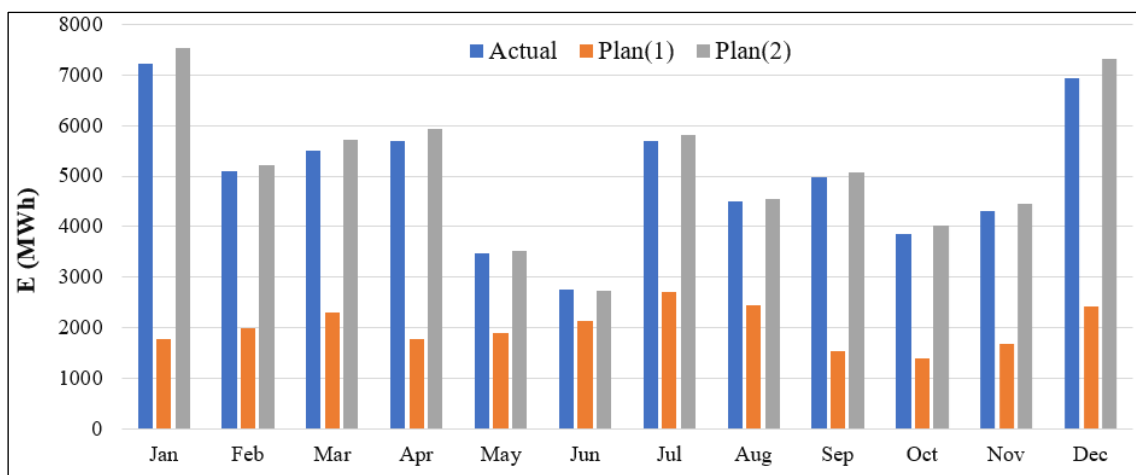
Figure 3. The energy generation amounts on the side based on EPİAŞ transparency platform and TRNSYS simulations.

According to Figure 3, it can be observed that the annual energy generation values for Plan (1) consistently exhibit their lowest values across all months, which was based on standard wind data

derived from the second generation of a representative meteorological year. It is evident from Figure 2 that the recorded velocity readings exhibit the lowest values in this particular scenario. The minimum and maximum values were simulated on a monthly basis, with the minimum value of 1,391.9 MWh occurring in October and the maximum value of 2,697.8 MWh occurring in July. Meanwhile, it was determined that the annual energy production, derived from standard wind data, amounted to 24,018.1 MWh. In accordance with Plan (1), several researchers have studied electricity generation using the TRNSYS-Type 90 model for wind energy conversion systems with meteorological year data [26-30]. Bakić et al. [26] conducted a dynamic simulation of a PV/wind hybrid system in the city of Belgrade, Serbia, where the average annual wind speed is 3.54 m/s. The simulation included wind turbines with capacities of 1 kW, 3 kW, and 5 kW, all modeled at a hub height of 20 m. The total annual energy production for the aforementioned capacities was computed as 983 kWh, 1,840 kWh, and 3,930 kWh, respectively, at the end of the simulations. In a numerical study done by Żołądek et al. [27] assessed energy and economic performances of a PV/wind/wood gasifier with battery/hydrogen energy storage system for the city of Agkistro, Greece. The simulation findings indicate that the annual total energy generation from the 110-kW wind turbine is 151,000 kWh. Yesilyurt et al. [28] performed conventional exergy analysis on a hybrid energy generation system that includes a vanadium redox flow battery and an air source heat pump. The system was analyzed specifically for the city of Istanbul. The annual energy production of a 2.5-kW wind turbine was calculated to be 5,827.9 kWh, considering a yearly average wind velocity of 4.5 m/s. Anaune et al. [29] applied a study to determine the appropriate size for a PV/wind system in Rabat, Morocco. They used the second generation of a typical meteorological year for their analysis. The annual electricity production of a 1-kW wind turbine was simulated to be 1,404 kWh, based on the average wind speed of 4.14 m/s at a hub height of 10 m. Panayiotou et. al [30] did a numerical study to analyse the technical and economic performances of two stand-alone systems (PV and PV/wind) in two distinct locations (Nicosia, Cyprus and Nice, France). According to data, wind turbines with 1-5 kW and 2.4-kW capacities produce 2,077 kWh and 2,353 kWh respectively in the city of Nice, which as a more favorable wind profile. The energy output per unit of capacity varied between 920 1/h and 2,331.16 1/h as a result of the wind turbine type and the weather data. The study produced a value of 1,334.3 1/h, which indicates that the result is within the allowed range for this value.

On the contrary, Figure 3 demonstrates that Plan (2) consistently exhibits the highest levels of annual energy production throughout various months, namely January (7,527.0 MWh), February (5,206.9 MWh), March (5,720.8 MWh), April (5,928.2 MWh), May (3,523.4 MWh), July (5,810.1 MWh), August (4,539.5 MWh), September (5,067.4 MWh), October (4,028.3 MWh), and December (7,155.2 MWh), with the exception of June (2,728.4 MWh). In this particular case, the wind data utilized in the analysis was derived from actual wind measurements collected on-site at the plant. Simulated work based on Plan (2) was successfully found the real-time production amounts. While the cumulative energy generation over the course of a year was determined to be 61,699.1 MWh based on Plan (2), it was obtained to be 60,176.2 MWh for the actual readings.

Table 2 presents the economic implications, specifically the associated imbalance fines, resulting from the differences seen between the energy output estimated using the TRNSYS model and the real-time generation data obtained from the EPİAŞ transparency platform.

Table 2. Imbalance penalties based on production estimation for Plan (1) and Plan (2), respectively

Mounts	Positive Imbalance (MWh)	Negative Imbalance (MWh)	PIP (TL)	NIP (TL)
Jan	5,904.7/516.5	430.8/819.2	181,895.9/13,828.4	11,566.1/24,839.6
Feb	3,674.7/396.1	577.1/513.7	91,516.1/11,039.4	10,890.1/10,348.3
Mar	4,376.5/602.6	1,180.9/809.4	144,361.6/17,778.1	53,818.3/28,882.7
Apr	4,512.4/487.4	584.1/711.7	176,191.9/13,263.0	21,988.2/24,296.4
May	2,739.7/549.4	1,179.1/608.6	132,136.0/19,939.3	53,873.8/22,142.0
Jun	1,608.3/570.8	986.6/540.7	43,627.5/15,601.3	30,742.3/17,776.4
Jul	3,847.3/643.0	832.0/751.2	177,451.7/25,052.1	15,858.9/19,110.1
Aug	3,000.9/643.4	961.5/694.7	211,819.8/44,737.8	24,577.9/16,315.8
Sep	3,999.3/678.2	545.0/773.2	359,123.7/44,861.0	10,522.5/19,726.3
Oct	3,193.0/581.5	725.4/735.5	175,102.7/33,050.7	28,575.3/39,118.2
Nov	3,417.6/473.4	773.2/635.9	229,754.7/23,782.0	56,610.5/61,311.0
Dec	5,452.4/509.0	700.2/774.9	456,128.8/47,942.9	32,294.6/53,319.7

Table 2 illustrates a notable disparity in positive imbalances between Plan (1) and Plan (2), with Plan (1) exhibiting much higher levels. The positive imbalance for Plan (1) ranges from 1,608.3 MWh in June to 5,904.7 MWh in January, resulting in an annual total of 45,726.7 MWh. In contrast, Plan (2) exhibits a monthly positive imbalance range of 396.1 MWh in February to 678.2 MWh in September, with a yearly sum of 6,651.3 MWh. The data presented in Figure 3 clearly demonstrates that the observed energy production levels exceed the estimated energy generation based on Plan (1) by a substantial margin. In the case of Plan (2), the actual energy generation amounts and the anticipated energy production amounts exhibit a high degree of similarity. Accordingly, the PIP for Plan (1) demonstrates a fluctuation from 43,627.5 TL in June to 456,128.8 TL in December. The economic assessments were undertaken on an hourly basis, resulting in the highest PIP observed in December, despite the presence of a maximum positive imbalance in January. In contrast, the PIP values for Plan (2) were found to be much lower compared to the PIP quantities for Plan (1). The recorded amounts vary from 11,039.4 TL in February to 47,942.9 TL in December. In accordance with PIP for Plan (1), the highest cost was achieved during the month of December. The annual PIP amounts for Plan (1) and Plan (2) were observed to be 2,379,110.4 TL and 310,875.9 TL, respectively. Table 2 also demonstrates that the negative imbalance amounts on a monthly basis for Plan (1) and Plan (2) are similar to each other. In February, March, May, June, July, August, and November, Plan (1) exhibits higher values compared to Plan (2), specifically 577.1 MWh to 513.7 MWh, 1,180.9 MWh to 809.4 MWh, 1,179.1 MWh to 608.6 MWh, 986.6 MWh to 540.7 MWh, 832.0 MWh to 751.2 MWh, 961.5 MWh to 694.7 MWh, and 773.2 MWh to 635.9 MWh, respectively. Conversely, for the remaining months, namely January (819.2 MWh to 430.8 MWh), April (711.7 MWh to 584.1 MWh), September (773.2 MWh to 545.0 MWh), October (735.5 MWh to 725.4 MWh), and December (774.9 MWh to 700.2 MWh), Plan (2) demonstrates higher values than Plan (1). Annual total negative imbalance amounts were found to be 9,475.9 MWh and 8,368.6 MWh for Plan (1) and Plan (2), respectively. The NIP for Plan (1) and Plan (2) exhibits a variation from 10,522.5 TL in September to 56,610.5 TL in November, and from 10,348.3 TL in February to 61,311.0 TL in November. The economic evaluations were conducted on an hourly basis, revealing that the largest NIP was seen in November for both Plan (1) and Plan (2). It is worth noting that despite experiencing a maximum negative imbalance in March for Plan (1) and in January for Plan (2), the NIP remained highest in November. The annual NIP amounts for Plan (1) and Plan (2) were recorded as 351,318.3 TL and 337,186.4 TL, respectively.

4. CONCLUSION

This study aimed to quantify the degree of disparity between the energy output estimated using the TRNSYS models and the real-time generation data from the EPİAŞ transparency platform. Additionally, the associated penalties resulting from this disparity were computed. Accurate assessment of energy generation has been demonstrated to be crucial in mitigating disparities. By employing accurate

calculations, it is possible to mitigate the potential for imbalance and the associated expenses that may arise from such imbalances. In conclusion, these calculations enhance the stability and long-term viability of the energy market. Within the present context, the study's findings are presented as follows.

- The collected wind velocity readings throughout the year 2021 (from 5.48 m/s to 9.08 m/s with an annual average of 7.20 m/s) exceeded the average values often observed in meteorological records (from 2.99 m/s to 4.20 m/s with an annual average of 3.58 m/s).
- The energy generation values for Plan (1) were simulated to range from 1,391.9 MWh to 2,697.8 MWh, with a total annual sum of 24,018.1 MWh. According to the literature studies conducted in accordance with Plan (1), The energy production per unit of capacity exhibited a yearly variation ranging from 920 1/h to 2,331.16 1/h. For this study, the energy output per unit of capacity was found to be 1,334.3 1/h, which falls within the acceptable range.
- The energy production values for Plan (2) were found to be between 2,728.4 MWh and 7,527.0 MWh having a yearly sum of 61,699.1 MWh. Therefore, simulated work based on Plan (2) was successfully found the real-time production amounts which was obtained to be 60,176.2 MWh along a year.
- The simulated energy generation values yielded positive imbalance values ranging from 1,608.3 MWh to 5,904.7 MWh, with a total annual sum of 45,726.7 MWh for Plan (1). For Plan (2), the positive imbalance values ranged from 396.1 MWh to 678.2 MWh, with a yearly total of 6,651.3 MWh. On the other hand, negative imbalance values ranging from 430.8 MWh to 1,180.9 MWh, with a total annual sum of 9,475.9 MWh for Plan (1). For Plan (2), the negative imbalance values ranged from 513.7 MWh to 819.2 MWh, with a yearly total of 8,368.6 MWh.
- The simulated positive imbalance amounts yielded PIP ranging from 43,627.5 TL to 456,128.8 TL, with a total annual sum of 2,379,110.4 TL for Plan (1). For Plan (2), the PIP values ranged from 11,039.4 TL to 47,942.9 TL, with a yearly total of 310,875.9 TL. On the other hand, the simulated negative imbalance amounts yielded NIP ranging from 10,522.5 TL to 56,610.5 TL, with a total annual sum of 351,318.3 TL for Plan (1). For Plan (2), the NIP values ranged from 10,348.3 TL to 61,311.0 TL, with a yearly total of 337,186.4 TL. The combined penalty payments (PIP and NIP) were found to be 2,730,428.8 TL for Plan (1) and 648.062,3 TL for Plan (2), respectively.

In future research, the impact of various parameters on energy generation can be investigated using the TRNSYS model. These characteristics may include turbulance intensity, shear exponent, turbine power loss, and others. Meanwhile, certain machine learning models can be utilized to do energy assessments with more precision. Hence, energy producers have the potential to receive economic rewards.

ACKNOWLEDGEMENTS

CONFLICT OF INTEREST

The author stated that there are no conflicts of interest regarding the publication of this article.

CRediT AUTHOR STATEMENT

Huseyin Gunhan Ozcan: Conceptualization, Methodology, Software, Validation, Formal analysis, Writing – Original Draft, Visualization.

REFERENCES

[1]   Gönül Ö, Duman AC, Deveci K, Güler Ö. An assessment of wind energy status, incentive mechanisms and market in Turkey. Eng Sci Technol Int J 2021; 24: 1383-1395.

[2]   Başaran HH, Tarhan İ. Investigation of offshore wind characteristics for the northwest of Türkiye region by using multi-criteria decision-making method (MOORA)☆. Results Eng 2022; 16: 100757.

[3]   Arslan H, Baltaci H, Akkoyunlu BO, Karanfil S, Tayanc M. Wind speed variability and wind power potential over Turkey: Case studies for Çanakkale and İstanbul. Renew Energy 2020; 145: 1020-1032.

[4]   Kılıç B. Determination of wind dissipation maps and wind energy potential in Burdur province of Turkey using geographic information system (GIS). Sustain Energy Technol Assess 2019; 36: 100555.

[5]   Kaytez F. Evaluation of priority strategies for the expansion of installed wind power capacity in Turkey using a fuzzy analytic network process analysis. Renew Energy 2022; 196: 1281-1293.

[6]   Ma Z, Mei G. A hybrid attention-based deep learning approach for wind power prediction. Appl Energy 2022; 323: 119608.

[7]   Yaniktepe B, Koroglu T, Savrun MM. Investigation of wind characteristics and wind energy potential in Osmaniye, Turkey. Renew Sustain Energy Rev 2013; 21: 703-711.

[8]   Akpınar A. Evaluation of wind energy potentiality at coastal locations along the north eastern coasts of Turkey. Energy 2013; 50: 395-405.

[9]   Bilir L, İmir M, Devrim Y, Albostan A. An investigation on wind energy potential and small scale wind turbine performance at İncek region–Ankara, Turkey. Energy Convers Manag 2015; 103: 910-923.

[10]   Qian GW, Ishihara T. A novel probabilistic power curve model to predict the power production and its uncertainty for a wind farm over complex terrain. Energy 2022; 261 (Part A): 125171.

[11]   Kim DY, Kim BS. Differences in wind farm energy production based on the atmospheric stability dissipation rate: Case study of a 30 MW onshore wind farm. Energy 2022; 239: 122380.

[12]   Hassanian R, Helgadóttir Á, Riedel M. Iceland wind farm assessment case study and development: An empirical data from wind and wind turbine. Cleaner Energy 2023; 4: 100058.

[13]   Cuevas-Figueroa G, Stansby PK, Stallard T. Accuracy of WRF for prediction of operational wind farm data and assessment of influence of upwind farms on power production. Energy 2022; 254: 124362.

[14]   Moradian S, Olbert AI, Gharbia S, Iglesias G. Copula-based projections of wind power: Ireland as a case study. Renew Sustain Energy Rev 2023; 175: 113147.

[15]   Paraschiv S, Paraschiv LS, Serban A, Cristea AG. Assessment of onshore wind energy potential under temperate continental climate conditions. Energy Rep 2022; 8: 251-258.

[16] Daoudi M, Mou AAS, Naceur LA. Analysis of the first onshore wind farm installation near the Morocco-United Kingdom green energy export project. Sci Afr 2022; 17: e01388.

[17] Ağbulut Ü. A novel stochastic model for very short-term wind speed forecasting in the determination of wind energy potential of a region: A case study from Turkey. Sustain Energy Technol Assess 2022; 51: 101853.

[18] Dinler A. Reducing balancing cost of a wind power plant by deep learning in market data: A case study for Turkey. Appl Energy 2021; 298: 116728.

[19] Sirin MS, Yilmaz BN. The impact of variable renewable energy technologies on electricity markets: An analysis of the Turkish balancing market. Energy Policy 2021; 151: 112093.

[20] Quint D, Dahlke S. The impact of wind generation on wholesale electricity market prices in the midcontinent independent system operator energy market: An empirical investigation. Energy 2019; 169: 456-466.

[21] Hu X, Jaraitė J, Kažukauskas A. The effects of wind power on electricity markets: A case study of the Swedish intraday market. Energy Econ 2021; 96: 105159.

[22] Liu T, Xu J. Equilibrium strategy based policy shifts towards the integration of wind power in spot electricity markets: A perspective from China. Energy Policy 2021; 157: 112482.

[23] Sirin SM, Uz D, Sevindik I. How do variable renewable energy technologies affect firm-level day-ahead output decisions: Evidence from the Turkish wholesale electricity market. Energy Econ 2022; 112: 106169.

[24] Sirin SM, Yilmaz BN. Variable renewable energy technologies in the Turkish electricity market: Quantile regression analysis of the merit-order effect. Energy Policy 2020; 144: 111660.

[25] https://www.epias.com.tr/en/

[26] Bakić V, Pezo M, Stevanović Ž, Živković M, Grubor, B. Dynamical simulation of PV/Wind hybrid energy conversion system. Energy 2012; 45(1): 324-328.

[27] Żołądek M, Figaj R, Kafetzis A, Panopoulos K. Energy-economic assessment of self-sufficient microgrid based on wind turbine, photovoltaic field, wood gasifier, battery, and hydrogen energy storage. Int J Hydrogen Energy 2024; 52: 728-744.

[28] Yesilyurt MS, Ozcan HG, Yavasoglu HA. Co-simulation-based conventional exergy evaluation of a hybrid energy generation-vanadium redox flow battery-air source heat pump system. Energy 2023; 281: 128301.

[29] Anoune K, Laknizi A, Bouya M, Astito A, Abdellah AB. Sizing a PV-Wind based hybrid system using deterministic approach. Energy Convers Manag 2018; 169: 137-148.

[30] Panayiotou G, Kalogirou S, Tassou S. Design and simulation of a PV and a PV–Wind standalone energy system to power a household application. Renew Energy 2012; 37(1): 355-363.

RESEARCH ARTICLE

CLASSIFICATION OF STUDENTS' ACADEMIC SUCCESS USING ENSEMBLE LEARNING AND ATTRIBUTE SELECTION

Derya ÇINAR [1] Sevcan YILMAZ GÜNDÜZ [2],*

[1] Computer Engineering Department, Engineering Faculty Eskişehir Technical University, Eskişehir, Turkey
cinar1983@gmail.com - 0009-0005-4729-2172

[2] Computer Engineering Department, Engineering Faculty Eskişehir Technical University, Eskişehir, Turkey
sevcany@eskisehir.edu.tr   - 0000-0002-1736-9942

Abstract

Students' success in high school plays an important role in shaping their lives, as it also affects their success in university placement. It is very important to be able to predict this situation so that in case of failure, precautions can be taken, and a solution can be produced. If success situations and failure can be predicted, success can be increased and stabilized with encouragement and support. In this study, students' academic performances were tried to be estimated with the datasets prepared with secondary school students in Portugal. The datasets include students' answers about the factors thought to affect their success-failure and their grades. The wide use and efficiency of machine learning algorithms have also affected studies on predicting student success. Different algorithms have been applied using different methods in the datasets and the correct prediction rate was tried to be maximized. Experiments were carried out using the 10-fold cross validation method. Deep learning, multilayer perceptrons, simple logistic regression, decision table, one rule, iterative classifier optimizer, logistic model tree and fuzzy unordered rule induction algorithm have been used to predict the student academic success. These algorithms have been tested with the classical and bagging methods. The experiments also tested the efficiency of the algorithms in predicting student success by selecting features and comparing the results.

1. INTRODUCTION

Predicting students' grades is important to guide students correctly [1]. To increase students' academic success, it is effective to identify the factors that reduce success, to eliminate these factors, or even if this is not possible, to reduce their effects. However, these factors are not easy to determine. The reason is that there are many factors that affect students' academic performance [2]. Another reason that makes this process difficult is the presence of unmeasurable factors. Student success may depend on socio-economic and physical conditions. It can be measured by factors such as the society in which one lives, family life, school conditions, and financial means. Individual differences such as talent, interest, and intelligence, are factors that affect success [3] and they cannot be measured easily. Economic conditions, the number of siblings, the education levels, and professions of family members are also factors affecting success [4].

It is possible to predict success with the survey answers in the datasets used to predict student success and the grades taken from school systems and to find out which of these data is effective with artificial intelligence methods. A lot of different data about students can be kept through surveys and records. The type and size of these data may vary [5]. Working with big data is more convenient for making inferences and predictions. Machine learning algorithms, which have become popular in many fields recently, can be used to predict student success. Using student data with machine learning algorithms, students' success is tried to be predicted [6]. Depending on the type of dataset and function, machine

learning techniques may change. Some of these techniques include clustering, classification, and feature selection. To make the classification results more efficient, in addition to simple methods, compound machine methods that use several methods together can also be used [7]. The dataset on which each algorithm works efficiently varies depending on the content of the set.

In this study, simple machine learning techniques and bagging ensemble learning techniques were used to predict students' academic achievements. In the study, two open-source datasets, prepared with secondary school student data in Portugal, containing socio-economic conditions as well as three grade information from mathematics and Portuguese courses, were used. The tests were carried out with eight different algorithms by using classical and bagging methods. Initially all the features were involved and then some of them were selected. The algorithms used are deep learning (DL), multilayer perceptrons (MLP), simple logistic regression (SL), decision table (DT), one-rule (One-R), iterative classifier optimizer (ICO), logistic model tree (LMT) and fuzzy unordered rule induction algorithms (FURIA). In this study, unlike many other studies, experiments were deepened by selecting features and using ensemble learning algorithms together. Using various feature selection algorithms and comparing the results to identify common features with the highest contribution has significantly enriched the literature in this field. Consequently, the attributes that play the most important role in predicting student success were identified. This information provides valuable insights for future research and practical applications in education. Another important feature that distinguishes it from other studies is its attempt to enhance various classification algorithms using the bagging method and comparing the results of bagging methods with classical classification techniques. This study represents a comprehensive investigation that incorporates both classical classification methods, feature selection techniques, and the bagging method.

2. LITERATURE OVERVIEW

For educational sciences, being able to predict student success classes is an important and necessary choice for the scope of education. There are various studies conducted in this field and some of them will be discussed in this section.

Cortez and Silva [8] compared machine learning techniques with two different datasets containing real-world pieces containing 33 different attributes and three exam scores in commonly seen locations in two different high schools in Portugal. To deepen the study, they have created systems that predict students' academic success by transmitting exam grades. Cortez and Silva [8] carried out their work in the experimental R programming environment. They used the RMiner Library, an open-source library, and DL methods such as random forest (RF), neural networks (NN), support vector machines (SVM), decision trees (DTrees) and naive estimator (NV) training. In their study, it was seen that previous life success situations were highly effective, but other relevant characteristics were also effective. To obtain accurate predictions in their study, 200 values were obtained by performing 10-fold cross validation 20 times for the derivative. Test findings of all data in ten times with 10% of the data. The dataset with the highest prediction success of the system was determined with the experiment including two exam grades, and the most successful development was determined as the NV.

V. Vijayalakshmi and K. Venkatachalapathy [9] trained the model with the R program using different algorithms for student performance prediction and stated that the algorithm gave the most successful results was the deep neural network (DNN) with an accuracy rate of 84%. They used many algorithms such as DTrees, SVM, Naive Bayes (NB), RF, k nearest neighbors (k-NN), DNN in their study. Tosunoğlu et al. [10] conducted a review of articles in the field of educational sciences with machine learning methods. They analyzed 201 articles published between 2015 and 2020. They found that the most used algorithm in the articles was the DTrees algorithm with a rate of 22.5%. Güvenç et al. [11] tried different machine learning methods to predict the academic success of students taking the Introduction to Information Systems Engineering course, but they could not achieve successful results due to the lack of sample dataset of 71 students. Hence, to increase the sample, they increased the dataset

to 300 student records with the Synthetic Minority Over-sampling Technique (SMOTE) and increased the correct prediction success of the most successful algorithm from 60% to 97.87% with the k-NN.

In their study, Salameh et al. [12] carried out the 2-stage (pass-fail) classification in the MATLAB program and used the enhanced binary genetic algorithm (EBGA) and binary genetic algorithm (BGA), which are feature selection algorithms. They stated that the NB algorithm and the EBGA feature selection method were the most successful methods with a rate of 87%, using k-NN, DTrees, NB, SVM and the hidden Latent Dirichlet allocation algorithm.

In their study, Quy et al. [13] worked on a 2-stage (pass-fail) classification with Portuguese course notes and tried the Adaboost boosting method as well as the classical methods. As a result, they achieved a success rate of 95%.

Özkan et al. [14] made a 2-stage (pass-fail) classification with the mathematics dataset in their study to find the most effective attribute. As a result of their study in the R program, they stated that the C5.0 algorithm was successful with a rate of 86% among different algorithms. In their study with a 2-stage mathematics course dataset, Başer et al. [15] carried out classification studies with various algorithms in the WEKA program and reached a 92.15% accuracy rate with the One-R algorithm. Çınar and Yılmaz Gündüz [16] worked with a 2-stage mathematics course dataset. In this study, the LMT algorithm gave the best result. Yavuzarslan and Erol [17] tried to predict student success using different algorithms in their study with 10-week log records of 93 students, but since the dataset did not work efficiently, they renewed the study by creating new dataset derivatives with the synthetic minority sample increase method, upsampling and class sampling methods. They achieved over 80% success in their study with these newly created dataset variants.

Kayalı and Buyrukoğlu [18] conducted a total of 24 different experiments with 2 datasets, using comprehensive forward selection, analysis of variance, embedded feature selection methods and DTrees, RF, and exchange of support machines to predict academic success in their country. As a result of the experiments, it was observed that the 84% accuracy rate obtained by using all attributes in the RF algorithm in the first dataset was increased to 86% by selecting attributes with advanced selection techniques. They stated that in the second dataset, the accuracy rate was increased from 82% to 90% by using all the features with the RF algorithm and SVM algorithms.

Bentaleb and Abouchabaka [19] stated in their study with datasets prepared with the notes of 3-grade mathematics and Portuguese courses, the most successful algorithm with an accuracy rate of 86% among DTrees, RF and SVM algorithms is the RF algorithm in the Python program.

Bozkurt Keser and Aghalarova [20] used a new hybrid ensemble learning algorithm (HELA) in their study. In this study, they used 3 different boosting algorithms and different combinations of these algorithms as input to the HELA. In their study, they used two and five stage classification datasets containing secondary school students' grades and other information about mathematics and Portuguese courses in Portugal. According to the results of their study, the HELA is more successful than the simple boosting algorithms.

This study offers a comprehensive analysis that distinguishes itself from other studies by combining classical algorithms, bagging methods, and feature selection. Also, this study demonstrates the contributions of feature selection in the educational dataset to the success of classical and bagging algorithms. In our study, two datasets containing mathematics and Portuguese courses of secondary school students in Portugal, which are frequently used in the literature [8,14,15,20,21,22,23], were studied. Initially, classification was made using all features with eight different algorithms. These algorithms are DL, MLP, SL, ICO, DT, FURIA, One-R, and LMT algorithms. The same classification algorithms were then used along with bagging ensemble learning method. Finally, by using various feature selection algorithms, the most effective features were selected for the datasets used. All

experiments were repeated by using these features. At first, the results were compared according to classification algorithms, ensemble learning methods and feature selection. Then, the results were compared with studies using the same dataset in the literature.

3. METHODS

In this section, the main classification algorithms used will be explained one by one with their general features. Then, the feature selection algorithms used in the experiments will be discussed. Finally, the bagging ensemble learning algorithm will be explained.

3.1. Classification Algorithms

In this section, the classification algorithms used in this study will be explained.

3.1.1. Deep learning

DL is an artificial intelligence and machine learning system that learns by imitating the way humans learn information. It is a data science that makes modeling using statistics and making predictions [24]. Most of the data studied in the DL system is structured and labeled. This is because it requires outputs as well as inputs to train the system [25].

DeepLearning4J library was used in this study. DeepLearning4J is a DL algorithm library used for classification and regression with MLP [26].

3.1.2. Multiplayer perceptron

MLP is an important basis of artificial NN [27]. It is one of the supervised learning algorithms. Both input and output data are given to the system and the model is created with the learning algorithm [28]. In the model, there are hidden layers between the input and output layers. It transmits the data coming from the input layer to the intermediate layers. The number of intermediate layers varies depending on the problem. Data from one layer is transmitted to the next intermediate layer. The number of outputs in the system is the number of objects in the output layer [29]. After training, the learned model is used to test new data.

3.1.3. Simple logistic regression

SL is a statistical method used to predict a binary outcome in a dataset. It is aimed to find a value for the dependent variable by analysing the links between the independent variables in the dataset. A definitive judgment is made with this value [30]. More than one input variable can be used in SL. By comparing the values read from these variables with previous results, the result is produced by calculating the probabilities for new inputs [31].

3.1.4. Iterative classifier optimizer

ICO algorithms use predictions obtained from neighboring nodes for each step [32]. In this algorithm, the errors found after classifying the first record in the dataset are used as feedback and the inputs are changed in this way. In this way, all outputs become improved inputs of the next process. This structure can be described as a brain neural network. The system is trained by repeating the records in the network [33]. This classifier selects the best number of repetitions for an algorithm that performs cross-validation [34].

3.1.5. Decision table

DT is the decision algorithm used for cases with more than one condition. The table contains conditions in rows and columns and actions in the intersection places. It is a rule-logic scheme programmed in a table form. New rules can be added by adding a line or column. One action can be reached with more

than one condition or can be directed with more than one action. According to the actions, the algorithm trained and makes classification [35, 36]. DT is simple and can be easily interpreted. It is easy to improve. Effective derivatives can be created, and the application area is wide to test. Even very complex data can easily turn into a DTrees [37].

3.1.6. Fuzzy unordered rule induction algorithm

FURIA uses fuzzy rule or rule stretching approach. It is used in classifications that contain non-sharp boundaries, that is, if there are different classes between two classes that do not have clear boundaries. It is appropriate to use it for classifications such as good-fair-bad, very good-good- satisfactory -pass-fail in a data set. It is more advantageous than strict classification rules. It works efficiently when there are no sharp boundaries between classes, that is, in classifications with smooth boundaries, which is the basis of fuzzy logic. During classification, the results are converted into sharp boundaries [38]. In this study, FURIA was used in the WEKA program as the FURIA.

3.1.7. One rule

One-R works like a single-stage DTrees. It has a simple working structure. It tries to select the feature that best predicts the target class and infers rules from error data. That is, it takes the best of the discriminative featuress, the one that gives the least erroneous result, and sets rules accordingly [39]. Considering the datasets, it takes the feature that gives the least error in the result classification and creates a rule between the result and the feature. It classifies all records according to this rule. It produces rules such as " Successful if absent less than 10 days " [40]. It can be evaluated as a single-level DTrees.

3.1.8. Logistic model tree

LMT algorithm is an algorithm created by combining DTrees induction and logistic regression algorithms [41]. It is a supervised classification model. This method is based on the tree structure previously found as a model. A piecewise linear regression model is provided from DTrees with constants in their leaves [42]. In the logistics part, a model is created at each node using the logitboost algorithm. The knot is broken using certain methods. The beginning of each stage is based on the result at the parent node. In the final stage, the tree is pruned. Classification is performed according to this tree model.

3.2. Feature Selection Algorithms

The second stage of the experiments was carried out by determining the most effective features. Feature selection was made using the feature selection algorithm in the WEKA program. In this algorithm, the entire set was used for training purposes. Correlation-based feature subset selection, gain ratio attribute evaluation, information gain attribute evaluation, correlation attribute evaluation, relief attribute evaluation, symmetrical unsert attribute evaluation, and One-R attribute evaluation algorihms were used in this study [43]. Best first, ranker and greedy stepwise are search methods for these evaluation algorithms. While some methods work with every algorithm, some of them work with certain algorithms. Feature selection was made by trying all of them to find suitable algorithms. The features found for each algorithm were scored and ranked, and the most effective ones were selected. Different features were found to be efficient for each dataset and classification group, and experiments were repeated with these features.

Although choosing attributes may seem ineffective in some experiments, it affects the completion time of the experiments and shows which attribute is effective for each course [44, 45].

3.3. Bagging Ensemble Learning Method

Bagging algorithm is an ensemble learning method. While operations are performed with a single algorithm in classical machine learning methods, algorithms can be applied together or sequentially in

the bagging method. Bagging is one of the heterogeneous ensemble learning models that combine training data from data separated into training and testing by selecting different parameters in a single algorithm or using different learning algorithms [46]. It combines different algorithms while training the training set with different samples and with this method many results are obtained. The majority of these classification results are taken as output [47].

4. DATASET

In this study, two datasets containing similar data were studied, including mathematics and Portuguese courses of secondary school students in Portugal [8]. The datasets include students' answers to survey questions that meet the criteria which affect their success, their grades, and a success class. The first dataset (Set 1) contains student information, mathematics course grades and success class, and the second dataset (Set 2) contains student information, Portuguese course grades and success class.

Set 1 includes information of a total of 395 students (208 women and 187 men) for the mathematics course and Set 2 includes information of a total of 649 students (383 women and 266 men) for the Portuguese course. There are 33 attributes in the datasets. Further details are presented in [48].

The datasets include information such as family information, student time use, success, or failure in previous years, as well as two exam grades with evaluation scores between 0 and 20 and the final exam grade. The final exam was used to predict student success. In Portugal, class success is determined by the final exam grade.

Table 1. Binary classification system [8]

Country	Pass	Fail
Portugal	10-20	0-9

The binary success criterion based on the exam score was created as shown in Table 1 and the 5-class success criterion based on the exam score was created as shown in Table 2, similar to other studies [8].

Table 2. 5-class classification system [8]

Country	Excellent	Good	Satisfactory	Sufficient	Fail
Portugal	16-20	14-15	12-13	10-11	0-9

5. EXPERIMENTS

In this study, the results were compared using eight different algorithms for mathematics and Portuguese courses datasets, and it was aimed to determine which algorithm would be more efficient in datasets containing such student information and to predict student success levels at the highest rate. The experiments were conducted in the WEKA program, utilizing the 10-fold cross-validation method on the datasets. The computer employed for this purpose featured an i7 processor, 8 GB RAM, and a 64-bit operating system. Version 3.8.6 of the WEKA program was utilized. Classical methods, along with 8 different algorithms as described previously, were applied to both variants of the experimental sets. Additionally, bagging ensemble learning method has also been tried with the same algorithms. The algorithms used in the experiments were applied to these two datasets, and the most efficient features were selected and used again to improve the results. Feature selection was made through the WEKA program and the most effective features were tried to be selected.

5.1. Results of Feature Selection Algorithms

In this study, different feature selection algorithms have been utilized. The obtained results were aggregated to enhance the model's performance and attain a more robust outcome. We can examine the

process of finding common features identified by different feature selection algorithms in four steps. In the first step, feature selection algorithms were applied to the given dataset, and results were obtained. In the second step, the outcomes of the feature selection algorithms were assessed. At this stage, the top 7-8 features with the highest gain from each feature selection algorithm's ranking were recorded. For some datasets, the correlation-based feature subset selection algorithm could only select five features. In the third step, common features obtained from the applied methods were identified. Common features are those consistently chosen under different algorithms, enhancing the model's performance. In the final step, classification algorithms were trained with the common obtained features, and the results were evaluated. The features obtained using the feature determination method employed in this study are listed in Tables 3 and 4 for Mathematics and Portuguese language courses, respectively.

Table 3. Results of Feature Selection Algorithms for Mathematics Dataset

Feature Selection Algorithm	Selected Attributes (binary classification dataset)	Selected Attributes (5 class classification dataset)
Correlation-based feature subset selection	G2, G1, failures, goout, higher, Mjob, guardian	Sex, failure, G1, G2
Gain ratio attribute evaluation	G2, G1, failures, higher, goout, schoolsup, guardian	G2, G1, failure, higher, schoolsup, Mjob, address, Fjob
Information gain attribute evaluation	G2, G1, failures, goout, higher, Mjob, Guardian	G2, G1, failure, Mjob, schoolsup, Fjob, higher
Correlation attribute evaluation	G2, G1, failures, goout, age, higher, Medu, Fedu	G2, G1, failures, medu, goout, age, higher
Relief attribute evaluation	G2, G1, failures, sex, Mjob, paid, schoolsup	G2, G1, Mjob, sex, failures, medu, goout
Symmetrical unsert attribute evaluation	G2, G1, failures, goout, higher, schoolsup, guardian	G2, G1, failures, higher, gout, Mjob, Fjob
One-R	G2, G1, failures, higher, sex, studytime, Fjob, reason	G2, G1, failures, absences, goout, paid, Fjob
Common attributes used in this paper	G2, G1, failures, higher, goout	G2, G1, failures, Mjob, goout

Table 4. Results of Feature Selection Algorithms for Portuguese Course Dataset

Feature Selection Algorithm	Selected Attributes (binary classification)	Selected Attributes (5 class classification)
Correlation-based feature subset selection	G1, G2, failures, higher, school	studytime, failures, schoolsup, paid, activities, internet, G1, G2
Gain ratio attribute evaluation	G1, G2, failures, higher, school, Fedu, studytime	G2, G1, failures, higher, school, medu, schoolsup, studytime
Information gain attribute evaluation	G1, G2, failures, higher, school, Fedu, reason	G2, G1, failures, higher, school, Mjob, Medu, studytime
Correlation attribute evaluation	G1, G2, failures, higher, school, studytime, Fedu	G2, G1, failures, higher, medu, school, studytime, paid
Relief attribute evaluation	School, G1, G2, failures, higher, reason, address, sex	G2, G1, school, higher, sex, failures, medu, paid, studytime
Symmetrical unsert attribute evaluation	G2, G1, failures, higher, school, Fedu, studytime	G2, G1, failures, higher, school, medu, studytime, mjob, reason, fedu, paid
One-R	G2, G1, failure, age, Fjob, guardian, traveltime	G2, G1, Medu, Fedu, traveltime, paid, failures, studytime
Common attributes used in this paper	G1, G2, failures, higher, school	G1, G2, failures, studytime, paid

5.2. Mathematics Dataset Results

In our first test, the mathematics course dataset was used. A binary and 5-class classification was made in the dataset created by subtracting the student's final grade. First, the accuracy rate, precision, sensitivity/recall, and the F-1 value were calculated with the selected classification algorithms using all

the features. Then, the experiments were repeated using the bagging for all algorithms. Later, various feature selection algorithms in the WEKA program were used. The common features in the results of these algorithms were selected. Finally, all experiments were repeated using these selected features. Binary classification experiment results for the mathematics dataset are given in Table 5, and 5-class classification results are given in Table 6.

Table 5. Mathematics Course Dataset Binary Classification Results

Methods	Algorithms	All Features				Selected Features			
		Acc. Rate %	Prec.	Sens.	F-1	Acc. Rate %	Prec.	Sens.	F-1
Classic Methods	DL	87,595	0,899	0,876	0,889	89,114	0,906	0,891	0,893
	MLP	87,342	0,873	0,873	0,873	88,101	0,880	0,881	0,880
	SL	92,152	0,922	0,922	0,922	91,899	0,924	0,919	0,920
	ICO	91,646	0,920	0,916	0,917	91,139	0,914	0,911	0,912
	DT	90,886	0,913	0,909	0,910	91,392	0,919	0,914	0,915
	FURIA	87,848	0,878	0,878	0,878	91,392	0,916	0,914	0,915
	One-R	91,899	0,924	0,919	0,920	91,899	0,924	0,919	0,920
	LMT	**92,658**	**0,927**	**0,927**	**0,927**	91,646	0,921	0,916	0,918
Bagging Methods	DL	86,835	0,897	0,868	0,872	88,101	0,897	0,881	0,884
	MLP	88,354	0,883	0,884	0,883	89,620	0,896	0,896	0,896
	SL	92,152	0,921	0,922	0,921	90,633	0,908	0,906	0,907
	ICO	91,392	0,918	0,914	0,915	91,392	0,918	0,914	0,915
	DT	91,899	0,922	0,919	0,920	91,646	0,921	0,916	0,918
	FURIA	91,899	0,920	0,919	0,919	91,899	0,920	0,919	0,919
	One-R	91,899	0,924	0,919	0,920	91,899	0,924	0,919	0,920
	LMT	91,646	0,916	0,916	0,916	90,127	0,901	0,901	0,901

According to Table 5, binary classification resulted in a high accuracy rate. The main reason for this is that the number of predicted classes is small and the boundary determining success is sharper than the 5-class classification. The best result obtained in this study is the LMT algorithm using classical methods and all features. The fact that there are only two classes to be predicted and the score difference is large is effective in achieving the 92.66% accuracy rate with the LMT. The influence of the features helped to sharply distinguish the branches in the tree structure. The selected attributes mentioned above were effective on these tree branches. Although similar values were obtained in the experimental results, the small number of classes enabled simple classical learning algorithms to be more successful than bagging algorithms.

The most important features in the mathematics dataset for binary classification are selected as follows: G2 (grade 2), G1 (grade 1), failures, mother's occupation, desire to pursue higher education, and going out. When examining the selected features in this experiment, it is evident that academic success indicators such as midterm grades and past failures, along with attributes influencing study habits such as aspirations for higher education and time spent going out, are effective in classification. When examining the experimental results with classical methods, we observed that reducing the number of attributes increased the success of DL, MLP, DT, and FURIA algorithms. However, there was a decrease in the success of SL, ICO, and LMT algorithms. The success of the One-R algorithm remained constant. Considering the bagging method, while DL and MLP gave more successful results with fewer attributes, the success rate with LMT and DT decreased slightly, and the success did not change in other algorithms. The reason for the increase in success in DL and MLP is that when the number of features decreases, the parameters that need to be learned in the model decrease and as a result, learning becomes easier.

Table 6. Mathematics Course Dataset 5-class Classification Results

Methods	Algorithms	All Features				Selected Features			
		Acc. Rate %	Prec.	Sens.	F-1	Acc. Rate %	Prec.	Sens.	F-1
Classic Methods	DL	52,658	0,517	0,527	0,505	53,165	0,513	0,532	0,474
	MLP	53,165	0,523	0,532	0,526	71,392	0,714	0,714	0,714
	SL	71,646	0,716	0,716	0,715	72,658	0,727	0,727	0,725
	ICO	77,975	0,785	0,780	0,777	76,962	0,773	0,770	0,768
	DT	77,722	0,782	0,777	0,775	**78,481**	**0,791**	**0,785**	**0,782**
	FURIA	75,190	0,753	0,752	0,752	77,468	0,778	0,775	0,772
	One-R	**78,481**	**0,791**	**0,785**	**0,782**	**78,481**	**0,791**	**0,785**	**0,782**
	LMT	71,646	0,716	0,716	0,715	71,899	0,721	0,719	0,719
Bagging Methods	DL	50,380	0,772	0,772	0,771	55,443	0,548	0,554	0,503
	MLP	55,696	0,541	0,557	0,547	73,418	0,736	0,734	0,735
	SL	71,899	0,721	0,719	0,718	73,924	0,743	0,739	0,739
	ICO	77,215	0,772	0,772	0,771	76,203	0,764	0,762	0,760
	DT	77,975	0,784	0,780	0,777	78,228	0,788	0,782	0,780
	FURIA	77,215	0,772	0,772	0,772	77,468	0,777	0,775	0,774
	One-R	**78,481**	**0,791**	**0,785**	**0,782**	**78,481**	**0,791**	**0,785**	**0,782**
	LMT	74,177	0,746	0,742	0,741	70,127	0,698	0,701	0,699

As seen in Table 6, the One-R algorithm was the best classifier algorithm with an accuracy rate of 78.481% for this dataset. DT reaches the same rate by selecting attributes using the classical method. With feature selection, the complexity of the model was reduced, and results were achieved faster [44, 45]. The selected features for this experiment are G2, G1, failures, mjob, and goout. One of the most significant factors affecting students' study discipline, the time spent going out, is inversely proportional to success. The prediction speed of the system increased when fewer features were used. Factors affecting coursework and midterm exam grades also affect mathematics course success. Again, the mother's profession is effective in academic success since it affects study habits. When the number of attributes decreased in classical methods, the success of ICO decreased, the success of One-R remained constant, and the success of all other algorithms increased. The increase or decrease in the success of algorithms in feature selection with the bagging method is similar to classical methods. However, the difference lies in the fact that when bagging was applied to the LMT algorithm specifically, there was a decrease in success in feature selection.

In experiments conducted with this dataset, binary classification in two different classification schemes has a higher accuracy rate than 5-class classification because the separation between classes is greater. Making five different class predictions in the same score range (0-20) is more difficult than making two different class predictions. Since the correlations between achievement classes in mathematics are less than in other lectures, the correct class prediction is lower.

Relevant studies using the same dataset and the results of these studies are given in Table 7. The success values of the relevant studies in Tables 7 and 10 have been directly taken from articles implementing the method. Although some studies may use the same algorithms, the way experiments are conducted (percentage split or cross-validation) and parameter adjustments can vary. This has also led to different outcomes in terms of success metrics. As seen in Table 7, two different classification levels were used to predict mathematics course success. In the binary classification, Bozkurt Keser and Aghalarova [20] obtained the best predictions with an accuracy rate of 96.6% with the HELA method. In the 5-class classification, this study has achieved the second-best ranking, with an accuracy rate of 78.5% with the One-R and DT algorithms.

Table 7. Studies Related on Mathematics Course Dataset

Used Dataset	Paper	Motivation	Used Program	Used Algorithms	Results (AC)
Maths, Binary	Özkan et al. [14]	Classify and find the effective attributes	R	C5.0, DL, RT, BoostedC5, LR, SVM, RF	86 % C5.0
Maths, Binary	Başer et al. [15]	Classification	WEKA	ICO, One-R, LogitBoost, YSA,	92.2 % One-R
Maths, Binary	Ünal [21]	Classification	WEKA	NB, RF, DT	93.67 % RF
Maths, Binary	Bozkurt Keser & Aghalarova [20]	Classification	Python	HELA, XGboost, LightGBM, GB,	96,6 % HELA
Maths, Binary	Cortez & Silva[8]	Classification	R	NV, NN, RF, SVM, DT,	78,5 % NV
Maths, Binary	Our study	Classification	WEKA	DL4MLP, MLP, SL, ICO, One-R FURIA, DT	92.7 % LMT
Maths, 5-class	Kızılkaya & Oğuzlar [22]	Between gender and success	-	C4.5, SVM, FFANN, KELM	KELM
Maths, 5-class	Felicia & Ferren [23]	Classification	RapidMiner	GLM, RF, NB	48.6 % NB
Maths, 5-class	Bozkurt Keser & Aghalarova [20]	Classification	Python	HELA, XGboost, LightGBM, GB,	78.2 % HELA
Maths, 5-class	Ünal [21]	Classification	WEKA	NB, RF, DT	79.5 % J48
Maths, 5-class	Our study	Classification	WEKA	DL4MLP, MLP, SL, ICO, One-R FURIA, DT	78,5 % One-R, DT

5.3. Portuguese Course Data Set Results

In this section, binary and 5-class classification was conducted with this dataset containing grades from the Portuguese course. The experiments performed on the mathematics data set were repeated for this data set as well. Since attributes such as student grades are different in this data set, the selected attributes have also changed because of the feature selection. The experimental results for the binary classification are given in Table 8, and the five-class experiment results are given in Table 9.

Table 8. Portegues Lesson Dataset Binary Classification Results

Methods	Algorithms	All Features				Selected Features			
		Acc. Rate %	Prec.	Sens.	F-1	Acc. Rate %	Prec.	Sens.	F-1
Classic Methods	**DL**	90,909	0,910	0,909	0,910	91,834	0,919	0,918	0,919
	MLP	89,676	0,894	0,897	0,895	93,374	0,932	0,934	0,932
	SL	93,220	0,929	0,932	0,929	93,220	0,929	0,932	0,930
	ICO	93,374	0,932	0,934	0,932	92,912	0,927	0,929	0,927
	DT	92,604	0,923	0,926	0,922	93,220	0,930	0,932	0,928
	FURIA	93,220	0,929	0,932	0,929	92,296	0,919	0,923	0,919
	One-R	**93,683**	**0,935**	**0,937**	**0,933**	**93,683**	**0,935**	**0,937**	**0,933**
	LMT	**93,683**	**0,935**	**0,937**	**0,933**	93,220	0,929	0,932	0,930
Bagging Methods	**DL**	91,063	0,909	0,911	0,910	92,142	0,920	0,921	0,921
	MLP	91,063	0,905	0,911	0,906	92,912	0,927	0,929	0,927
	SL	92,296	0,920	0,923	0,921	93,529	0,933	0,935	0,933
	ICO	**93,683**	**0,935**	**0,937**	**0,935**	93,374	0,932	0,934	0,933
	DT	93,220	0,930	0,932	0,928	92,604	0,922	0,926	0,922
	FURIA	93,220	0,930	0,932	0,930	93,220	0,930	0,932	0,931
	One-R	**93,683**	**0,935**	**0,937**	**0,933**	**93,683**	**0,935**	**0,937**	**0,933**
	LMT	92,758	0,925	0,928	0,926	92,296	0,920	0,923	0,921

In the binary classification, predictions made for the Portuguese course and the accuracy rates of the algorithm results were found to be close to each other and at high values. The students' success in the Portuguese course is related to environmental factors. In this experiment, the selected features are G1 (grade 1), G2 (grade 2), failures, higher education (higher), and school. Upon examination of these attributes, it is observed that the factors influencing Portuguese course grades generally include a student's past academic performance and their future aspirations. The selection of the school feature is related to the social structure of schools, whether they are in rural or urban areas, the family structures of students attending the school, and the academic performance levels of students, all of which contribute to the formation of school culture. School culture, in turn, influences students' everyday language usage and even the language of instruction, thereby indirectly affecting the success of language courses. When feature selection is applied to the dataset, it is observed that the success of DL, MLP, and DT algorithms increases, while the success of SL and One-R algorithms remains the same, and the success of ICO, LMT, and FURIA decreases for classical algorithms. When the effect of feature selection is examined in the bagging method, it is observed that for DL, MLP, and SL algorithms, the success has increased, remained the same for FURIA and One-R, and decreased for ICO, DT, and LMT.

In 5-class classification, higher success was achieved compared to the mathematics course data set. In this dataset, the One-R algorithm gave the highest result. In the classical and bagging methods, the single rule algorithm reached the highest accuracy rate of 76.733% with both all attributes and selected attributes. When we look at the result of the feature selection algorithm for the Portuguese course dataset, the student's study time and taking private lessons, their grades, and past failures, which are also effective in other experiments, are effective attributes.

Table 9. Portegues Lesson Data Set 5-Class Classification Results

Methods	Algorithms	All Features				Selected Features			
		Acc. Rate %	Prec.	Sens.	F-1	Acc. Rate %	Prec.	Sens.	F-1
Classic Methods	DL	52,851	0,528	0,529	0,526	60,247	0,580	0,602	0,577
	MLP	57,165	0,573	0,572	0,572	73,190	0,731	0,732	0,729
	SL	71,341	0,715	0,713	0,713	72,265	0,724	0,723	0,720
	ICO	74,114	0,740	0,741	0,733	75,655	0,758	0,757	0,752
	DT	74,114	0,740	0,741	0,733	76,425	0,777	0,764	0,760
	FURIA	71,341	0,711	0,713	0,708	74,422	0,745	0,744	0,737
	One-R	**76,733**	**0,782**	**0,767**	**0,764**	**76,733**	**0,782**	**0,767**	**0,764**
	LMT	71,649	0,718	0,716	0,716	72,265	0,724	0,723	0,720
Bagging Methods	DL	52,697	0,525	0,527	0,522	60,555	0,593	0,606	0,584
	MLP	58,089	0,579	0,581	0,578	72,727	0,730	0,727	0,725
	SL	72,111	0,722	0,721	0,720	72,265	0,723	0,723	0,721
	ICO	75,963	0,760	0,760	0,756	74,576	0,745	0,746	0,741
	DT	76,425	0,776	0,764	0,760	76,425	0,777	0,764	0,760
	FURIA	71,341	0,715	0,713	0,710	75,193	0,760	0,752	0,748
	One-R	**76,733**	**0,782**	**0,767**	**0,764**	**76,733**	**0,782**	**0,767**	**0,764**
	LMT	71,957	0,720	0,720	0,719	68,875	0,689	0,689	0,688

In binary classification, while socio-cultural environment-related attributes are effective in similar experiments, in this experiment, attributes indicating the student's study habits have proven to be effective in determining achievement levels. In classical methods, while the success remains the same for the One-R algorithm in feature selection, the success has increased with fewer attributes for all other methods. However, in the bagging method, feature selection has resulted in a decrease for ICO and LMT, remained the same for DT and One-R, and increased for all other methods.

Studies on the Portuguese and their comparative results are shown in Table 10. As seen in Table 10, although the results are close to each other in experiments conducted with different algorithms and different programs, the results vary in binary and 5-class classification. According to the experiment results, two different classification levels have been used to predict success in Portuguese course. In the 5-class classification, Bozkurt Keser and Aghalarova [20] achieved the highest accuracy of 78.5% using

the HELA method, while in the 5- class classification, this study obtained the best predictions with a 93.7% accuracy rate using the One-R, ICO, and LMT algorithms.

Table 10. Studies Related on Portegues Course Data Set

Used Dataset	Paper	Motivation	Used Program	Used Algorithms	Results (AC)
Portugues, Binary	Ünal [21]	Classification	WEKA	NB, RF, DT	93.2 % RF
Portugues, Binary	Bozkurt Keser & Aghalarova [20]	Classification	Python	HELA, XGboost, LightGBM, GB	91,3 % HELA
Portugues, Binary	Cortez & Silva [8]	Classification	R	NV, NN, RF, SVM, DT	93,0 % DT
Portugues, Binary	This study	Classification	WEKA	DL4MLP, MLP, SL, ICO, One-R FURIA, DT	93.7 % One-R, ICO, LMT
Portugues, 5-class	Ünal [21]	Classification	WEKA	NB, RF, DT	77.2 % RF
Portugues, 5-class	Bozkurt Keser & Aghalarova [20]	Classification	Python	HELA, XGboost, LightGBM, GB,	78.5% HELA
Portugues, 5-class	Cortez & Silva [8]	Classification	R	NV, NN, RF, SVM, DT,	76,1 % DT
Portugues, 5-class	This study	Classification	WEKA	DL4MLP, MLP, SL, ICO, One-R FURIA, DT	76.5 % One-R

6. CONCLUSION

In this study, it was aimed to predict the student's mathematics and Portuguese language achievement in binary and 5-class classification, and experiments were carried out for this purpose. When we look at the results in general, predicting the binary classification is more successful than the 5-class classification. As the number of classes decreases, the prediction rate increases. Students' information in the datasets is more effective in determining pass-fail situations. It is more difficult to process student data and identify classes with very little difference in scores between good and very good.

The content of the courses varies in terms of making predictions. Since the effective attributes for the mathematics course and the Portuguese course are different, the successful algorithms and the accuracy rates they find are also different. The reason for this is that the factors affecting the Portuguese course are the social environment, living space and cultural environment of the student, while for the mathematics course, more academic factors such as the socio-economic level of the family, the professions of the family members, the student's desire and preparation for higher education are effective. A student's success is based on success in previous years and family factors. The reason for this depends on the continuity of student success, the stability of success levels throughout the semester, and their educational perspectives and study habits come from the social environment they live in. Considering all these situations, student success depends on many criteria of families.

In this study, by comparing experiments conducted with different algorithms and determining effective attributes, it is aimed to predict student success with the highest accuracy and take the necessary precautions in advance, as well as to be able to make the necessary guidance by obtaining information about the criteria that affect student success.

CONFLICT OF INTEREST

The authors stated that there are no conflicts of interest regarding the publication of this article.

CRediT AUTHOR STATEMENT

Derya Çınar: Writing – Original Draft, Software, Conceptualization, Investigation, Validation, Formal analysis. **Sevcan Yılmaz Gündüz:** Supervision, Writing – Review & Editing, Conceptualization, Methodology.

REFERENCES

[1]   Rao K, Rao M, Ramesh B. Predicting learning behavior of students using classification techniques. International Journal of Computer Applications, 2016; 139(7).

[2]   Al-Radaideh QA, Al-Shawakfa E, Al-Najjar M. Mining student data using decision trees. In: International Arab Conference on Information Technology; January 2006; Yarmouk University, Jordan.

[3]   Şama E, Tarım K. Teachers' attitudes and behaviors towards students perceived as unsuccessful. Türk Eğitim Bilimleri Dergisi, Kış 2007; 5(1):135-154.

[4]   Sezer Ö. Some demographic characteristics of the repeating students and the opinions of the students and the teachers about repetition. (article in Turkish, summary in English). İnönü Üniversitesi Eğitim Fakültesi Dergisi, Güz 2007; 8(14): 31–48.

[5]   Yadav SK, Pal S. Data Mining: A prediction for performance improvement of engineering students using classification. World of Computer Science and Information Technology Journal, 2012; 2(2): 51-56.

[6]   Gadhavi M, Patel D. Student final grade prediction based on linear regression. Indian Journal of Computer Science and Engineering, 2017; 8(3): 274-279.

[7]   Erdoğan Z, Namlı Ö, Akarsu C. Öğrenci başarısının bileşik makine öğrenme teknikleri kullanılarak tahmini. In: International Symposium on Industry 4.0 and Applications, October 2017; Karabük, Turkey. pp.150-155.

[8]   Cortez P, Silva A. Using data mining to predict secondary school student performance. In: 5th Annual Future Business Technology Conference; 2008; Porto: pp. 5-12.

[9]   Vijayalakshmi V, Venkatachalapathy K. Comparison of predicting student's performance using machine learning algorithms. Intelligent Systems and Applications, 2019; 11(12): 34-45.

[10] Tosunoğlu E, Yılmaz, R, Özeren E, Sağlam Z. Machine learning in education: a study on current trends in researchs. (article in Turkish, summary in English). Journal of Ahmet Keleşoğlu Education Faculty, 2021; 3(2): 178-199.

[11] Güvenç E, Sakal M, Çetin G, Özkaraca O. Classification of students' course qualifications using machine learning techniques (article in Turkish, summary in English). Düzce Üniversitesi Bilim ve Teknoloji Dergisi 2022; 10(3): 1359-1371.

[12] Salameh Shreem S, Turabieh H, Al Azwar S, Baothman F. Enhanced binary genetic algorithm as a feature selection to predict student performance. Soft Computing, 2022; 26(1):1-13.

[13] Quy TL, Nguyen TH, Friege G, Ntoutsi E. Evaluation of group fairness measures in student performance prediction problems. Communications in Computer and Information Science, January 2023.

[14] Özkan Y, Önay Koçoğlu F, Selçukcan Erol Ç. Prediction of student performance by deep learning algorithm (article in Turkish, summary in English). In: 7th International Conference on Innovations in Learning for the Future, 2018; İstanbul University, İstanbul pp.136-145.

[15] Başer SH, Hökelekli O, Adem K. Predicting the performance of students studying in secondary education using data mining methods (article in Turkish, summary in English). Bilgisayar Bilimleri ve Teknolojileri Dergisi, 2020; 1(1): 22-27.

[16] Çınar D, Yılmaz Gündüz S. Prediction of secondary school students' mathematics success with machine learning. In:13th International Istanbul Scientific Research Congress on Life, Engineering, and Applied Sciences, Nisan 2023. İstanbul:pp.94-104

[17] Yavuzarslan M, Erol Ç. Using learning management system logs to predict undergraduate students' scademic performance. Bilişim Teknolojileri Dergisi 2022; 15(2): 199-207.

[18] Kayalı S, Buyrukoğlu S. Classification of academic performance of students with the implementation of machine learning algorithms (article in Turkish, summary in English). In: 2nd International Conference on Educational Technology and Online Learning; Ağustos 2022. Balıkesir, pp.330-336

[19] Bentaleb A, Abouchabaka J. Ensemble learning for mining educational data. Journal of Theoretical and Applied Information Technology 2022: 100(9): 2715-2722.

[20] Bozkurt Keser S,Aghalarova S. HELA: A novel hybrid ensemble learning algorithm for predicting academic performance of students. Education and Information Technologies 2022; 27: 4521–4552.

[21] Ünal F. Data mining for student performance prediction in education.In: Derya Birant,editor. Data Mining-Methods, Applications and Systems. e-book. 2020; pp. 423-432.

[22] Kızılkaya Y M, Oğuzlar A. Comparison of some supervised learning algorithms r programming language (article in Turkish, summary in English). Karadeniz Uluslararası Bilimsel Dergi, 2018; 37: 90-98.

[23] Felicia, Ferren. Exploring secondary school performance by using machine learning algorithms. Journal of Educational Analytics, 2022; 1(1): 41-60.

[24] Krizhevsky A, Sutskever I, Hinton EG. ImageNet classification with deep convolutional neural networks. In: F. Pereira and C.J. Burges and L. Bottou and K.Q. Weinberger,editors. Advances in Neural Information Processing Systems. 2012. pp. 1090–1098.

[25]   LeCun Y, Bengio Y, Hinton G. Deep learning. Nature 2015; 521:436-444

[26]   Raiko T, Valpola H, Lecun, Y. Deep learning made easier by linear transformations in perceptrons. In: Fifteenth International Conference on Artificial Intelligence and Statistics 2012; 22:924-932.

[27]   MW Gardner, SR Dorling. Artificial neural networks (the multilayer perceptron)—a review of applications in the atmospheric sciences. Atmospheric Environment 1998; 32: 2627-2636

[28]   EB Baum, On the capabilities of multilayer perceptrons. Journal of Complexity 1988; 4: 193-215

[29]   Bayır F. Artificial neural networks and application on forecasting. MSc İstanbul University, İstanbul, Turkey, 2006.

[30]   Diaz-Quijano FA. A simple method for estimating relative risk using logistic regression. BMC Medical Research Methodology 2012; 12: 1-6.

[31]   Hsieh FY, Bloch DA, Larsen MD. A simple method of sample size calculation for linear and logistic regression. Statistics in Medicine 1998;17(14):1623-1634.

[32]   Manikandan G, Vasudev A, Balasubramanian A. A survey to identify an efficient classification algorithm for heart disease prediction. International Journal of Pure and Applied Mathematics 2018; 119(12): 13337-13345.

[33]   Fan S, Huang B. Training iterative collective classifiers with back-propagation In: 12th International Workshop on Mining and Learning with Graphs, San Francisco, USA.

[34]   Vural T. Microwave brain mass lesion diagnosis by using data mining. MSc, Yıldız Technical University, İstanbul, Turkey, 2017.

[35]   Vanthienen J. A more general comparison of the decision table and tree: a response. DTEW Research Report 9224, 1992.

[36]   Kohavi R. The power of decision tables. In: Machine Learning: European Conference on Machine Learning;2005; 912; Springer, Berlin, Heidelberg: pp.174–189.

[37] Huysmans J. Dejaeger K. Mues C. Vanthienen J. Baesens B. An empirical evaluation of the comprehensibility of decision table, tree and rule based predictive models, Decision Support Systems; 2011;(51)1: 141-154.

[38]   Hühn J, Hüllermeier E. FURIA: an algorithm for unordered fuzzy rule induction. Data Min Knowl Disc 2009; 19: 293–319.

[39]   Olaru C. Wehenkel L. A complete fuzzy decision tree technique, Fuzzy Sets and Systems, 2003; 138(1): 221-254

[40]   Al-diabat M. Arabic text categorization using classification rule mining. Applied Mathematical Sciences 2012; 6(81): 4033-4046.

[41]   Karadağ M. Comparison of performances of decision trees and logistic regression analysis by a simulation study. MSc, Trakya University, Edirne, Turkey, 2014.

[42]   Landwehr N. Logistic model trees. University of Freiburg, Freiburg, Germany, 2003.

[43]   Witten IH., et al. Practical machine learning tools and techniques. In: Data mining. Amsterdam, The Netherlands: Elsevier, 2005. p. 403-413.

[44]   Guyon I, Elisseeff A. An introduction to variable and feature selection. Journal of Machine Learning Research, 2003; 3: 1157-1182.

[45]   Dash M, Liu H. Feature selection for classification. Intelligent Data Analysis, 1997; 1: 131-156.

[46]   Wang Z, Wang Y, Srinivasan R. A novel ensemble learning approach to support building energy use prediction. Energy and Buildings 2018; 159:109-122.

[47]   Onan A. A clustering based classifier ensemble approach to corporate bankruptcy prediction (article in Turkish, summary in English). Alphanumeric journal; 2018; 6(2); 365 – 376.

[48]   Çınar D. Prediction of secondary school students' success with machine learning. MSc, Eskisehir Technical University, Eskisehir, Turkey, 2023.

RESEARCH ARTICLE

PERFORMANCE COMPARISON OF ECC LIBRARIES FOR IOT DEVICES

İsmet Kaan ÇEKİŞ [1] , Armağan TOROS [2] , Nimet APAYDIN [3] , İlker ÖZÇELİK [4],*

[1] Department of Computer Engineering, Faculty of Engineering and Architecture, Eskişehir Osmangazi University, Eskişehir, Türkiye
cekiskaan@gmail.com - 0009-0001-9709-0465

[2] Department of Computer Engineering, Faculty of Engineering and Architecture, Eskişehir Osmangazi University, Eskişehir, Türkiye
armagantoros7@gmail.com - 0009-0008-8950-7559

[3] Department of Computer Engineering, Graduate School of Natural and Applied Sciences, Eskişehir Osmangazi University, Eskişehir, Türkiye
nimetapaydin02@gmail.com - 0009-0002-2110-3255

[4] Department of Software Engineering, Faculty of Engineering and Architecture, Eskişehir Osmangazi University, Eskişehir, Türkiye
ilker.ozcelik@ogu.edu.tr - 0000-0002-2032-1640

Abstract

As the prevalence of IoT devices increases, the need for strengthening security becomes inevitable. Lightweight encryption solutions play a pivotal role, particularly in addressing security concerns associated with IoT authentication and privacy. This study concentrates on the performance evaluation of open-source and lightweight encryption libraries. Various open-source encryption libraries underwent testing on a Raspberry Pi, revealing noteworthy variations in key generation, signing, verification times, and memory usage. This research provides comprehensive assistance for the selection of encryption libraries for IoT applications. Consideration extends beyond library performance, encompassing factors such as user base and documentation quality, to deliver optimal security solutions.

1. INTRODUCTION

The Internet of Things (IoT) is experiencing an explosive rise in popularity. Now with IoT devices all over the world, it is evident that this technology is rapidly transforming our lifestyle, work, and interactions with the world around us. From smart homes to industrial systems, the IoT is playing an increasingly critical role in shaping our future. As the use of IoT devices grows significantly, the importance of ensuring their security has increased. Currently, IoT devices are susceptible to vulnerabilities due to limited hardware capabilities, such as processing power and memory. These limitations prevent the use of complex security functions on these devices. Therefore, insufficient authentication and confidentiality are prominent security problems for the IoT domain. Cryptography can be used to address these issues.

Cryptosystems can be put into two broad categories: symmetric and asymmetric. Symmetric encryption uses the same key to encrypt and decrypt data. In this approach encryption and decryption can be done quickly. However, the key must be shared with the relevant parties that need to encrypt/decrypt data. Key distribution is usually a challenging task that can lead to critical security issues like intercepted or stolen keys especially on untrusted networks. Asymmetric encryption uses two different keys called public and private keypairs. The public key is made available to anyone who wants to send encrypted data to the key owner, but only the recipient has the private key to decrypt messages. This feature addresses the key distribution problem of symmetric cryptosystems, but it also works slower than symmetric encryption Moreover, the use of currently reliable and widely used asymmetric encryption methods such as River-Shamir-Adleman (RSA) on IoT devices is not always feasible because of the hardware limitations. Elliptic Curve Cryptography (ECC) has become a promising alternative because it requires less resources [1]. It uses a smaller key size compared to other asymmetric cryptographic methods like RSA and can be used on devices with limited resources and is considered more efficient. ECC is used in a variety of applications, including secure communications [2], data encryption [3], digital signatures [4], and blockchain technology [5].

It is both safer and recommended for application developers to use well-established cryptographic libraries rather than implementing cryptographic functions by themselves. There are many open-source cryptographic libraries available online that are reviewed and used in many projects by researchers. Most of the well-known crypto algorithms were implemented in these libraries. However, it is not always an easy task to decide which one of these libraries is best for the intended application. In this paper we address this problem and present results of a heuristic study that can help choose the right crypto library for resource constrained systems.

In ECC, both different key sizes and their implementation can affect the performance of key generation signing and signature verification. Therefore, choosing an ECC library that provides a variety of key sizes, and the best performance is crucial for IoT based implementations. We found several ECC libraries that are open source and suitable for IoT implementations, including BearSSL, libecc, Mbed-TLS, OpenSSL, MIRACL and RELIC. BearSSL, a C-based SSL/TLS implementation, targets small embedded systems and specialized contexts like bootstrap code; it prioritizes efficiency by avoiding dynamic allocation. It supports elliptic curves such as SECP256R1, SECP384R1, SECP521R1, and Curve25519 for ECDHE key exchange but lacks TLS 1.3 compatibility. OpenSSL is a cryptographic toolkit designed primarily for flexible applications in common computing environments, offering compatibility with a range of platforms such as web, Windows, Solaris, Linux, Android and OSX. The toolkit includes three core components: the libcrypto library, the libssl library and a command-line utility for performing cryptographic tasks. It enables TLS 1.3 support, key parameter generation, CSR and CRL creation as well as protocol support including SSL/TLS/DTLS/QUIC, and the handling of S/MIME signed or encrypted mail. MbedTLS is crafted to seamlessly integrate with diverse environments, spanning from embedded systems such as ARM-based platforms to personal computers, smartphones, and even gaming consoles. The range of features it offers includes handling X.509 certificates, supporting SSL/TLS and DTLS protocols. MIRACL (Multiprecision Integer and Rational Arithmetic Cryptographic Library) stands out by extending capabilities beyond traditional environments, catering to highly constrained platforms like embedded systems, mobile applications, and SCADA. It supports ECC, RSA and symmetric encryption. MIRACL's multifunctionality extends to programming languages including C/C++, Go, Rust, Python, Java, JavaScript and Swift. Libecc is a C++ elliptic curve cryptography library created for maximum speed and efficiency without heap allocation and relies solely on constant global variables. It supports various signature algorithms outlined in the ISO 14888-3:2018 standard, along with other signature algorithms and ECDH primitives. RELIC is a modern research-oriented cryptographic meta-toolkit with emphasis on efficiency and flexibility. RELIC can be used to build efficient and usable cryptographic toolkits tailored for resource-constrained environments like embedded systems. Like MIRACL, RELIC also provides various symmetric and asymmetric encryption, digital signature, and hashing techniques.

These libraries allow developers to customize them to meet the specific needs of their applications. Also, they are suitable for use in resource constrained IoT devices that need to process data in real time. In this paper, we performed a comparative analysis of five ECC libraries written in C/C++. We evaluated their performance under different key lengths. Our analysis includes benchmarking each library based on its execution time for key generation signing and verification.

The rest of the paper is organized as follows. Section II examines the fundamental aspects of ECC and gives necessary background information. Section III reviews previously published articles on the subject matter. Section IV overviews the performance metrics used in this study. The results are presented in Section V and finally the paper concludes with a discussion of the findings in Section VI.

2. ECC OVERVIEW

Public Key cryptographic systems are designed using public key schemes which contain a pair of public and private keys for each user. In contrast to the public key, which is accessible to all users, the private key is unique to each user and is kept confidential. The private key remains unpredictable, even with knowledge of the public key. The security of Public Key cryptographic systems relies on the difficulty of the mathematical approach used. In the literature, there are three well-known algorithms which use three different difficult problems to implement three different approaches. These algorithms are based on the factorization of integers, the discrete logarithm problem, and the elliptic curve discrete logarithm problem. Cryptosystems designed using these algorithms include examples such as RSA, ElGamal, and ECC. RSA uses the integer factorization algorithm based on the problem of finding the prime factors of a specially selected positive integer. ElGamal public-key encryption relies on the discrete logarithm problem in a finite field, and ECC is based on the difficulty of the elliptic curve discrete logarithm problem (ECDLP) [6].

Elliptic curve cryptography was introduced by Neal Koblitz and Victor Miller in 1985. It comprises a set of points defined on an elliptic curve generated over a finite field, with a prime field size [7]. Users have the flexibility to select different elliptic curves, even when they operate within the same finite field. The field parameters employed in the design of the elliptic curve play a pivotal role in determining the key size. In comparison to alternative algorithms, the chosen parameters enable a more compact key size [8].

In general, the equation form of the elliptic curve is as follows:

$$y^2 = x^3 + ax + b$$

The set of points (x, y) in the equation represents the elliptic curve. 'a' and 'b' are constant numbers. The given equation is the simplified form of the Weierstrass equation.

ECC provides low resource consumption, small parameters, and small key size compared to other algorithms for the same security levels. Therefore, it is preferred in various areas such as authentication systems in resource-limited devices, data sharing systems, and blockchain.

3. RELATED WORK

The popularity of elliptic curve cryptography has increased in secure IoT systems because it requires less power and memory. Many researchers have studied the implementation performance of this cryptosystem.

Hannes and Manuel [9] compared the performance of Symmetric, DH/DSA/RSA and ECC. They also explored the time required for sign and verify operations on various ARM-based devices using different ECC curves. They underscored the computational requirements of ECC, emphasizing that acceptable delays rely on the specific requirements of the application. The performance results provided in the paper are contingent on factors such as enabled optimizations, key sizes, curve type and CPU speed, showcasing the importance of selecting an appropriate microprocessor based on the expected usage environment. In a study conducted by Mahto and Yadav ECC was compared [10] with three RSA variants (Basic, Chinese Remainder Theorem (CRT), Multi-prime). The authors used NIST recommendations as key sizes and compared average encryption and decryption times. The authors concluded that ECC outperforms RSA and its variants in terms of operational efficiency and security with lesser parameters. The performance of RSA and ECC cryptosystems on wireless sensor networks (WSN) was compared by Zagrouba et. al. [11]. This study evaluated energy consumption and observed the time to encrypt and decrypt messages in different key sizes (8, 64 ,256 bits). The results showed that RSA encryption times are better than ECC. However, ECC gives better performance in key size, energy consumption and decryption time.

In a study done by Gupta et. al. [12] elliptic curve cryptography was utilized to improve SSL protocol performance. They tested RSA-based and ECC-based handshakes with and without client authentication. Additionally, they compared encryption, decryption, digital signature, and verification times. These authors observed performance improvements for both workstations and hand-held devices when using ECC-based cryptosystems. They concluded that ECC offers significant performance benefits to SSL clients and servers. Koppl et al. [13] measured and compared the time intervals for the sign, verify, and key generation operations of ECDH and ECDSA algorithms for different ECC curves (NIST and BRAINPOOL). They used the OpenSSL tool on the Ubuntu operating system to measure the time it took for each process. At first, they assumed that NIST curves provided more security than BRAINPOOL curves, but then they concluded that it is not necessary to prioritize the NIST curves over other curves by considering their test results.

Pigatto et. al. [14] compared the time performance of MIRACL and RELIC libraries using two curves (having key size of 160 and 256 bits) and different message sizes (50 and 100 kb). They performed their tests on a system with a Pentium Dual-Core CPU and Ubuntu Linux installed. The experiment results showed that using a 256-bit key size to encrypt and decrypt the same message took an average of 20.9 and 10.6 seconds for the MIRACL and RELIC libraries, respectively. The authors concluded that RELIC outperformed MIRACL on average response time. In another study, Popa et. al. [15] compared modern ECC libraries (MIRACL, RELIC) and WolfCrypt. The authors performed their tests on an ARM based 32-bit microprocessor (Infineon TC297) used in the automotive industry. Also, they compared the implementation performance of ECDH, BLS, ECDSA protocols on three libraries using different curves and hash functions. The results showed that TC297 could handle ECC-based cryptosystems and the RELIC library was the fastest and provided the most configuration possibilities.

The Di Matteo et al. [16] study introduces a noteworthy advancement in the field of elliptic curve cryptography (ECC) for real-time Internet of Things (IoT) applications, focusing on the development of a secure ECC crypto processor. This work emphasized the importance of hardware acceleration in enhancing the performance and energy efficiency of ECC in IoT devices. The study has been performed both on 45 nm Silvaco and 7 nm Artisan TSMC technologies and verified on a Xilinx ZCU106 board. By supporting key ECC schemes on NIST P-256/-521 (SECP256R1/SECP521R1) elliptic curves, the research highlights the processor's capability to provide high-speed cryptographic operations with robust security through smaller key sizes. This contribution is pivotal in demonstrating the vital role of hardware accelerators for secure and scalable IoT systems, offering a complementary perspective to the software-centric discussions in the existing literature. The study conducted by Aikins-Bekoe and Hayfron-Acquah [17] delves into the efficacy of Elliptic Curve Diffie-Hellman (ECDH) for securing

Wireless Sensor Networks (WSNs), comparing it against traditional algorithms such RSA. The tests were performed by using PyCryptodome and eciespy python libraries. Their findings highlight ECC's advantage of requiring smaller key sizes for equivalent security, which is crucial for the resource-constrained environments typical of WSNs. This research underscores ECC's superiority in computational efficiency and operational speed, making it an ideal cryptographic solution for WSNs. This comparison demonstrates the practical benefits of ECC in a specific application area.

These articles concentrated on various curves within the same cryptographic library or compared two ECC libraries for a specific purpose. Our study involved evaluating the performance of six different ECC libraries, BearSSL, libecc, MbedTLS, OpenSSL, RELIC and MIRACL. We conducted our tests on Raspberry Pi. We provide commentary on the strengths and weaknesses of each library, discussing the best-suited libraries for various use case scenarios.

4. PERFORMANCE EVALUATION

In this research, our emphasis was on exploring open-source libraries for Elliptic Curve Cryptography, with a detailed examination of three key metrics: key-pair generation time, sign time, and verification time. For our analysis, we chose three curves across these libraries, namely SECP256R1(NIST P-256), SECP384R1(NIST P-384), and SECP521R1(NIST P-521). Every curve starts with "SEC" to represent "Standards for Efficient Cryptography," followed by a "P" indicating parameters over a prime field (F_p), and then a number "x" signifying the bit length of the field size P, which also determines our key sizes. Following this, there is an "R" followed by a sequence of numbers "n" indicating that this curve is the nth recommended curve with an x-bit field size in the Standards for Efficient Cryptography Group (SECG) standards.

Our tests were performed on the Raspberry Pi 4 model B with 8GB RAM. The key generation, sign, and verify operations were repeated for 200 000 iterations to assess their efficiency. The obtained results revealed noteworthy variations in the speed of these operations across different libraries.

Key-Pair Generation:

The key-pair generation time, which represents the duration to create both a private key and its corresponding public key, is a critical factor influencing the efficiency of cryptographic systems. The efficiency of this key generation impacts the performance of cryptographic systems.

Signing and Signature Verification:

The sign and verify times provide insights into the duration required for both signing a message and subsequently verifying its signature. Digital signatures play a crucial role in guaranteeing the authenticity and integrity of data. In our assessments, these execution times serve as fundamental metrics, gauging the efficiency of ECC libraries in generating digital signatures (sign) or verifying signatures (verify). A reduced execution time signifies quicker cryptographic operations, a highly desirable trait for applications requiring real-time or low-latency performance.

5. RESULTS

In our evaluations, we measured the key generation, signing, and verification times of selected libraries across various key lengths. The average processing time for each function across different key lengths for each library is presented in Table 1. Furthermore, the performance of individual libraries for key generation, signing, and verification across different key lengths is illustrated in Figures 1, 2, and 3, respectively.

Table 1. Mean Time Performance (in milliseconds) Across Three Key Length.

Operation	MIRACL	BearSSL	Libecc	MbedTLS	OpenSSL	RELIC
Key Gen.	7.51	5.69	41.76	1.39	4.01	1.37
Sign	2.76	20.54	22.76	1.48	4.21	1.54
Verify	3.25	37.43	43.53	5.75	3.30	5.16

Key generation is a crucial aspect of cryptographic operations. While MbedTLS and RELIC stands out for its remarkably fast key generation, even with shorter key lengths, BearSSL, OpenSSL, and MIRACL exhibit comparable average performance. In contrast, Libecc demonstrates a relatively higher key generation time (see Figure 1).
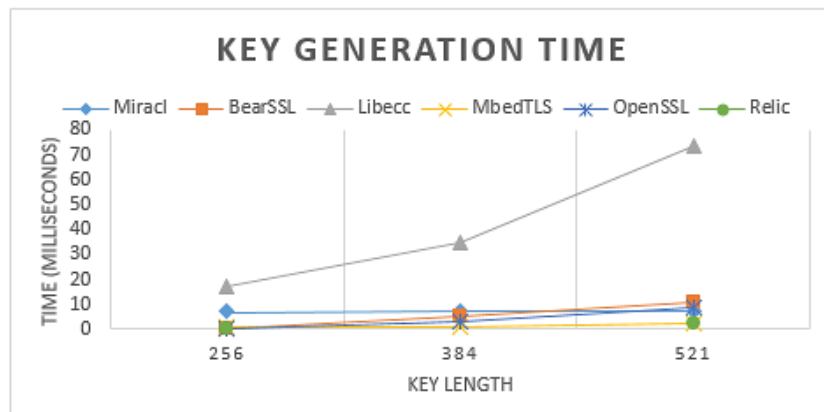
Figure 1. Key generation times (in milliseconds) of different libraries

When it comes to signing, MbedTLS and RELIC distinguish themselves yet again by delivering the fastest execution times among the listed libraries, especially with short key lengths. OpenSSL and MIRACL consistently demonstrate superior performance on average, as illustrated in Figure 2. Conversely, BearSSL and Libecc show slower signing speeds compared to their counterparts. Notably, as the key length increases, BearSSL and Libecc experience a significant decrease in performance.
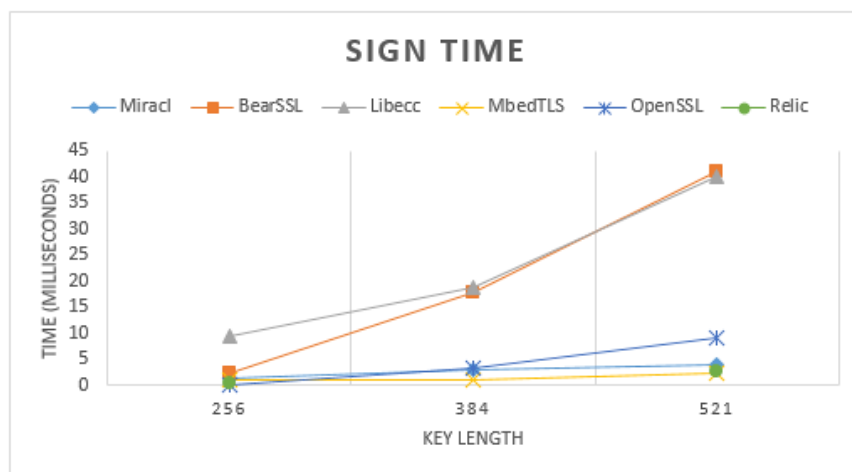
Figure 2. Signing times (in milliseconds) of different libraries

In the process of verification, MIRACL and OpenSSL libraries take the lead. While OpenSSL delivers the quickest results for short key lengths, it lags behind MIRACL on the average. MbedTLS and RELIC

follow behind, as illustrated in Figure 3. Conversely, BearSSL and Libecc highlight slower verification times across the range of libraries.
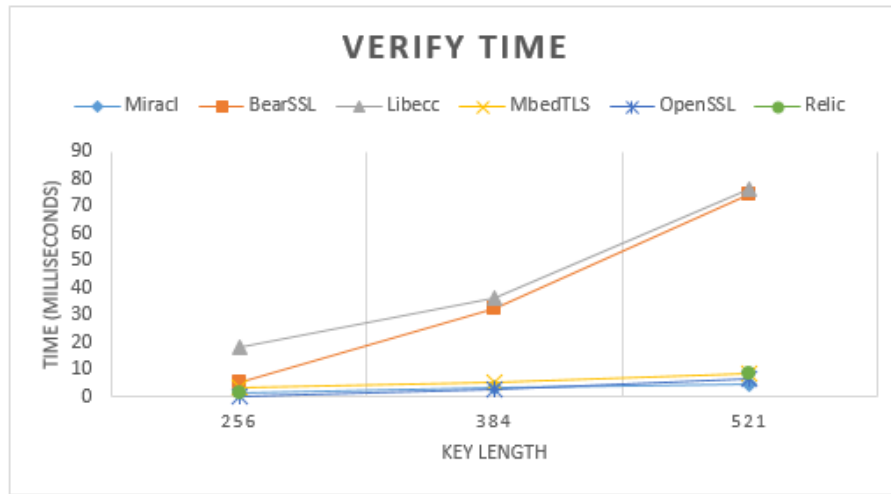
Figure 3. Verification times (in milliseconds) of different libraries.

Efficient memory utilization is a critical factor in cryptographic operations, particularly within resource-constrained environments. Table 2 presents the average memory consumption of libraries for various operations, while Figures 4, 5, and 6 illustrate the variations in memory consumption for key generation, signing, and verification across different key lengths.

Table 2. Memory Utilization Averages (in Bytes) for Three Different Key Lengths

Operation	MIRACL	BearSSL	Libecc	MbedTLS	OpenSSL	RELIC
Key Gen.	74837	74457	79889	109432	624404	75036
Sign	76885	76505	79889	131001	717221	75036
Verify	76885	76505	79889	198556	724491	75036

Upon a comprehensive analysis of memory usage across different curves, it became evident that MIRACL, RELIC, Libecc and BearSSL exhibit consistent behaviour regardless of the operation and key length, displaying efficient memory utilization within the range of 74837 to 79889 bytes. MbedTLS exhibits a significant increase in memory use, reaching up to 241,956 bytes depending on the operation. Additionally, the memory requirements of MbedTLS increase with key size, unlike other libraries. OpenSSL, while excelling in performance metrics, tends to consume notably more memory, with memory results for key generation ranging from 620,952 to 627,206 bytes and for sign-verify from 710,229 to 731,630 bytes. Due to this memory consumption, the details of Libecc and MbedTLS are difficult to distinguish in the table below; thus, a magnification of their results is provided in the speech bubble. It is also crucial to note that OpenSSL is primarily designed for general-purpose applications on traditional computing platforms, demanding more resources and potentially being unsuitable for certain IoT devices.
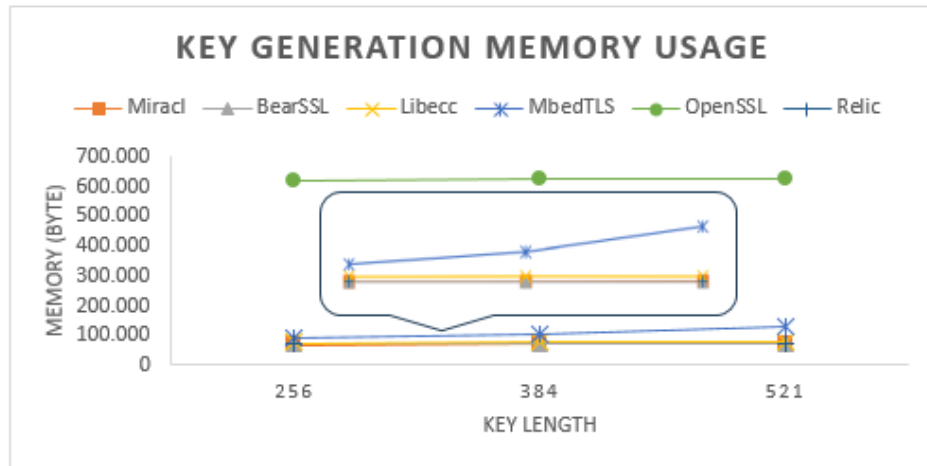
Figure 4: Key generation function memory usage (in bytes) of different libraries.
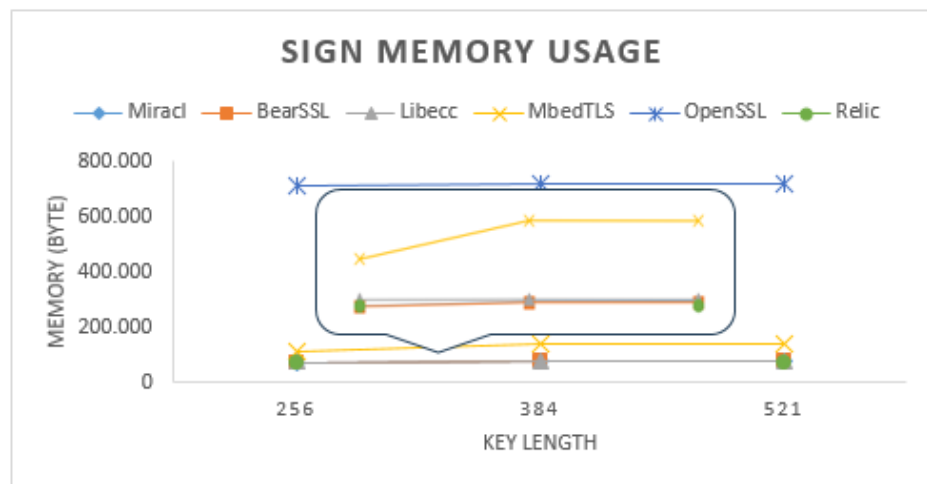
Figure 5: Sign function memory usage (in bytes) of different libraries.
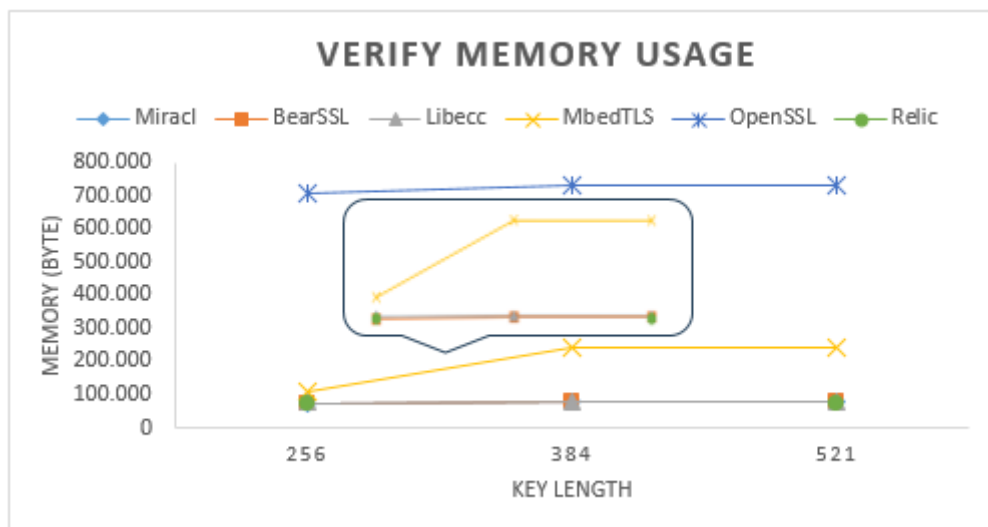
Figure 6. Verify function memory usage (in bytes) of different libraries.

6. DISCUSSION AND CONCLUSION

The rising prevalence of IoT devices necessitates improved security measures. Lightweight cryptographic solutions become crucial in addressing security concerns, particularly those related to authentication and confidentiality in the IoT domain. Given the challenges with key distribution in symmetric encryption, asymmetric methods, such as ECC, become more practical due to their lighter and additive operations when compared to resource-intensive multiplicative operations in methods like RSA. Consequently, our study focuses on performance tests of ECC-based open-source cryptographic libraries to help decide the right library for a target application.

In this study, we conducted tests on various open-source cryptographic libraries, including MIRACL, RELIC, BearSSL, Libecc, MbedTLS, and OpenSSL. The evaluations were conducted on a Raspberry Pi. Our findings underscore the importance of selecting cryptographic libraries based on platform constraints and performance requirements. For instance, OpenSSL demonstrates a salient performance for all operations, however it requires more resources (code size, memory usage) since it was designed for legacy computing environments and may not be feasible to run on certain IoT devices. The rest of the libraries evaluated in this study are optimized for resource constraint platforms. Our experiments revealed distinct performance differences in key generation, signing, verification durations of these libraries.

In our tests, RELIC and MbedTLS exhibited remarkable efficiency in key generation and signing but had an average verification performance. MIRACL showed comparatively slow key generation but balanced performance in signing and verification functions. BearSSL demonstrated efficiency in key generation but experienced longer signing and verification durations. Libecc was the slowest among all the libraries.

Memory requirements are another critical factor when deciding on a library. When we consider both performance and memory usage at the same time RELIC, MIRACL, MbedTLS and BearSSL stand out. When prioritizing key generation, notable options include RELIC, BearSSL and MIRACL. On the other hand, if signing and verification performance is paramount, MIRACL and RELIC are strong contenders. Alternatively for devices with less memory constraints MbedTLS presents a decent performance for all operations.

RELIC and MbedTLS demonstrate fast signing times and moderate verification times, rendering it a favourable choice for applications prioritizing quick signing operations. Also, RELIC, MbedTLS and BearSSL excel in key generation, and they are suitable for applications demanding rapid cryptographic key establishment. MIRACL demonstrates commendable performance for both signing and verification, making it suitable for applications where a balanced performance is critical. Therefore, MIRACL is recommended for applications requiring authentication or data integrity checks.

In this study we used a heuristic approach to compare six open-source crypto libraries. While our results provide valuable insights into performance variations between different open-source ECC libraries, aiding in the selection of an appropriate library for a specific application, we did not delve deeper into the reasons behind these variations through methods like clock cycle analysis or a meticulous code review. Future enhanced performance analysis and code review studies would help increase the efficiency of existing crypto-libraries and become a guide for future cryptosystem implementation projects.

Consequently, cryptographic libraries based on Elliptic Curve Cryptography (ECC) present viable choices for enhancing the security of IoT systems. Our findings empower informed decision-making when implementing security features on resource-constrained devices. Nevertheless, it is essential to

adopt a well-rounded approach to library selection, considering factors beyond performance. Alongside performance, considerations such as user base, development status, and documentation quality should be factored in when making a library choice.

ACKNOWLEDGEMENT

CONFLICT OF INTEREST

The authors stated that there are no conflicts of interest regarding the publication of this article.

CRediT AUTHOR STATEMENT

İsmet Kaan Çekiş: Software, Validation, Investigation, Writing-Original Draft, Visualization.
Armağan Toros: Software, Validation, Investigation, Writing-Original Draft
Nimet Apaydın: Writing-Original Draft
İlker Özçelik: Funding acquisition, Project administration, Supervision, Conceptualization, Writing-Original Draft, Review & Editing

REFERENCES

[1] Yassein MB, Aljawarneh S, Qawasmeh E, Mardini W, Khamayseh Y. Comprehensive study of symmetric key and asymmetric key encryption algorithms. International conference on Engineering and Technology (ICET) 2017; 1-7.

[2] Islam T, Youki RA, Chowdhury BR, Hasan AT. An ECC based secure communication protocol for resource constraints IoT devices in smart home. In Proceedings of the International Conference on Big Data, IoT, and Machine Learning 2021; 431-444.

[3] Tawalbeh LA, Mowafi M, Aljoby W. Use of elliptic curve cryptography for multimedia encryption. IET Information Security 2013; 7(2): 67-74.

[4] Caelli WJ, Dawson EP, Rea SA. PKI, Elliptic curve cryptography, and digital signatures. Computers & Security 1999; 18(1): 47-66.

[5] Alshahrani MY. Implementation of a blockchain system using improved elliptic curve cryptography algorithm for the performance assessment of the students in the e-learning platform. Applied Sciences 2021; 12(1): 74.

[6] Cheng R, Wu K, Su Y, Li W, Cui W, Tong J. An efficient ECC-based CP-ABE scheme for power IoT. Processes 2021; 9(7): 1176.

[7] Brychta J. Benchmarks with points on elliptic curves. InProc. 25th Conf. Student Eeict 2019; 520-524.

[8] Hijawi U, Unal D, Hamila R, Gastli A, Ellabban O. Performance evaluation of no-pairing ECC-based KPABE on IoT platforms. IEEE International Conference on Informatics, IoT, and Enabling Technologies (ICIoT) 2020; 225-230.

[9] Tschofenig H, Pégourié-Gonnard M. Performance investigations. IETF Proceeding 2015; 92.

[10] Mahto D, Yadav DK. Performance Analysis of RSA and Elliptic Curve Cryptography. Int. J. Netw. Secur. 2018; 20(4): 625-35.

[11] Kardi A, Zagrouba R, Alqahtani M. Performance evaluation of RSA and elliptic curve cryptography in wireless sensor networks. 21st Saudi Computer Society National Computer Conference (NCC) 2018; 1-6.

[12] Gupta V, Gupta S, Chang S, Stebila D. Performance analysis of elliptic curve cryptography for SSL. In Proceedings of the 1st ACM workshop on Wireless security 2002; 87-94.

[13] Koppl M, Siroshtan D, Orgon M, Pocarovsky S, Bohacik A, Kuchar K, Holasova E. Performance Comparison of ECDH and ECDSA. 2nd International Conference on Electronics, Communications and Information Technology (CECIT) 2021; 825-829.

[14] Pigatto DF, da Silva NB, Branco KR. Performance evaluation and comparison of algorithms for elliptic curve cryptography with El-Gamal based on MIRACL and RELIC libraries. Journal of Applied Computing Research. 2011; 1(2): 95-103.

[15] Popa L, Groza B, Murvay PS. Performance evaluation of elliptic curve libraries on automotive-grade microcontrollers. In Proceedings of the 14th International Conference on Availability, Reliability and Security 2019; 1-7.

[16] Di Matteo S, Baldanzi L, Crocetti L, Nannipieri P, Fanucci L, Saponara S. Secure elliptic curve crypto processor for real-time IoT applications. Energies. 2021; 14(15): 4676.

[17] Aikins-Bekoe S, Hayfron-Acquah JB. Elliptic curve Diffie Hellman (ECDH) analogy for secured wireless sensor networks. International Journal of Computer Applications. 2020; 176(10): 1-8.

RESEARCH ARTICLE

ON THE CONTROL AND SIMULATION OF THE THERMAL CONDUCTIVITY IN A HEAT EQUATION

Hakkı GÜNGÖR[1],*

[1] Department of Computer Technology, Vocational School, Ufuk University, Ankara, Turkey
hakki.gungor@ufuk.edu.tr - *0000-0002-9546-665X*

Abstract

This study operates the Gradient Method to control the leading coefficient function of a heat equation and presents a Maplet Application which facilitates the computation of control function. The control is the heat conductivity function and this function is controlled by aiming the desired value approximation of final heat. After mentioning the existence and uniqueness of the control, the application is submitted by MAPLE mathematical software program and the results are tested on a problem.

1. INTRODUCTION AND STATEMENT OF THE PROBLEM

Having a long history, control problems related to heat equations continue to be popular nowadays. In this context, researches are being conducted aiming to control any parameter in the problem for different purposes. There are many studies about the control of the initial condition, the boundary conditions or the external heat source function. Some of them are presented in the studies [1-3]. Besides them, the problem of controlling the heat conductivity function is very important in terms of the location of this function in the equation. In the studies [4-7], these kinds of problems have been investigated with different cost functionals.

Now, we will examine such a problem. Let us suppose that $h(x,t)$ is a function representing the heat value at time t and position x of a thin rod with length l. Then $h(x,t)$ is the solution to the following problem:

$$\frac{\partial h}{\partial t} - \frac{\partial}{\partial x}\left(k(x)\frac{\partial h}{\partial x}\right) = f(x,t), \quad (x,t) \in (0,l) \times (0,T) \tag{1}$$

$$h(x,0) = \varphi(x), x \in (0,l) \tag{2}$$

$$-k(0)h_x(0,t) = g_0(t), \quad k(l)h_x(l,t) = g_1(t), \quad t \in (0,T). \tag{3}$$

Here $k(x)$ is heat conductivity function, $f(x, t)$ is external heat source function, $\varphi(x)$ is initial heat distribution, $g_0(t)$ and $g_1(t)$ are outward fluxes of the heat at the boundaries.

The generalized solution rather than the classical solution of such a problem is more useful in the applications because it also includes discontinuous functions. The generalized solution of the problem (1)-(3) is the function $h \in V_2^{1,0}(\Omega)$ satisfying the equality of

$$\int_0^T \int_0^l (-h\eta_t + k(x)h_x\eta_x)dxdt = \int_0^T \int_0^l f\eta dxdt + \int_0^l \varphi(x)\eta(x,0)dx + \int_0^T g_1(t)\eta(l,t)dt$$

$$- \int_0^T g_0(t)\eta(0,t)dt \tag{4}$$

for each $\eta \in W_2^{1,1}(\Omega)$ with $\eta(x,T) = 0$, [4,5,6]. For equality (4) to be meaningful the data functions are chosen from the functional spaces

$$k(x) \in L_\infty(0,l), \ f(x,t) \in L_2(\Omega), \ \varphi(x) \in L_2(0,l), \ g_0(t) \in L_2(0,T), \ g_1(t) \in L_2(0,T).$$

The norms on $V_2^{1,0}(\Omega)$ and $W_2^{1,1}(\Omega)$ are defined respectively such as;

$$\|h\|_{V_2^{1,0}(\Omega)} = \max_{0 \le t \le T} \|h\|_{L_2(0,l)} + \|h_x\|_{L_2(\Omega)}$$

$$\|\eta\|_{W_2^{1,1}(\Omega)} = \left[\|\eta\|_{L_2(\Omega)}^2 + \|\eta_x\|_{L_2(\Omega)}^2 + \|\eta_t\|_{L_2(\Omega)}^2\right]^{1/2}.$$

Let us now assume that the rod is desired to close a given heat distribution $\mu(x)$ at final time T and let $k(x)$ be the control function that will perform this request. In this case, it is necessary to find the function $k(x)$ which will make the following functional minimum on an admissible set of controls K which is a closed and convex subset of $L_2(0,l)$.

$$I(k) = \int_0^l [h(x,T;k) - \mu(x)]^2 dx. \tag{5}$$

On the other hand, it is well-known that the minimization problem of the functional (5) is ill-posed. In the ill-posedness when a problem is solved numerically it is frequently encountered that $I(k_*) \cong I(l_*) \cong 0$ while $\|k_* - l_*\|_{L_2(0,l)} \gg 0$ for different control functions k_* and l_* generated by different minimizers $\{k_m\}$ and $\{l_m\}$. This means that the solution may be non-unique and small changes in the initial data reveal huge differences in solution when obtaining a numerical solution. To deal with this situation, a penalty term is included in the functional and regularized solution is investigated.

Hence, we consider the new functional

$$J(k) = \int_0^l [h(x,T;k) - \mu(x)]^2 dx + \alpha \int_0^l [k(x) - k^+(x)]^2 dx \tag{6}$$

and solve the problem

$$\min_{k \in K} J(k). \tag{7}$$

Here, control is searched around of a function k^+. The function k^+ has the role of an initial guess to the control function. Especially for the local results about convergence rates, the choice of k^+ is very crucial. Of course, available apriori information about the minimum element of the functional (5) has to enter into the selection of k^+ to get successful results. Besides, α in the functional $J(k)$ is the

regularization parameter which is used to balance between the two integrals of (6). The further information about the parameter α and function k^+ can be found in [8].

The solution of the problem (7) is called k^+-minimum norm control and represented by $k_*(x)$. The existence and uniqueness of k^+-minimum norm control $k_*(x)$ is based on the following facts;

- The space $L_2(0, l)$ is uniformly convex.
- K is closed and bounded in $L_2(0, l)$.
- $I(k)$ is continuous by the L_2 norm on K.
- $I(k)$ is bounded from below on K.

Then according to the Goebel Theorem [9] there is a dense subset G in $L_2(0, l)$ such that for $k^+ \in G$ and any $\alpha > 0$ the problem (7) has a unique solution. Similar analyzes have been carried out in the studies [4,5,6,7].

Also, it is known that obtaining a numerical solution and symbolic computation of control function in control problems is a very difficult issue. Moreover, there is no computer program or software prepared for such a problem.

This study has been prepared to fill a gap in this area and gives a Maple Application 'HCC (Heat Conductivity Control)' that produces the solution to the problem (7).

The used computer program Maple is a mathematical software that combines the world's most powerful mathematical engine with an interface that makes it extremely easy to analyze, explore, visualize, and solve mathematical problems. Besides, a Maplet Application is a graphical user interface containing windows, textbox regions, and other visual interfaces, which gives a user point-and-click access to the power of Maple. Users can perform calculations, plot functions, or display dialogs without using the worksheet interface [10].

2. APPROXIMATE SOLUTION TO THE CONTROL FUNCTION

In this section, we first state the necessary condition for a control function $\boldsymbol{k_*(x)}$ to be the solution of the considered problem.

By the theory of calculus of variations, the definition of Frechet differentiability is

$$\Delta J(k) = \langle J'(k), \Delta k \rangle_{L_2(0,l)} + o\big(\|\Delta k\|_{L_2(0,l)}\big)$$

with $\lim_{\|\Delta k\| \to 0} o(\|\Delta k\|)/\|\Delta k\| = 0$. With this definition, the derivation of the functional (6) after some manipulations is found by

$$J'(k) = -\int_0^T h_x \eta_x dt + 2\alpha(k - k^+). \tag{8}$$

Then according to [11], the necessary condition for a control $\boldsymbol{k_*(x)}$ to be the minimum element for the problem is given by the following inequality:

$$\langle J'(k_*), k - k_* \rangle_{L_2(0,l)} = \langle -\int_0^T (h_*)_x (\eta_*)_x dt + 2\alpha(k_* - k^+), k - k_* \rangle_{L_2(0,l)} \geq 0 \tag{9}$$

for $\forall k \in K$, Here, $\boldsymbol{h_*}$ is the solutions of the (1)-(3) state problem and $\boldsymbol{\eta_*}$ is the solution of

$$\eta_t + (k(x)\eta_x)_x = 0 \tag{10}$$

$$\eta(x,T) = 2[h(x,T;k) - \mu(x)] \tag{11}$$

$$k(0)\eta_x(0,t) = 0, \ k(l)\eta_x(l,t) = 0 \tag{12}$$

adjoint problem in the generalized sense, corresponding to $k = k_*$.

Now, we can discuss how to get an approximate solution for a control function. By Galerkin Method, the approximate solution $h^N(x,t)$ with N sum for (1)-(3) heat equation is constituted such as

$$h^N = v^N + w = \sum_{k=1}^N C_k^N(t)\varphi_k(x) + w. \tag{13}$$

Here, v^N is the solution of corresponding homogeneous Neumann problem and

$$w(x,t) = \frac{x^2}{2}\frac{1}{lk(l)}g_1(t) + \left(\frac{x^2}{2} - xl\right)\frac{1}{lk(0)}g_0(t)$$

is an auxiliary function.

Also, $\{\varphi_k(x)\}$ is an orthonormal basis of the functional space $L_2(0,l)$. Then $C_k^N(t)$'s are unknown functions which are the solutions of the following first order differential system;

$$\frac{d}{dt}\mathbf{C^N} + \mathbf{K C^N} = \mathbf{F}$$
$$\mathbf{C^N}(0) = \mathbf{A} \tag{14}$$

for the vector $\mathbf{C^N} = [C_1^N(t) \quad \cdots \quad C_N^N(t)]^T$, where the matrix $\mathbf{K}$ has the entries

$$K_{ij} = \int_0^l \left(k(x)\frac{d}{dx}\varphi_j(x)\right)\frac{d}{dx}\varphi_i(x)dx$$

for $i,j = 1,2,\dots,N$ and the vectors $\mathbf{F}$, $\mathbf{A}$ and $\mathbf{B}$ have the entries

$$F_i = \int_0^l \tilde{f}(x,t)\varphi_i(x)dx, A_i = \int_0^l \tilde{\varphi}(x)\varphi_i(x)dx \text{ for } i = 1,2,\dots,N.$$

with $\tilde{\varphi}(x) = \varphi(x) - w(x,0)$ and $\tilde{f}(x,t) = f(x,t) - w_t + (k(x)w_x)_x$.

The problem of finding the vector $\mathbf{C^N}$ from (14) is a Cauchy problem for the system of first order differential equations. The right-hand side of this system is in the class of square integrable functions. This system has a unique solution on the interval $[0,T]$ as known from the theory of ordinary differential equations.

In the same way, secondly, the approximate solution of (10)-(12) adjoint problem is carried out by the finite sum of

$$\eta^N = \sum_{k=1}^N (C_e)_k^N(t)\varphi_k(x).$$

Here $(C_e)_k^N(t)$'s are unknown functions which are the solutions of a second-order system of differential equations obtained by the generalized solution of the adjoint problem.

After then, using these solutions the approximate derivative of the cost functional (6) is obtained by

$$(J^N)'(k(x)) = -\int_0^T [h^N(x,t;k(x))]_x [\eta^N(x,t;k(x))]_x dt + 2\alpha[k(x) - k^+(x)]. \qquad (15)$$

Once these functions are found, the minimization stages can be carried out. Starting with an initial $k_0(x) \in K$ element, a minimizer $\{k_m(x)\}$ is constituted by Gradient Method with the rule

$$k_{m+1}(x) = k_m(x) - \beta(J^N)'(k_m(x)), \tau_m > 0, m = 0, 1, 2, \dots \qquad (16)$$

In each step of m, the parameter $\beta > 0$ is chosen sufficiently enough such that the minimizing condition

$$J^N(k_{m+1}) < J^N(k_m) \qquad (17)$$

holds.
The computations are executed up to the stopping criteria of

$$|J^N(k_m) - J^N(k_{m+1})| \le \varepsilon \qquad (18)$$

is provided by given small ε number. The $k_{m+1}(x)$ function satisfying this condition is accepted by the approximate control $k_*(x)$.

We can summarize this process with the following algorithm.

2.1. Algorithm for the Process

Selecting an initial control $k_0(x) \in K$, $k_{m+1}(x)$ is computed by the following scheme if $k_m(x)$ is known for $m \ge 0$.

1. Solve the system (14) and get approximate function $h_m^N(x,t)$.

2. Knowing $h_m^N(x,t)$, solve the adjoint equation (10)-(12) and get $\eta_m^N(x,t)$.

3. Using (15), set $k_{m+1}(x) = k_m(x) - \beta(J_m^N)'(k_m(x))$ by (16) and select the parameter β small enough to assure the condition (17) holds.

4. If condition (18) holds, take the control function as $k_*(x) = k_{m+1}(x)$ otherwise go to Step 3.

3. A MAPLET APPLICATION CALCULATING THE CONTROL FUNCTION AND TESTING THIS APPLICATION

In this section, using the software Maple 17 we submit a Maplet Application named HCC (Heat Conductivity Control). This application produces the heat conductivity function which is control function of the problem if data is entered. This application can be downloaded using the link given by [12].

Running this Maplet executes the following application;

Figure 1. Maplet Application Screen

Here the data of the application are such as;

Table 1. The data of the application.

In the Maplet		In the Problem
l	l	the length of the interval $(0, l)$
T	T	the length of the interval $(0, T)$
$f(x, t)$	$f(x, t)$	external heat source function
$\text{phi}(x)$	$\varphi(x)$	initial heat distribution
$k(0)$	$k(0)$	coefficient of left heat flux
$k(l)$	$k(l)$	coefficient of left heat flux
$g0(t)$	$g_0(t)$	left heat flux function
$g1(t)$	$g_1(t)$	right heat flux function
$\text{mu}(x)$	$\mu(x)$	desired target (final time heat distribution)
$alpha$	α	regularization parameter of the functional $J(k)$
$\text{kaplus}(x)$	$k^+(x)$	initial guess to the control function
$\text{kstart}(x)$	$k_0(x)$	initial element for the minimizer
N	N	the number of finite element used in h^N and η^N
$beta$	β	the value of parameter used in $k_{m+1}(x)$
eps	ε	the value of stopping criteria used in $|J^N(k_m) - J^N(k_{m+1})| \leq \varepsilon$

Besides, the outcomes of the application are such as;

Table 2. The application results.

In the Maplet	In the Problem
Draw the Control	The function $k_*(x) = k_{m+1}(x)$ obeying the stopping criteria
Distance to Target	Graph of the control function
Approximation to kaplus	The value of $I(k_*)$
Draw the Control	The value of $\|k_* - k^+\|_{L_2(0,l)}$

Note that the ability of calculation of the control function depends on the appropriate choice of $N, kstart(x), beta$ and eps. If the application does not give the control function these values should be re-arranged.

Now we give a test problem revealing the use and success of given Maplet application.

3.1. Problem

Let us consider the following problem on the domain $\Omega = (0,1) \times (0,1)$;

$$\min_{k \in K} \int_0^1 \left[h(x,1;k) - e^{-\pi^2} \sin \pi x \right]^2 dx + \alpha \int_0^1 \left[k(x) - (1+x) \right]^2 dx$$

subject to the problem of

$$\frac{\partial h}{\partial t} - \frac{\partial}{\partial x} \left(k(x) \frac{\partial h}{\partial x} \right) = \pi e^{-\pi^2 t} (\pi x \sin \pi x - \cos \pi x), \quad (x,t) \in (0,1) \times (0,1)$$

$$h(x,0) = \sin \pi x, x \in (0,1)$$

$$-h_x(0,t) = -\pi e^{-\pi^2}, \; h_x(l,t) = -2\pi e^{-\pi^2}, \; t \in (0,1).$$

Now we will use the given Maplet Application and get the control function. The data given by problem are such as

$$l = 1, T = 1, \mu(x) = e^{-\pi^2} \sin \pi x, k^+(x) = 1 + x$$

$$f(x,t) = \pi e^{-\pi^2 t} (\pi x \sin \pi x - \cos \pi x), \varphi(x) = \sin \pi x$$

$$k(0) = 1, g_0(t) = -\pi e^{-\pi^2 t}, k(l) = 2, g_1(t) = -2\pi e^{-\pi^2 t}.$$

Upon this, if we select as

$$\alpha = 0.4, \quad N = 2, \quad k_0(x) = 4, \quad \beta = 0.9, \quad \varepsilon = 0.0001$$

and enter these into the application then we get the following result;
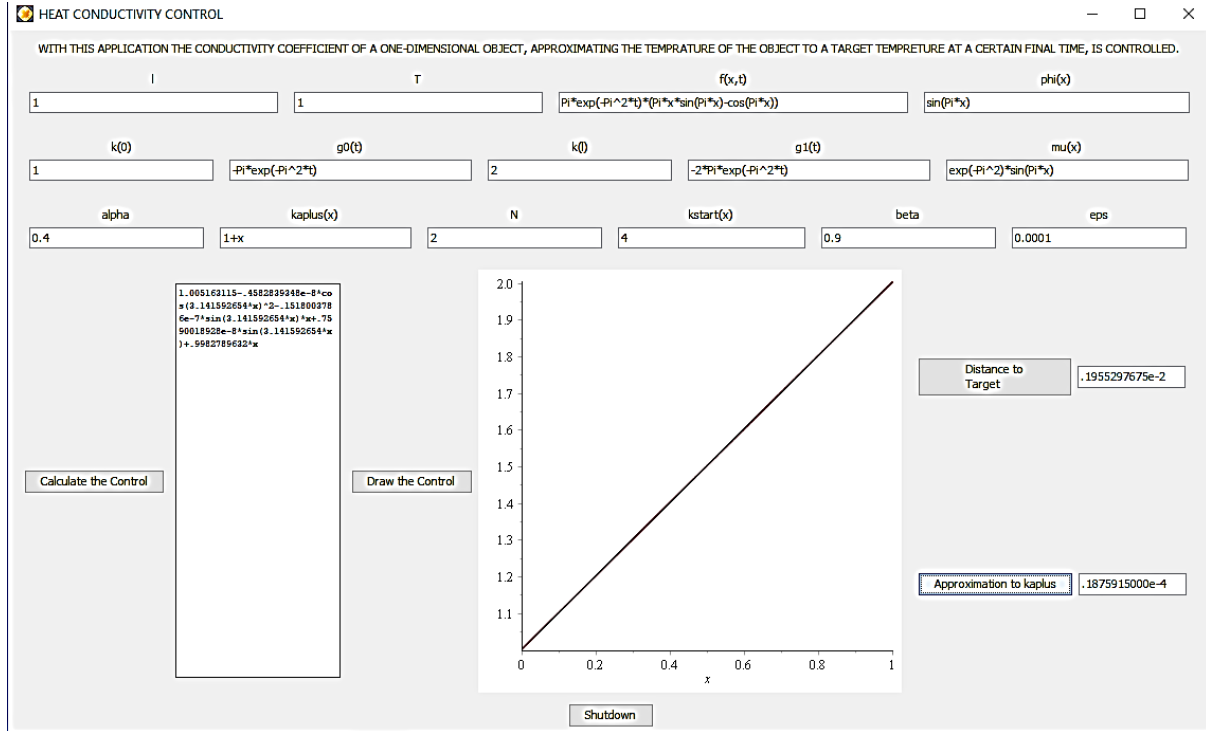
Figure 2. Maplet Application Screen for Test Problem

According to this application the control function is

$$k_*(x) = 1.00516311 - 0.458283934(E-8).\cos^2(3.141592654x) - 0.151800378$$
$$(E-7).\sin(3.141592654x) + 0.759001892(E-8).\sin(3.141592654x) + 0.9982789632x$$

Also, the distance to target is $I(k_*) = 0.1955297675(E-2)$ and approximation to kaplus is $\|k_* - k^+\|_{L_2(0,l)} = 0.1875915000(E-4)$.

On the other hand, the reason for the choice of $k^+(x) = 1 + x$ is the fact that

$$I(k^+) = \int_0^1 \left[h(x,1;k^+) - e^{-\pi^2} \sin \pi x \right]^2 dx = 0$$

for related heat problem.

Besides, in the following table there are some 'distance to target' and 'approximation to kaplus' values corresponding some α numbers for this example:

Table 3. $I(k_*)$ and $\|k_* - k^+\|^2_{L_2(0,l)}$ values for some regularization parameters.

α	Distance to Target $(I(k_*))$	Approximation to kaplus $(\|k_* - k^+\|^2_{L_2(0,l)})$
0.01	0.2027140817(E − 4)	0.2882505505
0.015	0.3348096495(E − 3)	0.1548949288
0.02	0.6706345202(E − 3)	0.8905348472(E − 1)
0.03	0.1069109391(E − 2)	0.4043347441(E − 1)
0.04	0.1289383661(E − 2)	0.2262586246(E − 1)
0.05	0.1556482205(E − 2)	0.1254192760(E − 1)
0.1	0.1779405106(E − 2)	0.2260406516(E − 2)

The following figure visualizes the approximations in the Table 1.
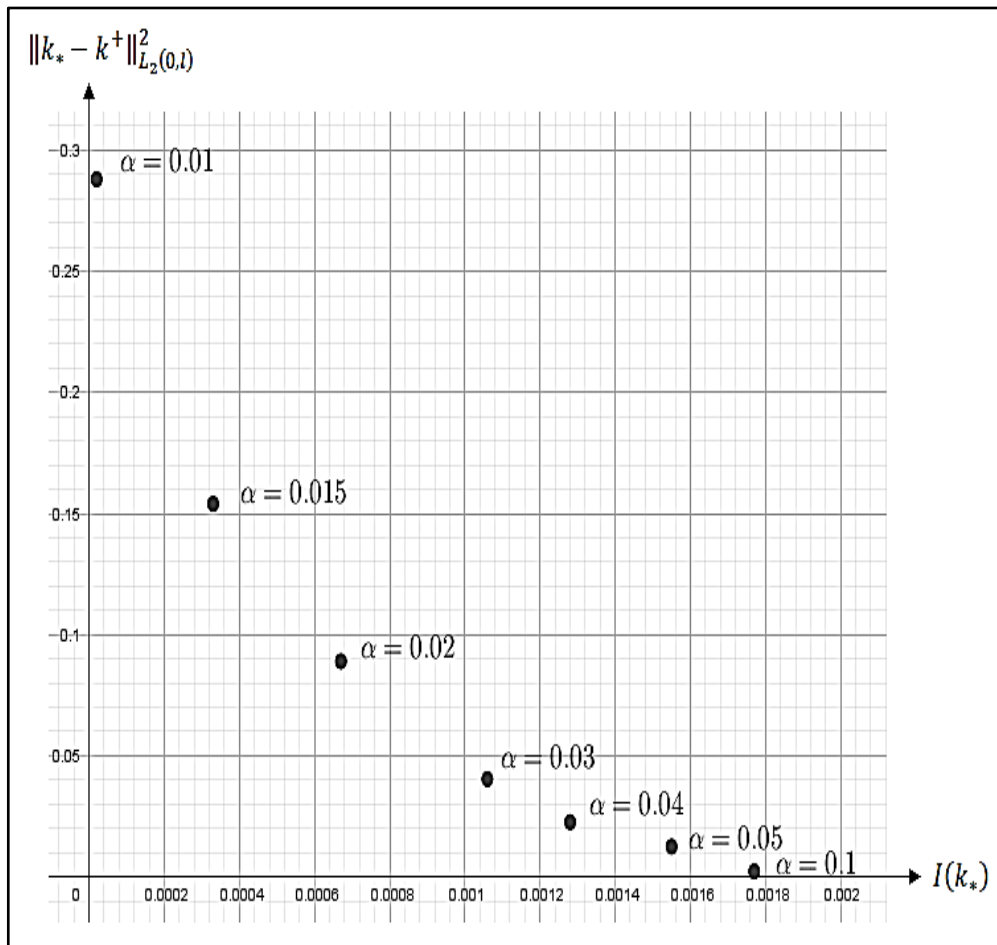
Figure 3. Visualization of $I(k_*)$ and $\|k_* - k^+\|^2_{L_2(0,l)}$ by some α values.

Now, using this application, we will examine the ill-posedness for $\alpha = 0$ as we mentioned in section 1.

Table 4. Ill-Posedness when $\alpha = 0$.

$kstart(x)$	$k_*(x)$	Distance to Target	Approximation to kaplus
4	$4 + 0.1924776275(E-10).\sin^2(3.1415926x)$ $-0.3515450763(E-9).\sin(3.1415926x)\,x$ $+0.1757725382(E-9).\sin(3.1415926x)$	$0.28959697(E-10)$	6.333333333
8	$8 - 0.151513001(E-11).\cos^2(3.1415926x)$ $-0.6456950391(E-10).\sin(3.1415926x)\,x$ $+0.3228475196(E-10).\sin(3.1415926x)$	$0.11341385(E-10)$	42.33333333
10	$10 - 0.71288010(E-12).\cos^2(3.1415926x)$ $-0.3906056418(E-10).\sin(3.1415926x)\,x$ $+0.1953028209(E-10).\sin(3.1415926x)$	$0.13574858(E-10)$	72.33333333

When $\alpha = 0$, the differences at the starting element of the minimizer produce quite different controls which bring the heat closer to the target. In this case, the distances from the obtained controls to the k^+ function have been increasing gradually. This situation imposes the numerical ill-posedness.

Let us take the value of $\alpha = 0.4$ and use the application. Then we get the following outcomes;

Table 5. The case $\alpha \neq 0$.

$kstart(x)$	$k_*(x)$	Distance to Target	Approximation to kaplus
4	$1.005163 - 0.45836(E-8).\cos^2(3.141592x)$ $-0.1518003786(E-7).\sin(3.1415926x)\,x$ $+0.75900189(E-8).\sin(3.1415926x)$ $+0.9982789632x$	$0.1956610(E-2)$	$0.1875915(E-4)$
8	$1.003373 - 0.47691(E-8).\cos^2(3.141592x)$ $-0.1563177542(E-7).\sin(3.1415926x)x$ $+0.7815887713(E-8).\sin(3.1415926x)$ $+0.9995181097x$	$0.1955720(E-2)$	$0.9830589(E-5)$
10	$1.004337 - 0.46141(E-8).\cos^2(3.141592x)$ $-0.1525642581(E-7).\sin(3.1415926x)x$ $+0.7628212905(E-8).\sin(3.1415926x)$ $+0.9995181097x$	$0.1954430(E-2)$	$0.1679713(E-4)$

As seen, the differences in the starting element of the minimizer have no important effect when $\alpha \neq 0$. All the obtained controls are close enough to k^+ function and achieve the same degree of convergence to the target. This situation removes the fact of being numerically ill-posedness.

4. RESULT AND DISCUSSION

The results of the test problem show that the given Maplet Application HCC works quite efficiently. The outcomes are quite consistent with the control theory. After this point, applications can be prepared for similar types of problems. Thus software that is easy to use for solutions based on a long computation of control problems is developed.

ACKNOWLEDGEMENTS

CONFLICT OF INTEREST

The author stated that there are no conflicts of interest regarding the publication of this article.

CRediT AUTHOR STATEMENT

Hakkı Güngör: Formal analysis, Writing - original draft, Visualization, Conceptualization.

REFERENCES

[1] Subaşı M. Optimal Control of Heat Source in a Heat Conductivity Problem. Optimization Methods and Software, 2002; 17, 239-250

[2] Effati S, Nazemi A, Shabani H. Time Optimal Control Problem of the Heat Equation with Thermal Source, IMA Journal of Mathematical Control and Information, Volume 31, 2014; pp. 384-402

[3] Teymurov R. Optimal control of mobile sources for heat conductivity processes, International Journal of Control, Volume 90, Issue 5, 2017; pp. 923-931

[4] Tagiyev R. Optimal Coefficient Control in Parabolic Systems, Differential Equations, Volume 45, no. 10, 2009; pp. 1526-1535

[5] Tagiyev R. Optimal control for the coefficients of a Quasilinear parabolic equation, Automation and Remote Control, volume 70, no. 11, 2009; pp. 1814-1826

[6] Tagiyev R. Optimal control problem for a Quasilinear parabolic equation with Controls in the coefficients and with State Constraints, Differential Equations, Volume 49, no. 3, 2013; pp. 369-381

[7] Tagiyev RK. Hashimov SA. On Optimal Control of the coefficients of a parabolic equation Involving Phase Constraints, Proceedings of IMM of National Academy of Sciences of Azerbaijan, volume 38 , 2013; pp. 131-146

[8] Engl HW, Hanke M, Neubauer A. Regularization of Inverse Problems. Kluwer Academic Publishers, Dordrecht, 1996.

[9] Goebel M. On existence of optimal control. Math.Nachrichten, 93, 1979; pp. 67–73

[10] https://www.maplesoft.com/support/help/maple/view.aspx?path=MapletsOverview, Date of Access: 2023.

[11] Vasilyev FP. Numerical Methods for Solving Extremal Problems. Nauka, 400 s, Moscow, 1981.

[12] https://drive.google.com/file/d/1dhlFVmxwnD2km3xyDut0098YPUKfc4j8/view?usp=sharing

RESEARCH ARTICLE

ON THE FUZZIFICATION OF GREEK PLANES OF KLEIN QUADRIC

Münevvere Mine KARAKAYA [1,*] Ziya AKÇA [2]

[1] Department of Mathematics and Computer Science, Faculty of Science, Eskisehir Osmangazi University, Eskişehir, Turkey
mine.zumruttas@gmail.com - 🆔 *0000-0003-1517-3409*

[2] Department of Mathematics and Computer Science, Faculty of Science, Eskisehir Osmangazi University, Eskişehir, Turkey
zakca@ogu.edu.tr - 🆔 *0000-0001-6379-0546*

Abstract

A projective space of dimension 3 over a finite Galois field $GF(q)$ is denoted as $PG(3,q)$. It is defined as the set of all one-dimensional subspaces of 4-dimensional vector space over this Galois field. Klein transformation maps a projective plane of $PG(3,2)$ to a Greek plane of the Klein quadric. This paper introduces the fuzzification of Greek planes passing through the base point, any point on the base line different from the base point, and any point not on the base line of the base plane of 5-dimensional fuzzy projective space.

1. INTRODUCTION

Zadeh introduced fuzzy sets in [11]. A fuzzy set is a function $\lambda: X \to [0,1]$. Fuzzy set theory provides a convenient method that is easy to implement in real-time applications, and also allows designers and operators to transfer their knowledge to the geometry. In the study [9], Lubczonok gave fuzzy vector spaces. Fuzzy point, fuzzy projective plane and fuzzy projective spaces from the fuzzy vector spaces were defined by Kuijken and Van Maldeghem in [8]. Akça et all showed the fuzzy line spreads of Fano projective plane in [1]. And then Akça et all gave the classifying fuzzy projective lines and fuzzy projective planes in [2, 3, 5]. Fibered harmonic conjugates, and the condition of Reidemeister in the fibered projective plane are determined [4].

Fuzzification is the method of transforming a crisp projective subspace into a fuzzy projective space. Formal tools for mathematical representation and efficient processing of any information can be provided by fuzzy sets.

This research investigates a fuzzification of the β-planes passing the base point of the Klein quadric.

Step 1. Determine the Greek planes of the Klein quadric passing through the base point of $PG(5,2)$.

Corresponding Author:mine.zumruttas@gmail.com

Step 2. In order to obtain a maximum flag, the coordinates of any point in these planes must be selected.

Step 3. The membership degrees of points in each subspace are assigned the appropriate real numbers such that the membership degrees in the 5-dimensional fuzzy projective space are the same.

Step 4. Fuzzification is completed by defining a fuzzy set.

2. PRELIMINARIES

The following definitions and theorem are taken from [6].

Definition 2.1 A projective plane in $PG(3, K)$ is the set of all points (x_1, x_2, x_3, x_4) satisfying a linear equation $a_1 x_1 + a_2 x_2 + a_3 x_3 + a_4 x_4 = 0$. This projective space is denoted by $[a_1, a_2, a_3, a_4]$.

Definition 2.2 A three-dimensional projective space $PG(3, K)$ satisfies the following axioms:
S1-) Any two distinct points are contained in a unique line,
S2-) Every line contains at least three points,
S3-) Three non-collinear points define a unique plane,
S4-) There are four points, no three of which are collinear and not all of which lie in the same plane.
S5-) Any two distinct coplanar lines intersect in a unique point.
S6-) Any line not on a given plane intersects the plane in a unique point.

Theorem 2.3 The points of $PG(3, q)$ over the Galois field of order q have a unique form which is $(1,0,0,0)$, $(x_1,1,0,0)$, $(x_1,x_2,1,0)$, $(x_1,x_2,x_3,1)$ for all $x_1, x_2, x_3 \in K$, and the planes of $PG(3, q)$ over the Galois field of order q have a unique form which is $[1,0,0,0]$, $[a_1,1,0,0]$, $[a_1,a_2,1,0]$, $[a_1,a_2,a_3,1]$ for all $a_1, a_2, a_3 \in GF(q)$.

Let V be 6-dimensional vector space associated projective space $PG(5, q)$. Now, we will describe a certain connection between the lines of $PG(3, q)$ and the certain points of $PG(5, q)$.

Definition 2.4

Let $M = \begin{bmatrix} O_3 & \frac{1}{2} I_3 \\ \frac{1}{2} I_3 & O_3 \end{bmatrix}$ be the matrix of the Klein quadric. Where $X = \begin{vmatrix} x_0 \\ x_1 \\ x_2 \\ x_3 \\ x_4 \\ x_5 \end{vmatrix} \in PG(5, q)$,

$$H^5 : X^T M X = x_0 x_3 + x_1 x_4 + x_2 x_5 = 0$$

is the equation of the Klein quadric H^5 in $PG(5,2)$.

Klein transformation maps a line in $PG(3,2)$ to the point $(l_{01}, l_{02}, l_{03}, l_{23}, l_{31}, l_{12})$ of $PG(5,2)$.
Klein transformation maps 15 points of $PG(3,2)$ into 15 Latin planes of H^5 and 15 planes of $PG(3,2)$ into 15 Greek planes of H^5.
Some results about Latin and Greek planes:

- The points of $PG(3, q)$ are the Latin planes in H^5.
- The points of H^5 are obtained from the lines in PG(3,q) by Klein transformation.
- Greek planes of H^5 are obtained from the planes in $PG(3, q)$ by Klein transformation.
- In H^5, two different Latin planes intersect a point.
- In H^5, two different Greek planes intersect a point.
- In H^5, a Latin and a Greek plane are either disjoint or meet in a line.
- In H^5, there are (q + 1) Latin planes and (q + 1) Greek planes.
- Each line in H^5 is the intersection of the Latin and Greek planes.
- In H^5, every point is contained in 2(q+1) planes such thet half of these planes are Latin and half are Greek planes.

In this section, some basic concepts about fuzzy logic are given.

There is no systematic approach to solving a particular problem. The rules in fuzzy logic control are very dependent on human experience.

There is no specific method for selecting membership functions. The most suitable function is found by trial method.

Definition 2.5 (See [11]) A fuzzy set λ on a set X is mapping $\lambda : X \to [0, 1]: x \to \lambda(x)$. The number $\lambda(x)$ is called the degree of membership of the point x in λ. The intersection of two fuzzy sets λ and λ' on X is given by the fuzzy set $\lambda \wedge \lambda' : X \to [0, 1]: x \to \lambda(x) \wedge \lambda'(x)$, where $\wedge$ denotes the minimum operator.

Let λ be a fuzzy subset of a set X and λ' be a fuzzy subset of a set X', then the fuzzy union of the fuzzy sets λ and λ' is defined as a function $\lambda \cup \lambda' : X \cup X' \to [0,1]$ given by

$$(\lambda \cup \lambda')(x) = \begin{cases} \max\{\lambda(x), \lambda'(x)\} & \text{if } x \in X \cap X' \\ \lambda(x) & \text{if } x \in X \text{ and } x \notin X' \\ \lambda'(x) & \text{if } x \in X' \text{ and } x \notin X \end{cases}.$$

Definition 2.6 Suppose V is an 2-dimensional vector space and let $\lambda: V \to [0, 1]$ be a fuzzy set on V. Then we call λ a fuzzy vector space on V if and only if
$\lambda(a\bar{u} + b\bar{v}) \geq \lambda(\bar{u}) \wedge \lambda(\bar{v}), \forall \bar{u}, \bar{v} \in V$ and $\forall a, b \in K$, [9].
Theorem 2.7 If $\lambda: L \to [0,1]$ is a fuzzy vector line on L, then $\lambda(\bar{u}) = \lambda(\bar{v})$,
$\forall \bar{u}, \bar{v} \in L \backslash \{\bar{0}\}$ and $\lambda(\bar{0}) \geq \lambda(\bar{u}), \forall \bar{u} \in L$.
Theorem 2.8 If $\lambda: V \to [0,1]$ is a fuzzy vector plane on V, then there exists a vector line L of V and real numbers $a_0 \geq a_1 \geq a_2 \in [0,1]$ such that λ is of the following form:
$$\lambda: V \to [0,1]$$
$$0 \to a_0$$
$$\bar{u} \to a_1 \text{ for } \bar{u} \in L \backslash \{0\}$$
$$\bar{u} \to a_2 \text{ for } \bar{u} \in V \backslash L.$$
Definition 2.9 Suppose V is an n-dimensional vector space. A flag in V is a sequence of distinct non-trivial subspaces $(U_0, U_1, \ldots, U_m)$ such that $U_j \subset U_i$ for all $j < i < n - 1$. The rank of a flag is the number of subspaces it contains. A maximal flag in V is a flag of length n.
Theorem 2.10 Let P be a 5-dimensional projective space over a finite field. The fuzzy projective space $[P, \lambda']$, $\lambda' : PG(5,2) \to [0,1]$, with $(q, U'_1, U'_2, \ldots, PG(5,2))$ is a maximal flag in $PG(5,2)$ and $a_1 \geq a_2 \geq \ldots \geq a_6$ are reals in $[0,1]$, then the fuzzy 5−dimensional projective space is

$$\lambda' : \quad PG(5,2) \to [0,1]$$

$$q \to a_1$$
$$p \to a_2 \qquad \text{for } p \in U_1' \setminus \{q\}$$
$$p \to a_3 \qquad \text{for } p \in U_2' \setminus U_1'$$
$$p \to a_4 \qquad \text{for } p \in U_3' \setminus U_2'$$
$$p \to a_5 \qquad \text{for } p \in U_4' \setminus U_3'$$
$$p \to a_6 \qquad \text{for } p \in PG(5,2) \setminus U_4'.$$

and the fuzzy Klein quadric $[H^5, \lambda'']$ is

$$\lambda'' : \quad H^5 \to [0,1]$$

$$q \to a_1$$
$$p \to a_2 \qquad \text{for } p \in U_1'' \setminus \{q\}$$
$$p \to a_3 \qquad \text{for } p \in U_2'' \setminus U_1''$$
$$p \to a_4 \qquad \text{for } p \in U_3'' \setminus U_2''$$
$$p \to a_5 \qquad \text{for } p \in U_4'' \setminus U_3''$$
$$p \to a_6 \qquad \text{for } p \in H^5 \setminus U_4''$$

where $(q, U_1'', U_2'', \ldots, H^5)$ is a chain of subspaces of H^5, in [3].

3. THE FUZZIFICATION OF β_i -PLANES OF KLEIN QUADRIC

Some results on the images under the Klein mapping of the projective 3-space of order 4 and the fuzzification of the Klein quadric in 5-dimensional projective space are given in [3].

Since $PG(3,2)$ has 15 points, 35 lines and 15 planes, the Klein quadric has 35 points, 15 the Latin planes α_i, $i = 1,2,\ldots,15$ and 15 the Greek planes β_i, $i = 1,2,\ldots,15$ in the projective space $PG(5,2)$.

In this section, we will construct the fuzzification of Greek planes passing through the base point, any point on the base line different from the base point, and any point not on the base line of the base plane of $[P, \lambda']$.

Theorem 3.1 Let ϕ be the projective plane in $PG(3,2)$, and the image of this plane under the Klein map be the Greek projective plane β_1 of $PG(5,2)$. If β_1 is the base plane of $[P, \lambda']$ then the fuzzy Greek plane λ_{β_1} is of the following form:

$$\lambda_{\beta_1} : \quad \beta_1 \to [0,1]$$

$$q \to a_1$$
$$p \to a_2 \qquad \text{for } p \in U_1'' \setminus \{q\}$$
$$p \to a_3, \qquad \text{for } p \in U_2'' \setminus U_1''.$$

Where (q, U_1'', U_2'') is a chain of subspaces of H^5, and $a_1 \geq a_2 \geq a_3$ are reals in $[0,1]$.

Proof. Let the image of the plane

$\phi : [0,0,0,1] = \{(1,0,0,0), (0,1,0,0), (0,0,1,0), (1,1,0,0), (1,0,1,0), (0,1,1,0), (1,1,1,0)\}$ in $PG(3,2)$ be the plane β_1. Since the plane β_1 is also a projective plane, it has seven points and seven lines. The distribution of points forming the maximal flag is obtained as follows:

Let the base point be $q = P_1 = (1,0,0,0,0,0)$, the base line be $L = U_1'' = \{ P_1 = (1,0,0,0,0,0),\ P_2 = (1,0,0,0,0,1),\ P_3 = (0,0,0,0,0,1)\}$, and the base plane of $[P, \lambda']$ be

$U_2'' = \{ P_1 = (1,0,0,0,0,0),\ P_2 = (1,0,0,0,0,1),\ P_3 = (0,0,0,0,0,1),\ P_4 = (1,1,0,0,0,0),\ P_5 = (1,1,0,0,0,1),\ P_6 = (0,1,0,0,0,1),\ P_7 = (0,1,0,0,0,0) \}.$

Since the image of the plane ϕ under the Klein map be the Greek projective plane $U_2'' = \beta_1$ of $PG(5,2)$, then the fuzzy Greek plane λ_{β_1} is of the following form:

$$\lambda_{\beta_1} :\ \beta_1 \to [0,1]$$
$$q \to a_1$$
$$p \to a_2 \qquad for\ p \in U_1'' \setminus \{q\}$$
$$p \to a_3, \qquad for\ p \in U_2'' \setminus U_1'',$$

where (q, U_1'', U_2'') is a chain of subspaces of H^5, and $a_1 \geq a_2 \geq a_3$ are reals in $[0,1]$.

Theorem 3.2 Let ϕ , φ and γ be three different projective planes passing through a line in $PG(3,2)$, and the image of these planes under the Klein map be the Greek projective planes β_1, β_2, and β_3 of $PG(5,2)$. If the Greek projective planes β_2, and β_3 intersect the base point of the base plane β_1 of $[P, \lambda']$ then the fuzzy Greek planes λ_{β_2} and λ_{β_3} are of the following form:

$$\lambda_{\beta_2} :\ \beta_2 \to [0,1]$$
$$q \to a_1$$
$$p \to a_4 \qquad for\ p \in U_3'' \setminus U_2''$$
$$p \to a_5, \qquad for\ p \in U_4'' \setminus U_3''$$

and

$$\lambda_{\beta_3} :\ \beta_3 \to [0,1]$$
$$q \to a_1$$
$$p \to a_4 \qquad for\ p \in U_3'' \setminus U_2''$$
$$p \to a_5, \qquad for\ p \in U_4'' \setminus U_3'',$$

where $(q, U_1'', U_2'', ..., H^5)$ is a chain of subspaces of H^5, in [3].

Proof. Let ϕ, φ and γ be three projective planes passing through a line in $PG(3,2)$. Three Greek planes β_1, β_2 and β_3 intersect at the base point $P_1 = (1,0,0,0,0,0)$ of $[P, \lambda'']$.

From Theorem 3.1, the base point $q = P_1 = (1,0,0,0,0,0)$, the base lines $L_1 = \{ P_1 = (1,0,0,0,0,0),\ P_2 = (1,0,0,0,0,1),\ P_3 = (0,0,0,0,0,1)\}\}$, the base plane

$\beta_1 = \{(1,0,0,0,0,1), (1,0,0,0,0,0), (0,0,0,0,0,1), (1,1,0,0,0,1), (1,1,0,0,0,0), (0,1,0,0,0,1), (0,1,0,0,0,0)\}$.

If we chose a point $(0,0,0,0,1,0)$ that is outside the plane β_1 and in the other plane

$\beta_2 = \{(1,0,0,0,0,0), (0,0,0,0,1,0), (1,0,0,0,1,0), (1,0,1,0,0,0),\ (0,0,1,0,0,0), (1,0,1,0,1,0), (0,0,1,0,1,0)\}$, then 3-dimensional projective subspace that satisfies the following equations is obtained:

$$x_5 = 0,\ \ x_1 + x_6 = 0,\ x_1 + x_2 = 0,\ x_1 + x_2 + x_6 = 0,\ x_1 = 0,\ x_2 + x_6 = 0,\ x_2 = 0,\ x_6 = 0.$$

That is, the equation of the 3- dimensional projective space obtained from these equations is $U_3'' = [0,0,x_3,x_4,0,0]$.

Also, Let a point in β_3, and outside the planes β_1 and β_2 in the other plane be $(0,1,1,0,0,0)$. Since β_3 is $\{(1,0,0,0,0,0),(0,1,1,0,1,1),(1,1,1,0,1,1),(0,1,1,0,0,0),(1,1,1,0,0,0),(1,0,0,0,1,1),(0,0,0,0,1,1)\}$, 4-dimensional projective subspace of $PG(5,2)$ has the equation $U_2'' = [0,0,0,x_4,0,,0]$.

Then the fuzzy Greek planes λ_{β_2} and λ_{β_3} are of the following form:

$$\lambda_{\beta_2}: \quad \beta_2 \to [0,1] \qquad\qquad \lambda_{\beta_3}: \quad \beta_3 \to [0,1]$$

$$q \to a_1 \qquad\qquad\qquad\qquad q \to a_1$$

$$p \to a_4 \quad\; for\; p \in U_3'' \backslash U_2'' \qquad and \qquad p \to a_4 \quad\; for\; p \in U_3'' \backslash U_2''$$

$$p \to a_5, \quad for\; p \in U_4'' \backslash U_3'' \qquad\qquad\qquad p \to a_5, \quad for\; p \in U_4'' \backslash U_3'',$$

where $(q,U_1'',U_2'',U_3'',U_4'')$ is a chain of subspaces of H^5, and $a_1 \geq a_2 \geq a_3, \geq a_4$ are reals in $[0,1]$.

Corollary 3.3 Let ϕ, φ' and γ' be three projective planes passing through a line in $PG(3,2)$. If the images of three planes under the Klein map are three Greek planes β_1, β_2', and β_3' intersect at the point on the base line different from the base point of $[P,\lambda'']$, then fuzzy Greek plane λ_{β_1} is

$$\lambda_{\beta_1}: \quad \beta_1 \to [0,1]$$

$$q \to a_1$$

$$p \to a_2 \quad for\; p \in L \backslash \{q\}$$

$$p \to a_3, \quad for\; p \in \beta_1 \backslash L$$

and the fuzzification of each the other two Greek planes of Klein quadric passing through this point is either in the form

$$\lambda_{\beta_2}': \quad \beta_2' \to [0,1]$$

$$q \to a_2$$

$$p \to a_4 \quad for\; p \in U_3'' \backslash U_2''$$

$$p \to a_5, \quad for\; p \in U_4'' \backslash U_3'',$$

or

$$\lambda_{\beta_2}': \quad \beta_2' \to [0,1]$$

$$q \to a_2$$

$$p \to a_4 \quad for\; p \in U_3'' \backslash U_2''$$

$$p \to a_6, \quad for\; p \in U_5'' \backslash U_4'',$$

or

$$\lambda'_{\beta_2}: \quad \beta'_2 \to [0,1]$$

$$q \to a_2$$

$$p \to a_5 \qquad \text{for } p \in U''_5 \setminus U''_4$$

$$p \to a_6, \qquad \text{for } p \in H^5 \setminus U''_5,$$

where $(q, U''_1, U''_2, \ldots, H^5)$ is a maximal flag in H^5 and $a_1 \geq a_2 \geq \ldots \geq a_6$ are reals in $[0,1]$.

Corollary 3.4 Let ϕ, φ'' and γ'' be three projective planes passing through a line in $PG(3,2)$. If the images of three planes under the Klein map are three Greek planes β_1, β''_2, and β''_3 intersect at the point not on the base line of $[P, \lambda']$, then the fuzzy Greek plane λ_{β_1} is

$$\lambda_{\beta_1}: \quad \beta_1 \to [0,1]$$

$$q \to a_1$$

$$p \to a_2 \qquad \text{for } p \in L \setminus \{q\}$$

$$p \to a_3, \qquad \text{for } p \in \beta_1 \setminus L$$

and the fuzzification of each the other two Greek planes of Klein quadric passing through this point is either in the form

$$\lambda''_{\beta_2}: \quad \beta''_2 \to [0,1]$$

$$q \to a_3 \qquad \text{for } p \in \beta_1 \setminus L$$

$$p \to a_4 \qquad \text{for } p \in U''_3 \setminus U''_2$$

$$p \to a_5, \qquad \text{for } p \in U''_4 \setminus U''_3,$$

or

$$\lambda''_{\beta_2}: \quad \beta''_2 \to [0,1]$$

$$p \to a_3 \qquad \text{for } p \in \beta_1 \setminus L$$

$$p \to a_4 \qquad \text{for } p \in U''_3 \setminus U''_2$$

$$p \to a_6, \qquad \text{for } p \in U''_5 \setminus U''_4,$$

or

$$\lambda''_{\beta_2}: \quad \beta''_2 \to [0,1]$$

$$q \to a_3 \qquad \text{for } p \in \beta_1 \setminus L$$

$$p \to a_5 \qquad \text{for } p \in U''_5 \setminus U''_4$$

$$p \to a_6, \qquad \text{for } p \in H^5 \setminus U''_5,$$

where $(q, U''_1, U''_2, \ldots, H^5)$ is a maximal flag in H^5 and $a_1 \geq a_2 \geq \ldots \geq a_6$ are reals in $[0,1]$.

5. CONCLUSION

Klein transformation maps a point, a line, and a projective plane of $PG(3,2)$ to appoint, a Latin plane, and a Greek plane of the Klein quadric, respectively. We give the fuzzification of Greek planes passing through the base point, any point on the base line different from the base point, and any point not on the base line of the base plane of the Klein quadric in $PG(5,2)$.

CONFLICT OF INTEREST

The authors stated that there are no conflicts of interest regarding the publication of this article.

CRediT AUTHOR STATEMENT

Münevvere Mine Karakaya: Formal analysis, Writing - original draft, Visualization, Conceptualization. **Ziya Akça:** Supervision, Visualization, Conceptualization**.**

REFERENCES

[1]   Akça Z, Bayar A, Ekmekçi S, Van Maldeghem H. Fuzzy Projective Spreads of Fuzzy Projective Spaces, Fuzzy Sets and Systems, 2006; 157(24): 3237-3247.

[2]   Akça Z, Bayar A, Ekmekçi S. On the classification of Fuzzy projective lines of Fuzzy 3-dimensional projective spaces, Communications Mathematics and Statistics, 2007; 55(2): 17-23.

[3]   Akça Z, Altıntaş A. Fuzzy Counterpart of Klein Quadric, International Electronic Journal of Geometry, 2023; 16(2): 680–688.

[4]   Bayar A, Akça Z, Ekmekçi S. A Note on Fibered Projective Plane Geometry, Information Science, 2008; 178: 1257-1262.

[5]   Ekmekçi S, Bayar A, Akça Z. On the classification of Fuzzy projective planes of Fuzzy 3-dimensional projective spaces, Chaos, Solitons and Fractals, 2009; 40: 2146-2151.

[6]   Hirschfeld JWP. Projective Geometries over Finite Fields, Oxford Mathematical Monographs, 1998.

[7]   Klein F. Uber die Transformation der allgemeinen Gleichung des zweiten Grades zwischen Linien-Koordinaten auf eine kanonische, Form Math., 1868; 539-578.

[8]   Kuijken L, Van Maldeghem H, Kerre E.E, Fuzzy projective geometries from fuzzy vector spaces, in: A. Billot et al. (Eds.), Information Processing and Management of Uncertainty in Knowledge-based Systems, Editions Medicales et Scientifiques, Paris, La Sorbonne, 1998; 1331-1338.

[9]   Lubczonok P. Fuzzy Vector Spaces, Fuzzy Sets and Systems, 1990; 38: 329-343.

[10]   Plucker J. On a New Geometry of Space, Philosophical Transactions of the Royal Society of London, 1865; 155: 725-791.

[11]   Zadeh L. Fuzzy sets, Information control, 1965; 8: 338-353.

RESEARCH ARTICLE

EXPLORING THE POTENTIAL OF SLAG WASTE GENERATED AFTER ZINC METAL RECOVERY IN GEOPOLYMER MORTAR PRODUCTION

Zahide BAYER ÖZTÜRK [1],*, Mehmet ENGÜR [2]

[1] Department of Metallurgy and Materials Engineering, Engineering-Architecture Faculty, Nevşehir Haci Bektaş Veli University, Nevşehir, Turkey.
z.ozturk@nevsehir.edu.tr - 0000-0001-8069-0694

[2] Department of Metallurgy and Materials Engineering, Institute of Science, Nevşehir Haci Bektaş Veli University, Nevşehir, Turkey
mehmet.enr@gmail.com - 0000-0002-9606-0125

Abstract

During the purification of zinc metal, the slag waste generated causes various problems such as environmental pollution and storage. It is necessary to evaluate these wastes in different areas for effective management. In this study, the effect of slag from zinc production facilities on the mechanical properties of mortars obtained by substituting slag for fly ash in geopolymers at a replacement rate of 10-50% by weight was evaluated. Mortar mixtures were subjected to various tests including workability, flexural strength, compressive strength, water-absorption, and void ratio. Mortar mixtures containing NaOH with a liquid/binder ratio 0.40 were subjected to thermal curing at 90°C for 24 hours. Flexural and compressive strength tests were conducted on 7 and 28 days of samples. As a result of the tests, it was determined that the flexural strengths of mortars produced with slag ranged from 3.0 MPa to 5.8 MPa after 28 days, while the compressive strengths ranged from 28.2 MPa to 45 MPa. Mortar mixtures containing slag achieved 48-136% higher compressive strength values than the control mixture containing fly ash (19MPa). High-temperature tests (400, 600, 800°C) revealed that mortar mixtures containing up to 30% slag achieved higher flexural and compressive strengths than the control. As the amount of slag in the mortar increased, water absorption and void ratios also increased. These results indicate that slag waste can enhance the mechanical performance of geopolymers.

1. INTRODUCTION

Geopolymers are promising inorganic polymer materials that stand out for their high mechanical performance and durability, as well as their potential for environmental protection and energy saving. Additionally, they boast lower greenhouse gas emissions compared to Portland cement production [1]. Geopolymer rely on the dissolution of alumina and silica-containing materials obtained from industrial waste or by-products in alkaline solutions, forming of 3D polymer chains connecting Al-Si-O structures. Various industrial wastes such as metakaolin, fly ash, blast furnace slag, and waste ceramic powders are among these materials. This chemical process offers a more environmentally sustainable method for material production [2-3]. Fly ash, a significant raw material in geopolymers production, is a waste product obtained from the capture of micron-sized particles emitted into the atmosphere from thermal power plant chimneys during coal combustion, collected in ash silos through electrostatic or mechanical filters [4]. This ash is widely used in geopolymer production, and the increasing demand for its use has led to increased costs due to the distance between production sites and thermal power plants. However,

---

the classification of fly ash and its expanding usability in this field has enabled its use as an alternative mineral additive, aggregate, or filler material in cement, concrete, soil improvement, and road applications. While many European countries are moving towards closing coal-fired power plants, Turkey is encouraging investments in renewable energy sources and restrictions on fly ash production are anticipated in our country's future [5-6].

Today, in the pursuit of sustainable construction materials, the use of waste powders as a fundamental material in the production of geopolymer mortar and concrete has emerged. This approach not only proves significant in terms of sustainability but also contributes to the recycling of waste generated in the relevant sector. Studies in the literature have evaluated how various types of waste, such as red mud [7-8], waste powders from brick production [9], waste from ceramic factories [5, 10-11], stone cutting waste [12], and ash-slag waste [13, 14], affect the performance of geopolymers. These evaluations highlight the potential of various post-production wastes from different sectors to contribute to the physical and mechanical properties of geopolymers.

The use of geopolymers in conjunction with waste presents an innovative approach to solving waste management issues and contributes to recycling, ensuring the efficient utilization of resources. Therefore, studies focusing on the utilization of different wastes in geopolymers hold significant potential in both industrial waste management and construction materials. In our study, we utilized waste from the Çinkur Factory (Çinkom, Kayseri) as an alternative material in place of fly ash in fly ash-based geopolymers.

The Zinc Production Factory is a recycling company that processes filter dust from iron and steel factories located in various provinces and regions of Turkey such as Iskenderun, Izmir, Osmaniye, Canakkale, and Bursa, to produce enriched zinc concentrate. This enriched zinc concentrate, which is entirely produced for export purposes and provides significant foreign currency inflow to our country, is processed as an intermediate product for use in metal production, although it is not a final product [15]. At the Çinkom Plant, zinc ore is processed in a rotary kiln with coke and limestone at temperatures between 900-1300°C to obtain zinc oxide. During this process, the zinc oxide is separated, and the residual material is removed from the furnace as slag in the form of iron calcium silicate and stored. Each year, after obtaining the desired metal compositions from the rotary kiln, granulated slag is obtained [16]. However, research on the use of zinc ore waste is quite limited. Studies by Alwaeli [17] examined the use of granulated lead-zinc slag in concrete by replacing sand at ratios of 25-50-75 and 100 percent and compared it with standard concrete. As a result of these studies, it was found that the slag exhibited higher strength in concrete samples and also attenuated gamma radiation [18]. Bayer Ozturk et al. [16] investigated the usability of the same slag in the concrete sector at certain ratios instead of aggregate and its effects on concrete performance. Similar strength results were obtained with aggregate concrete. In another sector, the effects of waste dust processed as raw and calcined pigment forms on the color performance of wall tile glazes were examined. It was found that it could be used to obtain brown tones on glazed tile surfaces without causing defects such as pinholes or cracks [19].

In a few limited studies involving the use of slag generated after zinc extraction in geopolymers, the compressive strength and toxic leaching of this slag-based geopolymer have been investigated. Geopolymer mortars produced with pure chemical reactants were used to study the solidification mechanism of heavy metals to eliminate the effects of components on the slag. Geopolymers containing ingredients such as metakaolin, cement, slag, and coal gangue were examined for their solidification behaviour by analysing their ion potential and electronegativity values [20-21].

This study aims to investigate the effect of zinc plant slag on the mechanical performance of geopolymer mortar. In this context, separate mortars were prepared with 12M NaOH at water-to-binder ratios of 0.40 and then cured at 90°C for 24 hours. The resulting samples were evaluated for physical and mechanical properties such as workability, unit weight, water absorption, void ratio, flexural strength,

and compressive strength. The experiments were conducted to thoroughly analyse the impact of this slag on the performance of geopolymer mortars. By focusing on the mechanical performance of geopolymer mortar incorporating zinc plant slag, the study fills a gap in understanding how this specific material affects the strength and durability of mortar formulations. This study aims to fill the existing comprehensive research gap regarding the inclusion of zinc ore slag in geopolymers.

2. EXPERIMENTAL

2.1. The used Material Properties

Slag obtained from the Zinc production facility (Çinkom, Kayseri), Sugözü thermal power plant fly ash (Class F), sodium hydroxide as the alkali activator, water, and river sand was used to obtain geopolymer mortars. The purity of sodium hydroxide used as activator is 98.2%. The saturated dry surface density of the river sand used in the study is 2.71, and the water absorption is 1.81% (TS EN 1097-6) [22]. The purity of the sodium hydroxide used as an activator is 98.27%. Tap water was used for preparing the mortars (TS EN 1008) [23]. The slag obtained from the zinc production facility was ground in a ring mill and sieved through a 125-micron sieve before use. The chemical analysis of the slag waste and fly ash is given in Table 1. The slag contains 14.18% SiO_2, 19.32% Fe_2O_3, and 31.93% CaO [19]. The fly ash contains 55.10% SiO_2, 27.41% Al_2O_3, and 5.93% Fe_2O_3. The sieve analysis of river sand is presented in Table 2. The phase analysis (X-ray diffraction) graphs of the slag and fly ash used are presented in Figures 2 and 3. In the phase analysis of fly ash, mullite, quartz, hematite, and low-intensity CaO peaks are notable, while in the phase analysis of slag, riversiderite, wustite, and calcium iron oxide phases were obtained. The occurrence of the identified phases in the waste, which contains high amounts of iron (Fe), calcium (Ca), and relatively high amounts of silicon (Si) in its chemical composition, is an expected condition.

**Figure 1.** Slag waste site, size reduction, and geopolymer mortars produced with slags
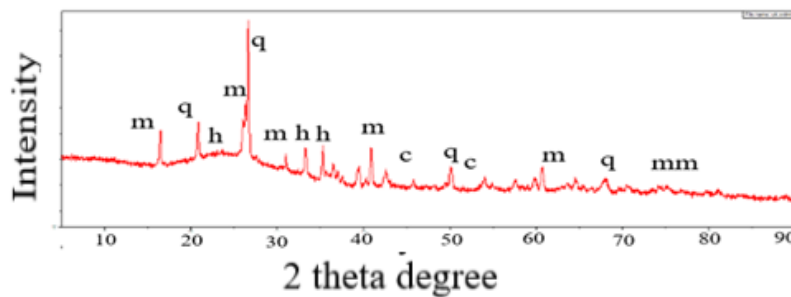
Figure 2. The XRD graph of fly ash (m: mullite, q: quartz, h: hematite, c: CaO)
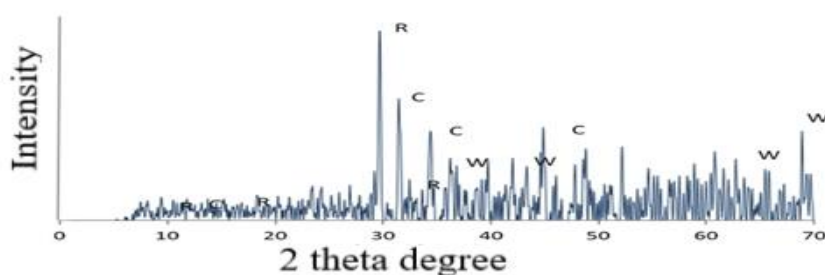
Figure 3. XRD graph of slag waste (R: riversiderite, w: wustite, c: Calcium ferro oxide) [18]

The morphology of fly ash and slag waste was investigated using scanning electron microscopy (FESEM, Zeiss Gemini 500) in Figure 4. The microstructures of the slag waste revealed the presence of irregularly shaped particles, measuring approximately 5-10 μm in size. Spherical particles ranging in size from two to five microns captured interest in the microstructure of the fly ash.
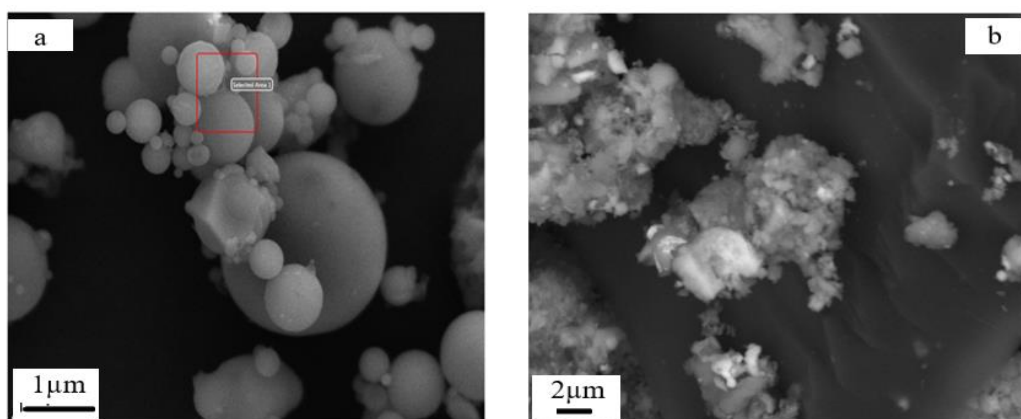
Figure 4. Secondary electron microscopy image of a) fly ash, b) slag waste

Table 1. The chemical analysis of the slag and fly ash used in the mixtures

Oxides	Slag	Fly ash
SiO_2	14.18	55.10
$Al_2O_3+TiO_2$	6.79	27.41
Fe_2O_3	19.32	5.92
CaO	31.93	2.44
MgO	1.54	1.99
SO_3	3.81	0.20
Na_2O	0.21	0.52
K_2O	0.68	3.44
BaO	0.07	0.08
PbO	2.60	-
ZnO	6.31	-
Loss on ignition	12.0	3.45

Table 2. The sieve analysis values of river sand.

Sieve diameter, mm	Sieved sand,%
5	100.0
4	96.0
3	88.3
2	77.3
1	54.9
0.60	26.5
0.45	24.5
0.33	10.9
0.19	3.4

2.2. Method

Fly ash was used at a rate of 450 g in single usage, while in combination with slag, it was replaced with slag at rates of 10-20-30-40-50%, resulting in weights of 405 g, 360 g, 315 g, 270 g, and 225 g, respectively. Codes were assigned to mortar mixtures based on the percentage of waste included in the mixture. For example, in the control mortar with only fly ash, labelled SM-0 (slag mortar-0), there was no slag present, whereas SM-10 indicates that 10% (45 g) of slag waste was used (Table 3). In the created mixtures, the liquid-to-binder ratio was determined as 0.40. The amount of water was added to glass jars to prepare the solution, and sodium hydroxide was added on top. The chemical was completely dissolved by shaking for approximately 1 minute. Since the reaction of sodium hydroxide with water is exothermic, it was expected to cool down to room temperature. Mortars were prepared by pouring the prepared solutions into moulds with dimensions of 40×40×160 mm according to TS EN 196-1[24].

Table 3. Mixture Ratios and codes in Mortars

Sample/	Slag Waste %	Fly ash %	Sand (g)	Water (g)	NaOH (g)
Control-SM-0	0	100	1350	180	87
SM-10	10	90	1350	180	87
SM-20	20	80	1350	180	87
SM-30	30	70	1350	180	87
SM-40	40	60	1350	180	87
SM-50	50	50	1350	180	87

After mixing the solution, ash, and slag in the mixing vessel for the first 30 seconds, river sand was added during the second 30 seconds. Then, it was mixed at high speed for 30 seconds under the standards. The mixing ceased and the mixture on the walls of the vessel was gathered in the center for the first 30 seconds, and then it was left for a total of 90 seconds. Subsequently, mixing continued at high speed for an additional 60 seconds to complete the mixing process. The mixed mortars were subjected to workability tests according to the (TS EN 1015-3) [25] standard. The samples for workability assessment were poured into a 3-part mould with dimensions of 40x40x160 mm. The pouring process was carried out in 2 stages. The poured samples were subjected to thermal curing in an oven at 90°C for 24 hours. After being removed from the oven, the mortars were subjected to flexural and compressive strength tests according to the (TS EN 1015-11) [26] standard after waiting for 7 and 28 days. The water absorption and void ratio of the samples waiting for 28 days were examined. Additionally, after the 28-day waiting period, the strengths of the mortars were examined after high-temperature application in a high-temperature furnace at 400, 600, and 800°C for 30 minutes with a temperature increase of 10°C/min.

3. RESULTS AND DISCUSSIONS

In the study, workability tests were initially applied to the freshly produced mortars, and the results are shown in Figure 5. The workability results of the samples produced with 10-40% slag waste ranged from 173-110 mm. When compared with the control sample containing 100% fly ash (225 mm), it was observed that the workability values decreased. Previous studies have indicated that factors such as specific surface area, particle shape, activator ratio, chemical composition, and reaction rate affect workability [12, 27-28]. In mortar mixtures where the activator ratio is constant, the use of slag, due to its irregular physical shapes (as shown in Figure 4) and differences in high Ca and Fe content, reduced workability compared to the smooth flow of fly ash with spherical particles.
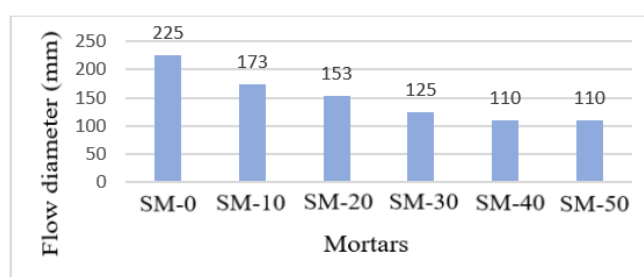
**Figure 5.** Workability results of mortars

The flexural strengths of the produced samples at 7 and 28 days are shown in Figure 6. The highest strength value at 7 days was 4.82 MPa in sample SM-20, and the highest strength at 28 days was 5.8 MPa in sample SM-20. The flexural strength values of samples containing 10%, 20%, and 30% slag at 28 days were 5.7 MPa, 5.8 MPa, and 3 MPa, respectively. When examining the strengths at 7 days, values of 3.79 MPa, 4.82 MPa, and 3.11 MPa were reached. The flexural strength of sample SM-50 was lower compared to the control sample at 7 and 28 days. For samples with 10-20% slag additives, the flexural strengths at 7 days were 45.21-84.67% higher than the control sample, and at 28 days, they reached 46.15-48.71% higher strength. The good bonding between the geopolymer mortar and aggregate is achieved through strong Si-O-Si interactions. While Si plays a significant role in alkali gel formation alongside Al and Ca, an increase in slag content leads to a decrease in the Si and Al content of the structure [27]. Therefore, the flexural strengths of mortars decrease when slag substitution exceeds 30% instead of fly ash.
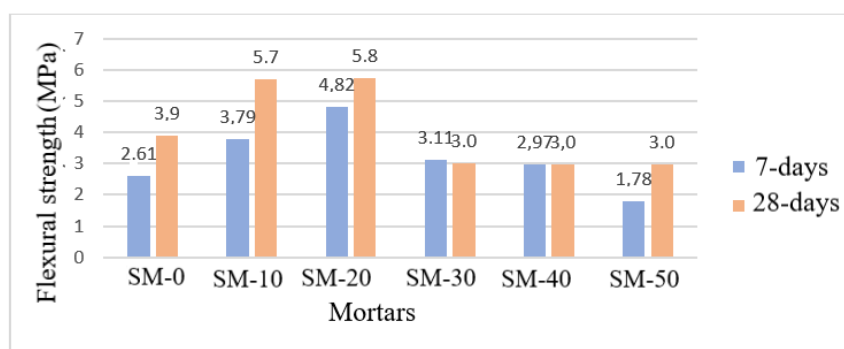
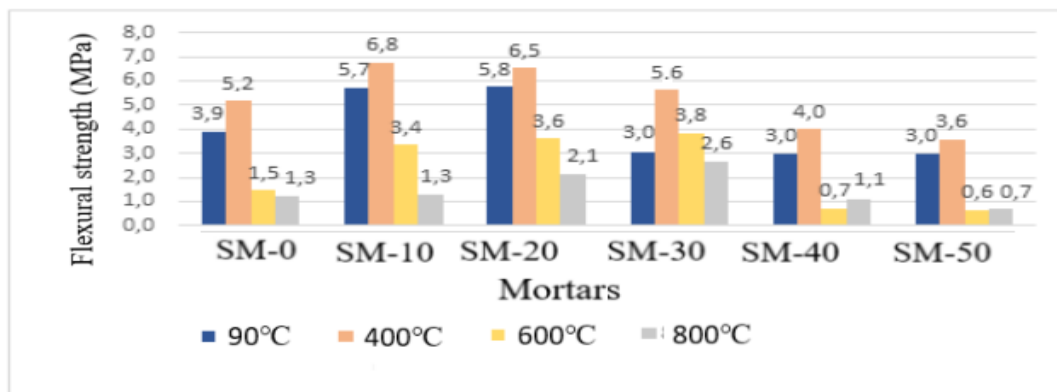**Figure 6.** Flexural strength results of mortars

The compressive strength results of the mortars are shown in Figure 7. As a result of the analyses, strength increases ranging from 77-106% were observed in samples SM-10-SM-50 up to a 30% substitution rate during the 7-days period. However, a decreasing trend in strengths was observed once

the 30% substitution rate was exceeded; however, in sample SM-50 (at a 50% substitution rate), a 23% increase compared to the control sample was determined. When comparing the 28-day compressive strength results with the control sample, it was found that samples SM10-SM50 reached compressive strengths 51-170% higher than the control sample. In the literature on geopolymer mortars, many studies indicate that the use of materials rich in Ca increases strength [29-33]. Additionally, an increase in the SiO_2/Al_2O_3 ratio may lead to an increase in strength by leading to Si–O–Si bonds, which are stronger than Si–O–Al bonds [28, 34-36]. In this context, the findings supporting the increase in flexural and compressive strength values of samples, particularly at substitution rates up to 30%, due to these oxides in the slag content, are supported.
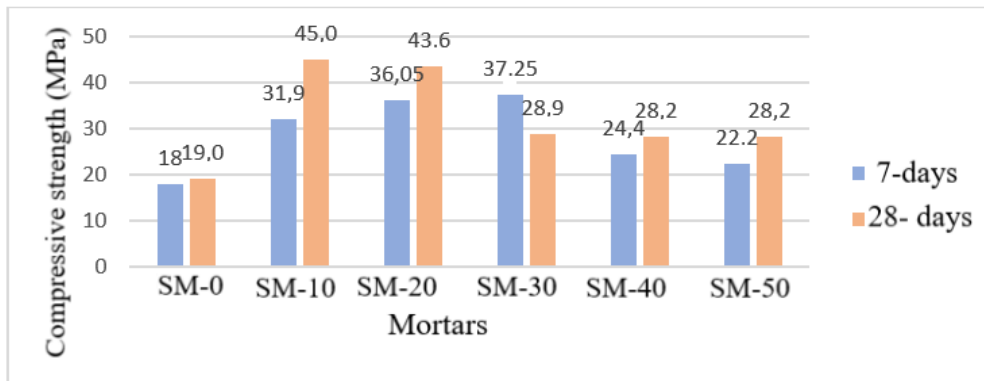
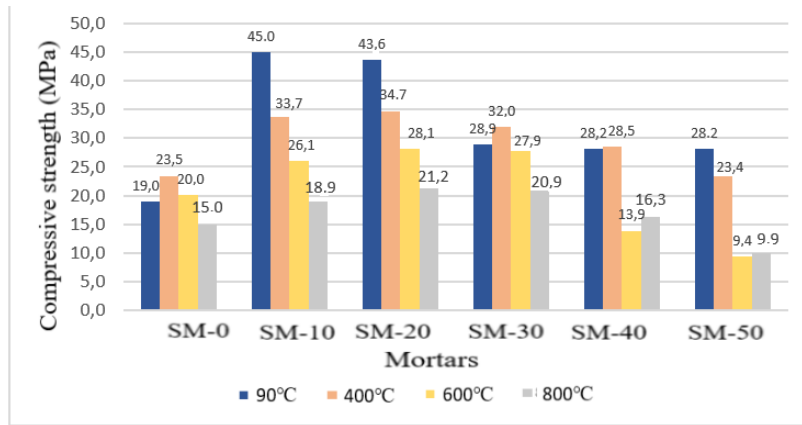**Figure 7.** Compressive strength results of mortars

The strength graphs of the produced samples before and after high temperatures (400-600-800℃) are shown in Figures 8 and 9. It is observed that the strengths increased up to a 30% slag substitution rate when compared to the control sample (SM-0). It can be seen that the strength results increased at 400℃, while the strength results of the mortars subjected to 600℃ and 800℃ decreased.

Figure 8. Flexural strength results of mortars after high temperature exposure

After the exposure to 400℃ temperature, it was detected that the flexural strengths of mortars with slag additives up to 30% increased by 7.7-30.76% compared to the control sample. At the same time, it was found that the flexural strengths decreased in samples with 40% and 50% additives. After the exposure to 600℃ high temperature, an increase of 126-153% was determined in flexural strengths up to a 30% substitution rate, and at 800℃, an increase of 61-100% was observed in flexural strength for 20-30% additions compared to the control sample, after which a decrease in flexural strength was observed after 30% addition.

Figure 9. Compressive strength results of mortars after high temperature exposure.

When the compressive strength results of the samples after high-temperature exposure were examined, it was determined that the change in strength increased by 43.40%, 47.65%, 36%, and 21.27% as the amount of additive increased in samples exposed to 400°C temperature. The SM-50 sample was found to be the same as the control sample at 400°C (23.5≈23.4). The increase in strength in samples containing 10-30% slag at 600°C temperature ranged between 30.5-40.5%. The increase in strength in mortars containing 10-40% slag exposed to 800°C temperature ranged between 8.6-41.33%. It was observed that as the temperature increased after the high-temperature application, the strengths decreased, but compared to the control sample, an increase in strengths was obtained for all three temperatures up to 30% slag addition. This indicates the substitutability of slag for fly ash up to 30%.

The decrease in compressive strength in mixtures can be attributed to several factors: the rise in temperatures (e.g., 600 and 800°C), reduced Si/Al content resulting from slag substitution exceeding 30%, and the formation of porosities due to reactions at elevated temperatures.

The measured water absorption and void ratio results of the mortars after 28 days are presented in Figure 10. The water absorption of mortars containing slag ranges from 3.24% to 7.63%, while the void ratio ranges from 6.39% to 14.83%. The water absorption rate of the control sample is 3.73%, while the void ratio is 7.41%. It is observed that as the percentage of slag in the mortar increases, both the void ratio and water absorption increase compared to the control mortar. It is noted that the water absorption in sample SM-10 is lower than that of the control sample. The reason for the increase in water absorption and void percentages in SM30-SM50 mortars compared to the control sample is the amount of CaO and Fe_2O_3 in the slag content. The increased presence of these components has enhanced the pozzolanic effect, altering the physical and internal structure of the mortar, thus increasing its water absorption capacity.
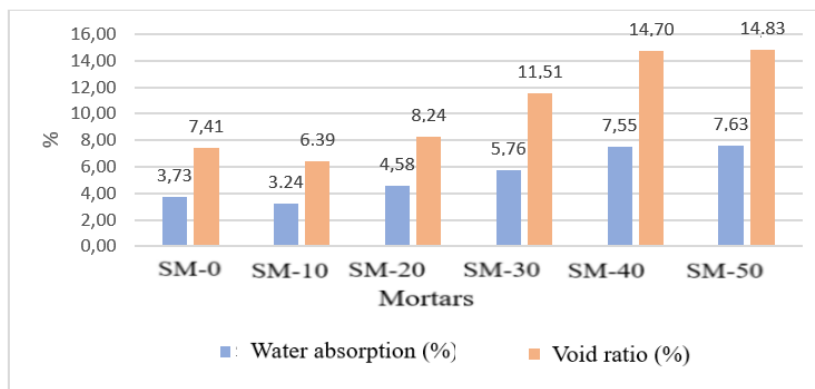
Figure 10. The water absorption and void ratio results of the mortars

4. CONCLUSIONS

This study evaluated the effect of slag waste generated after zinc recovery on the physical and mechanical properties of fly ash-based geopolymers, and reached the following conclusions:

• The workability values of produced geopolymers decreased as the slag waste content increased.
• Samples with slag substitution achieved higher flexural and compressive strength values compared to the control mix. This upward trend in strength continued up to a 30% waste addition, but decreased after the addition of 30% waste.
• It was observed that flexural strengths increased at 400 ℃ when the mortar was exposed to high temperatures. However, after exposure to 600 and 800 ℃, a downward trend in the flexural strength of the mortars was observed. Nevertheless, the strength results of mortars containing slag were higher than those of the control sample.
• The compressive strength results, which were examined for the effect of high temperatures, showed a similar trend to the flexural strength values.
• Compared to the control sample, the apparent porosity and water absorption values of mortars with slag were slightly higher.
• The use of slag in fly ash-based geopolymers could be a significant step towards reducing environmental impacts in the construction sector and producing high-strength geopolymers. This utilization can contribute to environmental sustainability by promoting the recycling of waste materials and more efficient use of resources.

ACKNOWLEDGEMENTS

CONFLICT OF INTEREST

The author(s) stated that there are no conflicts of interest regarding the publication of this article.

CRediT AUTHOR STATEMENT

Zahide Bayer Öztürk: Supervision, Resources, Writing - original draft, Visualization, Conceptualization, **Mehmet Engür:** Resources, Investigation, Methodology, Validation.

REFERENCES

[1]   Sun Q, Zhu H, Li H, Zhu H, Gao M. Application of response surface methodology in the optimization of fly ash geopolymer concrete, Romanian J Mater. 2018; 48; 45-52.

[2]   Atabey İİ, Bayer Ozturk Z. Investigation of usability of ceramic sanitaryware wastes in geopolymer mortar production, Int. J. Engineering Res. Develop, 2021; 13; 212-219.

[3]   Robayo-Salazar RA, de Gutiérrez, RM. Natural Volcanic Pozzolans as an Available Raw Material for Alkali-activated Materials in the Foreseeable Future: A Review, Constr. Build. Mater. 2018; 189, 109–118.

[4]   Kaplan G, Gültekin AB. Yapı Sektöründe Uçucu Kül Kullanımının Çevresel ve Toplumsal Etkiler Açısından İncelenmesi, International Sustainable Building Symposium, 2010; 1-8, Ankara.

[5]   Eser A, Bayer Ozturk Z, Atabey İİ, Çelikten S. Mechanical properties of geopolymer mortars produced with fly ash and various ceramic industry wastes, Nigde Omer Halisdemir University J Engineering Sci. 2024; 13; 550-557.

[6]   Web   site-1:   https://www.dw.com/tr/avrupak%C3%B6m%C3%B%   C3%BC-santralleri-kapat%C4%B1yor

[7]   Mudgal M, Singh A, Chouhan RK, Acharya A, Srivastava AK. Fly ash red mud geopolymer with improved mechanical strength, Clean. Engineering Tech, 2021; 4; 100215.

[8]   Kulkarni S. Experimental Study on Red Mud, Fly Ash, GGBFS Based Geopolymer Concrete. International J Engineering Res. Tech, 2018; 7; 107- 111.

[9]   Amin SK, El-Sherbiny SA, El-Magd AAMA, Belal A, Abadir MF. Fabrication of geopolymer bricks using ceramic dust waste. Construction and Building Materials, 2017;157; 610–620.

[10]   Bayer Ozturk Z., Cırık R., Atabey II. Sustainable environment approach by the usage of ceramic pottery waste in geopolymer mortar. Inter. J Envi. Sci. Tech, 2023; 20; 7577-7588.

[11]   Rashad AM, Essa GMF. Effect of ceramic waste powder on alkali-activated slag pastes cured in hot weather after exposure to elevated temperature. Cement and Concrete Composites, 2020; 111; 103617.

[12]   Bayer Ozturk Z, Çam T. Performance of eco-friendly fly ash-based geopolymer mortars with stone-cutting waste, Materials Chemistry and Physics, 2023; 307; 128112.

[13]   Mehta A, Siddique R. An overview of geopolymers derived from industrial by-products, Const. Build. Mater. 2016; 127; 183–198.

[14]   Aydın T, Pehlivanlı ZO. Jeopolimer esaslı gözenekli hafif yapı malzemelerinin geliştirilmesi, Dicle University J Engineering. 2017; 8; 227-236.

[15]   Web sitesi-2: http://cinkom.com/enindex.html

[16]   Bayer Ozturk Z, Bağıran MN, Sağlar B, Arslan L, Aycan Ş. Agrega Olarak Çinko Madeni Cürufu Kullanımının Beton Basınç Dayanımına Etkisi. J Int. Engineering Res. Develop. 2018; 10; 144-152.

[17]   Alwaeli, M. Investigation of gamma radiation shielding and compressive strength properties of concrete containing scale and granulated lead-zinc slag wastes. J. Clean. Prod. 2017; 156; 157–162.

[18]   Alwaeli, M. Application of granulated lead–zinc slag in concrete as an opportunity to save natural resources. Radiat. Phy. Chem, 2013;83; 54–60.

[19]   Bayer Ozturk Z, Pekkan K, Taşçı E, Yılmaz S. The effect of granulated lead–zinc slag on aesthetic and microstructural properties of single-fired wall tile glazes, J. Australian Ceram.Soc. 2020; 56; 609-617.

[20] Zhang Q, Cao X, Sun S, Yang W, Fang L, Ma R, Lin C, Li H. Lead zinc slag-based geopolymer: Demonstration of heavy metal solidification mechanism from the new perspectives of electronegativity and ion potential. Environmental Pollution 2022; 293; 118509

[21] Zhao S, Xia M, Yu L, Huang X, Jiao B, Li D. Optimization for the preparation of composite geopolymer usingresponse surface methodology and its application in lead-zinc tailings solidification. Construct. Build. Mater. 2021; 266; 120969.

[22] TS EN 1097-6, Agregaların mekanik ve fiziksel özellikleri için deneyler - Bölüm 6: Tane yoğunluğunun ve su emme oranının tayini, Türk Standartları Enstitüsü, Ankara, 2013.

[23] TS EN 1008, Beton-Karma suyu-Numune alma, deneyler ve beton endüstrisindeki işlemlerden geri kazanılan su dahil, suyun, beton karma suyu olarak uygunluğunun tayini kuralları, Türk Standartları Enstitüsü, Ankara, 2003.

[24] TS EN 196-1, Çimento Deney Metotları – Bölüm 1: Dayanım Tayini, Türk Standartları Enstitüsü, 2009.

[25] TS EN 1015-3/A1, Kâgir harcı- Deney metotları- Bölüm 3: Taze harç kıvamının tayini (yayılma tablası ile), Türk Standartları Enstitüsü, Ankara, 2006.

[26] TS EN 1015-11/A1, Kâgir Harcı-Deney Metotları-Bölüm 11: Sertleşmiş Harcın Basınç ve Eğilme Dayanımının Tayini, Türk Standartları Enstitüsü, Ankara, 2013.

[27] Shilar FA, Gnachari SV, Patil VB, Nisar KS, Abdel-Aty AH, Yahia IS. Evaluation of the effect of granite waste powder by varying the molarity of activator on the mechanical properties of ground granulated blast-furnace slag-based geopolymer concrete, Polymers, 2022; 14; 306.

[28] Liew YM, Heah CY, Li L, Jaya NA, Abdullah MMAB, Tan SJ, Hussin K. Formation of one-part-mixing geopolymers and geopolymer ceramics from geopolymer powder, Construct. Build. Mater. 2017; 156, 9-18.

[29] Qian J, Song M, Scrivener K, Favier A. (Eds.) Study on Influence of Limestone Powder on the Fresh and Hardened Properties of Early Age Metakaolin Based Geopolymer, Calcined Clays for Sustainable Concrete, Springer, 2015; pp. 253-259.

[30] Bernal SA, Rodriguez ED, Gutierrez M, Gordillo M, Provis JL. Mechanical and thermal characterization of geopolymers based on silicate-activated metakolin/slag blends. J. Mater. Sci. 2011; 46, 5477-5486.

[31] Yip CK, Provis JL, Lukey GC, Deventer JSJ. Carbonate mineral addition to metakalin-based geopolymers, Cement Concr. Compos., 2008; 30; 979-985.

[32] Peyne J, Gautron J, Doudeau J, Joussein E, Rossignol S. Influence of calcium addition on calcined brick clay based geopolymers: a thermal and ftir spectroscopy study, Construct. Build. Mater. 2017; 152; 794-803.

[33] Çelikten S. Mechanical and microstructural properties of waste andesite dust-based geopolymer mortars, Adv. Powder Technol., 2021; 32, 1-9.

[34] Duxson P, Provis JL, Lukey GC, Mallicoat SW, Kriven WM, Deventer JSJ. Understanding the relationship between geopolymer composition, microstructure and mechanical properties, Colloids Surfaces A Physicochem. Eng. Asp., 2005; 269; 47-58.

[35] Ozer I, Soyer-Uzun S. Relations between the structural characteristics and compressive strength in metakaolin based geopolymers with different molar Si/Al ratios, Ceram. Int.,2015; 41; 10192-10198.

[36] Lahoti M, Yang EH, Tan KH. Influence of mix design parameters on geopolymer mechanical properties and microstructure, Ceram. Eng. Sci. Proc. 2017; 37; 21-33.

RESEARCH ARTICLE

APPLICATION OF THE GENERALIZED KUDRYASHOV METHOD TO THE KOLMOGOROV-PETROVSKII-PISKUNOV EQUATION

Zeynep AYDIN [1], [*], Filiz TASCAN [2]

[1] Department of Mathematics and Computer Sciences, Faculty of Science, Eskişehir Osmangazi University, Eskişehir, Turkey
zeynepaydinn10@gmail.com - 0009-0002-0003-9370

[2] Department of Mathematics and Computer Sciences, Faculty of Science, Eskişehir Osmangazi University, Eskişehir, Turkey
ftascan@ogu.edu.tr - 0000-0003-2697-5271

Abstract

In this paper, we investigate the general solutions to the Kolmogorov-Petrovskii-Piskunov equation using the generalized Kudryasov method. It was demonstrated that all produced answers are supplied by exponential function solutions using the symbolic computer program Maple. These solutions are helpful for fluid dynamics, optics, and other fields. Lastly, we have presented some graphs for exact solutions of these equations with special parameter values. For the development of this method, the versatility and dependability of programming offer eclectic applicability to high-dimensional nonlinear evolution equations. The obtained results provided us with valuable insights on the suitability of the novel Kudryashov technique.

1. INTRODUCTION

Partial differential equations are an important part of applied mathematics. Many physical, social and natural events have been solved by modeling with non-linear partial differential equations. Examples of these include plasma physics, optical communications, laser technology, signal processing, and others, representing a significant challenge. Applied mathematicians have developed some methods to solve these models. Some of these methods; symmetry method [1], (G'/G)-expansion method [2], tanh-coth method [3], Baclund transformation method [4], exp-function method [5], first integral method [6], Kudryashov method [7] and so on.

Generalized Kudryashov method is one of the method to solve nonlinear partial differential equations. Also the generalized Kudryashov method is a more useful and effective approach to study consistent solutions of NLEEs. Therefore, we used this method to study the Kolmogorov-Petrovskii-Piskunov equation. The aim of this research is to create new analytical solutions for the Kolmogorov-Petrovskii-Piskunov equation using the method mentioned above.

$$u_t - u_{xx} + \mu u + \nu u^2 + \delta u^3 = 0. \tag{1}$$

Corresponding Author: zeynepaydinn10@gmail.com

This equation, the process we will examine in this article, first appeared in the examination of genetic models. It was used in some physics, biological and physical models. The KPP equation includes various nonlinear equations well known in mathematical physics; the Newell-Whitehead equation for $\mu = -1$, $v = 0$, $\delta = 1$ values, the FitzHugh-Nagumo equation for $\mu = a$, $v = -(a + 1)$, $\delta = 1$ values, and it is a special case of Fisher equation $\mu = -1$, $v = 1$, $\delta = 0$ [8].

In this study, firstly the steps of the generalized Kudryashov method will be defined. Then, by applying the generalized Kudryashov method to the Kolmogorov-Petrovskii-Piskunov equation, traveling wave solutions will be obtained for six different cases. In addition, 2D and 3D graphics of these solutions drawn with Maple will be given according to the special selected values. The results obtained will be shared in the last section.

2. GENERALIZED KUDRYASHOV METHOD

In this section, the working algorithm of the generalized Kudryashov method will be examined. Firstly, let's consider a nonlinear partial differential equation as follows.

$$\Omega\big(u, u_t, u_x, u_{tt}, u_{xy}, u_{xx}, \dots \big) = 0 \tag{2}$$

where Ω, represents to a polynomial containig derivates of $u_i (i = x, y, \dots, t)$.

Step 1: To reduce this partial differential equation to an ordinary differential equation, we substitute the equivalents of the partial derivatives in the equation using the $u(x, y, \dots, t) = U(\vartheta)$, $\vartheta = z_1 x + z_2 y + \cdots + z_n t$ travelling wave equation, where $z_k (k = 1,2,3, \dots n)$ are constants. Then we obtain the following ordinary differential equation

$$G(U, U_\vartheta, U_{\vartheta\vartheta}, U_{\vartheta\vartheta\vartheta}, \dots) = 0. \tag{3}$$

Step 2: In the generalized Kudryashov method, the solution of the ordinary differential equation seek in rational form as follows.

$$U(\vartheta) = \frac{\sum_{i=0}^{N} a_i Q^i(\vartheta)}{\sum_{i=0}^{M} b_j Q^j(\vartheta)} \tag{4}$$

where $a_i (i = 0,1, \dots, N)$, $b_j (j = 0,1, \dots, M)$ are different coefficients of $Q^i(\vartheta), Q^j(\vartheta)$ that are not zero. $Q(\vartheta)$ is the following function which is the solution of the equation $Q'(\vartheta) = Q^2(\vartheta) - Q(\vartheta)$

$$Q(\vartheta) = \frac{1}{1 + Ae^\vartheta} \tag{5}$$

here, A is the integral constant and is a non-zero and positive real number to be determined later.

Step 3: We need M and N values to find the $U(\vartheta)$ solution given in (4). To find these values, we use homogenous balance between the highest degree nonlinear term and the highest order linear term in the ordinary differential equation.

Step 4: After substituting Solution (4) into Equation (2), the left-hand side of Equation (2) can be converted into a polynomial in powers of $Q(\vartheta)$. Collecting the terms that include the same power of $Q(\vartheta)$ and equating each coefficient equal to zero, one obtains an algebraic equation system for unknown values.

Step 5: We solve the algebraic equations in the Step 4 with the help of Maple. Substituting the obtained values into Solution (4) by considering Equation (5), the solutions of the NLPE in equation (1) can be obtained.

3. APPLICATION OF THE GENERALIZED KUDRYASHOV METHOD TO THE KOLMOGOROV-PETROVSKİİ-PİSKUNOV EQUATION

In this section, the exact solutions of the KPP equation will be found by the generalized Kudryashov method.

If the wave transformation $u(x,t) = U(\vartheta) = kx - wt$ is applied to the KPP equation in partial differential form given in (1), we obtain the following ordinary differential equation.

$$-wU_\vartheta - k^2 U_{\vartheta\vartheta} + \mu u + vU^2 + \delta U^3 = 0. \tag{6}$$

Considering the homogenous balance between the highest order derivative term $U_{\vartheta\vartheta}$ with the highest degree nonlinear term U^3,

$$3N - 3M = N - M + 2. \tag{7}$$

If we choose M=1, then N=2 and equation (4) takes the form

$$U(\vartheta) = \frac{a_0 + a_1 Q(\vartheta) + a_2 Q^2(\vartheta)}{b_0 + b_1 Q(\vartheta)}, \tag{8}$$

where a_0, a_1, a_2, b_0 and b_1 are constants to be determined later.

Substituting Solution (8) into the Equation (6) yields a polinamial in $Q(\vartheta)$. A system of algebraic equations is obtained by setting each coefficient of the equation to zero.

$Q^6 = -2k^2 a_2 b_1^2 + \delta a_2^3,$

$Q^5 = -6k^2 a_2 b_0 b_1 + 3k^2 a_2 b_1^2 + 3\delta a_1 a_2^2 + va_2^2 b_1 - wa_2 b_1^2,$

$Q^4 = -6k^2 a_2 b_0^2 + 9k^2 a_2 b_0 b_1 - k^2 a_2 b_1^2 + 3\delta a_0 a_2^2 + 3\delta a_1^2 a_2 + \mu a_2 b_1^2 + 2va_1 a_2 b_1 + va_2^2 b_0 - 3wa_2 b_0 b_1 + wa_2 b_1^2,$

$Q^3 = 2k^2 a_0 b_0 b_1 + k^2 a_0 b_1^2 - 2k^2 a_1 b_0^2 - k^2 a_1 b_0 b_1 + 10k^2 a_2 b_0^2 - 3k^2 a_2 b_0 b_1 + 6\delta a_0 a_1 a_2 + \delta a_1^3 + \mu a_1 b_1^2 + 2\mu a_2 b_0 b_1 + 2va_0 a_2 b_1 + va_1^2 b_1 + 2va_1 a_2 b_0 + wa_0 b_1^2 - wa_1 b_0 b_1 - 2wa_2 b_0^2 + 3wa_2 b_0 b_1,$

$Q^2 = -3k^2 a_0 b_0 b_1 - k^2 a_0 b_1^2 + 3k^2 a_1 b_0^2 + k^2 a_1 b_0 b_1 - 4k^2 a_2 b_0^2 + 3\delta a_0^2 a_2 + 3\delta a_0 a_1^2 + \mu a_0 b_1^2 + 2\mu a_1 b_0 b_1 + \mu a_2 b_0^2 + 2va_0 a_1 b_1 + 2va_0 a_2 b_0 + va_1^2 b_0 + wa_0 b_0 b_1 - wa_0 b_1^2 - wa_1 b_0^2 + wa_1 b_0 b_1 + 2wa_2 b_0^2,$

$Q^1 = k^2 a_0 b_0 b_1 - k^2 a_1 b_0^2 + 3\delta a_0^2 a_1 + 2\mu a_0 b_0 b_1 + \mu a_1 b_0^2 + va_0^2 b_1 + 2va_0 a_1 b_0 - wa_0 b_0 b_1 + wa_1 b_0^2,$

$Q^0 = \delta a_0^3 + \mu a_0 b_0^2 + va_0^2 b_0.$

Using Maple to solve the aforementioned system of algebraic equations yields the following cases.

Case 1:

$$v = -\frac{(8k^2+\mu)\sqrt{2}}{4\sqrt{\frac{1}{\delta}}k},$$

$$w = -2k^2 + \frac{\mu}{2},$$

$$a_0 = 2\sqrt{2}\sqrt{\frac{1}{\delta}}b_0 k,$$

$$a_1 = -4kb_0\frac{\sqrt{2}}{\sqrt{\frac{1}{\delta}}\delta},$$

$$a_2 = 2\sqrt{2}\sqrt{\frac{1}{\delta}}b_0 k,$$

$$b_1 = -2b_0.$$

When the found values are substituted in the $U(\vartheta)$ solutions with using Equation (5) in Equation (8), the following solution $U_{1.1}(\vartheta)$ is obtained.

$$U_{1.1}(\vartheta) = \frac{2k\sqrt{2}A^2 e^{2\vartheta}}{\sqrt{\frac{1}{\delta}}\delta(A^2 e^{2\vartheta}-1)}. \tag{9}$$

After converting solution $U_{1.1}(\vartheta)$ from an exponential function to a hyperbolic function, we obtained at the following solution.

$$U_{1.2}(\vartheta) = 2k\sqrt{2}A^2\frac{cosh(\vartheta)+sinh(\vartheta)}{\sqrt{\frac{1}{\delta}}\delta(A^2\,cosh(\vartheta)+A^2\,sinh(\vartheta)-cosh(\vartheta)+sinh(\vartheta))} \tag{10}$$
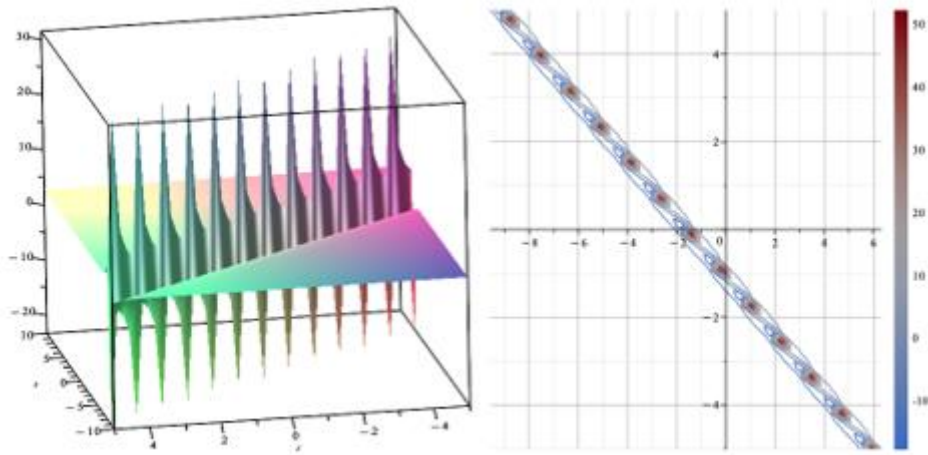
where

$$\vartheta = kx - t\left(-2k^2 + \frac{\mu}{2}\right). \tag{11}$$

Since A is free constant, we can choose the values of A randomly. If we take A=1 in solution $U_{1.2}(\vartheta)$, the Equation (6) has the following singular soliton solution

$$U_{1.3}(\vartheta) = k\sqrt{2}\frac{\left(coth\left(kx - t\left(-2k^2+\frac{\mu}{2}\right)\right)+1\right)\sqrt{\delta}}{\delta}. \tag{12}$$

Solution $U_{1.1}(\vartheta)$ contains unknown values of δ, A, k. and μ. When we choose these values as $\delta = 1, A = 5, k = 1$ and $\mu = 1$, we obtain the 3 and 2-dimensional graphics in Figure 1.

Figure 1. Solution $U_{1.1}(\vartheta)$ when $\delta = 1, A = 5, k = 1, \mu = 1$; in the range of x=[-10,10], t=[-5,5].

Case 2:

$$\mu = 2k\frac{\sqrt{2}\sqrt{\delta}\frac{v}{2} - k\delta}{\delta},$$

$$w = -k\frac{\sqrt{2}\sqrt{\delta}v - 3k\delta}{\delta},$$

$$a_0 = 0,$$

$$a_1 = -\sqrt{2}b_0\frac{k}{\sqrt{\delta}},$$

$$a_2 = -9k^2\frac{b_0}{v},$$

$$b_1 = \frac{9\sqrt{2}\sqrt{\delta}b_0 k}{2v}.$$

When the found values are substituted in the $U(\vartheta)$ solutions in Equation (8), the following solution $U_2(\vartheta)$ is obtained.

$$U_2(\vartheta) = 2v\frac{-a_2\sqrt{\delta} + \sqrt{2}b_0 k(1 + Ae^{\vartheta})}{\sqrt{\delta}\left(9\sqrt{2}b_0 k(1 + Ae^{\vartheta})\sqrt{\delta} + 2v(1 + Ae^{\vartheta})^2 b_0\right)} \qquad (13)$$

where

$$\vartheta = kx + tk\frac{\sqrt{2}\sqrt{\delta}v - 3k\delta}{\delta}. \qquad (14)$$

When we choose the values as $\delta = 5, A = 5, k = 1$ and $v = 1$ in solution $U_2(\vartheta)$, we obtain the 3 and 2-dimensional graphics in Figure 2.
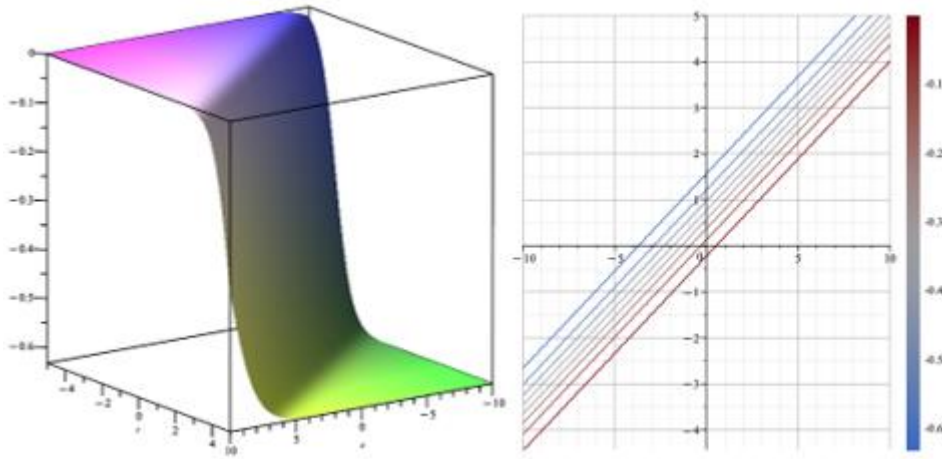
Figure 2. Solution $\mathbf{U_2(\vartheta)}$ when $\mathbf{\delta = 5, A = 5, k = 1, v = 1}$; in the range of x=[-10,10], t=[-5,5].

Case 3:

$$v = -2\delta\frac{2k^2 + \sqrt{2}\sqrt{(2k^4 + k^2\mu)} + \mu}{\sqrt{\left(\left(4k^2 + 2\sqrt{2}\sqrt{(2k^4 + k^2\mu)} + \mu\right)\right)}},$$

$$w = \left(4\left(4k^2 + 2\sqrt{4k^4 + 2k^2\mu} + \mu\right)\delta\frac{k^2}{\mu^2} + \left(4k^2 + 2\sqrt{4k^4 + 2k^2\mu} + \mu\right)\frac{\delta}{\mu} - \delta\right)\frac{\mu^2}{2\left(4k^2 + 2\sqrt{4k^4 + 2k^2\mu} + \mu\right)}$$

$$a_1 = -2a_0 ,$$

$$a_2 = -32\left(\frac{\left(k^2 - \frac{\mu}{8}\right)\sqrt{2}\sqrt{(2k^4 + k^2\mu)}}{2} + k^2\left(k^2 + \frac{\mu}{8}\right)\right)\frac{a_0}{\mu\left(4k^2 + 2\sqrt{2}\sqrt{(2k^4 + k^2\mu)} - \mu\right)},$$

$$b_0 = \sqrt{4k^2 + 2\sqrt{4\sqrt{k^4 + 2k^2\mu} + \mu})\delta}\frac{a_0}{\mu},$$

$$b_1 = -2\sqrt{4k^2 + 2\sqrt{4\sqrt{k^4 + 2k^2\mu} + \mu})\delta}\frac{a_0}{\mu}.$$
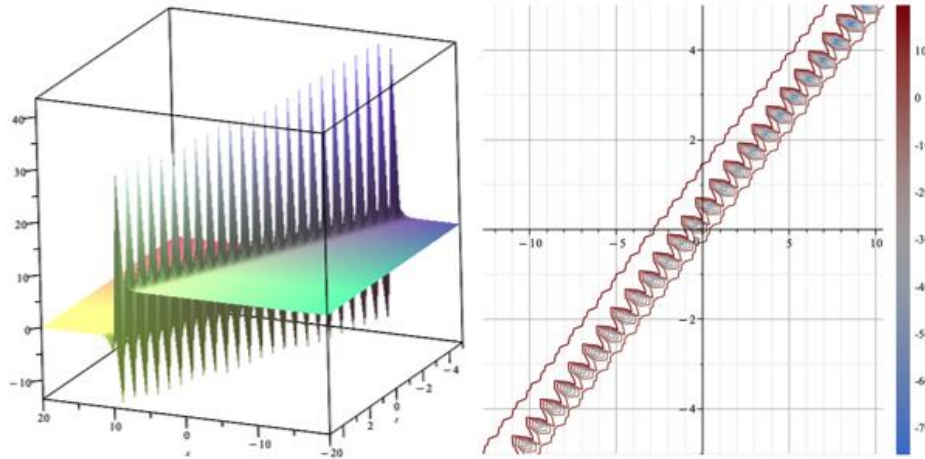
When the found values are substituted in the $U(\vartheta)$ solutions in Equation (3.3), the following $U_3(\vartheta)$ solution is obtained.

$$U_3(\vartheta) = \frac{4A^2 e^{2\vartheta}k^2\mu + 2A^2 e^{2\vartheta}\sqrt{2k^4 + k^2\mu}\sqrt{2}\mu - A^2 e^{2\vartheta}\mu^2 - 32k^4 - 16\sqrt{2}\sqrt{2k^4 + k^2\mu}k^2 - 8k^2\mu + \mu^2}{\sqrt{\left(4k^2 + 2\sqrt{2}\sqrt{2k^4 + k^2\mu} + \mu\right)\delta}\left(4k^2 + 2\sqrt{2}\sqrt{2k^4 + k^2\mu} - \mu\right)(A^2 e^{2\vartheta} - 1)} \quad (15)$$

where

$$\vartheta = kx - t\frac{\left(4\left(4k^2 + 2\sqrt{4k^4 + 2k^2\mu} + \mu\right)\delta\frac{k^2}{\mu^2} + \left(4k^2 + 2\sqrt{4k^4 + 2k^2\mu} + \mu\right)\frac{\delta}{\mu} - \delta\right)\mu^2}{2\left(4k^2 + 2\sqrt{4k^4 + 2k^2\mu} + \mu\right)}. \quad (16)$$

Solution $U_3(\vartheta)$ contains unknown values of a_0, δ, A, k and μ. When we choose these values as $a_0 = 1, \delta = 0.1, A = 2, k = 1$ and $\mu = 0.01$, we obtain the 3 and 2-dimensional graphics in Figure 3.

Figure 3. Solution $U_3(\vartheta)$ when $a_0 = 1$, $\delta = 0.1, A = 2, k = 1, \mu = 0.01$; in the range of x=[-20,20], t=[-5,5].

Case 4:

$$\delta = v^2 \frac{\sqrt{(\mu^2+4w^2)}- 2w}{2\mu\left(-\mu+ \sqrt{(\mu^2+4w^2)}\right)- 4w\left(-\mu + \sqrt{(\mu^2+4w^2)}\right)+ 4\mu^2 - 8\mu w + 8w^2},$$

$$k = \frac{\sqrt{-\mu+\sqrt{\mu^2+4w^2}}}{2},$$

$$a_1 = -2a_0,$$

$$a_2 = a_0 \frac{3\mu - 3\sqrt{(\mu^2+4w^2)}+ 2w}{\mu - 2\sqrt{(\mu^2+4w^2)}+ 4w},$$

$$b_0 = -v \frac{a_0}{\mu + \sqrt{\mu^2+4w^2}- 2w},$$

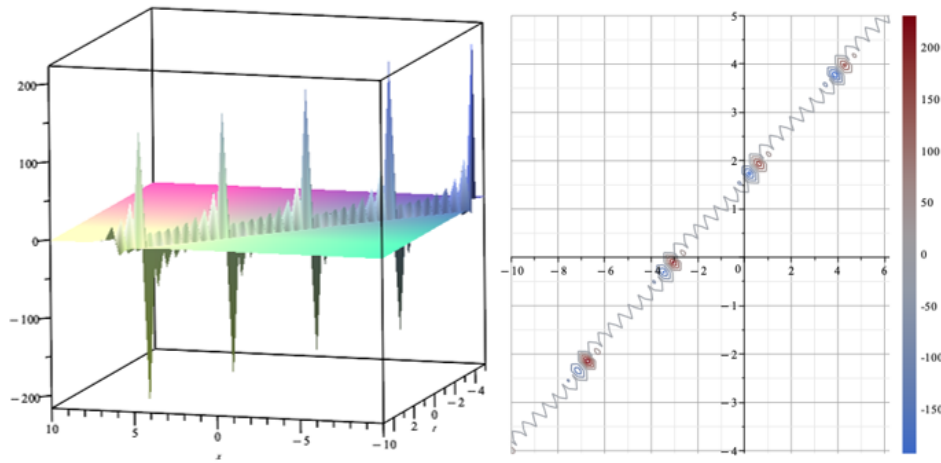$$b_1 = 2v \frac{a_0}{\mu + \sqrt{\mu^2+4w^2}- 2w}.$$

When the found values are substituted in the $U(\vartheta)$ solutions in Equation (8), the following $U_4(\vartheta)$ solution is obtained.

$$U_4(\vartheta) = -2 \frac{\left(A^2\left(\sqrt{\mu^2+4w^2}- 2w -\frac{\mu}{2}\right)e^{2\vartheta} +\frac{\sqrt{\mu^2+4w^2}}{2}+ w - \mu\right)\left(\mu + \sqrt{\mu^2+4w^2}- 2w\right)}{v\left(-\mu + 2\sqrt{\mu^2+4w^2}- 4w\right)\left(A^2 e^{2\vartheta}- 1\right)}, \tag{17}$$

where

$$\vartheta = \sqrt{-\mu + \sqrt{\mu^2 + 4w^2}}\frac{x}{2}- wt. \tag{18}$$

When we choose the values as $a_0, A = 5, w = 1, v = 1$ and $\mu = 1$ in solution $U_4(\vartheta)$, we obtain the 3 and 2-dimensional graphics in Figure 4.

Figure 4. Solution $U_4(\vartheta)$ when $a_0 = 1, A = 5, w = 1, v = 1, \ \mu = 1$; in the range of x=[-10,10], t=[-5,5].

Case 5:

$$k = \sqrt{2}\sqrt{\delta}\frac{w}{v},$$

$$\mu = -\frac{16\delta^2 w^2 - v^4}{4\delta v^2},$$

$$a_1 = -2a_0,$$

$$a_2 = \frac{8w\delta a_0}{4\delta w - v^2},$$

$$b_0 = \frac{2\delta v a_0}{4\delta w - v^2},$$

$$b_1 = -\frac{4\delta v a_0}{4\delta w - v^2}.$$

When the found values are substituted in the $U(\vartheta)$ solutions in Equation (3.3), the following $U_5(\vartheta)$ solution is obtained.

$$U_{5.1}(\vartheta) = \frac{-A^2(-4\delta w + v^2)e^{2\vartheta} + v^2 + 4w\delta}{2\delta v(A^2 e^{2\vartheta} - 1)}. \tag{19}$$

After converting solution $U_{5.1}(\vartheta)$ from an exponential function to a hyperbolic function, we obtained at the following solution.

$$U_{5.2}(\vartheta) = \frac{-A^2(-4\delta w + v^2)(cosh(2\vartheta)+sinh(2\vartheta)) + v^2 + 4\delta w}{2v\delta(A^2(cosh(2\vartheta)+sinh(2\vartheta)) - 1)} \tag{20}$$

where

$$\vartheta = -\sqrt{2}\sqrt{\delta}\frac{w}{v}x - wt. \tag{21}$$

Solution $U_{5.1}(\vartheta)$ contains unknown values of a_0, A, w, v and δ. When we choose these values as $a_0 = 1, A = 5, w = 1, v = 1 \ and \ \delta = 9$, we obtain the 3 and 2-dimensional graphics in Figure 5.
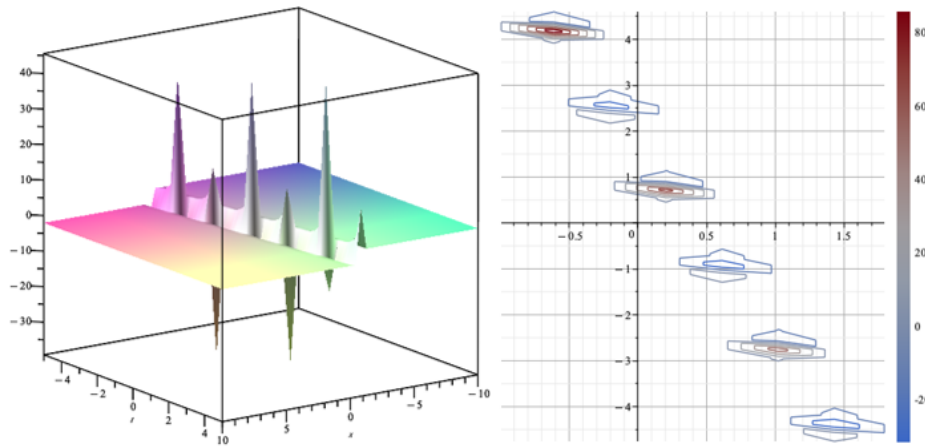
Figure 5. Solution $U_5(\vartheta)$ when $a_0 = 1, A = 5, w = 1, v = 1, \delta = 9$; in the range of x=[-10,10], t=[-5,5].

Case 6:

$$k = \frac{\sqrt{-\mu+\sqrt{\mu^2+4w^2}}}{2},$$

$$v = \left(-\mu - \sqrt{\mu^2 + 4w^2} - 2w\right)\frac{\delta}{\sqrt{\delta\left(\sqrt{\mu^2+4w^2}+2w\right)}},$$

$$a_1 = -2a_0,$$

$$a_2 = 2a_0 \frac{-(-9\mu^3 + 27\mu^2 w - 36\mu w^2 + 16w^3)\sqrt{\mu^2+4w^2} - 32w^4 + 72w^3\mu - 58w^2\mu^2 + 27\mu^3 w - 9\mu^4}{(9\mu^3 - 16\mu^2 w + 8\mu w^2)\sqrt{\mu^2+4w^2} + 16w^3\mu - 32w^2\mu^2 + 20\mu^3 w - 9\mu^4},$$

$$b_0 = \sqrt{\delta\sqrt{\mu^2 + 4w^2} + 2\delta w}\,\frac{a_0}{\mu},$$

$$b_1 =$$

$$\frac{4\delta a_0\left(27\mu^4 - 90\mu^3 w + 146\mu^2 w^2 - 112\mu w^3 + 32w^4\right)\sqrt{\mu^2+4w^2} + 64w^5 - 224w^4\mu + 300w^3\mu^2 - 208w^2\mu^3 + 90\mu^4 w - 27\mu^5}{\sqrt{\delta\sqrt{\mu^2+4w^2}+2w\mu}\left(9\mu^2\sqrt{\mu^2+4w^2} - 16\mu w\sqrt{\mu^2+4w^2} + 8w^2\sqrt{\mu^2+4w^2} - 9\mu^3 + 20\mu^2 w - 32\mu w^2 + 16w^3\right)\left(3\mu - 3\sqrt{\mu^2+4w^2} + 4w\right)}.$$

When the found values are substituted in the $U(\vartheta)$ solutions in Equation (8), the following $U_5(\vartheta)$ solution is obtained.

$$U_6(\vartheta) =$$

$$-\frac{\left(\left(\left(\frac{(w^2-2\mu w+\frac{9}{8}\mu^2)\mu A^2 e^{2\vartheta}}{2} - 2w^3 + 4\mu w^2 - \frac{19\mu^2 w}{8} + \frac{9\mu^3}{16}\right)\sqrt{\mu^2+4w^2} + A^2\mu\left(w^3 - 2\mu w^2 + \frac{5}{4}\mu^2 w - \frac{9}{16}\mu^3\right)e^{2\vartheta} - 4w^4 + 8w^3\mu - \frac{21w^2\mu^2}{4} + \frac{17\mu^3 w}{8} - \frac{9\mu^4}{16}\right)\left(\frac{3\mu}{4} - \frac{3\sqrt{\mu^2+4w^2}}{4} + w\right)\sqrt{\left(\delta\left(\sqrt{\mu^2+4w^2} + 2w\right)\right)}\right)}{2(1 + Ae^{\vartheta})\delta\left(\left(\frac{1}{2}w^4 - \frac{7}{4}w^3\mu + \frac{73}{32}w^2\mu^2 - \frac{45}{32}\mu^3 w + \frac{27}{64}\mu^4\right)\sqrt{\mu^2+4w^2} + w^5 - \frac{7w^4\mu}{2} + \frac{75w^3\mu^2}{16} - \frac{13w^2\mu^3}{4} + \frac{45\mu^4 w}{32} - \frac{27\mu^5}{64}\right)(Ae^{\vartheta} - 1)}$$

$$(22)$$

where

$$\vartheta = \sqrt{-\mu + \sqrt{\mu^2 + 4w^2}}\,\frac{x}{2} - wt. \qquad (23)$$

When we choose the values as $\mu = 5, A = 5, w = 1$ *and* $\delta = 5$ in solution $U_6(\vartheta)$, we obtain the 3 and 2-dimensional graphics in Figure 6.
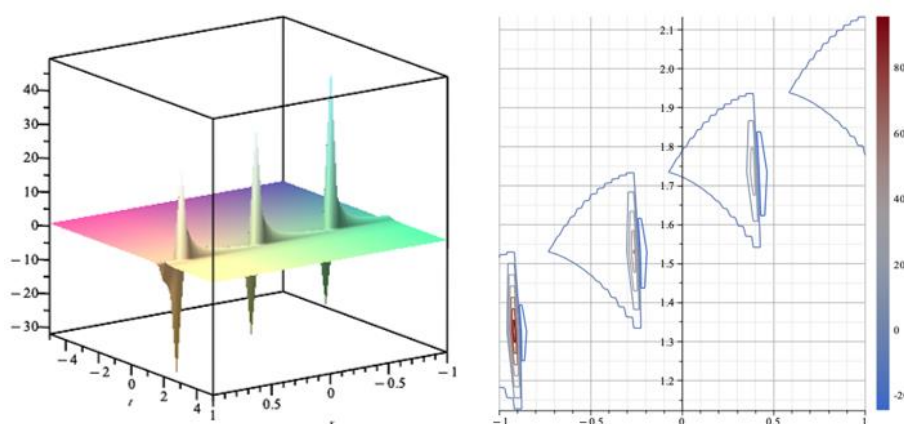
Figure 6. Solution $U_6(\vartheta)$ when $\mu = 5, A = 5, w = 1, \ \delta = 5$; in the range of x=[-1,1], t=[-5,5].

4. CONCLUSION

In this study, we examined some exact solutions of the Kolmogorov-Petrovskii-Piskunov equation using the generalized Kudryashov method. We reduced this partial differential equation to an ordinary differential equation with the traveling wave equation. We investigated the solution form in accordance with the steps of the generalized Kudryashov method. As a result, we found six cases. We obtained six solutions from these six cases, and in addition to these solutions, we found two singular soliton solutions. For our solutions, we had 3D and 2D graphics drawn with the help of Maple. The newly found hyperbolic function solutions may be particularly useful in understanding long-wave propagation, shallow water wave dynamics, and physical phenomena in plasma fluid. The results showed us the applicability of the generalized Kudryashov method to the KPP equation.

ACKNOWLEDGEMENTS

CONFLICT OF INTEREST

The author(s) stated that there are no conflicts of interest regarding the publication of this article.

CRediT AUTHOR STATEMENT

Zeynep Aydın: Software, Validation, Investigation, Resources, Writing–Original Draft, Visualization
Filiz Tascan: Conceptualization, Writing–Review & Editing, Supervision, Project administration

REFERENCES

[1]   Bluman GW, Kumei S. Symmetries and Differential Equations. Springer-Verlag, New York, 1989.

[2]   Wang M, Li X, Zhang J. The (G'/G)-expansion method and travelling wave solutions of nonlinear evolution equations in mathematical physics. Phys. Lett. A. 2008; 372(4): 417–423.

[3]   Wazwaz AM. The tanh–coth method for solitons and kink solutions for nonlinear parabolic equations. Appl. Math. Comput. 2007; 188(2): 1467–1475.

[4]   Miura RM. Backlund Transformation, Springer-Verlag, New York, 1973.

[5]   He JH, Wu X.H. Exp-function method for nonlinear wave equations. Chaos, Solitons & Fractals 2006; 30(3): 700-708.

[6]   Feng ZS. The . rst integral method to study the Burgers-KdV equation. J. Phys. A: Math. Gen. 2002; 35(2): 343-349.

[7]   Zayed EME, Shohib R, and Alngar MEM. Cubic-quartic optical solitons in Bragg gratings fibers for NLSE having parabolic non-local law nonlinearity using two integration schemes. Optical and Quantum Electronics. 2021;53(8): 452.

[8]   Ünal AÖ. On the kolmogorov-petrovskii-piskunov equation. Communications Faculty of Sciences University of Ankara Series A1 Mathematics and Statistics. 2013; 62(1): 1-10.